Development of Quantitative In Situ Transmission Electron Microscopy for Nanoindentation and Cold-Field Emission

Ludvig de Knoop

Université de Toulouse

THÈSE

En vue de l'obtention du

DOCTORAT DE L'UNIVERSITÉ DE TOULOUSE

Délivré par : *l'Université Toulouse 3 Paul Sabatier (UT3 Paul Sabatier)*

Présentée et soutenue le *21/02/2014* **par :**

Ludvig de Knoop

Development of Quantitative *In Situ* Transmission Electron Microscopy for Nanoindentation and Cold-Field Emission

---

JURY

Prof Florence Pettinari-Sturmel	Université Paul Sabatier	Président
Prof Martha McCartney	Arizona State University	Rapporteur
Prof Erdmann Spiecker	Universität Erlangen-Nürnberg	Rapporteur
Prof Karine Masenelli-Varlot	INSA de Lyon	Examinateur
Dr Bernand Deconihout	Université de Rouen	Examinateur
Dr Matthias Büchner	Université Paul Sabatier	Examinateur

École doctorale et spécialité :

SDM : Physique de la matière – CO090

Unité de recherche :

Centre d'Élaboration de Matériaux et d'Études Structurales – CEMES-CNRS (UPR 8011)

Directeurs de thèse :

Dr Martin Hÿtch et Dr Marc Legros

Development of Quantitative In Situ Transmission Electron Microscopy for Nanoindentation and Cold-Field Emission

A study of cold-field emission properties of a carbon cone nanotip using *in situ* TEM electrical probing, off-axis electron holography and finite element method (FEM) modeling; and the plastic behavior in Al thin films using *in situ* TEM–nanoindentation and FEM.

Groupe Nanomatériaux (nMAT) and
Groupe Matériaux Cristallins sous Contraintes (MC2)
Centre d'Élaboration de Matériaux et d'Études Structurales (CEMES-CNRS)
29 rue Jeanne Marvig
FR–31055 Toulouse, France
Telephone: +33 (0)5 62 25 78 00
www.cemes.fr

Author contact information:
Ludvig de Knoop
CEMES-CNRS

Telephone: +33 (0)5 62 25 78 00
Email: deknoop@cemes.fr, ludvig@deknoop.se
www.deknoop.se
www.nanofactory-user-group.org
www.in-situ-tem.com

Made with LaTeX

Printed in France
by COREP Impression
Toulouse, France 2014

To my family

Preface

IN October 2005 I attended the Quantitative Electron Microscopy School on the French Riviera, as a sales representative for a company (Nanofactory Instruments, Sweden) that I had joined only three weeks earlier. During the school, a discussion on a collaboration project for a new type of *in situ* TEM sample holder was initiated with Martin Hÿtch and Marc Legros. After an extended development project, in January 2010, I came to CEMES-CNRS for the training and acceptance of the ready holder. Eight months later I had quit my job and arrived to Toulouse to begin this PhD.

Acknowledgements

FIRST of all I would like to extend a big thank you to my supervisors Martin Hÿtch and Marc Legros for giving me the opportunity to do this thesis. Even though it meant quitting my job as a sales representative at Nanofactory Instruments, I am truly happy for moving to Toulouse to do this thesis for you. Thank you for your advices and for sharing your vast knowledges. These years have taught me so many things. So thank you once again for all the time that you have given and for your friendships. Here I would also like to thank the director of CEMES, Alain Claverie, for his support. Thank you also to the director during my first year, Jean-Pierre Launay.

I would like to acknowledge Martha McCartney and Erdmann Spiecker for taking their valuable time to be the *Rapporteurs* of the thesis, and also for traveling from the US and Germany. Thank you also to *Le Président du Jury* Florence Pettinari-Sturmel. The attendance and feedback from the remaining members of the jury, Karine Masenelli-Varlot, Mathias Büchner and Bernard Deconihout, was highly appreciated. Thank you all very much again.

Secondly, I express my deepest gratitude to my family in Göteborg, who have supported me through-out this work and in life. Dad, Mum, Tea, Gabbe, Agge, Edde och Nina, you are the reason that I'm moving back to Sweden next year! And although I'm looking forward to the move back, at the same time there are many people here in Toulouse, mentioned further down, that I will miss gravely.

The work presented in this thesis evidently stems from a lot of hard work by me, but more importantly, the work is a co-joint adventure between many people. Without their contributions, this work would not exist. I would in particular like to thank the co-authors of the two articles that we authored during my thesis. These are Florent Houdellier, Christophe Gatel, Aurélien Masseboeuf, Marc Monthioux, Etienne Snoeck and of course also Martin Hÿtch and Marc Legros.

My deepest and humblest thank you goes to Florent Houdellier, without

whom it would not have been possible to finish this work. So thank you not only for your indispensable proofreading of the thesis, but also for the research discussion in the lab, at the Melting Pot Pub and on our balconies. I have learned so many things from you! As I have said many times before, during all my trips to different laboratories around the world (when I was working as a sales representative), I have never ever met someone as genius as you when it comes to understanding and explaining the workings of and the physics behind a transmission electron microscope. Thank you for this but also for the trips to the ocean and to the mountains, while listening to Ace of Base. I'm looking forward to more of this and also to show you and Téré Sweden when you visit! And thank you for your great and invaluable friendship.

Another person who was essential for the proofreading of the thesis is Christophe Gatel. Christophe, Oh Wizard of Digital Micrograph, I know also of the countless hours you have put into processing our holograms. Thank you so much for these, for all the pleasant hours in front of the Tecnai and for the fun times at conferences.

Thank you Shay Reboh for introducing me to the wonderful world of finite element method modeling, a technique which has proven to be indispensable throughout the thesis. And for being my surf-buddy. When I arrived at CEMES I was very happy to learn about a Brazilian surfer. We have had numerous great trips to the ocean and we have many more to come.

Thank you Robin Cours, Master of the FIB, for the fun times in front of the FIB during our trial and error approach for the *in situ* samples. TEM sample preparation is tricky, sample preparation for *in situ* TEM is trickier and sample preparation for our Nanofactory holder is the trickiest. And for your kindness and friendship and for that you together with Patou insisted on only speaking French with me from the start, which must have been as frustrating for you as it sometimes was for me. But, thanks to your efforts, here I am, speaking French with only the slightest of (Toulouse?) accent ;-)

Thank you also Aurélien Masseboeuf, for sharing your expertise in manipulating a carbon cone nanotip using the FIB. And of course, thank you for the memory of you presenting at the Sfμ conference in Strasbourg barefooted!

Thanks Axel Lubk, who stayed at CEMES for the first year, for your scientific discussions, humor and trips to the ocean and to the mountains. I hope we can meet up more often then only occasionally at conferences.

Thank you Etienne Snoeck, for your geniality, positivism and help. And for taking me on as a postdoc under the ESTEEM2 project.

Thank you to the basque Arnaud Arbouet with whom I together with Florent worked briefly with for the FemtoTEM project. And Arnaud, now after that you have joined us for IMC18 in Prague, you have to come to all of the

microscopy conferences!

During these years we have had various collaborations with Nanofactory Instruments. I would like to thank all of my ancient co-workers there, not only for the good times when I worked at Nanofactory, but also for helping me out when I had questions and for the "fika-pauser" (very important Swedish coffee break) when I came to visit you.

Also the following people are worthy of a big thank you for their help on different subject:

- The ever-pleasant Aurore Pruvost for her help and patience with the numerous changes to my contracts.
- Sebastien Joulie for his instructions in TEM and help during the short time that we were working together.
- Michel Errecart, the definition of a basque; straight-forward and sometimes short-tempered; a personage that I truly like. And thanks for showing us your beautiful village La Bastide-Clairence and how to *Fêter comme un Basque*! It's a memory that I will never forget. One day I will be back in the Basque Country. And thank you also Pascal Païva for your help in different matters and for your always good humor!
- The happy office of Mireille Trupin and Clémence Vidal for help with *les missions* and similar things (sorry Mireille, I'm bringing the banana plant with me to Sweden!).
- Philippe Salles for his FIB-SEM training, mixed up with French classes, as this was just after having arrived at CEMES. This was my first shocking encounter with the strong Toulouse accent!
- When I arrived at CEMES in January 2010 as a company representative, I remember the very warm welcome that I received from Genevieve when I entered through the front doors of CEMES. This was my first memory of CEMES, and it being a very positive one. Thank you Genevieve.
- During my first year Giullio Pozzi was a guest researcher at CEMES for six months. Thank you for shared lunches and discussions on field emission and electron holography.
- Olivier Bancilhon and the friendly people at Service Informatique for their computer help, Pierre Abeilhou and the others at Service Mécanique, Lionel Pettiti and Christian Pertel at Service Électronique for their fast and competent help and friendship.

- Gerard Benassayag for insightful COMSOL discussions regarding field emission.
- Joël Douin for his patient answers to all my questions regarding the partly cumbersome process of submitting a thesis.
- Catherine and Jacque Crestou, and Dominique Lamirault for their valuable and insightful knowledge on sample preparation.
- I belonged to both the NanoMAT and the MC2 groups. Thank you to everyone of these groups.

Passing three years in Toulouse meant not only hard work, but also some recreational time. Specially since Toulouse is located within driving distance to such enticing entities as the Pyrenees and the Atlantic ocean. There were times spent with many people from CEMES, but also with people from outside of work. And there are also many people at CEMES with whom no true scientific contents were discussed. Some of these occasions were shared with the people below. Thank you to:

- The Spanish gang, Miguel, Sandra, Albertito, Jorge, Serge, Ana, Celia, Marc, partly for teaching me how to say *Sí sí claro, comprendo tódos*, a phrase which always can be used, or the weather-related important phrases *Hace bueno* and *Hace un tiempo de mi***a*.
- The Swedish speaking gang Hermann and Sviatlana.
- Miguel for our trips to the pub and the amazingly fun co-voiturage to Barcelona.
- Ana (and also Wojciech) for the numerous French classes taken together.
- Celia for amazing cakes and a fun conference in Boston.
- The third research group at CEMES; GNS, for allowing me, not being a GNSien, to join for a skiing weekend in the Pyrenees.
- Romain for his humor and for teaching me French slang (most words coming from him I usually didn't understand).
- Julien and Robin for finding the thesis presents; especially the Brice de Nice statuette that now permanently lives in the surfing van.
- Armin for friendship and our interesting discussions on Iran and USA.
- For fun times skiing with Thomas (Walther), Axel, Flo of course, Katia and Vladimir and more.

- Nikolay for his peculiar Russian humor (in fact not that far from Swedish humor).
- Marc, not only for supervising my thesis, but also for taking your time to help out with a lot of things when I arrived, e.g. apartment, washing machine and so on.
- Gilbert Combarieu for letting me use the water hose and the industrial vacuum cleaner during the numerous weekends I spent at CEMES tending to my surf-camper-van.
- The tall American-Irish Josh, with whom I during his visits to CEMES both surfed and snowboarded with.
- Nicolas Bizière for his much appreciated black humor, Arnaud and Vincent and Jesse for interesting lunch-discussion on various subjects.
- Aurélien for being The Fixer, either for QEM2013 or for IMC18. And thanks to Etienne, Béné, Cecile and Robin for fun times sharing an apartment in Prague.
- Chloé and the two Juliens, for my numerous interruptions of their work in my search for coffee. And trips to bars and mountains with them and of course also with Mr. ESTEEM2 himself; Paul Bersans (plus Flo, Téré, Victor, Robin and Zofia). I am looking forward to future trips as well!
- Thank you Téré, for all our countless occasions with Flo at The Melting Pot, Les Avions and restaurants. I greatly appreciated all our discussions. It was always good to have another foreigner around, which understands what it means to live in another country!
- I've changed office a number of times, sharing office with (in chronological order) Martin, Axel, Etienne, Florent, Marc, Luis-Alfredo, Thibaud and now Sebastien. Thanks to all of you!
- During the first year, many trips and evenings were spent with Shay, Axel, Elsa, Patricia, Mayerling, Flo and Charlotte, like for example the ski-trip to Patou's house in the Spanish Pyrenees.

And thank you to all of you not mentioned above! CEMES has been an amazing place to spend these years at. Apart from that CEMES internationally is a renowned lab, the main reason I wanted to do my thesis at CEMES was because of the friendly, open and creative environment I experienced when I visited CEMES in January 2010.

There are also people outside of CEMES that I would like to thank. Firstly, my neighbors Thomas and Bertille for your many always pleasant dinners, your huge marriage and for our travels to the ocean. I have truly enjoyed having you close by all these years and I'm looking forward to your visits to Sweden! Thank you also to Cecile, who sheltered us all (Thomas, Bertille, Marine, Martin and more) numerous times in Guéthary.

Finally, I would like to end with a congratulation to Flo, Robin, Christophe, Thomas, Bertille, Victoire and Martin for surviving the Surströmming Dinner, where we ate not only rotten fish (a speciality of northern Sweden (Non mais ALLO quoi !)), but also IKEA meatballs made out of horse-meat, stew of hairy african maggots, kopi lewak coffee, bad cake and beer which had expired. You survived (perhaps thanks to the snaps), passed the test and can now proudly call yourself Swedish Vikings (which naturally are way better than the Norwegian and Danish ones)!

Ett stort tack till er alla igen! A huge thank you to all of you again! Encore une fois, un grand remerciement à tous !

Amicalement,
Ludvig
Imsouane, Morocco

Abstract

THIS thesis has focused on *in situ* transmission electron microscopy (TEM) techniques and especially quantitative *in situ* TEM. We have used a special TEM nano-probing sample holder, which combines local electrical biasing and micro-mechanical testing. Finite element method (FEM) modeling was used to compare with the experimental results. Different electron holography techniques have been used to measure electric fields and strains.

The first part of this thesis addresses cold-field emission of a carbon cone nanotip (CCnT). This novel type of carbon structure may be used as an alternative to W-based cold-field emission guns (C-FEG), which are the most advanced electron guns used in TEMs today. When a sufficiently strong electric field is applied to the CCnT, electrons can tunnel through the energy barrier with the vacuum, which corresponds to the phenomenon of cold-field emission. The important parameters are the local electric field around the tip and the exit work function of the material.

The experiment was realized by applying, inside the TEM holder, a potential to an anode facing the CCnT. By approaching the CCnT to the anode and increasing the bias, the electric field increased until field emission began. The electrons in the imaging beam of the TEM, arriving perpendicular to the electrons emitted from the CCnT, acquire a phase shift when traveling through the strong electric field. A map of the relative phase shift was obtained using off-axis electron holography. Combining the results with FEM, a quantitative value of the critical local electric field around the tip was obtained for the CCnT emission (2.5 V/nm). Finally, using this information together with one of the Fowler-Nordheim equations, which describes the field emission process, a value of the exit work function of the CCnT is determined (4.8$\pm$0.3 eV). We have also measured the charges on the CCnT, before and after the onset of field emission.

The second part of the thesis focuses on the plastic deformation of an Al thin film deposited on an oxidized substrate to test dislocation-interface inter-

actions. Here, we used a diamond-equipped microelectromechanical system (MEMS) sensor, to measure the force transmitted to a cross-sectional type sample. This configuration allows the simultaneous observation of moving dislocations processes in the sample and a measure of the applied force. Nanoindentation of a thin sample causes it to bend, and impede a stable image formation. Here, focused ion beam (FIB) was used to sculpture electron transparent sample windows in an H-bar configuration, which provides support for the sample. FEM was used to find the optimum window size that is a good balance between the stiffness provided by the H-bar shape and the side effects generated from the bulk part of the sample.

According to dislocation theory, a dislocation close to an interface with a stiffer material should be repelled by it. The force being inversely proportional to the distance, a dislocation under an applied stress should be stationary at a certain distance from the interface. Here, we find that dislocations moving towards the oxidized interface are absorbed by this stiffer interface at room temperature. The stress at which this absorption occurs is derived from a combination of load-cell measurements and FEM calculations, and compared with supposed image force. This extends the findings of dislocation absorption at Al/SiO_2 interfaces made at higher temperatures. Finally, a first try to combine *in situ* indentation and dark-field electron holography is reported. The goal there is to acquire a strain map of the indented sample directly from phase analysis.

In addition of being a unique tool to see mechanisms unraveling in materials, *in situ* TEM techniques can nowadays provide quantitative information. This is achieved both by the development of sensor equipped TEM holders and by expanding previously static imaging techniques, modeling and analysis.

Résumé

CETTE thèse porte sur la microscopie électronique à transmission (MET) *in situ* et surtout à l'aspect quantitatif de cette technique. Nous avons utilisé un porte objet MET spécial à pointe, qui combine polarisation électrique locale et tests de micro-mécanique. La cartographie par modélisation aux éléments finis (MEF) a été utilisée pour comparer les différents résultats expérimentaux. L'holographie électronique a aussi été utilisée pour mesurer des champs électriques et de déformation.

La première partie de cette thèse traite de l'émission de champ froid d'une nanopointe faite d'un cône de carbone (CCnT). Ce nouveau type de structure carbone peut être utilisé comme une solution de rechange aux canons à cathode froide (C-FEG) à pointe de tungstène qui sont les sources d'électrons les plus avancées dans les MET modernes. Quand un champ électrique suffisamment fort est appliqué au CCnT, les électrons peuvent passer par effet tunnel à travers la barrière d'énergie avec le vide, ce qui correspond au phénomène d'émission de champ froid. Les paramètres importants sont le champ électrique local autour de la pointe et le travail de sortie du matériau. L'expérience a été réalisée en appliquant, à l'intérieur du porte-objet, un potentiel à une anode faisant face au CCnT. En s'approchant le CCnT de l'anode et en augmentant la polarisation, le champ électrique augmente jusqu'à ce que l'émission de champ se produise. La pointe est observée en même temps avec le faisceau d'électrons rapide du MET. L'holographie électronique consiste à faire interférer des électrons qui ont passé près de la pointe avec les électrons qui ont traversé une région de faible champ, ce qui permet d'obtenir une carte du déphasage relatif. En combinant les résultats avec les simulations MEF, une valeur quantitative du champ électrique local critique autour de la pointe CCnT a été obtenue pour l'émission (2,5 V/nm). Enfin, en utilisant ces informations en même temps que l'équation de Fowler-Nordheim, qui décrit le processus d'émission de champ, une valeur de la fonction de travail de sortie du CCnT est déterminée (4,8$\pm$0.3 eV). Nous avons également étudié les charges

sur le CCnT, avant et après le début de l'émission de champ.

La deuxième partie de la thèse porte sur la déformation plastique d'un film mince d'Al déposé sur un substrat oxydé pour tester les interactions des dislocation – interface. Ici, nous avons utilisé une pointe diamant montée sur un capteur de force micro-électro-mécanique (MEMS) pour mesurer la force transmise à un échantillon en section transverse. Cette configuration permet l'observation simultanée des processus de dislocations dans l'échantillon et une mesure de la force appliquée. La nanoindentation d'un film mince impose une flexion du film, ce qui perturbe l'acquisition d'image. Ici, un microscope ionique à sonde focalisée (FIB) a été utilisé pour sculpter des fenêtres transparentes aux électrons dans une configuration dite "H–bar", qui offre un maintien mécanique à l'échantillon. Les simulations MEF ont été utilisées pour trouver la taille optimale de la fenêtre, c'est à dire le bon équilibre entre la rigidité grâce à la forme en H et les effets de bord générés par la partie massive de l'échantillon. Selon la théorie des dislocations, une dislocation à proximité d'une interface avec un matériau plus rigide doit être repoussée par celle-ci. La force étant inversement proportionnelle à la distance, une dislocation sous contrainte appliquée doit s'arrêter à une certaine distance de l'interface. Ici, nous constatons que les dislocations qui vont vers l'interface oxydée sont absorbées par cette interface rigide à température ambiante. La contrainte à laquelle cette absorption se produit est dérivée d'une combinaison de mesures de forces par le capteur et de calculs MEF. Ils sont comparés à la force image supposée de la dislocation. Cela étend la validité des résultats d'absorption de dislocations aux interfaces Al/SiO_2 faites à des températures plus élevées. Enfin, un premier essai pour combiner indentation *in situ* et holographie électronique en champ sombre est rapporté. L'objectif est d'acquérir une carte des contraintes de l'échantillon indenté directement à partir de l'analyse de phase.

En plus d'être un outil unique pour voir les mécanismes actifs à l'échelle du nanomètre dans les matériaux, les techniques de MET *in situ* peuvent aujourd'hui fournir des informations quantitatives. Ceci est dû à la fois au développement des porte-objets MET équipé de capteurs et à l'élargissement des techniques d'imagerie statiques.

Table of Contents

Symbols and abbreviations in Chapters 1 and 2

TEM	transmission electron microscopy/microscope
FEM	Finite element method
CCnT	Carbon cone nanotip
C-FEG	Cold-field emission gun
MEMS	Microelectromechanical system
FIB	Focused ion beam
SEM	Scanning electron microscopy/microscope
ETEM	Environmental TEM
STM	Scanning tunneling microscopy/microscope
AFM	Atomic force microscopy/microscope
CCD	Charge-coupled device
GIS	Gas-injection system
S-FEG	Schottky field emission gun
GIF	Gatan imaging filter
TL11	First transfer lens of CEOS image C_s-corrector
PCB	Printed circuit board
hat	Part of the nanomanipulator that holds the sample (see Figs. 2.1 and 3.5)
V_{bip}	Voltage on biprism
d_{h}	Width of biprism
s	Spacing between holographic fringes in a hologram
$\Psi_{\mathrm{O,R}}$	Wave function of electron object and reference wave, respectively
$A_{\mathrm{O,R}}$	Amplitude of electron object and reference wave, respectively
$\mathbf{r}$	Position in space
$\mathbf{k}_{\mathrm{O,R}}$	Wave vector of object and reference wave, respectively
$\varphi_{\mathrm{O,R}}$	Phase of electron object and reference wave, respectively
I_{holo}	Intensity of hologram
$\overline{\Psi}$	Complex conjugate of Ψ
$\mathbf{q}_{\mathrm{c}}$	Carrier frequency
$\varphi(\mathbf{r})$	The phase measured with electron holography
$\mathcal{F}$	Fourier transform
ω	Fourier transform variable
$\delta(\omega)$	Dirac peak (in Fourier space)
V_{MIP}	Mean inner potential
GPA	Geometric phase analysis
TL11	First transfer lens of the C_s-corrector

1 Introduction

TRANSMISSION electron microscopy (TEM) is a powerful tool for characterizing materials. Although extensively used in static experiments, *in situ* TEM gives the opportunity to directly study a change in a specimen while it happens, which provides better understanding of the sample.

In situ techniques have been developed since the beginning of TEM. Without modifying anything in the microscope, the electron beam could be used for irradiation or heating experiments [Faress et al., 1994, Banhart, 1999]. To take *in situ* further, mainly two paths have been utilized.

1.1 Modifying the TEM

The first path constitutes in modifying the TEM. For example, using special apertures above and below the specimen together with differential pumping system, gases can be introduced around the specimen. This allows chemical reactions to be observed *in situ* [Boyes and Gai, 1997,Gai, 2002]. Commercially available *in situ*, or "environmental", TEMs (ETEM) exists, e.g. the Hitachi H-9500 TEM [Zhang and Kamino, 2006] or the FEI Titan ETEM G2.

More recently, developments have been made to incorporate lasers into the TEM, in order to e.g. pulse the electron beam to obtain nanosecond and even femtosecond time resolution of the measurements (see e.g. Chapter 3 in [Dehm et al., 2012] or [Espinosa et al., 2012]).

Modifying TEMs is expensive since a large part of the column needs to be altered. The benefit with an ETEM over the alternative, which is having a liquid cell mounted into the sample holder (see below), is that the sample in an ETEM is directly exposed to the electron beam (in a liquid cell, the beam has to traverse windows that confine the gas within the cell).

But, to enable electrical or mechanical probing, other solutions have to be sought.

1.2 Modifying the sample holders – *in situ* TEM holders

The second path to allow *in situ* TEM measurements is by adding the functionality directly into the sample holder. This requires no modification of the TEM. A difficulty with this approach arises from the extremely limited space available between the two pole pieces in the TEM. The smallest pole piece distance is 1.8 mm, which put special demands on the miniaturization of the parts required to construct such a holder.

By modifying the sample holder, not only chemical reactions can be observed, but also the response of the sample to e.g. electrical, magnetic or mechanical stimuli. To name a few of the holders that exist: heating, cooling or liquid cell holders or gas-injections systems allow studying vapor and liquid phases and oxidation; microelectromechanical systems (MEMS) and push-pull devices to apply and measure forces, or biasing holders to measure conductivity or to study electromigration. Adding biprisms in the TEM makes electron holography possible, with which magnetic, electric and strain fields can be examined. The latest inventions include optical fibers inside the sample holders in order to study e.g. cathodoluminescence.*

Marton was the first to examine biological samples with an electron microscope, when he in 1935 introduced a liquid cell in a sample holder [Marton, 1935]. *In situ* straining holders were developed starting from the mid 50's (see the state-of-the-art of mechanical probing holders that will be covered in Section 5.2) [Hirsch et al., 1956, Wilsdorf, 1958] and temperature holders a couple of years later [Kear, 1960]. In 1995, Lutwyche et al. managed to incorporate a scanning tunneling microscope (STM) inside the TEM [Lutwyche and Wada, 1995]. Other important work was made by Kizuka in 1998, where he observed the atomic process of a Au point contact [Kizuka, 1998a]. In 2001, Erts et al. added a three dimensional movable STM probe and atomic force microscope (AFM) to a TEM holder [Erts et al., 2001], with a continuation of the work being carried out by Svensson et al. [Svensson et al., 2003] and Nafari et al. [Nafari et al., 2008]. In the beginning, the STM-TEM combination was used to perform high-resolution scans of the sample surface that is parallel to the electron beam. Today, it is mainly used for electrical probing to locally study the current-voltage characteristics of the region of interest that has been located using the TEM [Espinosa et al., 2012].

*See `www.bnl.gov/newsroom/news.php?a=11327`.

Apart from the essential techniques that makes *in situ* measurement possible, also the imaging techniques play an equally important role. Dynamic responses in materials exposed to mechanical or electrical stresses, is much faster than the available time-resolution of a standard camera with 24 frames per second. With new cameras, that utilize direct electron detection, movies with hundreds of frames per second can be captured. These omit the step of translating electron signals to optical and then back to electrical signals, used by CCD (charge-coupled devices) cameras. But, with an acquisition time in the millisecond range, few electrons are available per image to produce images with sufficient intensity. TEM guns with higher intensity, without compromising the other properties of the gun, could perhaps provide a solution to this problem.

Good and recent review articles on partially *in situ* holders has been written by Espinosa et al. [Espinosa et al., 2012] and Petkov [Petkov, 2013]. The book *In-situ Electron Microscopy*, edited by Dehm, Howe and Zweck [Dehm et al., 2012], is warmly recommended as well.

1.3 Existing *in situ* TEM holders

In the last 5-10 years, the number of *in situ* TEM holders and companies providing them have seen a large increase. A table of such holders has been compiled below (Table 1.1).* Some of the properties in Table 1.1 can be combined, e.g. electrical probing with AFM or liquid cell. Double-tilt functionality exists for some of the holders. Another table, that summarizes well the functionality of the different *in situ* holders, can be found in the work by Espinosa et al. [Espinosa et al., 2012].

There exist also many research groups that develop new type of *in situ* holders, e.g. the groups at Mid Sweden University†, TU Delft‡, Northwestern University§, Nagoya University¶ or here at CEMES-CNRS.

In Fig. 1.1, some of the holders that were available from Nanofactory before they went bankrupt‖ can be seen. The scale is 1:1.

*The information has been obtained from `www.nanofactory.com`, `www.hysitron.com`, `www.gatan.com`, `www.hummingbirdscientific.com`, `www.fischione.com`, `www.denssolutions.com` and `www.protochips.com`.

†`http://apachepersonal.miun.se/~hakoli/`

‡`http://nchrem.nl/people/prof-dr-h-w-zandbergen-henny/`

§`mech.northwestern.edu/people/faculty/profiles/espinosa-horatio.html`

¶`http://en.nagoya-u.ac.jp`

‖Some information can be found at `www.nanofactory-user-group.org`.

TABLE 1.1 – *In situ TEM holders and the companies that manufacture them. NFI – Nanofactory Instruments, Hy – Hysitron, Ga – Gatan, HS – Hummingbird Scientific, Fi – Fischione, DS – DENS Solutions, Pr – Protochips. A question mark indicates uncertainty in the information.*

	NFI	Hy	Ga	HS	Fi	DS	Pr
Heating	–	–	★	★	–	★	★
Cooling	–	–	★	★	★	★?	–
Straining/push-to-pull devices	–	★	★	–	–	–	–
MEMS	★	–	–	★	–	★	★
Electrical biasing	★	★	–	★	–	★?	★
Manipulation	★	★	–	★	–	–	–
Nanoindentation	★	★	–	–	–	–	–
AFM	★	–	–	–	–	–	–
Cathode-luminescence/optical	★	–	★	–	–	–	–
Multiple electrical contacts	★	–	–	★	–	–	–
Liquid and/or gas cell	–	–	–	★	–	★?	★
Magnetizing	–	–	–	★	–	★?	–
Double-probe	★	–	–	–	–	–	–
Tomography	–	–	★	★	★	–	–

1.4 Challenges with *in situ* TEM holders

As more and more techniques are being demanded by scientists to be added to the *in situ* holders, it is now not only the pole piece which is the limiting factor, but the TEM holder rod itself. The three main manufacturers of TEMs; Hitachi, FEI and JEOL, all have different sized sample holders. For example, the rod diameter of a standard FEI sample holder is 6.6 mm, whereas for a Hitachi it is 8 mm. On the other side of the scale, the JEOL holder has a diameter of 16.5 mm (see a comparison between an FEI and a JEOL holder in Fig. 1.1 (a) and (b)). With the extra space available in the JEOL holders, not only does some *in situ* holders exist only for JEOL TEMs, but also the double tilt range is increased, when compared with an FEI or Hitachi holder. On the other hand, the most common JEOL TEM is the version with ultra-high resolution pole piece gap, where the distance between the pole pieces is only 1.8 mm, thus making the large diameter of the body of the holder inutile.

Another problem that often trouble *in situ* experiments comes from the instability of the TEM stage for moving the sample holder in x, y and z (the

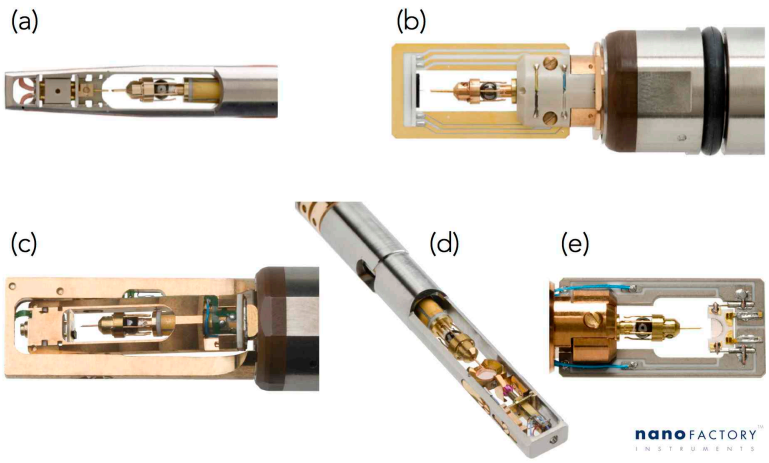

FIGURE 1.1 – *Some examples of Nanofactory in situ holders. The scale is 1:1. (a) Electrical probing holder for FEI. (b) Nanoindenter holder for JEOL. (c) Double-tilt AFM holder for JEOL. (d) Double-tilt electrical probing holder for FEI. (e) Multiple contact holder for JEOL. All images copyright Nanofactory Instruments.*

goniometer). Also here, the difference between the manufacturers is large. For example, the stability of the JEOL piezo-driven goniometer is superior to the others. The Hitachi goniometer is very stable, but suffers from having a sapphire contact point in the very front of the holder (which is the same for Zeiss and older Phillips TEMs).* For *in situ* holders, where optimization of available space is crucial in order to fit as many techniques as possible, sometimes a small amount of material in the holder frame remains. When the goniometer moves the stage in y direction (see Fig. 2.1 for the definition of the directions), the holder will shear, which can be observed as a relative motion between the probe and the sample. The FEI goniometer is the most troublesome of the TEMs that I have used.† When using these, the sample and probe should be out of contact when moving the stage.

In conclusion, if a demand could be made to the TEM manufacturers on the specifications for their next TEM, I would ask for thicker rods in combination with a wide pole piece gap and piezo-driven goniometers.

*This is used to translate the holder in the $-x$ direction, i.e., out of the TEM.

†To put some quantified data behind this statement, I have used around 35 FEI, 15 JEOL, 5 Zeiss and a couple of Hitachi TEMs.

1.5 The contents of this thesis

In this thesis we are going to concentrate on nanoindentation and local electric field measurements. The main limitation of *in situ* TEM is to be quantitative, which is what we are trying to address here [Legros et al., 2010]. We have used an *in situ* TEM holder which has a piezo and MEMS load-sensor to apply and measure a force, and an electrical circuit for biasing measurements. Combining this with electron holography and modeling, fully quantitative data could be obtained.

The thesis is divided up in the following way. Succeeding this introductory chapter, sample preparation and experimental techniques are covered in Chapter 2. Here, the unique *in situ* TEM holder that we have used and the holography techniques will be explained in detail.

Following these chapters, *Part I* contains two chapters that covers results from electron cold-field emission of a carbon cone nanotip (CCnT). More specifically, Chapter 3 is about characterization of important field emission parameters, while Chapter 4 shows results from counting charges before and during the onset of field emission, using a recent developed technique.

In *Part II*, Chapter 5 shows plastic deformation of Al thin films on oxidized Si substrate. Here, interfacial dislocations appear to be absorbed by interfaces to a stiffer material. Radius of curvature measurements have been made to verify finite element models that were used to obtain a strain map of the film.

In the final chapter, apart from the conclusions, a perspective experiment where dark-field electron holography combined with *in situ* nanoindentation is discussed. Some first results are shown as well.

Symbols and abbreviation have been put in the beginning of each chapter, except for the first two chapters, were this has been put after the Table of Contents. State-of-the-art will be covered in beginning of each chapter.

I, the writer of this thesis, have performed the following work. I have been handling and controlling the *in situ* TEM holder. For the sample preparation, I have done the extraction of the CCnT and focused ion beam (FIB) milling for the samples in Chapter 5, using a FIB-SEM (scanning electron microscope). All modeling has been done by me. I have extracted phase maps from the holograms, but in some cases with the help of others (their contributions are mentioned in the appropriate parts of the text). I have done the analysis and interpretation, but with input and help from others.

2 Experimental techniques

THE experimental techniques in this thesis comprises of different sample preparation techniques, transmission electron microscopy (TEM) techniques and modeling.

For the sample preparation, a short introduction of tripod polishing and focused ion beam-scanning electron microscope (FIB-SEM) will be presented.

Following, the different TEM techniques are covered, with focus on the specialized *in situ* TEM sample holder that enable electrical and force probing and that has been used throughout this thesis. The special requirements and characteristics that comes with such a holder are discussed.

Electron holography has ben used extensively, and has been explained in detail, including the new technique of dark-field electron holography.

Finite element method (FEM) modeling is introduced here, with a more thorough explanation on how it has been used in their respective chapter.

2.1 Sample preparation

We will start by defining two kinds of samples. One being suitable for *in situ* and the other for conventional TEM. Let us artificially call them the *in situ* and the non-*in situ* sample.

The non-*in situ* sample needs to have a large area that is transparent to electrons. A good *in situ* sample is defined by other criteria being important, e.g. stability when doing nanoindentation or electronically well connected when doing electrical probing. In the following two sections, the general sample preparation will be explained. For this work, where different *in situ* TEM methods has been used, the peculiarities of each sample preparation will be specified separately in Sections 3.3.3 and 5.3.2.

2.1.1 Tripod polishing

For a sample to be used in a TEM, it needs to be thin enough to be electron transparent. The tripod (South Bay Inc.) consists of a metal assembly that you hold in your hand over a rotating polishing wheel in order to mechanically thin down a sample to usually a couple of μm [Williams and Carter, 2009]. By using an extremely fine final polishing paper, it is possible to directly thin down a sample to electron transparency, but for the samples used in this thesis this was not feasible for reasons that will be discussed in Section 5.3.2. To further thin down the sample to the required thickness, other techniques has been used (see Section 2.1.2 below).

2.1.2 Focused ion beam and dual-beam

A focused ion beam (FIB) is used to perform basic operations on a bulk sample like cutting, welding and milling. This makes it very useful for TEM sample preparation. The interest of the so called dual-beam FIB systems is that the microscope incorporates all the functionality of a scanning electron microscope (SEM). The electrons are mainly used for observing the sample, while the ion beam is used for milling, welding or depositing protection layers. In order to further protect a sample, also the electron beam can be used for the latter.

A gas-injection system (GIS) system was used in order to weld the samples onto their support, or for depositing protective layers. It consists of needles (see e.g. Fig. 3.4 (g)) that contains a tungsten- or platinum-precursor gas, which when illuminated by the ion beam is transformed into a solid weld. The weld is electrically well conducted, which is required in order to prevent charging of the sample from then electron beam in the TEM, and to ensure a good conductivity necessary for electrical measurements.

The ion and electron parts of the microscope consists of a gun that generates a beam, accelerated under 1–30 kV, followed by deflectors and electromagnetic lenses for deflecting and condensing the beam. The sample sits on a stage, which can tilt, rotate and move in x, y and z. When the ions or electrons, focused into a small spot, scans over the surface they interact with the atoms in the sample, creating a number of signals. These signals, collected by detectors nearby, can contain information about the topography or chemical composition of the sample. The output from the detectors together with the position of the beam creates the image.

The FIB-SEMs used, a Cross Beam XB 1540 (Zeiss) and a Helios Nanolab 600i (FEI), where also equipped with a Kleindiek microtweezer and an Omniprobe probe, respectively, which were used to manipulate the sample mechanically.

For this thesis, the ion beam has been utilized to cut carbon cone nanotips (CCnTs) in halves and weld them onto supports, and mill out H-bar structures for nanoindentation. See Sections 3.3.3 and 5.3.2 on how this has been done.

2.2 TEM Techniques

2.2.1 The TEM

How a TEM functions will not be described. For the interested reader on the basics of TEM, see Williams and Carter [Williams and Carter, 2009], or De Graef for conventional TEM techniques [De Graef, 2003].

The TEM that has been used is a FEI F20 with a Schottky field-emission gun (S-FEG) and a C_s (spherical aberration) imaging corrector from CEOS GmbH. Just like for the SEM, it consists of deflectors to tilt and shift the beam, electromagnetic lenses to change the electron dose, the size of the beam and to create an image, and cameras and detectors to record images and signals. The microscope has been used in 100 and 200 kV mode. It is equipped with a USC1000 2k camera (Gatan), a Gatan imaging filter (GIF) Tridiem 865 and a rotatable biprism (FEI). The first transfer lens in the corrector (TL11) has been used as a Lorentz lens, which was made possible using the free-lens control software of the TEM.

For controlling the TEM, software version FEI 3.1.3 was used. For the camera and acquiring of images, GMS 1.9.5 with DigitalMicrograph 3.9.5 (Gatan) was utilized. The Nanofactory Instruments *in situ* holder was operated with versions 3.5.2.0 to 3.6.3.0 of the software NFC, with either the electrical or the nanoindentation mode activated. To correlate experimental data from NFC with TEM images, the software CamStudio captured the screen. At some times, a dedicated correlation plug-in to NFC was used. This enabled direct correlation by imprinting data on each captured video-frame.

2.2.2 The *in situ* TEM sample holder

The holder (Figs. 2.1 and 2.2) used in this thesis was a commercially manufactured *in situ* TEM sample holder, developed as a collaboration project between CEMES and Nanofactory Instruments AB. The holder is specialized in the sense that it is possible to either use it for electrical probing or for nanoindentation. For the former, one can apply up to 140 V between the probe and the sample, and with the latter one can indent the sample using a diamond tip while measuring the force using a microelectromechanical system (MEMS) sensor. Sensors of different force ranges have been used, with sensor spring

constants varying between 450 N/m and 5000 N/m (which also approximately equals the maximum force in μN). The noise floor depends on the sensor, but usually ranges from 0.5 μN to 3 μN.

What makes the holder unique, is the double- or β-tilt functionality, which allows the holder to be tilted $\pm 4^{\circ}$ around a second axis (the tilt around the axis parallel with the length-axis of the holder, the α-tilt, is done by the TEM stage). The double-tilt is realized by a piezo step-motor, attached to the back of the holder. It controls a rod and a plate that transfers the forward motion to a rotating one. In the front part of the holder, an inner frame that contains the piezo tube, sample and sensor part, are tilted together. The inner frame and one of the two pivot points around which the frame revolves, can be seen in the bottom part of Fig. 2.1. Having such a long inner frame combined with the very restricted space between the TEM pole pieces, explains the limited β-tilt range.

The holder has a piezo, with which coarse and fine motion is controlled, from sub-nanometers to millimeters. This will be explained in detail in the following section.

2.2.2.1 The nanomanipulator

In order to make a contact between the probe and the sample, one of them needs to approach the other. This is done with a nanomanipulator, which sits in the front part of the holder, where a piezo tube is used for both the coarse and the fine motion (see Fig. 2.1). The piezo is driven by maximum ± 140 V, connected to five electrodes. Two each for the y- and z directions and one for the x. The directions are defined in Fig. 2.1. This definition is consisted throughout the thesis, with the directions being marked out in almost every image. The piezo has a sensitivity of around 5 nm/V in the x direction and 50 nm/V for the y- and z directions.

The coarse motion is realized by a so called slip-stick motion. By applying a short negative pulse on e.g. the x-electrode, the piezo will become around 1 μm shorter. Since the pulse is in the μs range, the friction between the ball and the hat (where the sample is attached, see Figs. 2.1 and 3.5) will be overcome, making the hat slip over the ball a distance of a couple of hundreds of nm to tens of μm, depending on the applied voltage. Following this, the piezo is elongated with a long pulse, making the hat and ball move together (i.e., stick). This is repeated numerous times in order to move the hat/sample to a wanted position. Similarly, to move the hat in the y- and z directions, the other electrodes are used.

The coarse motion is neither accurate nor repeatable, so when the the probe

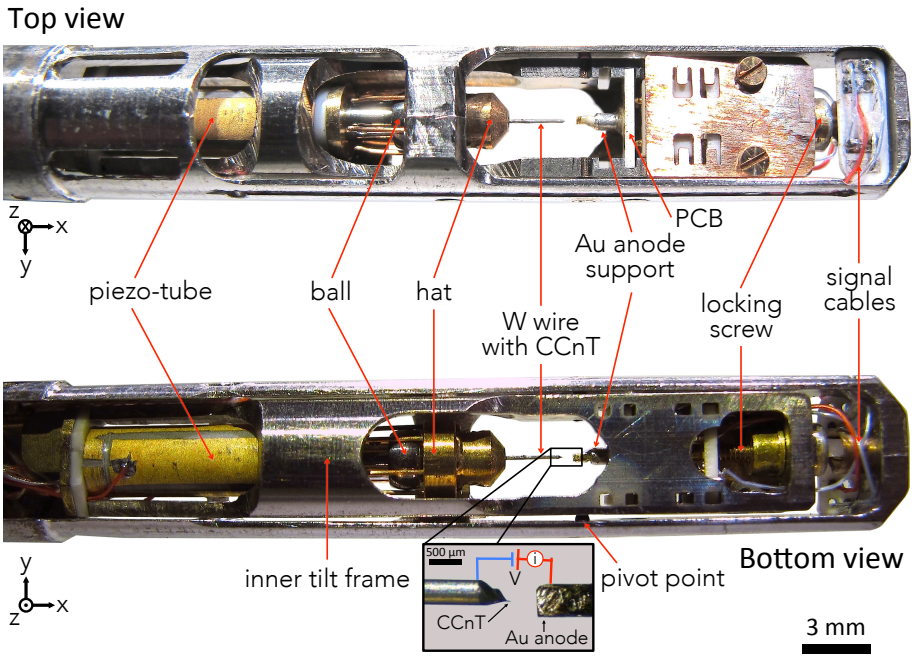

FIGURE 2.1 – *The front part of the holder, here configured for electrical probing. The nanomanipulator, which comprises of the piezo-tube, ball and hat, which carries the W wire where a carbon cone nanotip (CCnT) is welded onto can be seen in both top- and bottom view. Opposite the CCnT is the Au-anode mounted into the tube sitting on the printed circuit board (PCB). The locking screw secures the PCB and makes sure the contacts between the signal cables and the PCB are good. In the bottom-view, one of the two pivot points can be seen, around which the inner frame revolves, thus enabling a β-tilt of $\pm 4°$. In the bottom view a scheme of the electrical circuit is illustrated between the CCnT and anode. The definition of the x, y, z directions, with the electrons in the imaging beam going in the z direction, will be used consistently throughout this thesis.*

is positioned within range of the sample, the fine motion is used. By applying long pulses on the piezo in the three directions [Svensson et al., 2003], the hat/sample will move together with the piezo. The range of the piezo is 700 nm for x and 7 μm for y and z. The spatial resolution on the movement is less than 0.2 pm in x and 2 pm in y and z, but, due to the noise level in the applied voltage, it is diminished to < 0.02 nm for x and < 0.2 nm for y and z. When relying on the piezo to measure distances, e.g. during nanoindentation, caution of a piezo's inherent properties of creep and hysteresis has to be made. For these occasions, calibration images using the camera of the TEM should be used.

2.2.2.2 *Electrical probing*

In Fig. 2.1, the holder has been configured for electrical probing. The printed circuit board (PCB) with a tube with a diameter of 0.4 mm has been mounted in the holder. It is secured with the locking screw at the right end of the holder. In Fig. 2.1, a Au anode has been inserted into the tube, secured with Ag epoxy. Au pads running through the PCB connects the bias applied to the anode to the wires in the front part of the holder (only one of the four wires are used during electrical probing). The nanomanipulator, where for this thesis a CCnT has been attached (see Chapter 3), is connected to ground.

2.2.2.3 *Nanoindentation and the MEMS sensor*

In Fig. 2.2 the holder is configured for nanoindentation, by exchanging the PCB with a tube in Fig. 2.1 to one where a MEMS sensor has been attached. The sensor is electrically connected with the PCB via two bond-wires, which are used for its capacitive force read-out. A diamond tip is perpendicularly glued onto the upper plate of the capacitor (see Fig. 2.2), which hinges on eight Si-springs. The bottom plate is fixed and separated 1.5 μm to the upper plate. With a load applied to the diamond tip, the distance between the plates decreases and the capacitance increases, which is translated into a force via some calibration values. In short the calibration is done by putting known weights onto the sensor, which together with the gravitational acceleration gives a force for a given capacitance [Nafari et al., 2007]. In other words, after the nanomanipulator has been used in its coarse slip-stick motion mode to approach the sample to the diamond-tip, the fine motion of the piezo is used as a transducer, to push the sample into the diamond tip. The sample in Fig. 2.2, being a 1.5 mm wide tripod sample, is glued onto a mechanically cut Cu grid (originally being 3.05 mm wide), which is glued using Ag epoxy onto a wire with a diameter of 0.33 mm. The wire with sample is inserted into the hat, secured by two locking screws situated on each side of the hat.

2.2.2.4 *Ease of use*

Fitting so many techniques into a TEM sample holder is not an easy feat, considering the limited space available, due to the small diameter of the sample holder.* There is an inverse relationship between complexity and usability, that is, the trade-off by having a combination of many techniques, is that it will hamper the ease of use. For example, the β-tilt, where the sensor plus the entire manipulator (which comprises of the piezo and the sample mounting

*In some cases, e.g. for a JEOL TEM equipped with ultra-high resolution pole pieces, the distance between the pole pieces is the limiting factor, being 1.8 mm.

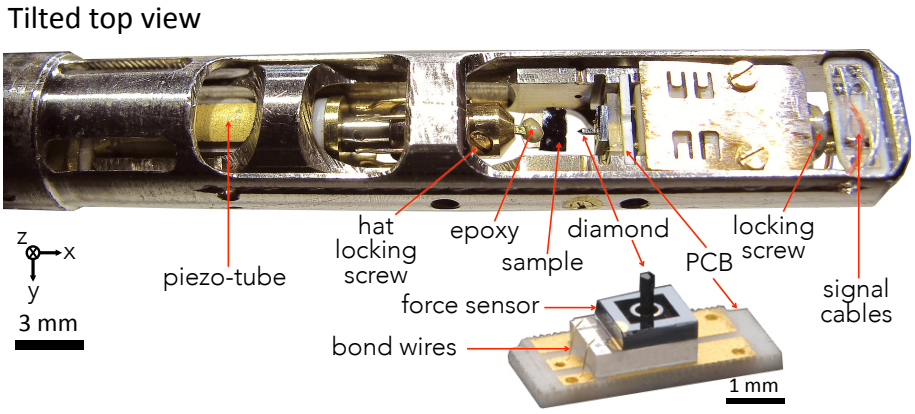

FIGURE 2.2 – *The front part of the holder, here configured for nanoindentation. The nanoindentation MEMS sensor is the black square with the diamond tip sticking out in the middle.*

structure) is tilted the space available for the sample is diminished. So instead of the standard 3.05 mm sized grid, an ideal maximum width of the sample is 1.5 mm (see Fig. 2.2). And when using the holder for electrical probing, the space for the probe or the sample is very limited, as one of them has to be of a maximum length of 1 mm and secured in a cylinder using friction or glue (see the Au anode support in Fig. 2.1).

2.2.3 Off-axis electron holography

Electron holography is a technique invented in 1948 by Dennis Gabor to improve the resolution of TEM by removing the effect of lens aberrations affecting the electron phase [Gabor, 1948]. The idea of Gabor was to retrieve the phase from an interference between two electron waves. One wave should be unperturbated, and the other modified in phase through interaction with the sample.

Later on, by adding a thin and positively biased wire (biprism), Möllenstedt and Düker [Möllenstedt and Düker, 1955] developed off-axis electron holography [Lichte, 1986, McCartney and Smith, 2007]. The biprism divides the incoming wave packet in two. The part of the beam going through the sample is called the object beam whereas the part going through vacuum is called the reference beam. These two beams do not have the same optical axis, which explains the name off-axis electron holography. Since the biprism is positively biased, the two beams will converge and interfere*, which creates holographic fringes that contain information about the phase shift between the reference

*Even though we say "beam", it is in fact the wave packet of each electron that is divided and interfered with itself [Tonomura, 1987].

and the object wave. The fringes superimposed with the amplitude image, is called the hologram, which is then observed in a plane below the biprism. See Figs. 2.3 and 2.4 (a).

To maximize the contrast of the fringes*, the electrons should be spatially coherent and parallel. High spatial coherence is obtained by using a FEG since the emitter tip is very sharp, thus the electrons are emitted from a small area†. The most coherent FEG is the cold-FEG (C-FEG), but the most commonly used is the Schottky FEG (S-FEG)‡. High coherence in only needed in the direction perpendicular to the the biprism and fringes. By elongating the beam (i.e., making it elliptic) in the direction perpendicular to the biprism, the coherence is increased in this direction while decreased in the other [Midgley, 2001].

The voltage (V_{bip}) applied on the biprism determines the size (d_{h}) of the hologram and the spacing between the fringes (s). A higher voltage gives a wider hologram and a smaller fringe spacing ($\nearrow\ V \Rightarrow \nearrow\ d_{\mathrm{h}}$ and $\searrow\ s$) and *vice versa*. The formula for the width of the hologram and the fringe spacing, can be found for example in [Midgley, 2001]. The distance between the fringes correlates directly with the spatial resolution of the phase that is later obtained from the hologram. Using highly coherent electrons makes it possible to use a fine spacing between the fringes but still have enough contrast in the hologram. If the contrast is lost, no data can be extracted from the fringes.

When recording an image in TEM, the information about the phase is lost, as can be seen in eq. (2.1). If we define an electron's wave function§ as $\Psi = A(\mathbf{r})\mathrm{e}^{i\varphi(\mathbf{r})}\mathrm{e}^{2\pi i\mathbf{k}\cdot\mathbf{r}}$, where $A(\mathbf{r})$ is the amplitude at a position $\mathbf{r} = (x, y, z)$ in space, $\mathbf{k}$ is the wave vector and $\varphi(\mathbf{r})$ is the phase, then the intensity $I(\mathbf{r})$ of the image can be described as

$$I(\mathbf{r}) = |\Psi|^2 = \Psi \cdot \overline{\Psi} = A^2(\mathbf{r}) \tag{2.1}$$

where $\overline{\Psi}$ is the complex conjugate of Ψ. The idea of electron holography is that the electron phase can be retrieved as well. In other words, the complete information of the wave function can be obtained, amplitude and phase.¶.

*The contrast is defined as $\mu = \frac{I_{\max} - I_{\min}}{I_{\max} + I_{\min}}$, where $I_{\max/\min}$ is the maximum and minimum intensity of the fringes, respectively [Völkl et al., 1999].

†A technique usually utilized in EELS to improve the temporal coherence, but that we have seen to also increase the spatial coherence, is to set the gun to telefocus mode. In this mode the beam has its first crossover after the accelerator. In other words, the coulomb-interactions of the electrons (the Boersch effect) take place in a faster part of the gun and is therefore less important. In the mode usually used, the cross-over mode, the first cross-over occurs inside the accelerator, which leads to the Boersch effect being more important.

‡Electron emission in general and cold-field emission in particular will be discussed in Chapter 3.

§The wave function is a solution to the Schrödinger equation, being the partial differential equation that portray the quantum state of in this case an electron.

¶This also explains the name; in Greek, the words *hólos* means whole and *gramma* means something written or drawn.

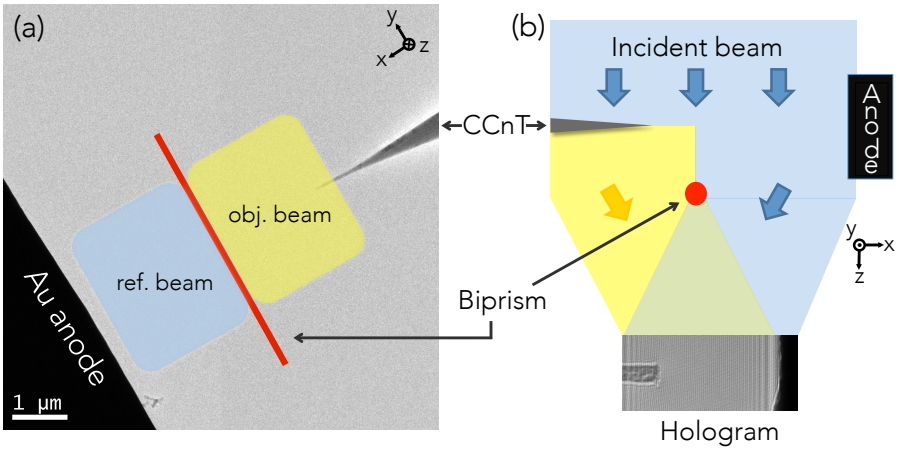

FIGURE 2.3 – *(a) A TEM micrograph showing the Au anode and the apex of a CCnT plus drawings showing the biprism splitting the beam into a reference and an object part. In (b), a side view of the same setup, with the two beams converging and creating the hologram can be seen.*

2.2.3.1 *Retrieving the electron phase*

When the object and reference waves traverse regions with different potentials, they will obtain different phases.

Let us start by defining the wave function of the object beam for $\Psi_{\mathrm{O}} = A_{\mathrm{O}}(\mathbf{r})\mathrm{e}^{i\varphi_{\mathrm{O}}(\mathbf{r})}\mathrm{e}^{2\pi i\mathbf{k}_{\mathrm{O}}\cdot\mathbf{r}}$, $A_{\mathrm{O}}(\mathbf{r})$ being the amplitude, $\varphi_{\mathrm{O}}(\mathbf{r})$ being the phase and $\mathbf{k}_{\mathrm{O}}$ being the wave vector, for the object wave. Similarly we have $\Psi_{\mathrm{R}} = A_{\mathrm{R}}(\mathbf{r})$ $\mathrm{e}^{i\varphi_{\mathrm{R}}(\mathbf{r})}\mathrm{e}^{2\pi i\mathbf{k}_{\mathrm{R}}\cdot\mathbf{r}}$ for the reference wave.

By setting the reference amplitude $A_{\mathrm{R}} = 1$, the reference phase $\varphi_{\mathrm{R}} = 0$ and by using Euler's formulae $\mathrm{e}^{\pm i\alpha} = \cos\alpha \pm i\sin\alpha$ we get that [Völkl et al., 1999, Dunin-Borkowski et al., 2003]

$$\begin{aligned} \mathrm{I}_{\mathrm{holo}}(\mathbf{r}) &= |\Psi_{\mathrm{R}} + \Psi_{\mathrm{O}}|^2 = |1 + \Psi_{\mathrm{O}}|^2 = \left(1 + A_{\mathrm{O}}(\mathbf{r})\mathrm{e}^{i\varphi_{\mathrm{O}}(\mathbf{r})}\right)\left(1 + A_{\mathrm{O}}(\mathbf{r})\mathrm{e}^{-i\varphi_{\mathrm{O}}(\mathbf{r})}\right) \\ &= 1 + A_{\mathrm{O}}^2(\mathbf{r}) + 2\,A_{\mathrm{O}}(\mathbf{r})\cos\left(2\pi\mathbf{q}_{\mathrm{c}}\cdot\mathbf{r} + \varphi(\mathbf{r})\right) \end{aligned} \tag{2.2}$$

So, in the plane of the hologram the intensity distribution can be seen as a cosine term with periodicity $\mathbf{q}_{\mathrm{c}}$ (carrier frequency) and phase φ. The carrier frequency $\mathbf{q}_{\mathrm{c}}$ is the vector describing the different paths of the reference wave and the object wave, having travelled on different sides of the biprism, i.e., $\mathbf{q}_{\mathrm{c}} = \mathbf{k}_{\mathrm{R}} - \mathbf{k}_{\mathrm{O}}$. The phase shift from having gone through the sample is $\varphi(\mathbf{r}) = \varphi_{\mathrm{R}} - \varphi_{\mathrm{O}}$. This is the phase measured with electron holography.

Equation 2.2 describes mathematically the nature of the hologram, with the first two terms in the result of the equation corresponding to the image,

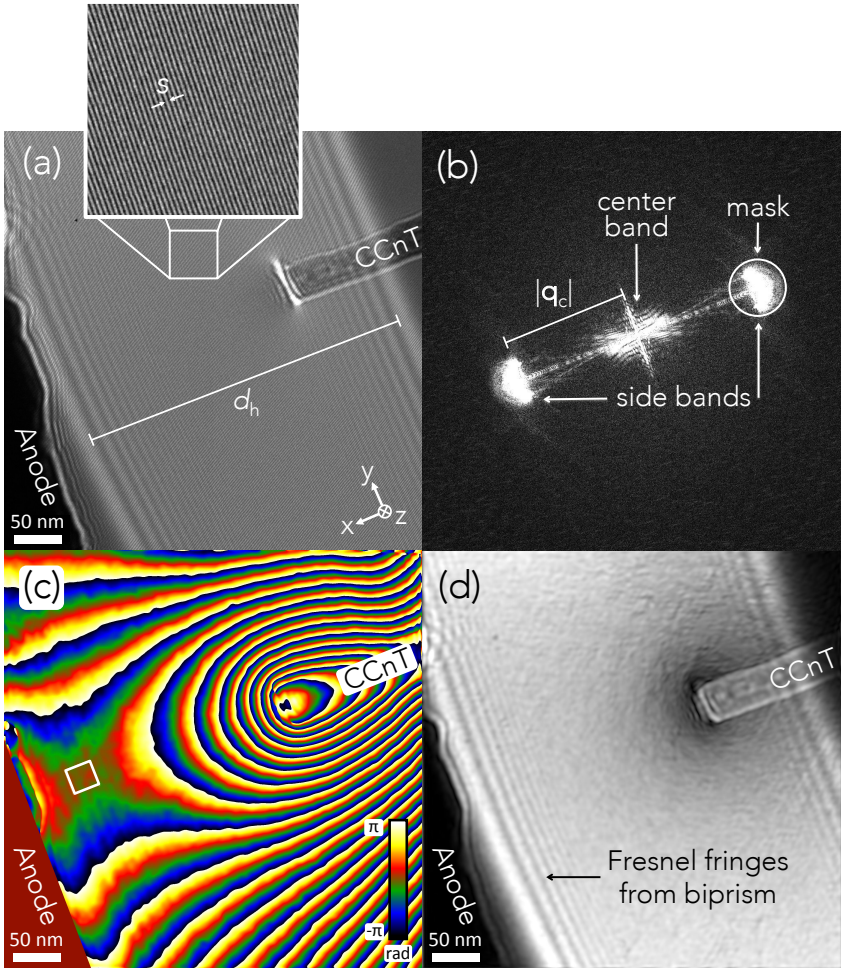

FIGURE 2.4 – *(a) Hologram of the Au anode and the apex of a CCnT, showing the hologram width d_h and fringe spacing s in the inset. (b) A 2x magnified Fourier transformation of (a), with q_c being the carrier frequency vector. Inverted Fourier transformation of the circled sideband towards the CCnT reconstructs the phase image seen in (c) (the white square indicates the area of the internal reference area) and the amplitude image seen in (d).*

whereas the fringes are the cosine term.* In the hologram in Fig. 2.4 (a), which displays a CCnT and anode, one can see the superposition of the image and the holographic fringes. The inset shows a zoom-in of the fringes. The larger, unevenly spaced fringes are Fresnel fringes, which are a result from interaction between the beam and the edges of the biprism (see Fig. 2.3 (b)†). These

*The cosine wave shape can be seen in the fringes in the inset in Fig. 2.4 (a), since the intensity extremes in the hologram are the maxima and minima of the cosine term.

†They can also be seen in the Fourier transformed image in Fig. 2.4 (d) as the white lines between the center band and the sidebands.

are artifacts, and how they can be removed will be explained further down.

To calculate the phase shift a Fourier transformation $\mathcal{F}$ of the hologram is done, which results in a complex image like the one in Fig. 2.4 (b). Mathematically this is described as follows.

$$\mathcal{F}\big(I_{\mathrm{holo}}(\mathbf{r})\big) = \delta(\omega) + \delta(\omega) \otimes \mathcal{F}\big(A_{\mathrm{O}}^2(\mathbf{r})\big) + \delta(\omega + \mathbf{q}_{\mathrm{c}}) \otimes \mathcal{F}\big(A_{\mathrm{O}}(\mathbf{r})\mathrm{e}^{i\varphi_{\mathrm{O}}(\mathbf{r})}\big) + \delta(\omega - \mathbf{q}_{\mathrm{c}}) \otimes \mathcal{F}\big(A_{\mathrm{O}}(\mathbf{r})\mathrm{e}^{-i\varphi_{\mathrm{O}}(\mathbf{r})}\big) \quad (2.3)$$

where ω is the transform variable. The four terms in the equation correspond to different parts of the Fourier transformed hologram in Fig. 2.4 (b). In the center of the complex image, i.e., for $\omega = \mathbf{0}$, the first term, $\delta(\omega)$, is the Dirac peak coming from the homogenous intensity of the reference beam, since we earlier had set its amplitude $A_{\mathrm{R}} = 1$. The second term, also in the origin, corresponds to the Fourier transformation of the intensity of the object. These are the center band. The last two terms are Dirac peaks positioned at $\omega \pm \mathbf{q}_{\mathrm{c}} = 0$, convoluted with the Fourier transformation of the object wave and its complex conjugate. These are the sidebands and can be seen in the image 2.4 (b) displaced $-\mathbf{q}_{\mathrm{c}}$ and $\mathbf{q}_{\mathrm{c}}$ from the center.

Now, in order to reconstruct the phase and the amplitude images we select only the low frequencies of one of the sidebands. This is done by first placing a mask around it, centered at a position $\mathbf{q}_{\mathrm{c}}$, as can be seen in Fig. 2.4 (b)*. Then, the mask is shifted to the center of the image ($\omega = 0$) and finally an inverse Fourier transformation is applied to the information inside the mask. This reconstructs the phase and amplitude images solely from the frequencies chosen. When choosing a sideband the software centers the mask here. By using an internal reference area in the phase image (depicted as a white rectangle in Fig. 2.4 (c)) we can manually shift the mask slightly, in order to center it to where we believe the highest intensity in the sideband is. In the phase image, this is where the presence of the sample (i.e., the area where you want to measure the phase) should affect the phase difference the least.

2.2.3.2 Using a reference hologram

The presence of a CCD camera, projectors, lens aberrations and the mean inner potential (V_{MIP}) of a sample usually introduces unwanted phase shifts. These and the before mentioned biprism Fresnel fringes can normally easily be removed by subtracting a so called reference hologram from the sample holograms [Völkl et al., 1999, McCartney and Smith, 2007]. For best results a reference hologram should be recorded after each sample hologram, under

*In this case we chose a size of the mask for a resulting resolution of 6.22 nm.

the same conditions, except for that the sample should be out of the field of view [Völkl et al., 1999].

In this work this has been done in a slightly different manner, for reasons that will be discussed in Section 3.4.2. As an example, in Fig. 2.4, a reference hologram has not been used, which e.g. can be seen from that the resolution in the phase map in (c) is not very good.* This partly comes from the fibre optics in the camera affecting the resolution of the hologram.

The software used for the analysis and treatment of the holograms was a modified version of GPA Phase 2.0 (HREM Research) which is a plug-in for the TEM image and data processing software DigitalMicrograph 3.8 (Gatan Inc.).

In order to not see the actual biprism but the fringes created by it, it needs to be out of focus. The norm, which also was used here, is to have the biprism mounted at the same position as the selected area aperture, in the first image plane of the objective lens [Midgley, 2001]. In order to have a large field of view we had the TEM set to a corrected Lorentz mode, which means that the objective lens was turned off and that the first transfer lens (TL11) of the C_s-corrector was used as Lorentz lens.

From now on, when we say electron holography, we speak only of the off-axis version.

2.2.4 Dark-field electron holography

By combining the Moiré technique and off-axis electron holography, dark-field electron holography was invented by Hÿtch et al. in 2008 for the measurement of strain [Hÿtch et al., 2008]. The Moiré technique is an old technique for observing strain [Sciammarella, 1982]. In short, two samples are stacked on top of each other. A diffracted reference beam that goes through the known and unstrained sample ("Diffracted beam A" i Fig. 2.5 (a)), is superimposed with a diffracted measurement beam from the strained sample ("Diffracted beam B" i Fig. 2.5 (a)).

In dark-field electron holography, just as for off-axis electron holography, a biprism is used to split the beam in two. And like in the Moiré technique, a diffracted reference beam goes through an unstrained zone of the sample, while the measurement half goes through a strained region. With a positive bias on the biprism, the two beams will interfere, creating interference fringes (see Fig. 2.5 (c)).

The phase difference can be extracted from the fringes, which depends largely on the geometric phase [Hÿtch et al., 1998, Hüe et al., 2008, Hÿtch et al., 2003]. The geometric phase contains information about the strain field, com-

*Compare with the phase maps in Section 3.4.2.

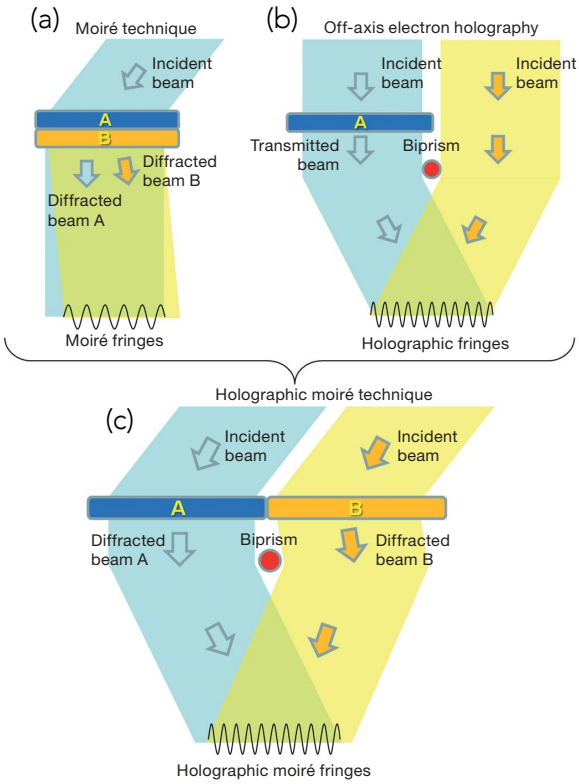

FIGURE 2.5 – *Principal of dark-field electron holography; a combination of the Moiré technique and off-axis electron holography. Image from [Hÿtch et al., 2008].*

ing from a distortion of the atomic lattice. This, which was dubbed geometric phase analysis (GPA), was developed in 1998 by Hÿtch et al. in order to locally study the fields using high-resolution TEM [Hÿtch et al., 1998]. To observe the stress and strain fields over a larger area, without compromising the resolution of GPA, dark-field electron holography was created.

The advantage with dark-field electron holography is that one can have a nanometer spatial resolution while simultaneously measure the strain over a large field of view. Also, the specimen can be fairly thick, which decreases issues with relaxation of the crystal at the two free surfaces.

2.3 Finite element method modeling

To solve an equation describing a complex physical problem is usually too time consuming to be feasible. So in order to simulate physical phenomena, finite element method (FEM) modeling can be used. In a modeling software a phys-

ical model is first made of the sample. Then the model is divided into small subdomains or finite elements, e.g. in the shape of triangles, which is called the mesh. For each element, approximated equations to the problem at hand are found. These equation are easier to solve compared with the original equations, which usually are partial differential equations. To minimize error and to ensure that a stable solution is found, different weigh and error functions are used.

The FEM software we used was COMSOL Multiphysics from COMSOL AB, version 4.3.

Part I

IN SITU ELECTRICAL PROBING

Symbols and abbreviations in Chapter 3

CFE	Cold-field emission
C-FEG	Cold-field emission gun
S-FEG	Schottky field emission gun
ϕ	Exit work function
F-N	Fowler-Nordheim
FEM	Finite element method
E_{loc}	Local electric field around the apex of the tip
CNT	Carbon nanotube
CCnT	Carbon cone nanotube
E_{F}	Fermi level
r_{s}	Virtual electron source radius
r	Physical electron source tip radius
i_{e}	Field emission current
α_0	Beam convergence semi-angle
β	Brightness
β_{red}	Reduced brightness
V_{acc}	TEM acceleration voltage
J_{RD}	Current density in the Richardson-Dushman equation
T	Temperature
B	Richardson constant
k_{B}	Boltzmann's constant
m_{e}	Electron rest mass
e	Elementary charge
h_{P}	Planck's constant
Lab_6	Lanthanum hexaboride
A	Emitting area/virtual source size
t_{F}	First special field emission elliptic function
v_{F}	Second special field emission elliptic function
a	First Fowler-Nordheim constant
b	Second Fowler-Nordheim constant
ΔE	Energy spread of the beam
λ_{c}	Temporal coherence length
v	Electron velocity
EELS	Electron energy loss spectroscopy
$\Delta\phi$	Change in work function from the Schottky effect
J_{S}	Current density from the Schottky equation
J_{ES}	Current density from the extended Schottky equation

FE	Field emission
q	Dimensionless parameter in the extended Schottky law (eq. (3.8))
ϵ_0	Permittivity in vacuum
$\varphi(x, y)$	Phase shift measured with electron holography
C_E	TEM acceleration voltage dependent parameter
λ_e	Relativistic electron wavelength
c	Speed of light
E_e	Relativistic electron energy
E_0	Electron rest energy
t	Integration length in eq. (3.14)
$\langle E \rangle$	Map of the average in-plane electric field
FIB-SEM	Focused ion beam-scanning electron microscope
$i(V)$	Current–voltage curve
$i_\mathrm{e}(V)$	Field-emission current–voltage curve
GIS	Gas-injection system in the FIB-SEM
hat	Part of the nanomanipulator that holds the sample (see Figs. 2.1 and 3.5)
d	Tip-anode separation distance
V_bip	Potential on biprism
V	Potential between anode and CCnT
V_MIP	Mean inner potential
$\varphi_\mathrm{ano} = \varphi$	Phase shift from voltage applied on the anode
φ_tot	Total phase shift
φ_MIP	Phase shift from mean inner potential
φ_dist	Phase shift from distortions
φ_proj	Phase shift from projector lenses
φ_aber	Phase shift from aberrations in lenses
φ_cam	Phase shift from camera
φ_Ff	Phase shift from Fresnel fringes
FFT	Fast Fourier transformation
FFT^{-1}	Inverse fast Fourier transformation
γ	Field enhancement factor
$E_{\vert\vert}$	Electric field between two parallel plates
w	Width and height of simulated anode
P	Vacuum pressure inside the TEM
EH	Electron holography

3 Cold-field emission from a carbon cone nanotip

"If the electron is a wave, then why can't I surf it?"

ELECTRON field emission was first observed by Wood in 1897 [Wood, 1897]. In short, when a sufficiently strong electric field is present around a cathode, electrons will quantum mechanically tunnel through the metal/vac-uum barrier. When this occurs from a cathode at room temperature, one speaks of cold-field emission (CFE). The energy barrier plays a significant role in the process and part of it is called the exit work function ϕ. Another important parameter for a cathode shaped like a tip, is its sharpness. Since these two parameters are critical for the onset of field emission, this work has been focused on them.

Schottky reported in 1923 about the decrease of the tunneling barrier in a strong electric field (the Schottky effect) [Schottky, 1914] and Millikan and Lauritsen discovered in 1929 that the logarithm of the cold-field emission current showed a linear behavior when plotted with one over the electric field [Millikan and Lauritsen, 1928].

In 1929 Fowler and Nordheim described the phenomena theoretically, leading to the so-called Fowler-Nordheim (F-N) equations (this will be detailed in Section 3.2.2) [Fowler and Nordheim, 1928]. Müller created a field emission projector in 1936 [Müller, 1936], but Crewe et al. were first with realizing CFE at high voltages in 1968 [Crewe et al., 1968].

Applications of field emission range from neutralizing charge on space crafts to large area emitters in vacuum microelectronics, and, for emitting electrons inside cold-field emission guns (C-FEG). This part of the thesis has concentrated on the latter, in which we have looked into utilizing a new type of carbon material as an emitter [de Knoop et al., 2014]. The future goal to greatly

improve the properties of the C-FEG [Houdellier et al., 2012]. Here, we have used a specialized *in situ* TEM sample holder, in order to apply a sufficiently high voltage for field emission to commence, which was studied *in situ*. Using electron holography together with finite element method (FEM) modeling, the local electric field E_{loc} around the emitting tip could be obtained quantitatively. Combining these results with one of the F-N equations, the exit work function ϕ of the CCnT was found. This presents a novel way in obtaining ϕ for a cold-field emitter.

3.1 Carbon materials as cold-field emitters

Following its discovery by Iijima in 1991 [Iijima, 1991], the carbon nanotube (CNT) and similar carbon structures have been the subject for many studies for possible applications. One of them is as a cold-field emitter. In 1998 [Wang et al., 1998] and 2000 [Saito and Uemura, 2000], field emission displays were demonstrated, using CNTs as electron emission sources. Others have used disordered matrix arrays [Collins and Zettl, 1997], multiwalled yarns [Chen et al., 2009] or thin films [Obraztsov et al., 2000, Sinitsyn et al., 1997, Nilsson et al., 2001a,Nilsson et al., 2001b] of CNTs to perform and study field emission.* For a good review of CFE of CNTs, see the work done by de Jonge and Bonard [de Jonge and Bonard, 2004].

We will focus solely on the use of carbon based materials as field emitters inside a C-FEG. This was first realized in 1995, when de Heer et el. presented a high-intensity FEG from a film of aligned CNTs [de Heer et al., 1995].

The CNT has some remarkable properties that should make them an excellent choice as a cold-field emitter. First, their high aspect ratio and small tip radius enhances the local electric field, which thus ensures a low extraction voltage to start the emission process. They are chemically less reactive than standard W emitters, which is important since adsorbates attach to the tip, disturbing the emission process. They also show high mechanical strength and are capable of emitting a large amount of electrons with uniform properties. In 2002, de Jonge et al. presented CFE from a single CNT [de Jonge et al., 2002], but many other studies have been performed as well [Bonard et al., 2001, Collins and Zettl, 1996, de Heer et al., 1995, de Jonge, 2009, de Jonge and Bonard, 2004, de Jonge et al., 2005, Zhou et al., 2001].

*Many more articles exist on the subject, e.g. [Bonard et al., 2002b, Dean and Chalamala, 2000, Dean and Chalamala, 1999b, Dean and Chalamala, 1999a, Dean et al., 1999, Fransen et al., 1999b, Gröning et al., 2000, Hazra et al., 2011, Jin et al., 2005, de Jonge and van Druten, 2003, de Jonge et al., 2004, Kim et al., 2011, Kokkorakis et al., 2002, Luo et al., 2002, Ribaya et al., 2008, Rinzler, 1995, Saito et al., 2005, Sanchez et al., 2007, Solá et al., 2009, Sveningsson et al., 2005, Yuge et al., 2012].

Nevertheless, CNTs suffer from a couple of important problems. First, their huge aspect ratio make them prone to vibrate, an effect not desirable in a C-FEG [Gao et al., 2001]. Secondly, they are small and difficult to handle, which is a critical criteria in the event of a future commercialization.

The type of carbon structure that we have been working with in this thesis, the carbon cone nanotip (CCnT), was discovered by Jacobsen and Monthioux in 1997 [Jacobsen and Monthioux, 1997]. As will be shown in Section 3.3.2, they exhibit a large base with a conical shape that ends in a nanometer sized tip. The conical shape prevents vibration and the base enables easy handling. In other words, a CCnT overcomes the problems plaguing the CNT as a field emitter, but maintains its favorable properties.

The CCnTs have been shown to function in a working microscope where a CCnT was mounted on a regular C-FEG support and operated as an emitter of the gun in a modified Hitachi HF2000 TEM [Houdellier et al., 2012]. The gun was demonstrated to have remarkable performance, with a low energy spread, high brightness and an increased emission stability and emitter lifetime. Some first *in situ* electron holography experiments using the *in situ* holder described in Section 2.2.2 were made as well.

In a recent paper, electron holography has been used to *in situ* study the potential shift over a p-n junction in biased Si nanowires, using a similar sample holder as in this thesis [He et al., 2013].

Finally, an important and pioneering paper preceding the work done in this thesis, is by Cumings et al. in 2002 [Cumings et al., 2002]. As done here, they performed electron holography *in situ* combined with modeling, in order to determine the electric field quantitatively.

3.2 Theory of electron emission

There exists a number of different types of emission processes for the electron guns used in electron microscopes. These processes can be classified in the physical process used by the electron to conquer the vacuum-barrier and leave the material. Remember that the barrier consists of the Fermi level E_{F} of the metallic tip/filament plus the exit work function ϕ. That is, for the electrons to leave the material they need to have an energy $\geq E_{\mathrm{F}} + \phi$.*

Important parameters for an emission gun will be explained here. To begin with, the intensity, which defines the total number of electrons, i.e., the current in the beam. The brightness can be expressed as the intensity at a certain

*For an electron with zero initial energy, the Fermi level is the energy needed to add an electron to a system. In other words, it is the maximum energy an electron can have in a solid at 0 K.

area for a certain convergence angle (e.g. a laser has high brightness while a light bulb has high intensity). Another important parameter is the temporal coherence, or energy spread. High spatial coherence follows high brightness. Different guns excel at different applications, depending on how they perform on these parameters.

Perhaps the least easy parameter to understand is the brightness. We will therefore define it a bit more detailed here. If a source is having a tip radius of r_{s}* (thus a current density of $i_{\mathrm{e}}/\pi r_{\mathrm{s}}^2$, i_{e} being the field emission current) and a convergence semi-angle α_0 from within the electrons are emitted (giving a solid angle of πa_0^2), then the brightness can be defined as [Williams and Carter, 2009]

$$\beta = \frac{i_{\mathrm{e}}}{\pi r_{\mathrm{s}}^2}/\pi\alpha_0^2 = \frac{i_{\mathrm{e}}}{(\pi r_{\mathrm{s}}\alpha_0)^2} \tag{3.1}$$

The dimension of eq. (3.1) is A m^{-2} sr^{-1}. A less frequent but more convenient definition of the brightness is the reduced brightness, which is defined as $\beta_{\mathrm{red}} = \beta/V_{\mathrm{acc}}$, where V_{acc} is the acceleration voltage of the TEM. The reason is that since the acceleration voltage affects the current density and the energy spread, in order to be able to compare different sources, it is preferable to use this definition.†

The following section will give a summary of the different electron emission types available. Focus has been on cold-field emission.

3.2.1 Thermionic emission

In the first process, thermionic emission, the electrons have an energy according to the Fermi-Dirac distribution. When the cathode is heated, the energy addition permits the electrons to be emitted. This process is governed by the Richardson-Dushman equation, which gives the current density J_{RD} of the source as a function of the temperature T (and of the work function ϕ of course);

$$J_{\mathrm{RD}} = B(k_{\mathrm{B}}T)^2 \exp\left(-\frac{\phi}{k_{\mathrm{B}}T}\right), \tag{3.2}$$

where B is Richardson constant, T is the temperature, ϕ is the work function and k_{B} is Boltzmann's constant [Richardson, 1901]. Richardson constant is defined as

$$B = \frac{4\pi m_{\mathrm{e}} e}{h_{\mathrm{P}}^3}, \tag{3.3}$$

*Note that it is the radius of the virtual source and not the tip radius r that we speak of here.

†Also other versions of the brightness exist, e.g., Bronsgeest et al. argue that something called practical brightness should be used [Bronsgeest et al., 2008].

m_e being the electron rest mass, e the elementary charge and h_P Planck's constant*. As can be seen in the equation, an energy addition of at least the work function is necessary for having $J_{RD} > 0$. A schematic drawing, like the one in Fig. 3.1 can give an illustrative pointer to this.

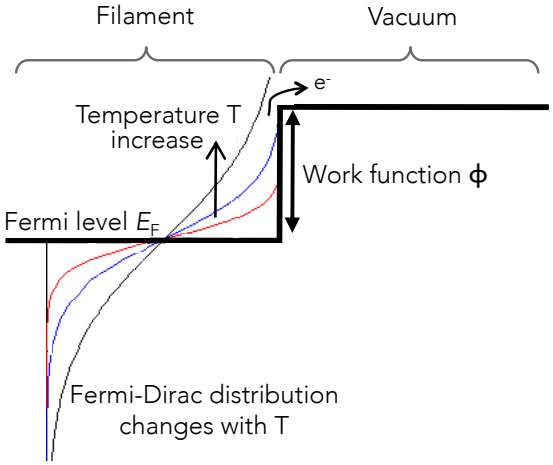

FIGURE 3.1 – *Sketch describing thermionic emission with a metallic filament. As the temperature increases the Fermi-Dirac distribution changes, allowing more electrons to escape the material. Courtesy of F. Houdellier, CEMES-CNRS.*

As can be seen, the Fermi-Dirac distribution changes with temperature. At 0 K, the electrons have too little energy in order to leave, and are trapped effectively in the material. As the cathode is heated up, a growing fraction of the electrons will have an energy sufficient to escape to the vacuum. The tail of the Fermi-Dirac distribution is exponential, which means that a slight increase in temperature corresponds to a significant increase in emitted electrons.

The most common electron sources are for thermionic emission W filament and LaB_6 (Lanthanum hexaboride) crystal, with work functions $\phi = 4.5$ and 2.5 eV, respectively. The extremely low work function of LaB_6 allows a typical operational temperature about 1 800 K, compared with about 2 700 K for a W filament.

The benefits of thermionic emission are good emission stability and a technique that is easy to use and thus cheap to realize. By increasing the temperature on the cathode, lots of electrons can be emitted, that is, high intensity is easily achieved. It suffers from low brightness, i.e., it has low spatial coherence, since the electrons are emitted from a large area (see Table 3.1). The temporal coherence is low since the emitted electrons have a high energy spread. These

*Depending on what the emitter is made out off, a material correction factor is added to B.

are the reasons that a thermionic emitter is useful for conventional TEM, but not for spectroscopy or holography.

3.2.2 Cold-field emission

In the second process, cold-field emission, the energy barrier at the metal-vacuum interface (or Schottky-Nordheim barrier) is reshaped due to the presence of an electric field, which can be illustrated by the triangular shape of the barrier seen in Fig. 3.2. When the barrier is thin enough, electrons can quantum-mechanically tunnel through it. This is realized from when an electron in a metal approaches the end of the tip, it has a probability of escaping the metal. With an electric field at the surface, the escape probability is increased, and with a sufficiently strong field (in the order of > 1 V/nm), electrons can start to tunnel through, as illustrated in Fig. 3.2.

It should be noted that the representation of the barrier is a simplification. In reality the band structure of the electronic states are modified by the electric field, allowing emission. The interested reader can explore the review paper of Gadzuk and Plummer [Gadzuk and Plummer, 1973].

Cold-field emission is governed by the Fowler-Nordheim (F-N) equations. In 1928, Fowler and Nordheim came up with an equation that described how electrons could tunnel through a Schottky-Nordheim barrier [Fowler and Nordheim, 1928] when an electric field is applied between two infinite and parallel plates in vacuum at 0 K. This model is idealistic and thus unrealistic [Forbes and Wikipedia, 2011], which led to modified and corrected equations, for example by Murphy and Good in 1956 [Murphy and Good, 1956]. The simplified and so called standard F-N equation describing the field emission current i_{e} can be seen in the equation below:

$$i_{\mathrm{e}} = A\frac{a}{t_{\mathrm{F}}^2\phi}E_{\mathrm{loc}}^2 \exp\left(\frac{-v_{\mathrm{F}}b\phi^{3/2}}{E_{\mathrm{loc}}}\right) \tag{3.4}$$

where A is the emitting area (or, the virtual source size), t_{F} and v_{F}* are the so called "special field emission elliptic functions" [Forbes and Deane, 2007].† Following, a and b are the so called "first Fowler-Nordheim constant" and "second

*The "F" stands for forward, meaning that the function applies for electrons moving towards and normal to the emitter surface.

†Or, recommended by Forbes and Deane in 2007 [Forbes and Deane, 2007] to be called "the Schottky-Nordheim barrier functions".

Fowler-Nordheim constant", defined respectively by [Forbes and Deane, 2007]

$$a \equiv e^3/8\pi h_{\mathrm{P}} \approx 1.54 \times 10^{-6}\,\mathrm{A\,eV\,V^{-2}}$$
$$b \equiv \frac{8\pi}{3}\frac{2m_{\mathrm{e}}^{1/2}}{e\,h_{\mathrm{P}}} \approx 6.83 \times 10^{9}\,\mathrm{eV^{-3/2}\,V\,m^{-1}}$$

Further approximations of the equation [Spindt et al., 1976,Brodie and Spindt, 1992], mainly of the elliptic functions t_F and v_F, yielded the following relation,

$$i_{\mathrm{e}} = A\frac{1.54 \times 10^{-6}}{\phi}E_{\mathrm{loc}}^2 \exp\left(\frac{10.4}{\sqrt{\phi}}\right)\exp\left(-\frac{6.44 \times 10^{9}\phi^{3/2}}{E_{\mathrm{loc}}}\right) \qquad (3.5)$$

which is the equation that will be used here (the work function is in eV) [Bonard et al., 2002b, Anderson, 1993].

Whilst the F-N equation was conceived for emission between two parallel plates at 0 K, it has been shown that other situations, such as emission from a tip, can be adequately described by eq. (3.5) [Good and Mueller, 1956, Forbes and Wikipedia, 2011].

The local electric field depends not only on the potential drop between cathode tip and anode, but also largely on the tip radius of the emitter. Therefore, to generate very high electric fields, a sharp tip is used. The crystallographic direction of tungsten for which the work function is the lowest and thus most electrons are emitted is [310]. These and other parameters of cold-field emission can be found in Table 3.1.

Quite recently, a modified theory has been proposed by Forbes and Deane [Forbes and Deane, 2007, Forbes, 2008], where they delve into more accurate approximations of the special field emission elliptic functions. Utilizing this modified theory can be crucial when using metallic nanowire large-area field emitters, but less important for carbon-based field emitters [Forbes, 2012].

3.2.2.1 Drawbacks with cold-field emission

One issue with cold-field emission is that the beam is quite noisy; the intensity fluctuates randomly over time, seen as a flickering of the beam. This flickering of the beam is inversely proportional to the size of the emitting area (the virtual source size) of the tip. Since the tip radius in a cold-field emitter is small (see Table 3.1), the beam noise is high. Another factor is that even with a vacuum of 10^{-9} Pa inside the gun, molecules adsorb onto the tip, which apart from increasing the work function and therefore decreasing the current, also create fluctuations in the current due to migration of the adsorbates* on the emitting surface [de Jonge, 2009].

*This is called Brownian motion, which is important even at 300 K.

An effect which has an even larger effect on the emission stability is something called flicker noise. Due to anode degassing, ions are created from collisions with the emitted electrons, which subsequently accelerate towards and bombard the negatively biased tip, which also mechanically deforms it. This is more prominent at higher currents [Todokoro et al., 1982]*

Of a more serious note, after some time, more and more adsorbates will accumulate on the tip, which eventually will create an arc between the tip and the gun housing, which most likely will cause the tip to explode, with the time consuming operation of changing the tip to follow. To prevent this the tip is flashed, that is, heated up during some μs which removes the adsorbates (and anneals the craters created from the ion bombardment). The need for UHV and flashing of the tip makes the technology complicated and expensive.

A drawback of having a small tip radius and virtual source size, is that less electrons can be emitted, i.e., the intensity is limited.

3.2.2.2 Benefits with cold-field emission

Due to the small tip radius of the cold-field emitter, the C-FEG is the brightest source available (see eq. (3.1) and Table 3.1). This allows for a small and electron-dense probe [de Jonge, 2009], or, a wide and parallel beam with very little divergence.† The former is beneficial e.g. for spectroscopy, or monochromated scanning TEM [Krivanek et al., 2013] and the latter e.g. for electron holography.

Another benefit of high brightness and that the electrons are emitted from a very small area, is that this produces spatially coherent electrons. And as explained in Section 2.2.3 this is a crucial parameter for electron holography, where the resolution in the phase maps obtained from the holograms is largely dependent on the spatial coherence of the electrons.

An CFE source also produces high temporal coherent electrons, i.e., with small energy spread. When the electric field around the tip increases, the barrier becomes "thinner" and at some point the evanescent wave that describes the probability distribution of the electrons inside the barrier, reaches the vacuum. That is, the first electrons start to tunnel through. And since these electrons have the same energy (of just below the Fermi level), the beam will have a small energy spread ΔE. With a higher applied field, the energy spread will increase, but compared with other sources, it is still very small. The Boersch effect will eventually decrease the temporal (and spatial) coherence [Hawkes, 2011].

*It will be discussed more in detail in Section 3.8.1.

†This statement is the same, since in the column a small beam in the diffraction plane is a large and parallel beam in the image plane.

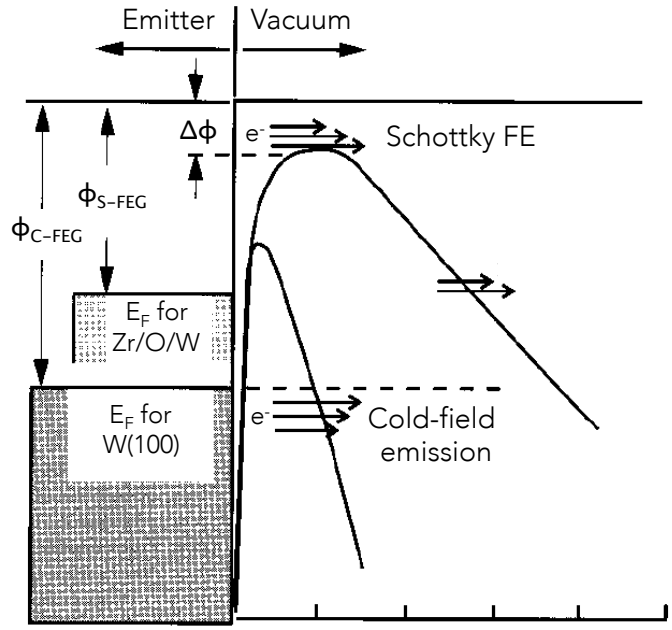

FIGURE 3.2 – *Sketch showing Schottky field emission and cold-field emission. As the local electric field around the tip increases, the barrier is reshaped; first by being lowered, i.e. the Schottky effect ($\Delta\phi$ is the decrease in work function), which allows for Schottky field emission, but also by being thinner, which enables electrons to tunnel through, i.e., cold-field emission. E_{F} is the Fermi level, $\phi_{\mathrm{C-FEG}}$ and $\phi_{\mathrm{S-FEG}}$ is the work function for a C-FEG and S-FEG, respectively (modified sketch, originally from Kim et al. [Kim et al., 1997]).*

The temporal coherence of the electrons is measured by their coherence wave length, defined by

$$\lambda_{\mathrm{c}} = \frac{v\, h_{\mathrm{P}}}{\Delta E} \tag{3.6}$$

with v being the electron velocity. For electron energy loss spectroscopy (EELS) this is an ideal source, where a small energy spread is of great importance.

3.2.3 Schottky emission

The third process, the Schottky emission, is quite often categorized as field emission process, which in reality only partly is true. The process enabling the emission is the Schottky effect, which lowers the barrier due to the presence of a strong electric field.* By having a lowered barrier and by heating up the tip by continuously running a current through it, the electrons can overcome the barrier (see Fig. 3.2).†

*When the Schottky effect is present one speaks of the reduced work function.
†This Schottky effect is also present in CFE, but plays no part since the temperature is too low.

So what is the difference between the thermionic emission described in the previous chapter? Since the intensity of the electric field depends on the tip radius and distance to the anode, the Schottky effect will be most important at the apex of the tip, i.e., it is here that the work function will be the lowest and where a majority of the electrons will be emitted. This in combination with a small tip radius provides high brightness and coherence but low overall intensity. The electric field still makes the barrier thinner and in combination with higher energy electrons, some of them can tunnel through "higher up" where the triangular barrier is thinner. But in reality usually no significant number of electrons tunnel through. The reason is that the Schottky emission tips usually are too large to create a strong enough electric field to enable tunneling. Perhaps a more suitable name could be field-assisted thermionic emission.

Other means to lower the barrier is by coating the W tip with zirconium dioxide (ZrO_2). This is done by heating up a ZrO_2 reservoir sitting further up the W tip, which wets the W tip. As can be seen in Table 3.1, this lowers the work function to around 3.0 eV, thus increasing the number of emitted electrons for same extraction voltage.

As mentioned above the tip radius is <1 μm, which is 10 times larger when compared with a CFE tip (and even more so for the virtual source area thanks to the Schottky effect). Even though this decreases the beam noise (due the inverse relationship between beam noise and virtual source area), adsorbates still attach to the tip, increasing the noise, just like the flicker noise from anode degassing and ion bombardment do. This is solved, also here, by flashing. But when compared with CFE, the differences is that it is done continuously by constantly running a current through the tip-support, which heats up the tip to around 1700 K.*

Also, the shape of the tip is kept constant by a thermal-field equilibrium. As the high temperature from the continuos flashing melts the ZrO_2 that coats the W-tip†, the tip radius increases. But, the high electric field, being strongest at the apex, counters this process, and thus keeps the size of the tip in a state of equilibrium.

To accommodate for the presence of the Schottky effect and that Schottky tips potentially cold-field-emit electrons, modified versions of eq. (3.2) exists [Fransen et al., 1999a, Fransen et al., 1998]. The first one is described by the Schottky law, which only includes the increased (thermionic) emission due to the reduced work function arising from the Schottky effect. The equation

*Event though the elevated temperature increases the Brownian motion of the adsorbates, the continuous flashing removes them as soon as they adhere to the tip.

†The W used here are orientated in the [100] direction.

TABLE 3.1 – *Properties of different electron emitters. The data for field emission energy spread has been found in [Krivanek et al., 2013] and [Kohno et al., 2010]. Part of the other data has been found on page 145 in Hawkes and Spence [Hawkes and Spence, 2007] and on page 74 in Williams and Carter [Williams and Carter, 2009]. Note that the energy spread value of 30 meV for Cold FE is with a monochromator.*

	Thermionic		Schottky FE	Cold FE
Cathode material	W	LaB_6	ZrO/W[100]	W[310]
Work function ϕ [eV]	4.5	$\simeq 2.5$	3.0	4.5
Richardson's constant [A/m^2K^2]	6×10^9	4×10^9	n/a	n/a
Operating temperature [K]	$\simeq 2\,700$	$\simeq 1\,800$	$\simeq 1\,700$	300
Emission current [μA]	~ 100	50	30-70	10-30
Emission current density, (100 kV) [A/m^2]	5	10^2	10^5	10^6
Emission current stability [%/hour]	< 1	< 1	< 1	~ 5
Brightness (100 kV) [A/m^2sr]	10^{10}	5×10^{11}	5×10^{12}	10^{13}
Energy spread at gun exit (100 kV) [meV]	3 000	1 500	700	30-400
Vacuum [Pa]	10^{-2}	10^{-4}	10^{-6}	10^{-9}
Cathode radius [nm]	60 000	10 000	$< 1\,000$	< 100
Effective (virtual) source radius [nm]	15 000	5 000	15	2.5
Emitter lifetime [hour]	100	1 000	$> 5\,000$	$> 5\,000$

describes the current density J_S, as seen below:

$$J_S = B(k_B T)^2 \exp\left(-\frac{\phi - \Delta\phi}{k_B T}\right). \tag{3.7}$$

The Richardson constant B is defined in eq. (3.2). The $\phi - \Delta\phi$ is the reduced work function, i.e., the remains after the Schottky effect has been accounted for.

When the temperature and electric field is high enough, also tunneled electrons can be emitted and eq. (3.7) will be modified to

$$J_{ES} = B(k_B T)^2 \exp\left(-\frac{\phi - \Delta\phi}{k_B T}\right) \frac{\pi q}{\sin \pi q} \tag{3.8}$$

which is the extended Schottky law. The dimensionless parameter q is defined as

$$q = \frac{h_{\mathrm{P}}\,(4\pi\epsilon_0 e)^{1/4} E_{\mathrm{loc}}^{3/4}}{2\pi^2 m_{\mathrm{e}}^{1/2} k_{\mathrm{B}} T} = 1.656 \times 10^{-4} \frac{E_{\mathrm{loc}}^{3/4}}{T} \tag{3.9}$$

with ϵ_0 being the permittivity in vacuum [Swanson and Schwind, 2009]. With a value of $q = 0.5$ half the current comes from tunneled electrons.*

The properties of a Schottky source is a combination and compromise of the properties of a thermionic and a cold-field emission source. The brightness is good, but not as good as for the cold-field emitter. The technique is still expensive, but less difficult to use than for the C-FEG and the emission stability is good. Being in the middle ground, it has proven to be the most common source for electron microscopes. But, with improved instrumentation, like for example better pumps around the gun and it not anymore being necessary to turn off the high voltage when flashing the tip, the popularity of the C-FEG equipped TEM is now increasing.

3.3 Materials and methods

In this section we will explain how the carbon cone nanotips (CCnTs) were produced, extracted using a focused ion beam-scanning electron microscope (FIB-SEM) and mounted inside the TEM sample holder.

3.3.1 Requirements for electrical probing

When doing electrical *in situ* measurements, it is important that all contacts (depicted in Fig. 2.1) are good. This has been established, which ensures that the results are coming from the sample, and not from the holder. For example the welding between the CCnT and the etched W wire must be conductive, the wire should be in good physical and thus electrical contact to the hat (see Fig. 2.1), just as for the contact between the Au anode and the tube holding it.

Maintaining good contact inside the TEM can be troublesome. With a vacuum being in the order of 10^{-5} Pa, hydro-carbons will quickly cover every surface exposed to the electron beam with a thin insulating layer. This occurs due to that the electrons in the imaging beam hits the particles which consequently are deposited onto the closest surface. This layer thickens by the minute, therefore care has to be taken to the time the interesting area is illuminated. Hence, before a measurement is made, the probe should be brought into contact to a usually well conductive part of the sample in order to test the conductivity by

*For example with $E_{\mathrm{loc}} = 1 \times 10^9$ V/m and $T = 1\,800$ K.

running a small current through it. At first, an $i(V)$-curve (current-voltage) obtained from such a measurement show a resistance in the GΩ range. But by continuously increasing the potential between probe and sample, eventually the current will break through and remove the layer, i.e., cleaning the surface [de Knoop et al., 2005]. After this takes place, the resistance will be in a more normal range, which is around 6–800 Ω for a CCnT.*

Also for this thesis, where non-contact $i_{\mathrm{e}}(V)$ measurements (field emission) have been made, it is important having well conductive surfaces, to avoid affecting the field emission process.

For a microscopist doing conventional TEM, the insulating layer is unwanted, since it perturbs the signal of the image or the accuracy of the electron energy loss spectrum (EELS) map.

3.3.2 Production of the carbon cone nanotip

The CCnT was first reported of by Jacobsen and Monthioux [Jacobsen and Monthioux, 1997] in 1997. Its shape is quite unique, with a large base in the μm range consisting of disordered and squashed sheets of graphene, followed by usually two smooth carbon cones at the sides, ending in very sharp tips or CNTs in the nm range (see Fig. 3.3).

The CCnTs were produced using a catalytic method to create carbon nanofilaments with a diameter of around 5 nm. This was followed of depositing carbon onto them, using chemical vapour deposition at a temperature of $1\,300$ °C [Jacobsen and Monthioux, 1997, Allouche et al., 2003].

3.3.3 Sample preparation

The CCnTs are then scraped off from residual materials from the synthesis onto a conductive tape with carbon (carbon tape). Before being able to use them in the TEM, I used a FIB-SEM to extract them, as illustrated in Fig. 3.4.

First they were transferred onto a SEM-sample holder (stub) with carbon tape on top (see Fig. 3.4 (a)). On the same stub holder, a W wire with a diameter of 0.33 mm was installed, on which the CCnT was to be attached. The wire in Fig. 3.4 (g) was electro-chemically etched using Kingswater (or Aqua Regia, concentration 3:1 of hydrochloric acid (HCL) and nitric acid (HNO3)) and an alternating current.† Wires that were mechanically cut using hand pliers were used also (see e.g. inset in Fig. 3.6). After having located a suitable CCnT, a Kleindiek mechanical gripper, or so called micro tweezer, was used to grab the CCnT (Fig. 3.4 (b)). Then, by using the high energetic ions, it was cut in two.

*See Fig. A.3 for an example where the contamination layer was thick enough to require the W-tip to be heated up to above its melting temperature (3 422 °C).

†Etched tips provided by Aurélien Masseboeuf at CEMES-CNRS.

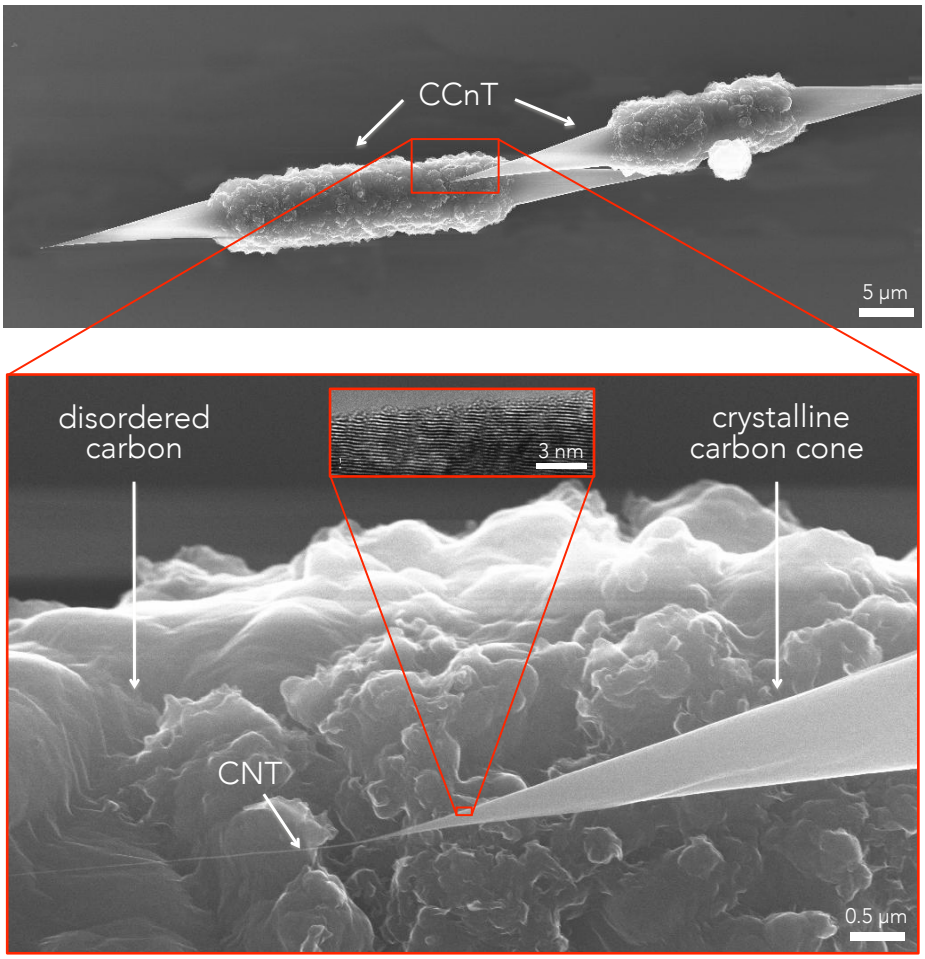

FIGURE 3.3 – *Top micrograph showing two CCnTs. In the bottom micrograph (big inset), the large base consisting of disordered carbon and, the cone, here ending in a long CNT can be seen. The small inset displays the layered carbon structure.*

In Fig. 3.4 (c) the first marks of the ion beam have appeared, and in (d) the CCnT is cut in half and lifted up by the micro tweezers. In (e) the CCnT has been transported and approached closely to the etched W wire. Earlier, the tip of the wire had been cut off with the ion beam, in order to easily attach the CCnT to it, as can be seen in (e) and (f). In (f), the gas-injection system (GIS)* had been used to weld the CCnT onto the end of the W wire. Two of the GIS-needles show in the top of image (g). Here, also larger parts of the micro tweezers and the W wire can be seen. And, in (h), the CCnT is now attached to the end of the etched part of the wire.

*See description in Section 2.1.2.

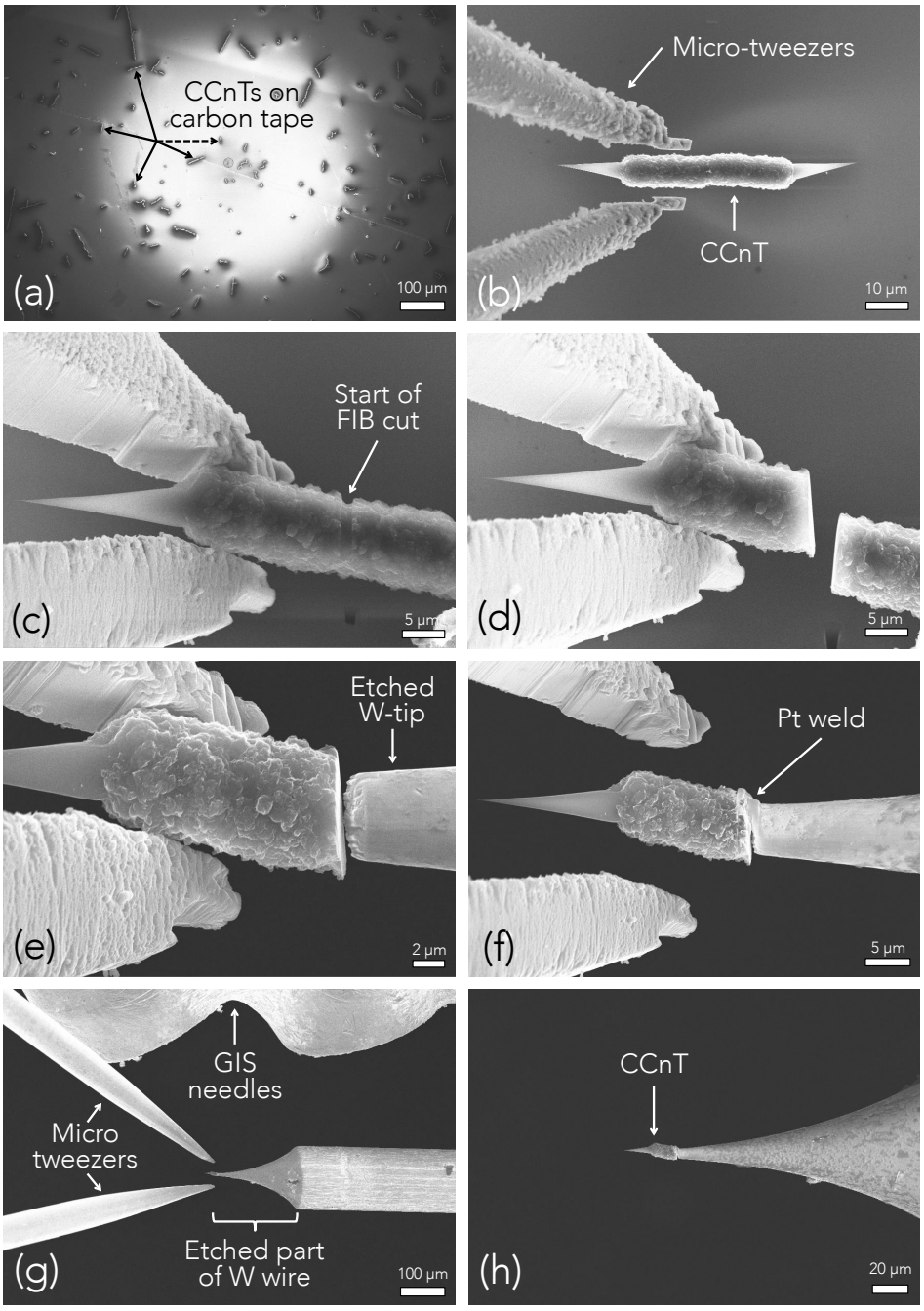

FIGURE 3.4 – *Sample preparation in the FIB-SEM. (a) Overview of the carbon tape with CCnTs deposited. (b) – (d) Cutting the CCnT in two and securing it with the micro tweezers. (e) – (h) The CCnT being transported and welded to the etched W wire.*

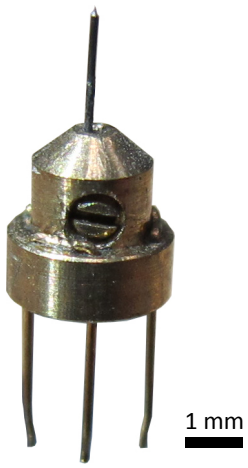

FIGURE 3.5 – *Support for the sample (the "hat"), with a W wire inserted. At the top of the wire, a CCnT is attached (not visible).*

Finally the wire was inserted into the hat and secured with the locking screws, as can be seen in Fig. 3.5,* which thereafter was slid onto the ball of the nanomanipulator in the holder (see Fig. 2.1).

3.4 *In situ* electron holography

3.4.1 Calculation of the phase shift

The phase shift $\varphi(x, y)$ of an electron traversing an electrostatic potential V is given by integrating the potential along the beam path [Völkl et al., 1999], as seen in the equation below.

$$\varphi(x, y) = \int_{\text{beampath}} C_{\text{E}}\, V(x, y, z)\, \mathrm{d}z \tag{3.10}$$

with the term C_{E} is dependent on the TEM acceleration voltage. It is defined as

$$C_{\text{E}} = \frac{2\pi}{\lambda_{\text{e}}} E_{\text{e}} \tag{3.11}$$

where λ_{e} is the relativistic electron wavelength, defined as

$$\lambda_{\text{e}} = \frac{h_{\text{P}}}{\sqrt{2 m_{\text{e}}\, e\, V_{\text{acc}}}} \frac{1}{\sqrt{1 + \frac{e\, V_{\text{acc}}}{2 m_{\text{e}}\, c^2}}} \tag{3.12}$$

*Note that only three of the six legs of the hat can be seen here.

with V_{acc} being the acceleration voltage of the TEM and c the speed of light. With an acceleration voltage of 100 kV* the wavelength is 3.70 pm.

E_{e} of eq. (3.11) is the relativistic electron energy, defined as

$$E_{\mathrm{e}} = \frac{E + E_0}{E(E + 2E_0)} \tag{3.13}$$

where $E = 100$ keV is the electron acceleration energy and $E_0 = m_{\mathrm{e}}c^2/e$ is the electron rest energy in eV, which gives that $E_{\mathrm{e}} = 5.446 \times 10^{-6}$ and that $C_{\mathrm{E}} = 9.25 \times 10^6$ rad V^{-1} m^{-1}.

From eq. (3.10) we know that the phase shift is obtained from integrating the potential along the electron beam path. The phase shift maps (scalar fields) that are extracted from the holograms† correspond to potential maps in the x and y direction that are integrated along the z axis. But, since the potential around the tip and along the electron path is continuously varying, it is not possible to directly obtain the electrostatic field (in three dimensions) by taking the gradient of the phase shift, i.e., the gradient of eq. (3.10). The result from this operation can be seen in the equation below, which is a qualitative but not quantitative representation of the three-dimensional electrostatic field.

The phase measured with electron holography is only a function of x and y. Therefore, we have integrated over z and only have access to the gradient in x and y. Using $\mathbf{E}(\mathbf{r}) = -e\nabla V(\mathbf{r})$ (with $\mathbf{r} = x\hat{\mathbf{x}} + y\hat{\mathbf{y}} + z\hat{\mathbf{z}}$), eq. (3.10) and $\nabla = \frac{\partial}{\partial x}\hat{\mathbf{x}} + \frac{\partial}{\partial y}\hat{\mathbf{y}}$, we get:

$$\begin{aligned}
\nabla\varphi(x,y) &= C_{\mathrm{E}}\left(\int \frac{\partial}{\partial x} V(x,y,z)\,\mathrm{d}z\,\hat{\mathbf{x}} + \int \frac{\partial}{\partial y} V(x,y,z)\,\mathrm{d}z\,\hat{\mathbf{y}} \right) \\
&= C_{\mathrm{E}}\left(-\int E_{\mathrm{x}}(z)\,\mathrm{d}z\,\hat{\mathbf{x}} - \int E_{\mathrm{y}}(z)\,\mathrm{d}z\,\hat{\mathbf{y}} \right) \\
&= C_{\mathrm{E}}\left(-\langle E_{\mathrm{x}}\rangle\, t\,\hat{\mathbf{x}} - \langle E_{\mathrm{y}}\rangle\, t\,\hat{\mathbf{y}} \right) \\
&= -C_{\mathrm{E}}\,\langle \mathbf{E}_{\mathrm{x,y}}\rangle\, t
\end{aligned} \tag{3.14}$$

where t is the integration length. If we would assume that the electric field is concentrated in a thin slab, then $\langle E\rangle$ is a map of the average in-plane electric field. This is of course semi-quantitative, because the electric field is in three dimensions, i.e., not concentrated in a thin slab.

Since we are pursuing a fully quantitative value, a three-dimensional model was developed using FEM. By comparing the two-dimensional experimental with the integrated modeled results, a quantitative value of the local electric

*This was done in order to reduce the knock-out damage of carbon atoms in the CCnT [Banhart, 1999].

†See Section 2.2.3 on how this was done.

field around the tip could be found. This part will be explained in detail in Section 3.6.

3.4.2 Phase shift from electron holography

3.4.2.1 Recording the holograms

The experiment was carried out in an image Cs-corrected Schottky-FEG FEI Tecnai F20, operated at 100 kV (as mentioned earlier, this acceleration voltage was used in order to decrease the risk of damaging the CCnT). The initial distance between the CCnT and the Au anode can be seen in Fig. 2.1, being in the order of hundreds of μm. Using the slip-stick functionality of the nanomanipulator, the hat and W wire with the CCnT attached were approached to the anode. A TEM overview micrograph can be seen below in Fig. 3.6. The distance d is the tip-anode separation distance, now around 10 μm, was reduced further to less than 1 μm to perform the experiment. The voltage was increased until the onset voltage was reached (we define the onset voltage to when a field emission current above the floor noise is observed) and the cold-field emission process started, with the current of the emitted electrons collected by the positive anode and recorded, as depicted by the electronic schematic in Fig. 3.6.

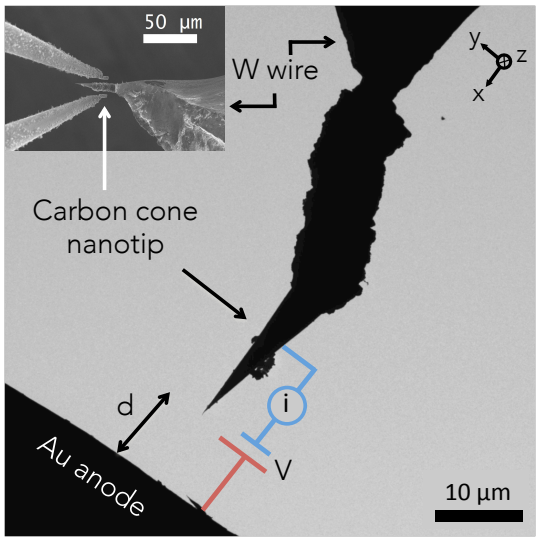

FIGURE 3.6 – *TEM micrograph showing the overview of the CCnT and anode. The SEM inset image shows the micro tweezers releasing the CCnT after having been attached to a cut W wire (as opposed to the etched tip used in Fig 3.4).*

Electron holography was performed for different tip-anode distances and bias. For the experiment reported here, the tip-anode distance $d = 680$ nm. A

Möllenstedt biprism was introduced in a plane below the sample*, and biased to $V_{\mathrm{bip}} = 74.5$ V, superimposing the two beams, with the object beam going through the strong electric field around the apex of the CCnT, and with the reference beam traveling through an area close to the anode, similarly as shown in Fig. 2.3.† Even though the reference hologram is a not in a field-free region, this position of the biprism is the most practical one. In Section 3.6.3 we will discuss how the models were treated in order to account for the non field-free reference region of the holograms.The voltage V between the CCnT and anode was increased in steps of 1 V, from 0 V, with one step per second. Holograms (2048×2048 pixels) were recorded with an exposure time of 5 seconds, every 10 V or less.

3.4.2.2 Processing the holograms

As mentioned in Section 2.2.3 an unusual approach was used to remove the unwanted phase shifts coming from the presence of a CCD camera, projectors, lens aberrations, mean inner potential (V_{MIP}) and Fresnel fringes ($\mathrm{F_f}$).

When a hologram is recorded, all contributions to the phase are included. These comprise of phase shifts from the sample, i.e., from the potential applied onto the anode (φ_{ano}) and from the mean inner potential (φ_{MIP}) of the CCnT, and, from distortions from the TEM (φ_{dist}). In other words, the total phase shift can be expressed as

$$\varphi_{\mathrm{tot}} = \varphi_{\mathrm{ano}} + \varphi_{\mathrm{MIP}} + \varphi_{\mathrm{dist}}, \tag{3.15}$$

where φ_{dist} contains phase shift from the projector lenses (φ_{proj}), aberrations (φ_{aber}, mainly from the imaging lens), camera (φ_{cam}) and Fresnel fringes (φ_{Ff}). That is,

$$\varphi_{\mathrm{dist}} \approx \varphi_{\mathrm{proj}} + \varphi_{\mathrm{aber}} + \varphi_{\mathrm{cam}} + \varphi_{\mathrm{Ff}}. \tag{3.16}$$

The goal is to remove φ_{dist} and φ_{MIP} from eq. (3.15), leaving only the phase shift φ_{ano}, stemming from the applied potential on the anode. To remove φ_{proj}, φ_{cam} and phase shift coming from e.g. dirt on the biprism, normally a reference hologram is acquired and subtracted from the phase image. But, this was not possible here. The reason is that when recording a reference hologram, the sample must be moved out of field of view. Since we recorded the field emission current simultaneously with our holograms, removing the CCnT from the field of view would take too long time, causing a significant drop in the field emission current.‡ Also, after removing the tip from the field of view, the long

*The same plane as the selected area aperture, but when working in high magnification mode of the TEM, the image plane is below the biprism.

†Florent Houdellier at CEMES-CNRS aided in capturing the holograms.

‡For reasons that have been discussed in Section 3.2.2. The effect of the current decreasing even during the time it took to record the holograms will be discussed in Section 3.8.1.

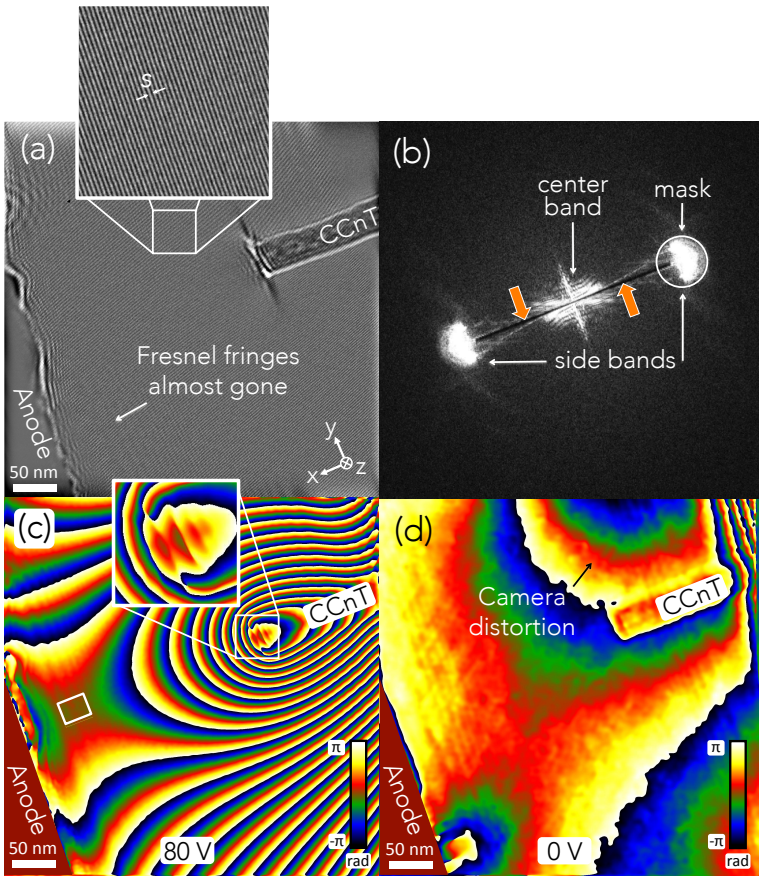

FIGURE 3.7 – *(a) The re-constructed hologram after the Fresnel fringes have been removed. Some remains of the Fresnel fringes can be seen (compare with Fig. 2.4 (a)). In (b) the orange arrows points to the areas that before contained the Fresnel fringes information (compare with Fig. 2.4 (b)). (c) Improved resolution after the 0 V phase map in Fig. 3.8 (a) has been subtracted from Fig. 2.4 (c). The inset will be discussed further down. (d) The 0 V phase map before the camera distortions have been removed.*

range electric field would affect the reference hologram, even if displacing the tip a large distance. And, setting the potential on the anode to zero between holograms was for obvious reasons also not an option. A reference hologram should also always be recorded shortly after the object hologram, otherwise changes in the beam, sample or biprism can cause the two holograms to capture the distortions differently, which will render the reference hologram unusable.

Instead, to remove φ_{dist}, we assumed and did the following. Regarding the projector lenses distortion φ_{proj} it could be neglected since we work with

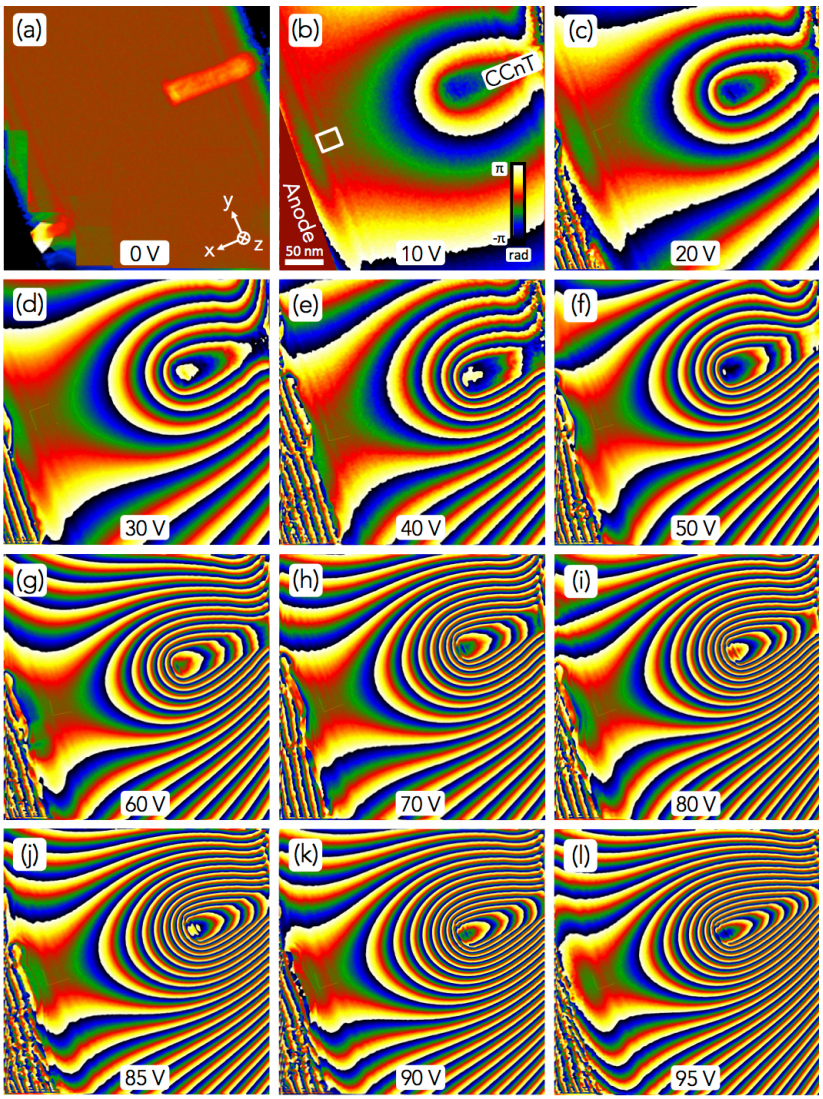

FIGURE 3.8 – *Phase maps showing the increase in phase shift when increasing the potential between the anode and CCnT from 0 to 95 V.*

a high magnification, that is, we had a small field of view. This, together with the fact that the phase shift from the applied potential was large, resulted in $\varphi_{\mathrm{proj}} \ll \varphi_{\mathrm{ano}}$. Also the phase shift from the aberration distortion φ_{aber} is much smaller than φ_{ano} and could thus be omitted. The phase shift from the camera distortions φ_{cam} are important and can not be disregarded. But these distortions are available from the camera's Ronchigram, and their contribution to

the phase shift could therefore easily be removed*. Finally, the Fresnel fringes† were subtracted by using a special mask that removed the information between the two sidebands, which corresponds to the Fresnel fringes (spanning over a large frequency spectrum, i.e., alternating wavelength in real space). Comparing Fig. 3.7 (b) with Fig. 2.4 (b) it can be seen that the white areas between the center and side bands have been removed. And, when comparing Fig. 3.7 (a) with Fig. 2.4 (a) one can see that most of the Fresnel fringes are gone.‡ This procedure was applied to each hologram.§ The software used for calculating the phase was a modified version of GPA Phase 2.0 (HREM Research).

At this point, $\varphi_{\mathrm{dist}} = 0$ and eq. (3.15) is reduced to $\varphi_{\mathrm{tot}} = \varphi_{\mathrm{ano}} + \varphi_{\mathrm{MIP}}$. To remove φ_{MIP}, we subtracted the phase of the 0 V hologram from all other holograms. The 0 V hologram was obtained when no bias was applied to the anode (see Fig. 3.8 (a)). In other words, for the holograms in Fig. 3.8 (b) – (l)¶, $\varphi_{\mathrm{tot}} = \varphi_{\mathrm{ano}}$. From here on, when we write φ, we speak of φ_{ano}.

In Figs. 3.7 (c) and 3.8 (b), the white rectangle illustrate the chosen internal reference area. This is the area where we set the phase shift and the phase gradient to be zero, i.e., where we assume that the potential is zero (see the end of Section 2.2.3.1 for a more thorough explanation).

3.4.2.3 Phase shift from the 80 V hologram

At 80 V the onset of field emission started, which will be seen in $i_{\mathrm{e}}(V)$-curves further down. This is the potential we chose to compare the experimental and the simulated phase shift. The reason for this choice is that *after* the onset of field emission, the emitted electrons will decrease the local electric field, which is something not accounted for in our model. The impact on the phase shift and the electric field after the onset of field emission will be elaborated on in Section 4.3.2.

To calculate the total phase shift of the electrons, the phase map in Fig. 3.7 (c) was unwrapped, that is, the 2π reoccurrence were added up, thus creating a continuous phase shift without the phase jumps, as can be seen in Fig. 3.9 (a). A profile of the unwrapped phase map in Fig. 3.9 (a) was obtained, direction and location indicated by the white arrow. The result can be seen in Fig. 3.10. The

*Removing the effect from the optical fiber in the CCD camera is the main reason for the decrease in noise of the phase map, which can be seen when comparing Fig. 2.4 (c) and Fig. 3.7 (c).

†More precisely, the Fresnel fringes does not affect the phase, but rather increase the noise.

‡These special treatments were done with the help of Christophe Gatel at CEMES-CNRS.

§The hologram in Fig. 3.7 (a) was created by first taking the original hologram, making a fast Fourier transformation (FFT, as explained in Section 2.2.3), cutting out the Fresnel fringes in the resulting complex image and finally making an inverse fast Fourier transformation FFT (FFT^{-1}) of the entire complex image, which re-constructed the modified hologram.

¶The observant reader notice that the phase shift is more or less constant after 80 V. The reason for this will be discussed in Section 4.3.2.

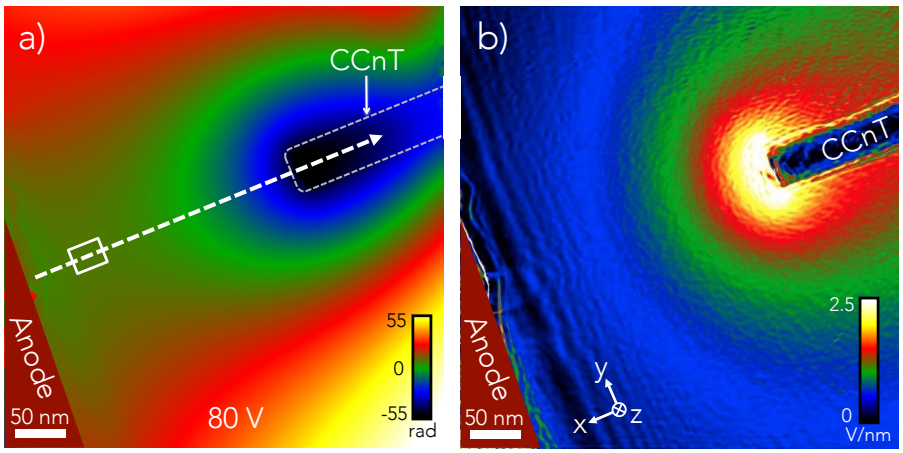

FIGURE 3.9 – *(a) The unwrapped phase map of Fig. 3.7 (c) with the dotted arrow representing the position and direction from where the profile of the phase shift was obtained (see Fig. 3.10). In (b), the gradient of the phase shift is shown, which is a projection of the electric field.*

dotted grayed out area outlines the CCnT (as in Fig. 3.9 (a)). The white square shows the internal reference area. In Fig. 3.9 (b), the gradient of the phase map in Fig. 3.7 (c) provides qualitative information of the electric field around the tip (according to eq. (3.14)). The legend was added only as an indication of the later quantitatively obtained field.

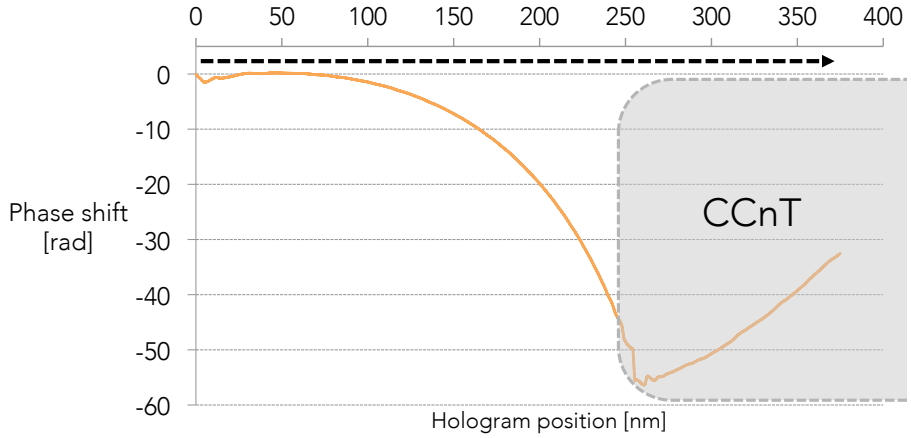

FIGURE 3.10 – *The orange curve shows the profile of the unwrapped phase shift map in Fig. 3.9 (a). The dotted black arrow corresponds to the dotted white arrow in Fig. 3.9 (a).*

One issue when unwrapping a phase map is that every contribution to the phase is added up, thus potentially giving localized erroneous result. As can be

seen in the inset of Fig. 3.7 (c), phase jumps can be seen also inside the CCnT, which contributes to the sharp phase increase that show at the very apex of the CCnT in Fig. 3.10. That these are artifacts we believe can be seen in the inset of Fig. 3.7 (c) by that the phase lines are not continuous. If one instead counts the number of phase jump in Fig. 3.7 they are around 7. With each corresponding to 2π and with an error of approximately π, the resulting phase shift is $\varphi = 14\pi \pm \pi = 44 \pm 3$ rad, which also is the result displayed n Fig. 3.10.

The reason for the negative phase shift can be found in eq. (3.10), which states a direct relationship between the potential and the phase shift, i.e., the electrons close to the anode are phase-changed more when compared with those close to the tip.

3.5 *In situ* field emission and the Fowler-Nordheim plot

Figure 3.11 shows the field emission $i_{\mathrm{e}}(V)$-curve that was obtained with the holograms. The voltage V on the anode was increased in 1 V per second and only the data during the first second after the increase in voltage was used. When a hologram was obtained, it was acquired just after the voltage was increased (see Section 3.8.1 on a discussion on this). The field emission current was recorded from 0 V but here only the data from the onset of field emission at 80 V is displayed. As can be seen, the data is quite noisy. The reason for this will be discussed in Section 3.8.1. The inset shows the F-N plot, which was made by plotting $\ln(i_{\mathrm{e}}/V^2)$ over $1/V$ starting at 96 V and ending at 80 V.

3.5.1 The field enhancement factor γ

The local electric field E_{loc} in the Fowler-Nordheim equation (eq. (3.5)) is the local field around the emitting tip. As mentioned before, the local field is enhanced around the tip, with respect to the situation with parallel plates. If one compares this local field with the reference electric field from two parallel plates, $E_{||} = V/d$, V being the applied voltage and d the separation distance, the field is enhanced by a factor γ, that is,

$$E_{\mathrm{loc}} = \gamma E_{||} = \gamma \frac{V}{d}. \tag{3.17}$$

In other words, eq. (3.5) can be expressed as [Bonard et al., 2002b]

$$i_{\mathrm{e}} = A \frac{1.54 \times 10^{-6}}{\phi} \left(\frac{V}{d}\right)^2 \gamma^2 \exp\left(\frac{10.4}{\sqrt{\phi}}\right) \exp\left(-\frac{6.44 \times 10^9 \phi^{3/2} d}{V\gamma}\right). \tag{3.18}$$

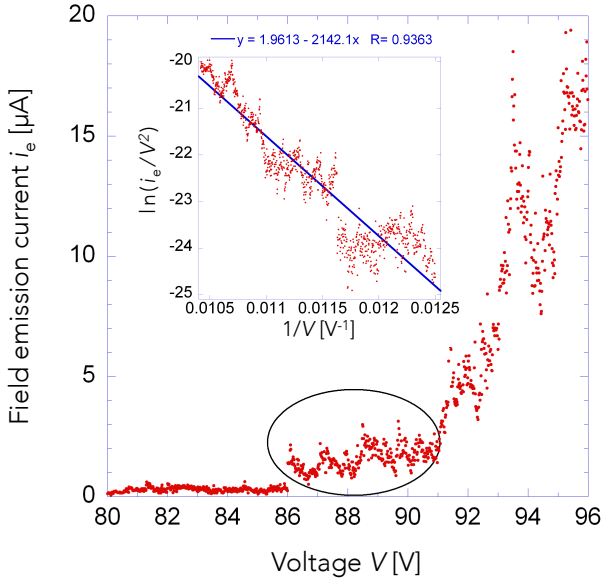

FIGURE 3.11 – *The $i_e(V)$-curve obtained from the onset of field emission at 80 V. The inset shows the Fowler-Nordheim plot with the blue line being a linear fit. The circled peaks will be discussed in Section 3.8.1.*

We will use these equations to find the work function ϕ of the CCnT. This is possible since $-\frac{6.44\times10^9\phi^{3/2}d}{\gamma}$ of eq. (3.18) corresponds to the slope in the logarithmic F-N plot in Fig. 3.11 [Bonard et al., 2002b]. And, since we know V and easily can measure d in the TEM, only γ needs to be found in order to have ϕ. From eq. (3.17) we see that if we know the local electric field E_{loc} we will have γ. And to obtain the local electric field, we will use FEM and electron holography (EH), as will be shown in the following section. In other words,

$$\text{FEM} + \text{EH} \Longrightarrow E_{\text{loc}} \overset{\text{Eq. 3.17}}{\Longrightarrow} \gamma \overset{\text{Eq. 3.18}}{\Longrightarrow} \phi. \tag{3.19}$$

3.6 Finite element method modeling

Simple physical models have been used in the past to find for example the field enhancement factor γ, e.g. the "hemisphere on a post" model [Dyke and Dolan, 1956, Forbes et al., 2003]. Here, we have chosen to use finite element method (FEM) modeling to simulate the behavior of the electrostatic potential and field around the tip, which provided us with a complete map of the fields.

From the model and by using eq. (3.10) we can calculate the corresponding phase shift. If the phase from the model matches the phase obtained from the

holography results, we can be assured that the model is correct and that the electric field from the model is the field that we had around the tip. Before this could be done there were a number of obstacles that needed to be overcome.

First of all, it is not possible to model the entire system, which is composed of parts with large differences in size: The apex of the CCnT is in the 10 nm range and the anode in the 100 μm range. A ratio of $10\,000$ between the two imposes an almost insurmountable task for the capability of both the writer's FEM knowledge and his computer's calculation power. Only parts of the full setup were therefore modeled. In order to ensure that this would not adversely affect the results, we made a number of convergence simulations, with a few of them being discussed and displayed in Section 3.6.2 below.

Secondly, in order to be able to compare the phase shift from the model in a meaningful way, the phase shift has to be treated in the same was as the phase shift from the electron holography. How this was done will be explained in Section 3.6.3.

3.6.1 How the model was created

The experimental set-up was simulated by a three dimensional model, built in Cartesian coordinates using the electrostatic module of the commercially available FEM software from COMSOL Multiphysics (version 4.3). To begin with, the two-dimensional axial symmetric functionality was exploited, made possible due to the axial symmetry of our system, which speeded up the processing multifold. We used this to perform a multitude of convergence simulations, parametric sweeps and to optimize the model, which otherwise would have taken an unreasonable amount of time. Once the model was functional, we rebuilt it in three dimensions and compared the results with those acquired from the two-dimensional model. Another reasons to build the model in three dimensions is that it was more straightforward to get a clear picture of the structure and results. It was also easier to calculate the phase shift according to eq. (3.10) for technical reasons.

The materials assigned to the different parts of the model were air* for the empty cube, and Au and C [100], for the anode and CCnT, respectively (parameters supplied by the built-in module and the MEMS module). For the electrostatic boundary conditions the sides of the empty cube and the CCnT faces were grounded.† A potential of $V = 80$ V was applied to the anode. An overview and zoom-in of the mesh of the system can be seen in Fig. 3.12.

As can be seen in the figure, the system is made up of a $60\,\mu$m sided empty cube which encapsulate the Au anode and CCnT. The width and height of the

*Using air is indifferent from vacuum.

†The default values for the charge conservation, zero charge and initial values were used.

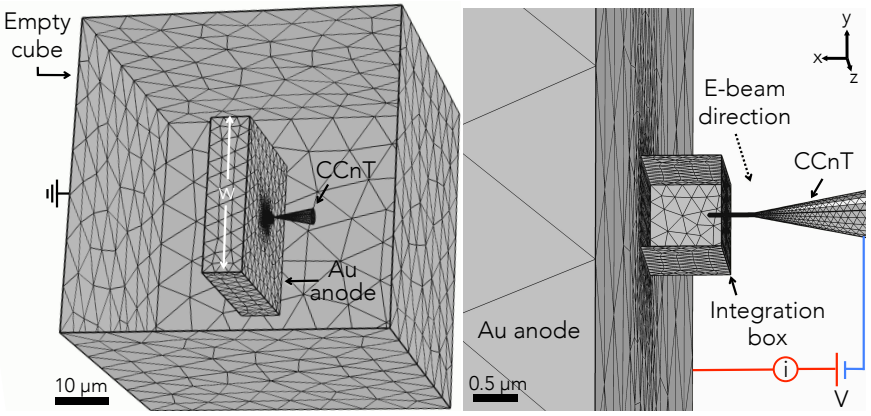

FIGURE 3.12 – *(a) The triangulized FEM mesh showing the cube that contains the CCnT and anode. The side of the cube facing out of the paper has been made transparent for illustration purposes. (b) A zoom-in of the dark area in the center of (a), showing the apex of the CCnT, the anode and the integration box (which also has the side facing out of the paper removed).*

simulated anode was $w = 20\,\mu$m, and its thickness was $5\,\mu$m. The CCnT constituted a semi-spherical top with radius 20 nm followed by a 500 nm long cylindrical structure* that was connected to a $5\,\mu$m long cone with a base diameter of $2\,\mu$m. The tip of the CCnT was separated 680 nm from the anode. The direction and propagation of the TEM electron beam is along the z-axis.†

The number of elements in Fig. 3.12 was over $108\,000$. And as can be seen, we concentrated them in the very center of the structure of (a), since the intent for highest accuracy was here. Zooming in on this area, illustrated in (b), the integration box appears. This is is the volume which we integrate over according to eq. (3.10). How this was done will be explained in Section 3.6.3.

3.6.2 Convergence simulations to verify model

To be computable, the model needs to be optimized. One way to do this is to make the model smaller than the real system it simulates. Firstly, we only model a small part of the CCnT, as seen in Fig. 3.12 (a). We then compared with a large model to make sure that the approximation was valid.

Secondly, we reduced the dimensions of the Au anode, which in reality measured $250 \times 30 \times 1000\,\mu$m. By alternating the width and height w and

*See Fig. 2.3 for the reason for this shape.

†For the sake of orientation, the electrons emitted from the CCnT, travel to the anode in the positive x-direction.

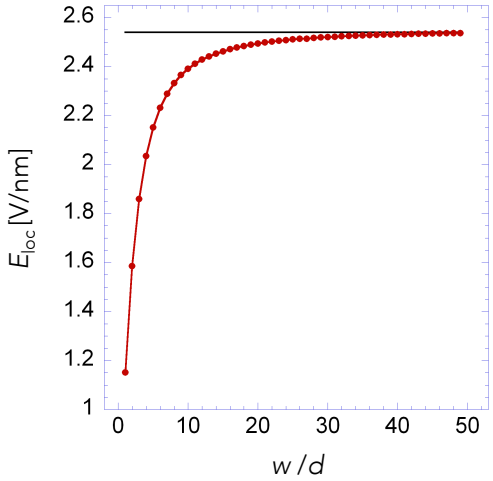

FIGURE 3.13 – *Plot from convergence simulations of the electric field E_{loc} as a function of the ratio of the width/height w of the anode and the tip-anode separation distance d.*

thickness of the anode and the tip-anode separation distance d, we could see the changes in the local electric field E_{loc}. Since the results depended largely on the ratio between the width/height of the anode and the tip-anode separation distance, but less on the thickness of the anode, we plotted the electric field as a function of w/d*, which can be seen in Fig. 3.13. Having a simulated thickness of 5, 10 or $50\,\mu$m made no difference.

For ratios $w/d \geq 30$, the error is in the order of a couple of percent. The plot also illustrates the significant error introduced by making the anode too small. In other words with a tip-anode separation distance $d = 680$ nm, we made the width and height of the anode $w = 20\,\mu$m. The black line points to the value of 2.55 V/nm that we later used.

The optimum size of the integration box was investigated by varying its dimensions in the z and y-directions (see Fig. 3.12 (b)). Having z and $y \geq 1\,\mu$m, the difference with larger model was below a couple of percent. We also did some further studies of z, since this was the direction that we integrated along to calculate the phase shift according to eq. (3.10). We varied z from 2 to $16\,\mu$m, without seing any distinguishable difference. This is also understandable since the potential gradient is highly localized around the tip.

Additionally, we varied the pixel-density when exporting the simulations from COMSOL Multiphysics to the software DigitalMicrograph (Gatan Inc.). We saw a difference in the results between 1 and 2 pixels per nm, but not be-

*The reason for plotting the ratio is so that it could be used for systems with different tip-anode separation distances.

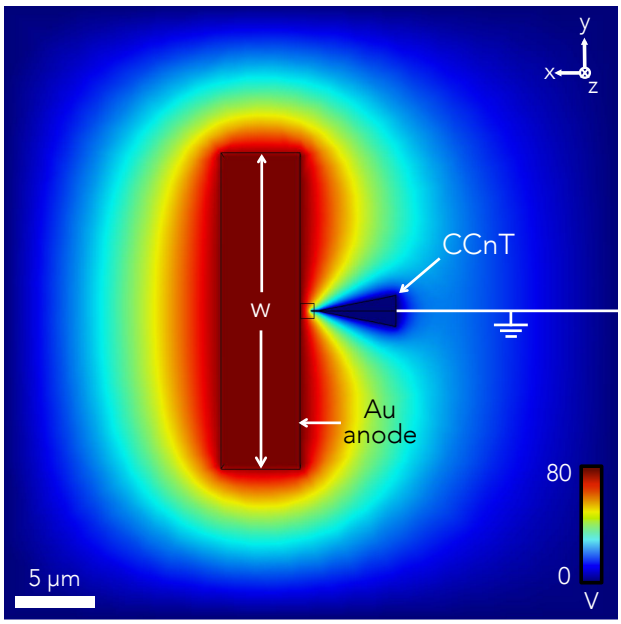

FIGURE 3.14 – *The in-plane electrostatic potential field, in the plane $z = 0$. The CCnT and and outside borders are grounded while the Au anode is biased to 80 V.*

tween 2 and 4. We therefore used 2 pixels per nm.

We studied other parameters; the number of mesh elements, the size of the empty cube, the vacuum inside the cube, having the CCnT not perpendicular to the anode, different shaped apexes of the CCnT, different shaped supports of the CCnT, and more. If they made a difference, the converged value was used.

The surface of the modeled objects will never be an exact replica of the real surfaces. This will be discussed in Section 3.8.2, particularly for the apex of the CCnT where the electric field is the strongest.

3.6.3 Phase shift from modeling

3.6.3.1 The simulated potential and electric fields

An overview of the simulation can be seen in Fig. 3.14. It displays the full simulation (as in Fig. 3.12 (a)) of the in-plane electrostatic potential when a voltage of 80 V is applied to the anode. The small square at the apex of the CCnT is the integration volume and also the areas displayed in Figs. 3.15 (a) and (b).

In Fig. 3.15 (a) one can see how the decrease of the potential accelerates closer to the CCnT. The presentation in 5 V steps was made in order to clearer

visualize this acceleration. The profile of the lower part of Fig. 3.15 (a) shows this plainly as well. The electric field norm `es.NormE` found in the electrostatic module of COMSOL was used. It is defined as

$$\texttt{es.NormE} = \sqrt{|E_x|^2 + |E_y|^2 + |E_z|^2}. \tag{3.20}$$

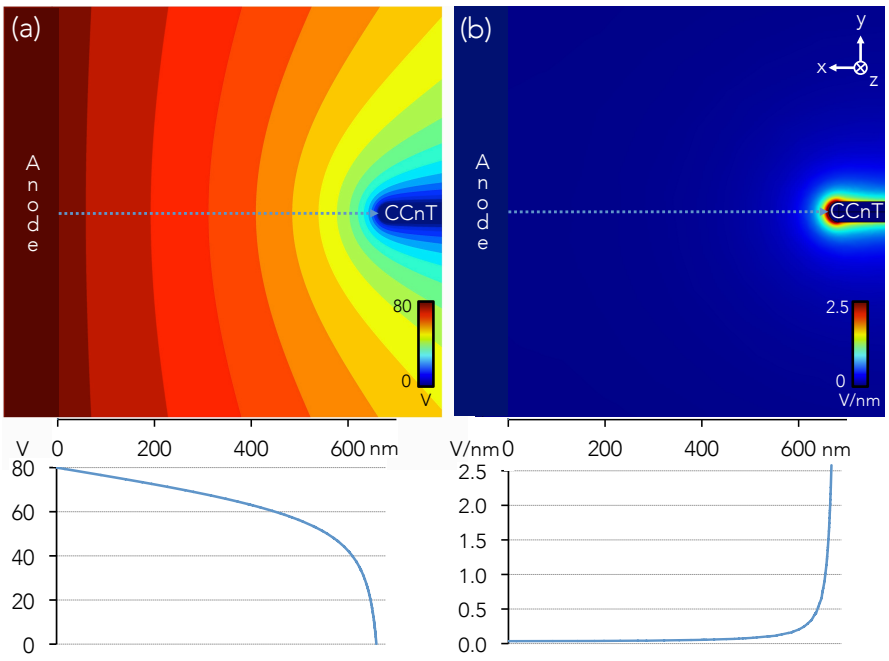

FIGURE 3.15 – *(a) The tip image shows the in-plane electrostatic potential field (with $z = 0$), here represented in 5 V steps. The plot below is a profile of the same field (but without the stepwise illustration) from the left at the anode to the CCnT to the right. In (b) the electrostatic field and its profile can be seen, for the same conditions as in (a), i.e., with 80 V applied to the anode.*

In Fig. 3.15 (b) the electric field corresponding to the same conditions as in (a) can be seen. Worthy to note is how localized the electric field is around the CCnT.

3.6.3.2 The integration using COMSOL

We started out by exporting the electrostatic potential field from COMSOL and subsequently performed eq. (3.10) using DigitalMicrograph, but later executed all steps directly in COMSOL.* Both methods produced same results. Figure

*A new operator using the general projection functionality was created and assigning to a created variable, which later was implemented to the integration box. Please note that due to a bug in the software, the y's and z's in the Source and Destination Maps of the General Projection

3.16 shows an integration along z, resulting in a two-dimensional map in x and y. In the figure, the projected value is shown for every position in z. There is no data bar present since the constant C_{E} from eq. (3.11) has not yet been applied.

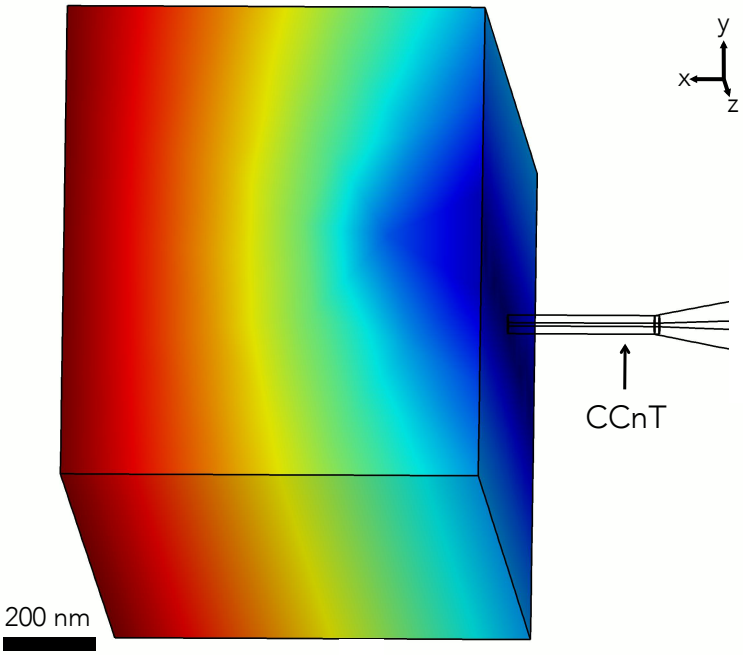

FIGURE 3.16 – *The projected potential in the integration box.*

The size of the integration box is $x, y, z = 0.88, 1, 2\,\mu$m (see Fig. 3.16). The size in x is twice the sum of the width $d_{\mathrm{h}} = 350$ nm of the hologram and the width of the biprism $d_{\mathrm{bip}} = 90$ nm (see Fig. 2.4). In other words, this is the object and reference wave before they are divided up and superimposed by the biprism. The width of the biprism was measured in the TEM, being in focus and with 0 V applied to it. Finally, C_{E} was applied by multiplying it to the exported data.

3.6.3.3 The processing in DigitalMicrograph

As the holograms were treated in DigitalMicrograph, we treated also the phase maps from the simulations here.

The exported simulation phase maps were imported into the software, and a reference and a object part was created by dividing the maps in two. Then the reference half was subtracted from the object half. The reason is that the difference between the reference and object halves is measured in a hologram, with

window must be exchanged.

the phase coming from the reference part being assumed to be zero ($\varphi_R = 0$ in eq. (2.2)). When this is not the case, like here, we need to subtract the phase in the reference half from the phase coming from the object half. Therefore, since the electron phase depends on the potential, and with the highest potential is close to the anode (which is the reference part), the resulting phase map displays negative values.

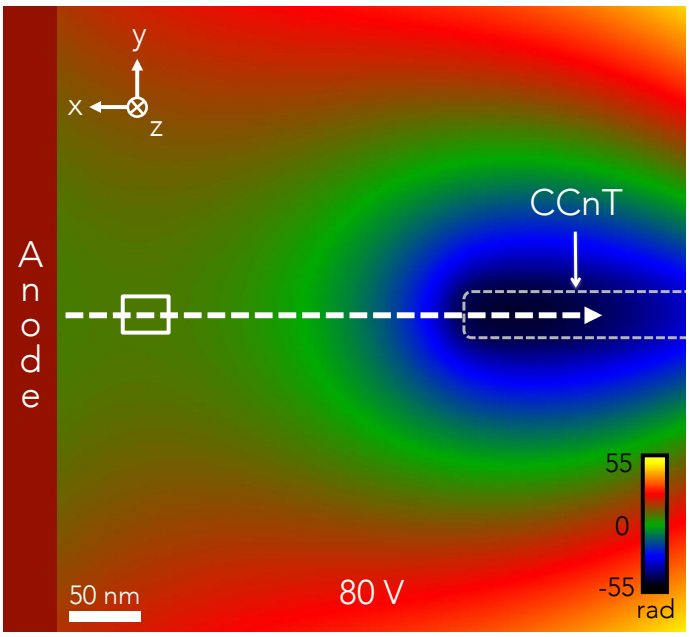

FIGURE 3.17 – *The simulated phase map with the dotted arrow representing the position and direction from where the profile of the phase shift was obtained (see Fig. 3.18). The image is after the reference map has been subtracted from the image map. Therefore, the apparent tip-anode separation distance is 250 nm is not the true distance, i.e., like for a hologram.* $V = 80$ *V.*

To the resulting phase map, the internal reference area used in the holograms was inserted (see at the end of Section 2.2.3.1 for at detailed explanation on its function in a hologram). As mentioned before, the internal reference area was in a non potential-field-free part of the hologram (just like the reference half of the electron beam). Therefore, not only the phase shift, but also the phase gradient from this area was subtracted from the phase map. The results can be seen in Figs. 3.17 and 3.18, with the former showing the phase map and the latter the profile. A more detailed explanation of these steps can be found in Appendix C.1.

Before the electric field from the model can be used, the modeled and experimental phase shift should match. The reference area in the simulated map

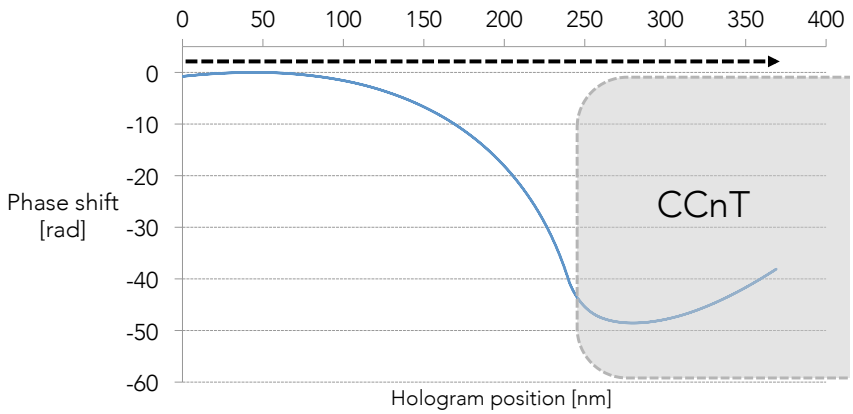

FIGURE 3.18 – *The blue curve shows the profile from Fig. 3.17, with the dotted black arrow corresponds to the the dotted white arrow in Fig. 3.17.*

should be chosen with caution since a small difference in the gradient could make a significant difference. We have studied the error in the phase from this step, and it was below 10%.

3.7 Results

In this section we will begin by comparing the phase shift from the holograms and the simulations. We will then use this knowledge together with the F-N equation in order to retrieve the work function ϕ of the CCnT.

3.7.1 Comparing phase shift from electron holography and FEM

For an easy comparison between the experimental phase map in Fig. 3.9 (a) and the simulated one in Fig. 3.17, they are displayed next to each other in Fig. 3.19 below. As can be seen, they look very similar.

If we now compare the two phase profiles from Fig. 3.19 (or simply superimpose Figs. 3.10 and 3.18), we arrive at Fig. 3.20. Here, it is even clearer that the match between the experimental and simulated data is excellent. Not only do the values but also the shapes of the curves agree well (for a discussion on the error on the data, see Section 3.7.2.1). The fit is all the more remarkable, because it is not an adjusted fit. That is, parameters like the tip radius or voltage has not been changed to get the best fit (observe the error from the internal reference area mentioned in Section 3.6.3.3).

Having this agreement, we can be assured that the model is correct and that the electric field from the model in Fig. 3.15 (b) indeed is the the electric field

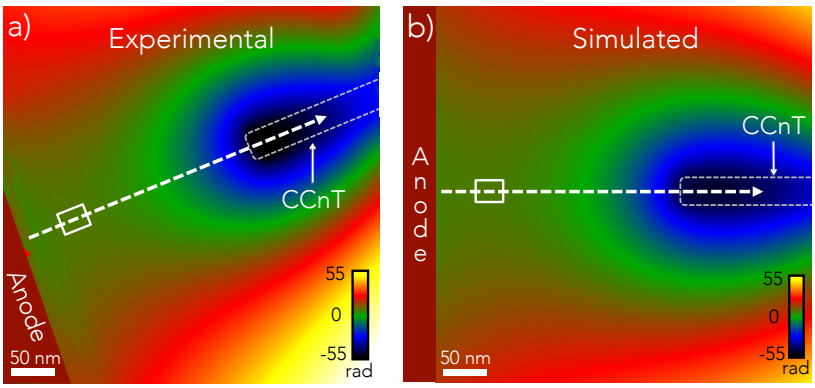

FIGURE 3.19 – *Comparison of the experimental phase map from Fig. 3.9 (a) and the simulated one from Fig. 3.17.*

from the experiment, being $E_{\text{loc}} = 2.55\ \text{V/nm}$.

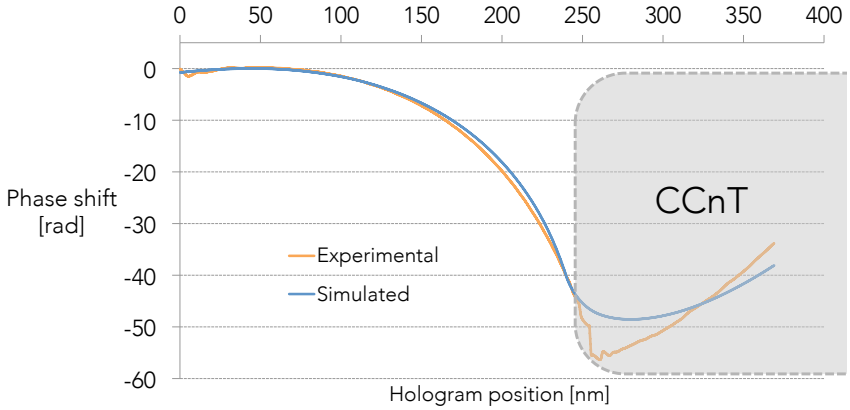

FIGURE 3.20 – *Profiles from the experimental (orange) and the simulated (blue) phase maps. The dotted greyed out area shows the position of the CCnT.*

By now having a quantitative value of the local electric field, we can obtain the work function in the following way.

3.7.2 The work function ϕ

From eq. (3.17) we have that the field enhancement factor

$$\gamma = \frac{d}{V} E_{\text{loc}} \tag{3.21}$$

and with $E_{\mathrm{loc}} = 2.55$ V/nm, $V = 80$ V and $d = 680$ nm we find that $\gamma = 21.7$*. The F-N theory (see Section 3.5.1) gives that:

$$-\frac{6.44 \times 10^9 \phi^{3/2} d}{\gamma} = \text{Slope in the F-N-plot.} \tag{3.22}$$

From the F-N plot in the inset of Fig. 3.11 we see that the data has been fitted using a linear function, resulting in it being described with

$$y = 1.96 - 2142x,\ R = 0.9363 \tag{3.23}$$

where $y = \ln(i_{\mathrm{e}}/V^2)$, $x = 1/V$ and R describes the error in the fit. Combining equations 3.22 and 3.23 we get that

$$\phi = \left(\frac{2\,142\,\gamma}{6.44 \times 10^9\, d}\right)^{2/3} = \left(\frac{2\,142 \cdot 21.7}{6.44 \times 10^9 \cdot 680 \times 10^{-9}}\right)^{2/3} = 4.83\,\text{eV}. \tag{3.24}$$

3.7.2.1 Error analysis of ϕ

To begin our discussion regarding the error of the work function, we have to acknowledge the uncertainty of some of the input parameters used in the model. First of all the accuracy of measuring the tip radius give that $r = 20 \pm 1$ nm. Secondly, due to the unevenness of the surface of the anode, and from shadowing effect of the same, together with that one has a typical magnification error of the TEM of 2%, we estimate the tip-anode separation distance to be $d = 680 \pm 10$ nm. To decrease the uncertainty coming from the shadowing of the anode, the CCnT was lightly brought into contact to the anode before it was retracted to the desired separation distance.† From the results of the convergence simulations in Section 3.6.2, we have that the error from decreasing the size of the modeled anode is around 2%. These errors combined, created an inaccuracy of 4% of the simulated local electric field, i.e., $E_{\mathrm{loc}} = 2.55 \pm 0.1$. Entering these errors into eq. (3.21), we arrive at a field enhancement factor of $\gamma = 21.7 \pm 0.8$.

A possible contribution to the error of the F-N plot, is whether or not all of the emitted electrons are being collected by the small anode. But, considering the proximity of the CCnT to the anode, being separated with a mere 680 nm, we assume this having a negligible effect. The error on the fit of the F-N plot was estimated to be around 7%. Now, combining that $\gamma = 21.7 \pm 0.8$ and that

*Other work where the field enhancement factor from small emitters has been discussed can be found in the following articles [Pogorelov et al., 2009, Huang et al., 2005, Smith and Silva, 2009, Smith et al., 2005, Wang et al., 2004, Zeng et al., 2009].

†At the same time we made sure that the CCnT was positioned approximately in the middle opposite the anode.

the slope in the F-N plot $= 2\,142 \pm 138$ and using the extremities of both in eq. (3.24), we get that $\phi = 4.8 \pm 0.3$ eV.

Finally, a discussion regarding the effect that space charge can have on the field emission current i_{e} and the local electric field E_{loc} will be discussed in Section 4.3.2.

3.7.2.2 Value of ϕ using other techniques

Gao et al. utilized a method which relied on the mechanical resonance response of multiwalled carbon nanotues (CNTs), obtaining a work function of 4.7 ± 0.1 eV [Gao et al., 2001] for some CNTs and around 5.6 eV for others. They suggested that the CNTs with higher work function were semiconductive. Considering the conical shape of the CCnT, we believe that this method is not feasible here.

de Jonge obtained in 2009 that $\phi = 5.1 \pm 0.1$ eV for three to five-walled CNTs [de Jonge, 2009]. An energy spectrum of the emitted electrons was acquired, with a value of $\phi = 5$ eV being assumed. Then, using the outcome, the F-N equation was used to arrive at the reported value.

Shiraichi and Ata found a work function of $\phi = 5 \pm 0.05$ eV of bundles of single- or multiwalled CNTs, using photoelectron emission and the *ab initio* method [Shiraishi and Ata, 2001]. Liu et al. studied thermionic emission to study the work function from the middle of bundles, resulting in $\phi = 4.8 \pm 0.1$ eV [Liu et al., 2008]. Further work on the work function of CNTs can be found in [Shan and Cho, 2006, Shan and Cho, 2005, Suzuki et al., 2000, Suzuki et al., 2004].

3.8 Discussion

3.8.1 The irregular $i_{\mathrm{e}}(V)$-curve

As was mentioned in Section 3.2.2 one reason for the irregularity of the $i_{\mathrm{e}}(V)$-curve in Fig. 3.11 comes from inherent properties of cold-field emission. There are basically two different properties that create fluctuations in the current. First of all, molecules can be adsorbed onto the tip, which apart from increasing the work function and thus decreasing the field emission current, also create fluctuations in the current from the migration of the adsorbates [de Jonge, 2009]. This effect is lessened by the CCnT as it is less reactive than a standard W tip [Saito and Uemura, 2000]. But since the vacuum of the column is around 10^{-5} Pa and within a cold-field emission gun it is in the order of 10^{-8} Pa, the effect was altogether more prominent. The important parameter here is the

vacuum pressure P times the current i_e. In our experiments, where the field emitting tip was located in the column of the TEM where the pressure was 2.4×10^{-5} Pa, a value of $P \cdot i_e = 2.4 \times 10^{-5} \cdot 2 \times 10^{-6} \approx 5 \times 10^{-11}$ PaA was obtained. Todokoro et al. found that below 7×10^{-12} PaA the fluctuations in the current was under 1% [Todokoro et al., 1982].

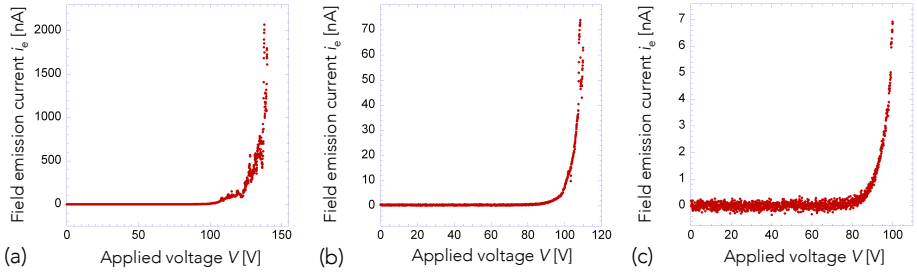

FIGURE 3.21 – *Three graphs showing continuously obtained field emission $i_e(V)$-curves from the same experiment, where data in (b) and (c) are taken from from (a), but plotted only from 0 to 110 and 100 V, respectively.*

Secondly, ions bombarding the emitter surface also generate fluctuations in the current. Todokoro et al. [Todokoro et al., 1982] concluded that for pressures higher than 1.8×10^{-8} Pa, the dominating reason for fluctuations in field emission current is from ion bombardment. They also found that the origin of these ions is close to the emitting area. The reason for this is that the emitted electrons collide with residual gas atoms, which has been created from electron bombardment of the anode (anode degassing), with the subsequently created ions (cations) falling into the negatively charged emitter (flicker noise). These fluctuations are naturally more prominent at higher currents, which Todokoro et al. and also we have observed. And, considering the proximity of the anode in our experiment, the anode degassing effect could be more important than normally.

The three graphs in Fig. 3.21 come from the same continuously obtained field emission $i_e(V)$-curve*, with the difference that in (b) and (c), only the current for voltages from 0 to 110 and 100 V, respectively, are plotted. Comparing (a) with (c), the ion bombardment effect can clearly be seen. If compared with Todokoro et al., it is in our case more obvious at lower currents, due to the lower vacuum in our experiment. Houdellier et al. also showed that when a vacuum of 10^{-9} Pa was used (in a bench experiment), the field emission current from a CCnT was more stable than shown here [Houdellier et al., 2012].

Another reason for the unevenness of the $i_e(V)$-curve comes from the fact

*In other words, not while recording hologram simultaneously.

that the holograms had an exposure time of 5 seconds, during which the current decreased. Therefore, in order to get as continuous field emission $i_{\mathrm{e}}(V)$-curves as possible, the voltage was increased 1 V per second and only the data during the first second after the increase in voltage was used. The peaks indicated by the oval in Fig. 3.11 could come from that the voltage was increased in 1 V steps, since having a non-analogue increase of the voltage gives a peak in the current, but directly after the current goes down.

3.8.2 Difference in real and modeled tip shape

The tip of the CCnT was modeled as a semi-sphere. As can be seen in the hologram in Fig. 3.7 (a), this is not the case. In reality, the apex of the CCnT comprises of two edges and an uneven surface with small protrusions. So how does this affect the results?

One might say that this is not important since the phase gradient behaves smoothly close to the tip, and no clear local concentration of electric field is visible (see Fig. 3.9). However, the fact that we view the electric field in projection will naturally smooth out any sharp variations, diminishing this argument somewhat. But, simulations that we have made of small protrusions, both on the anode and on the apex of the CCnT, shows that these do not play a part in the local electric field. We argue that it is a combination of tip radius and length of the structure that decides the strength of the electric field. We also argue that the importance of the length diminishes with the same, i.e., it is the combination of a small tip radius with a long structure after the tip which matters, but only to a certain length; an infinitely long structure after the tip would only negligible increase the local electric field. Numerical simulations of single and multiple CNTs of the electrostatic field from de Jonge and Bonard [de Jonge and Bonard, 2004] motivates this argument as well and also that structures surrounding the emitting part play an important role in shielding the emitter. This being said, the electric field that we discuss here is not the electric field on an atomistic scale. It is rather the electric field on a mesoscopic level. See e.g. Vurpillon et al. where numerical simulations reveal an electric field that fluctuates largely at the surface of an atom probe tip [Vurpillot et al., 1999].

3.8.3 The danger with the field enhancement factor γ

To discuss the results in a larger context, we have made a range of simulations from which we have extracted the local electric field E_{loc} and determined the corresponding field enhancement factor γ. As can be seen in Fig. 3.22*, the

*In Fig. A.4, a graph shows the evolution of γ for distances up to 100 μm, for $r = 20$ nm and $V = 80$ V.

field enhancement factor is not only dependent on the tip radius r, but also largely on the tip-anode separation distance d (all simulations here were made with an anode potential of 80 V). Our wish is that when comparing different field enhancing systems, the tip-anode separation distance should always be specified. This has also been pointed out before by Bonard et al. [Bonard et al., 2002a] and by de Jonge and Bonard [de Jonge and Bonard, 2004].

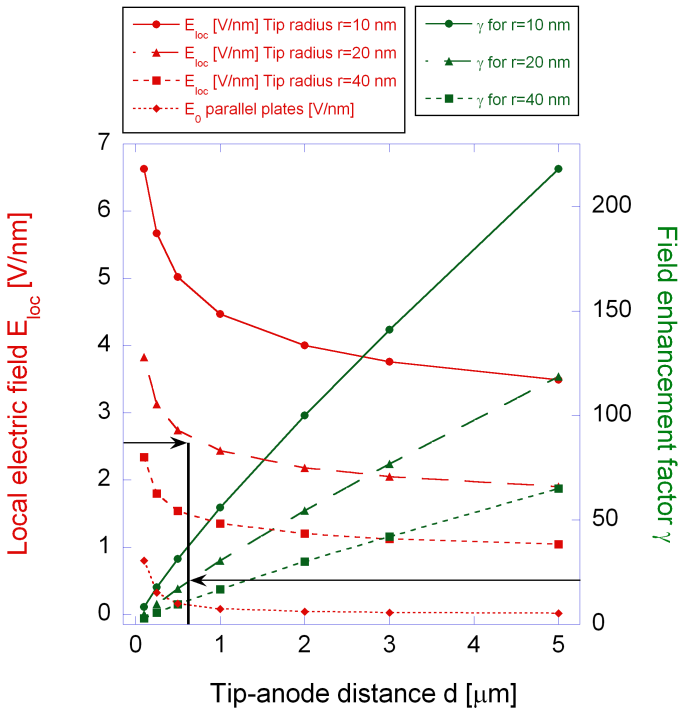

FIGURE 3.22 – *Dependence of the field enhancement factor γ of the tip anode separation distance d and tip radius r. $V = 80$ V.*

The graph in Fig. 3.22 and in Fig A.4 could also be useable when estimating the local electric field and field enhancement factor for similar systems.

But, a word of warning must be issued regarding the area in the beginning of the curve. As will be discussed in Chapter 4, after the onset of field emission, the local electric field E_{loc} seems to stay at a constant value even with an increase of the applied potential (the macroscopic field $E_{||}$ should continue to increase though). The emittance of electrons is not something taken into account in the model; in other words, the model will display erroneous values of E_{loc} after the onset. This means that E_{loc} and γ in Fig. 3.22 will be inaccurate to the left of the vertical black line, for a tip radius of $r = 20$ nm. For $r = 40$ and $r = 10$ nm, this will begin somewhat to the left and right on the E_{loc}-plots, respectively.

3.9 Summary and conclusion

We have combined different techniques in a novel way to extract important parameters for a new type of carbon-shaped cold-field emitter. Usually when the F-N equation is used to extract the local electric field E_{loc}, either the field enhancement factor γ or the work function ϕ is assumed [Nilsson et al., 2001a, Bonard et al., 2002b, de Jonge and Bonard, 2004, Bonard et al., 2002a]. But here, from the same experiment, we have obtained E_{loc}, γ, the tip-anode distance d, the field-emission current i_{e} and most importantly $\phi = 4.8 \pm 0.3$ eV, without assuming any of the parameters. The quantitative value of the local electric field was obtained by comparing the experimental phase shift with that from a model. For the experimental setup in this experiment, an onset value for field emission of $E_{\mathrm{loc}} = 2.55$ V/nm was found.

For future experiments, we will work with the I^{2}TEM, a state-of-the-art Hitachi 300 kV C-FEG TEM, specialized for *in situ* TEM work. It is equipped with multiple biprisms that removes Fresnel fringes and delivers higher accuracy in the electron holography measurements. Additional pumps provides higher vacuum around the sample area. We hope that this, together with improved and automated electron holography techniques that permits capturing continuous field emission $i_{\mathrm{e}}(V)$-curves simultaneously with the holograms, will allow us to determine the work function with a smaller error. For example, by removing the error on the slope of the F-N plot (see Fig. 3.11 and eq. (3.23)) we could reduce the error on the work function ϕ from 0.3 to 0.1 eV.

It would also be interesting to perform the same experiment and calculations for a standard W cold-field emitter, to see if those results would correspond with results from other techniques.

3.9.1 Carbon cone nanotip to be used in a C-FEG?

A high-brightness C-FEG equipped with a CCnT would be invaluable for e.g. electron holography, since the contrast of the holographic fringes strongly depends on the spatial coherence of the electrons. For dark-field electron holography this is especially true, due to the lower intensity of a diffracted beam.

The true (but sometimes very long term) purpose of research is to make some kind of contribution to society. For the work here, the natural question is if the CCnT could be used as an emitter inside a new generation of C-FEGs. Houdellier et al. have already patented and realized a proof of concept [Houdellier et al., 2012] of this, where they modified a HF2000 Hitachi C-FEG TEM to incorporate a CCnT as the emitter. Their results are quite remarkable. They showed that the gun had a six times higher reduced brightness (1.6×10^9 A m^{-2} sr^{-1} V^{-1}), half the energy spread (0.32 eV) and a superior

long-term stability (the current slope damping is less than 16% per hour), when compared with a standard HF2000 C-FEG TEM. In other words, the results are promising for a potential bright future for the CCnT.

Symbols and abbreviations in Chapter 4

CCnT	Carbon cone nanotip
V_{MIP}	Mean inner potential
V_{Q}	Potential field from the charge
φ_{Q}	Phase shift of electron
C_{E}	TEM acceleration voltage dependent parameter
$\mathbf{r} = (x, y, z)^T$	Vectorial components in three dimensions
$\mathbf{R} = (x, y)^T$	Vectorial components in two dimensions
$\mathbf{d}$	Shift in the horizontal plane between object and reference beam
$\mathbf{B}$	Magnetic field
S	Closed surface in eq. (4.3)
$\mathrm{d}\mathbf{A}$	Vector magnitude equal area of infinitesimal part of S
ρ	Charge density
$\mathbf{E}$	Electric field
ϵ_0	Permittivity in vacuum
Φ_{E}	Electric flux through a closed surface
Q_{tot}	Total number of charge
l	Line parameter in eq. (4.6)
$\mathbf{N}$	Outward normal in eq. (4.6)
E_0	Global electric field
E_{loc}	Local electric field around the apex of the CCnT

4 Charge measurements

Electron holography can be used not only to measure the electric field, but also to count elementary charges. Using a recent developed technique [Gatel et al., 2013] with which an accuracy of one elementary unit of charge has been achieved, we will in this chapter show an example where we measure the number of elementary charges on a carbon cone nanotip (CCnT).

We have used the holograms of the CCnT obtained during the *in situ* measurements in Chapter 3 to calculate the distribution and number of charges on the apex of the CCnT before and after the onset of field emission.

4.1 Introduction

Off-axis electron holography has been used for quite some time to measure charges on objects inside the TEM [Chen et al., 1989, Cherns and Jiao, 2001, Chung et al., 2011], but these measurements are indirect, i.e., they rely on modeling of the electrostatic potential. Beleggia et al. have recently directly measured the charges on a nanoscopic level by using Gauss's Law [Beleggia et al., 2011] and the work by Gatel et al. is a continuation of this work [Gatel et al., 2013].

4.2 Theory

The theory for this section was obtained from the work of Gatel et al. [Gatel et al., 2013]. The approach for counting the charges is by using Gauss's Law together with eq. (3.10), which we used in the previous chapter for calculating the phase shift φ.

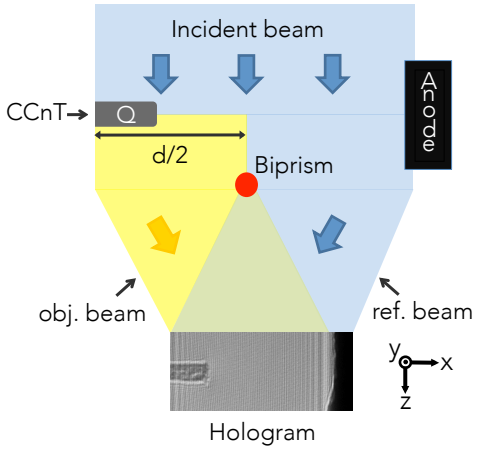

FIGURE 4.1 – *Sketch of setup for charge measurement on a CCnT with charge Q*

If we separate the potential field in two parts; the mean inner potential V_{MIP} and the potential field V_{Q} from the charge, eq. (3.10) can be modified to

$$\varphi_{\mathrm{Q}}(\mathbf{R}) = C_{\mathrm{E}} \int V \,\mathrm{d}z = C_{\mathrm{E}} \int (V_{\mathrm{MIP}} + V_{\mathrm{Q}}) \,\mathrm{d}z. \tag{4.1}$$

Putting to one side for the moment the potential from the MIP, and dividing up the potential field in an object and a reference part, we obtain

$$\varphi_{\mathrm{Q}}(\mathbf{R}) = C_{\mathrm{E}} \int V\left(\mathbf{r} + \frac{\mathbf{d}}{2}\right) - V\left(\mathbf{r} - \frac{\mathbf{d}}{2}\right) \mathrm{d}z \tag{4.2}$$

where $\mathbf{r} = (x, y, z)^T$, $\mathbf{R} = (x, y)^T$ are the vectorial components in three and two dimensions, respectively. $\mathbf{d}$ corresponds to a shift in the horizontal plane between the object and reference beam, as displayed in Fig. 4.1. As before, $C_{\mathrm{E}} = 9.25 \times 10^6$ rad V^{-1} m^{-1} depends on the TEM acceleration voltage and universal constants (as defined in eq. (3.11)).

Magnetic contributions to the charge count is not an issue, thanks to Gauss's Law for magnetism; $\nabla \cdot \mathbf{B} = 0$ ($\mathbf{B}$ being the magnetic field), in its differential form. The integral form of Gauss's Law states that the net flux of the magnetic field out of any closed surface is zero, which is expressed as

$$\oiint_S \mathbf{B} \cdot \mathrm{d}\mathbf{A} = 0, \tag{4.3}$$

S being a closed surface and $\mathrm{d}\mathbf{A}$ is a vector with a magnitude equal to the area of an infinitesimal part of S.

We assume that no charges exist in the reference beam in Fig. 4.1*, that is,

$$\iiint \rho\left(\mathbf{r}-\frac{\mathbf{d}}{2}\right)\mathrm{d}^3r = 0 \tag{4.4}$$

where ρ is the charge density. Then, together with Gauss's Law for electric fields ($\nabla\cdot\mathbf{E}=\rho/\epsilon_0$ or $\Phi_\mathrm{E}=Q_\mathrm{tot}/\epsilon_0$, Φ_E being the electric flux through a closed surface, ϵ_0 the permittivity in vacuum and Q_tot is the total number of charges) we can obtain the total charge inside a given region. This is done by integrating a two-dimensional Laplace operator $\nabla^{2\dagger}$ on the phase map $\varphi_\mathrm{Q}(\mathbf{R})$, as depicted below.

$$\begin{aligned}
\iint \nabla^2_\mathrm{R}\varphi_\mathrm{Q}(\mathbf{R})\,\mathrm{d}^2R &\overset{\text{Eq. 4.2}}{=} C_\mathrm{E}\iiint \nabla^2_\mathrm{R}\left(V_\mathrm{Q}\left(\mathbf{r}+\frac{\mathbf{d}}{2}\right)-V_\mathrm{Q}\left(\mathbf{r}-\frac{\mathbf{d}}{2}\right)\right)\mathrm{d}^3r \\
&\overset{\lim_{z\to\infty}E_\mathrm{z}(\mathbf{r})=0}{=} C_\mathrm{E}\iiint \nabla^2_\mathrm{r}\left(V_\mathrm{Q}\left(\mathbf{r}+\frac{\mathbf{d}}{2}\right)-V_\mathrm{Q}\left(\mathbf{r}-\frac{\mathbf{d}}{2}\right)\right)\mathrm{d}^3r \\
&\overset{\text{Gauss's Law \& eq. (4.4)}}{=} -\frac{C_\mathrm{E}}{\epsilon_0}\iiint \rho\left(\mathbf{r}+\frac{\mathbf{d}}{2}\right)\mathrm{d}^3r \\
&= -\frac{C_\mathrm{E}}{\epsilon_0}Q_\mathrm{tot}
\end{aligned} \tag{4.5}$$

where V_Q is the potential field from the charge. ∂^2V/∂^2z was added to the second line. Since the electric field goes towards zero at infinity, the integration of this is zero, according to $\int(\partial^2V/\partial^2z) = E_\mathrm{z}|_{-\infty}^{\infty}$. Then, a two dimensional contour integral was used to express the same integral as in eq. (4.5) in the following way;

$$\iint \nabla^2_\mathrm{R}\varphi_\mathrm{Q}(\mathbf{R})\,\mathrm{d}^2R = \oint_\mathrm{C}\nabla_\mathrm{R}\varphi_\mathrm{Q}(\mathbf{R}(l))\cdot\mathbf{N}(\mathbf{R}(l))\,\mathrm{d}l, \tag{4.6}$$

where l is a line parameter and $\mathbf{N}$ is the outward normal. And, by combining equations 4.5 and 4.6, we arrive at a closed line integral describing the amount of charge Q_tot inside the contour.

$$Q_\mathrm{tot} = -\frac{\epsilon_0}{C_\mathrm{E}}\oint_\mathrm{C}\nabla_\mathrm{R}\varphi_\mathrm{Q}(\mathbf{R}(l))\cdot\mathbf{N}(\mathbf{R}(l))\,\mathrm{d}l \tag{4.7}$$

Using this equation we are now free to choose the contour that is most suitable for the studied object. By choosing different contours for the same object, a mean value of the charge can be obtained, resulting in a greatly increased sensitivity. An additional benefit is that the equation describes the total charge within any given contour, without having to take care of any influence of exter-

*For a field emission current of 5 μA, there are1 only a couple of electrons at each instant between the tip and the anode

†The Laplacian describes the flux density of the gradient flow of a given function.

nal charges or of their positions. Figure 4.2 shows a charge Q inside the sample (the grey box). The dotted line show the path of the integration in eq. (4.7). To the far left a first integration contour contains zero charge. The second one integrates half the sample, which gives $Q_{\mathrm{tot}} = 1/2$ Q. For the third contour $Q_{\mathrm{tot}} = 1$ Q and for the fourth and so on $Q_{\mathrm{tot}} = 1$ Q.

Comparing with other methods, where a model of the electric field must be made, the influence of the electric field as a whole has to be taken into account.

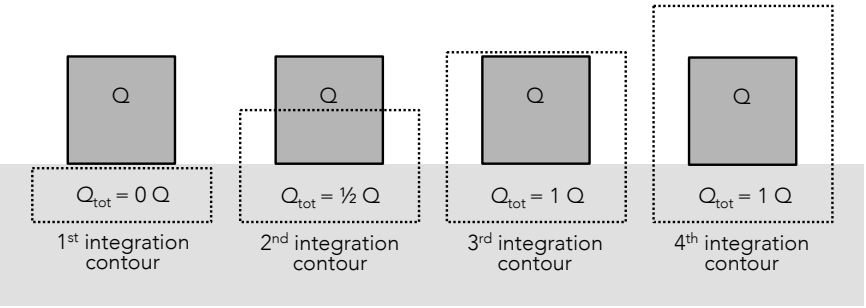

FIGURE 4.2 – *Simple model describing the technique. This is true if assuming uniform distribution of charge Q in the sample (grey box).*

According to eq. (4.8), the MIP will also affect the line integral. The phase shift φ_{MIP} coming from the MIP is expressed as

$$\varphi_{\mathrm{MIP}}(\mathbf{R}) = C_{\mathrm{E}} \int_0^{t(\mathbf{R})} V_{\mathrm{MIP}}(\mathbf{r})\,\mathrm{d}z \approx C_{\mathrm{E}} V_{\mathrm{MIP}} t(\mathbf{R}). \tag{4.8}$$

This means that the variation in thickness or V_{MIP} will contribute to the integral. One way to minimize these contributions is to choose contours which lie parallel to any gradient in V_{MIP} or $t(\mathbf{R})$, i.e., that $\nabla\varphi_{\mathrm{MIP}} \cdot \mathbf{N}(l) = 0$. This route was applied by Gatel et al. [Gatel et al., 2013]. Here, in fact, we subtract the phase φ_{MIP} coming from the mean inner potential, by using a reference hologram.

4.3 Counting electrons on a CCnT

4.3.1 Sample preparation

A CCnT was prepared and extracted using a FIB-SEM and then attached to the nanomanipulator (Fig. 2.1), as explained in detail in Section 3.3.

4.3.2 Results from the CCnT

We began by subtracting the φ_{MIP} from the phase maps with the aide of the hologram at 0 V from Fig. 3.8 (a). The integral was performed using DigitalMicrograph and in-house software developed by C. Gatel.

By applying eq. (4.7) onto the phase maps in Fig. 4.3 (a) – (c) the number of electrons inside the dotted red and white integration contour could be measured. The red indicate where $x = 0$ in (d). The integration path is indicated by the arrows around the contour. It is the same phase maps as in Fig. 3.8.* In Fig. 4.3 (a), a first integration has been done, in (b) a second and in (c) the n^{th} one ($n \approx 1800$) with a total length in $x \approx 320$ nm.† The results from Fig. 4.3 (a) – (c) can be seen in the 10 V curve in (d). The total number of electrons when 10 V had been applied to the anode were $154 \pm 4\mathrm{e}^-$. The dashed arrows (white in (a) – (c) and black in (d)) show the direction of the expanding integration contours.

After the n^{th} integration was performed on the 20 V hologram (like for the 10 V hologram in Fig. 4.3 (c)), a result of 302 ± 4 e^- was obtained. This can be seen in the 20 V curve in Fig. 4.3 (d). The same treatment was done for all holograms up to 95 V.

In Fig. 4.3 (d), the number of electrons initially increase with the applied voltage. But, once the field emission started at 80 V, the number of electrons began to saturate. At 80 and 95 V, values of 1193 ± 5 e^- and 1233 ± 5 e^-, respectively, were obtained.

To more easily illustrate this phenomena, Fig. 4.4 (a) shows the number of electrons in the part of the CCnT that is limited by the integration border in Fig. 4.3 (a) as a function of voltage. Here it can be seen clearly that at, or just after, the onset of field emission, a plateau is reached. Figure 4.4 (b) shows that the average value of the electron surface density in the last 5 nm of the CCnT is constant as well. Not only the number of charges, but also the phase shift appears to stay constant after the onset of field emission, as can be seen in Fig. 4.4 (c).

In Fig. 4.4 (d) it can be seen that the field emission current increases even after the onset of field emission, due to the increase of applied voltage. That is, the charge density is constant while simultaneously the current density increases exponentially.

*The internal reference area has been chosen inside the CCnT, which explains the different appearance of the phase maps in Figs. 3.8 and 4.3. This also explains the difference in phase shift seen in Fig. 4.3 (c) and e.g. Fig. 3.9 (a). The position of the internal reference area is unimportant for the charge measurements.

†Similarly as depicted in Fig. 4.2.

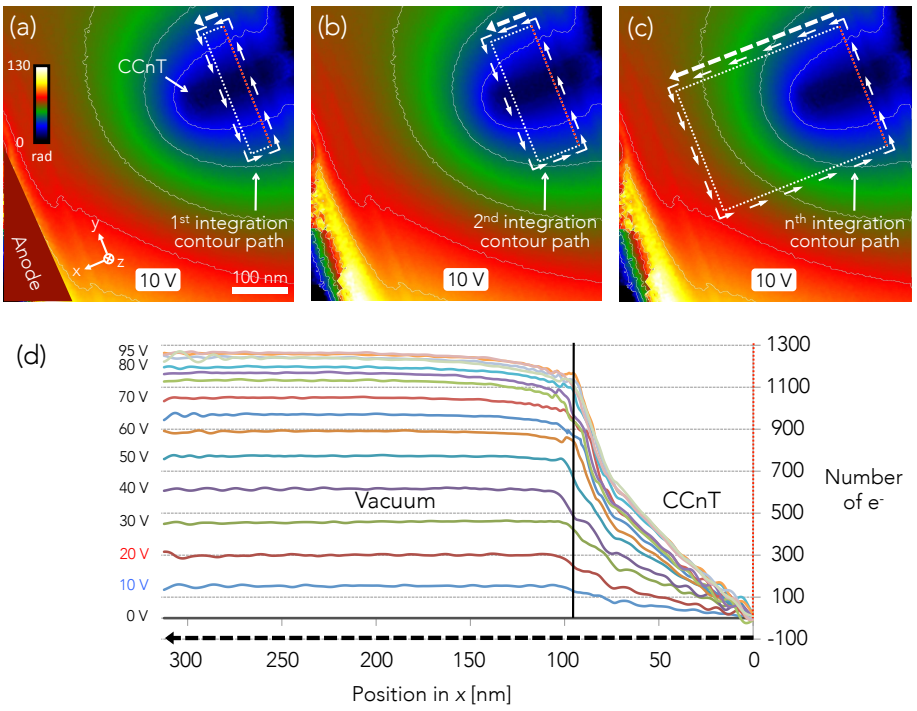

FIGURE 4.3 – *(a) – (c) Unwrapped phase map for 10 V on the anode. The dotted lines with arrows in (a) – (c) illustratively show the* 1^{st}*,* 2^{nd} *and* n^{th} *integration contour paths (i.e., the increase in the size of the paths is not to scale). (d) Counting of electrons as a function of position. The number of electrons inside the* n^{th} *integration path for 0 to 95 V. The black vertical line indicates the CCnT/vacuum interface.*

4.3.2.1 *The double-slope*

In Fig. 4.3 (d), the curves of the number of electrons inside the CCnT have two distinct parts. For the 95 V curve, from 0 to around 75 nm in x, the increase is 9 electrons per nm. In the steeper part, from 75 to 95 nm, the increase is 23 electrons per nm.

4.3.3 Comparing with FEM

To compare the experimental results above with the model used in Section 3.6, we modified it to show the surface charge density (using the `es.Dn` expression in COMSOL).* Comparing Fig. 4.5 (a) and (b) one can see that the number of electrons seem to match well. Here, the color range for the simulation has been adjusted to better fit the color range of the experimental results.

*With a tip-anode separation distance of 680 nm and a tip radius of 20 nm.

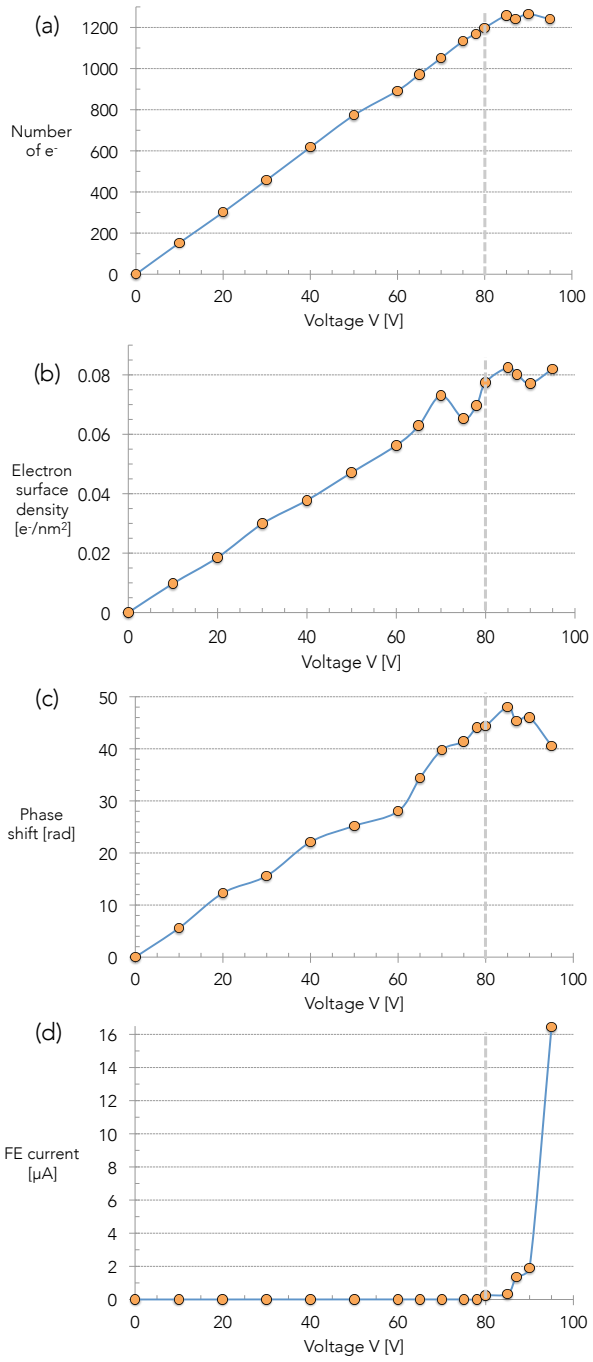

FIGURE 4.4 – *Plots of (a) the number of electrons, (b) the electron density in the front part of the CCnT, (c) the phase shift and (d) the field emission current as a function of the applied voltage. The grey dotted line marks the onset of field emission.*

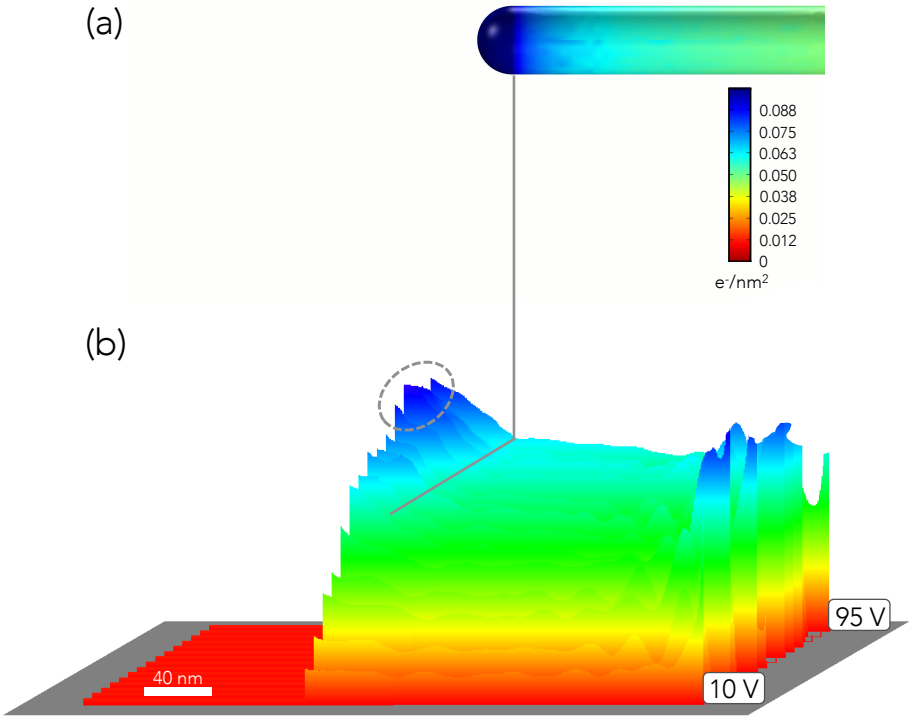

FIGURE 4.5 – *(a) Simulation of surface charge density at 80 V. (b) Profiles of the experimental surface charge density along the CCnT and in the vacuum, from 0 to 95 V. The grey dotted oval shows the region of field emission (i.e., 80 to 95 V).*

The area which is circled in Fig. 4.5 (b) indicate where field emission occurs, i.e., above 80 V.

4.4 Discussion

As was seen in Fig. 4.4 (a), the number of charges in the CCnT current saturated once field emission commenced. It is possible that any excess charge is immediately emitted once field emission process begins in earnest. There is no longer then the possibility of building up further charges on the tip. Carbon nanotubes are conductive [de Knoop et al., 2005], just like the CCnTs. When taking a CCnT into contact with the anode, a resistance of 800 Ω was measured. Therefore the electrons should be located on the surface of the CCnT, and, the field-penetration should be minimal.

The applied voltage on the anode and thus the global electric field E_0 is increased also after the onset of field emission. But since electrons are emitted,

locally, the electric field should be affected. Since the number of electrons remain constant in the CCnT after the onset of field emission (Fig. 4.4 (a)), then should also the local electrical field E_{loc} and thus the potential gradient around the apex of the CCnT stay constant. This in turn, should affect the phase shift measured from the phase maps in Fig. 3.8. The result of such a measurement, showed that this seemed to be the case, with the phase shift reaching a plateau, as shown in Fig. 4.4 (c).

As shown in Fig. 4.4 (d) there is an exponential increase in field emission current while simultaneously the charge density on the CCnT was constant. The only explanation we can think of is that the CCnT is charged and discharged at a higher rate, i.e., the drift velocity of the electrons in the CCnT is increased exponentially.* Or, perhaps what we are seeing is an artifact. Although, if it is an artifact then it is interesting that it is only observable just after the onset of field emission.

But, it is puzzling that the phase shift and thus the local electric field E_{loc} can be constant (Fig. 4.4 (c)) while the field emission current increases (d). With E_{loc} converging, also the width and height of the tunneling barrier should go towards a constant value (See Fig. 3.2). But then again, perhaps an increased drift velocity of the electrons can explain the exponential increase in field emission current. It should be noted that Hazra et al. found that for high electric fields the width of the tunneling barrier reaches an almost constant value [Hazra et al., 2011]. But, they concluded that this would limit the field emission current, which is not something that we have seen.

There exist another effect that limits both the field emission current and the local electric field in field emission at high electric field, which comes from the presence of space charge. As the field emission current increases, the electric field from the space charges in the vacuum screens the cathode from the global acceleration electric field E_0 [Schamber, 1999]. At a certain level, the cathode will be screened to such a level that the current and thus the local electric field E_{loc} will be saturated. An effect of this is that it is necessary to increase the applied voltage for in order to have the same electric field [Anderson, 1993]. Others have experimentally found that for current densities over 5×10^6 A/cm^2, space charge will come into effect [Dyke and Trolan, 1953, Barbour et al., 1953, Batrakov et al., 1999]. We do not know the virtual source size of the CCnT, and can therefore not calculate the current density. And furthermore, we have not seen this effect.

The reason for the steeper slope close to the apex of the tip in Fig. 4.3 (d) could come from that the electrons are being hindered by the barrier and con-

*As a reference, the drift velocity, that is, the speed with which electrons travel, in a Cu wire, is around 300 μm/s.

centrated at the apex, before being field-emitted. This is also the area where the data for the plot in Fig. 4.4 (b) has been chosen from.

4.5 Conclusion

We have applied a recently developed method for directly measuring charges on a CCnT. It was found that after a linear increase of charge with the anode bias, a plateau was reached at, or just after, the onset of field emission. The phase shift showed a similar behavior, indicating that the observed local electric field became saturated also. A complete explanation for this phenomena has not yet been found. Further studies are envisaged to better understand the results.

Part II

IN SITU TEM NANOINDENTATION

Symbols and abbreviations in Chapter 5

fcc	Face-centered cubic
CTE	Coefficient of thermal expansion
MEMS	Microelectromechanical system
FIB-SEM	Focused ion beam scanning electron microscope
$h_{\mathrm{f,o}}$	Film, oxide thickness
F_{b}	Force per unit length
$\mu_{\mathrm{f,s,o}}$	Shear modulus of film, substrate, oxide
$\mathbf{b}$	Burgers vector
b	Length of Burgers vector
d	Distance from dislocation to interface
$\mathbf{F}$	Externally applied force
A	Surface onto where $\mathbf{F}$ is applied; indentation surface
σ	Tensile or compressive stress
$\mathbf{n}$	Slip plane's normal
λ	Angle between $\mathbf{F}$ and $\mathbf{b}$
ϕ	Angle between $\mathbf{F}$ and $\mathbf{n}$
F_{s}	Shear force in the slip direction
A_{s}	Area of slip plane
τ	Shear stress
S	Schmid factor
α	Angle between sample surface and the indentation surface A
FEM	Finite element method
$\beta_{\mathrm{s,o}}$	Substrate, oxide constant in the Nix model
$\nu_{\mathrm{f,o,AlO}}$	Poisson's ratio of film, oxide, AlO
μ_{eff}	Effective shear modulus
σ_{Nix}	Tensile stress according to the Nix model
$E_{\mathrm{f,o,AlO}}$	Young's modulus of film, oxide, AlO
λ_{L}	Lamé's first constant
σ_{v}	Von Mises stress
si	Sample i , $\mathrm{i} = 1, 2, 3$
t_{si}	Thickness of sample i , $\mathrm{i} = 1, 2, 3$
r	Radius of dislocation
a	Unit cell length for Al
$r_{\mathrm{proj_{si}}}$	Projected radius of dislocation, sample si, $\mathrm{i} = 1, 2, 3$
$k_{\mu_{\mathrm{im}\perp 1,2}}$	Shear modulus term, image dislocation 1,2, sample s2
$F_{\mathrm{b}_{\mathrm{im}\perp 1,2}}$	Force per unit length, image dislocation 1,2, sample s2
MD	Molecular dynamics

5 | *In situ* plastic deformation of Al thin films

"The movement of a dislocation within a material is like the movement of a wave in the ocean. It is not the medium itself that advances, but an energy within it."

MATERIALS in the form of thin films have invaded our everyday life in the form of hard coatings (tools, ceramic products), optical filters (glasses, windshields) or protective layers (zinc or chromium covered steels). They are often technically advanced structures, that once stacked, can provide the desired properties for a given application [Freund and Suresh, 2003].

In microelectronics, thin metallic, oxide or semiconducting films are often patterned following their deposition to obtain complex devices with specific functions. During the fabrication that involves various deposition processes (physical/chemical, temperature, pressure), internal stress and strain develop in the artificial structure [Josell et al., 2002]. Their impact in microelectronic engineering can be negative (delamination, device failures [Ciappa, 2002]) or positive (faster carriers in strained Si [Welser et al., 1994]).

5.1 Introduction — Strength of thin metallic films

Here, we will focus on metal thin films. Those with face-centered cubic (fcc) structures such as Cu, Al or Au are often used in the form of interconnects in microelectronic devices. In most of these devices, electric power causes a global heating through Joule effect. With increased integration and downscaling, power concentrations and heat evacuation become an issue. Mechanically, heat cycles causes stresses that originate from the difference in coefficient of thermal expansion (CTE) between metals, oxides and semiconductor parts.

The metal is the softer part, with the highest CTE, and therefore is prone to plastically deform first. Usual macroscopic thermo-mechanical tests are run using a so-called wafer-curvature experiment; the stress induced in the expanding metal film by thermal cycles imposes a radius of curvature to the substrate. The relation between this radius and the biaxial stress in the film is given by the Stoney formula [Flinn et al., 1987, Flinn, 1991, Stoney, 1909, Janssen et al., 2009]. For most of the metallic films studied by this method, a strong size effect was found; the thinner the film, the higher the stress needed to plastically deform it. To measure this yield stress (the film's "strength"), one can refer to the deviation from elastic yielding in stress-temperature curves, but this returns two values; one for heating and one for cooling. Most of the authors therefore consider the stress at room temperature, even if this is not standardized. One can argue that it has nothing to do with a yield stress [Saada et al., 2007], however, a gradual decrease of thermal cycle amplitudes (from a maximum of 500°C typically down to 200°C) shows that this room temperature stress is maintained although the plastic deformation seen by the film is reduced to zero (Legros in [Ponchet et al., 2011]). A recent review about the strength of various films on substrates can be found in [Wiederhirn, 2007], where the stress at room temperature after a thermal cycle is normalized by the shear modulus of each metal. This shows a clear $1/h_\mathrm{f}$ increase, h_f being the film thickness (see Fig. 5.1) Free standing thin films, tested in tension or using bulge testing [Kalkman et al., 2001, Vlassak and Nix, 1992] also show a stress increase, but not as much as a film on a substrate, and the increase is more related to grain size that often scale down with film thickness. Recently, it has been found that free standing Mg films do not show a stress increase [Sharon et al., 2014].

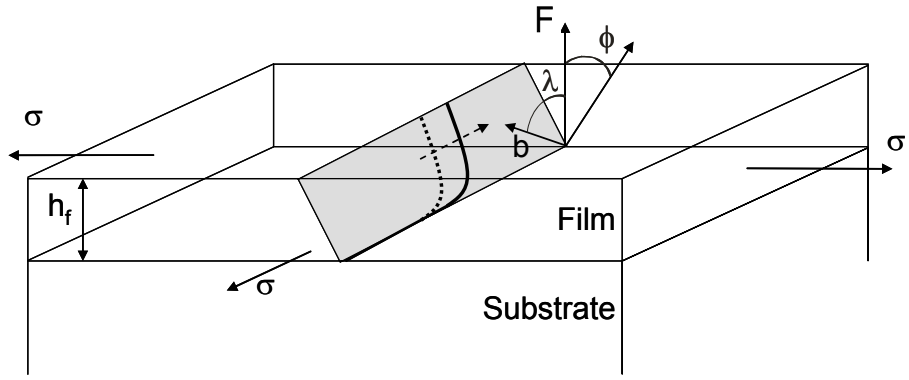

FIGURE 5.1 – *Sketch showing the Nix model. The threading dislocation deposits an interfacial dislocation at the film/substrate interface. Original image from Nix [Nix, 1989].*

The role of the substrate in film strength is thus of prime importance, and, following the analysis by Matthews and Blakeslee [Matthews and Blakeslee, 1974, Matthews and Blakeslee, 1975] for epitaxial semiconductors, this can be rationalized in term of threading dislocations, interfacial dislocations and image forces; the plastic deformation of thin film is due to the propagation of threading dislocations on (111) type planes. Doing so, each of them trail an interfacial dislocation that lies at the intersection of the glide plane and the interface.

5.1.1 The Nix model — Strength inversely related to film thickness

5.1.1.1 Definition of the image force

The Nix model states that the creation of misfit, or interfacial, dislocations at the interfaces being one of the reasons that thinner films are stronger films (also higher grain boundary density in thin films adds to this), a dislocation being in proximity to an interface feels a mirror or image force from the previously mentioned mirror dislocation [Nix, 1989]. Using an image dislocation is a mathematical method to calculate the energy of a dislocation at a certain distance from an interface. The force is attractive if the dislocation is in the material with the higher shear modulus and repulsive otherwise. For a thin film encapsulated between the substrate and an oxide passivation layer, the force per unit length acting on a screw dislocation* can be described as [Freund and Suresh, 2003] (see Fig. 5.13).†

$$F_{\mathrm{b}} = -\frac{\mu_{\mathrm{f}} b^2 k_\mu}{4\pi d}, \qquad k_\mu = \frac{\mu_{\mathrm{f}} - \mu_{\mathrm{s}}}{\mu_{\mathrm{f}} + \mu_{\mathrm{s}}} \tag{5.1}$$

where μ_{f} and μ_{s} is the shear modulus of the film and the substrate, respectively, b is the length of the Burgers vector and d is the distance from the dislocation to the interface. In most cases the substrate is stronger than the thin film material, resulting in that the image force hinders dislocation movement in the film. From the equation follows that a dislocation moving towards an interface should become stationary at a certain distance from it, when equilibrium between an externally applied force and the image force is reached [Öveçoğlu et al., 1987]. This is contrary to what we have observed at several occasions, where dislocations have continued to push towards and into the interfaces. And, during unloading, the dislocations does not move back, which means

*The relationship is less clear for an edge dislocation, but like for the screw dislocation, the direction of the force is towards the less stiff material. The difference in the image force between an edge and screw dislocation is around 20-30%.

†Note that there is a b missing in the formula on page 427 in Freund and Suresh [Freund and Suresh, 2003].

that the process is irreversible. In other words, interfacial dislocations are not stable also at room temperatures.

5.1.1.2 The slip system and the Schmid Factor

When applying a force **F** to a crystal, the plane that eventually slips is usually the plane with highest density. In a fcc crystal, these planes are of the $\{111\}$ type. The direction of the slip in the plane usually occurs along the $\langle 110 \rangle$ directions, which are the Burgers vectors. For a fcc crystal, there are two Burgers vectors. Each of them are shared between two slip planes, i.e., there are three vectors in each plane. Since there are four slip planes, a fcc crystal has twelve slip systems. In general, only a few slip systems are activated at the onset of plastic deformation. Which those are can be determined by the Schmid factor, as defined below.

If **F** is a force applied perpendicular to a surface A, as depicted in Fig. 5.2, then the tensile or compressive stress σ, parallel to **F**, is F/A. We define the angle between **F** and a slip plane's Burgers vector **b** to λ, and the angle between **F** and the slip plane's normal **n** to ϕ. Then the component of the force in the slip direction, the shear force, is $F_\mathrm{s} = \cos\lambda$ and the area of the slip plane $A_\mathrm{s} = A/\cos\phi$. Now, with eq. (5.2) below, the shear stress τ can be found:

$$\tau = F_\mathrm{s}/A_\mathrm{s} = \frac{F\cos\lambda}{A/\cos\phi} = \frac{F}{A}\cos\lambda\cos\phi = \sigma S \tag{5.2}$$

The term $S = \cos\lambda\cos\phi$ is called the Schmid factor, which has a value between 0 and 0.5. The slip system with the highest Schmid factor are generally activated first.

Further definitions in Fig. 5.2 are the sample surface and the indentation surface, perpendicular to one another, and the angle α, which is the angle between the sample surface and the Burgers vector **b**. Since **b** is in the slip plane, $\phi + \lambda \triangleq 90°$.

The Schmid factor describes how much of an externally applied force that is acting on a slip plane and a dislocation in it. The more parallel the slip plane is to the direction of the applied force (that is, $\lambda \to 0°, \phi \to 90°$) the more of the force is "pushing" on the dislocation. But, at the same time, the projected area on which the force is effectively acting on is small, i.e. S and the shear stress τ is small, which leads to that the probability of moving a dislocation is small. When $\lambda \to 90°$and thus $\phi \to 0°$, all of the external force is directly applied onto the slip plane, but since it is applied perpendicular to it, it will be difficult to move the dislocation in this particular system. When $\lambda = \phi = 45°$, then the maximum of the applied stress σ is transmitted to shear stress τ into the glide

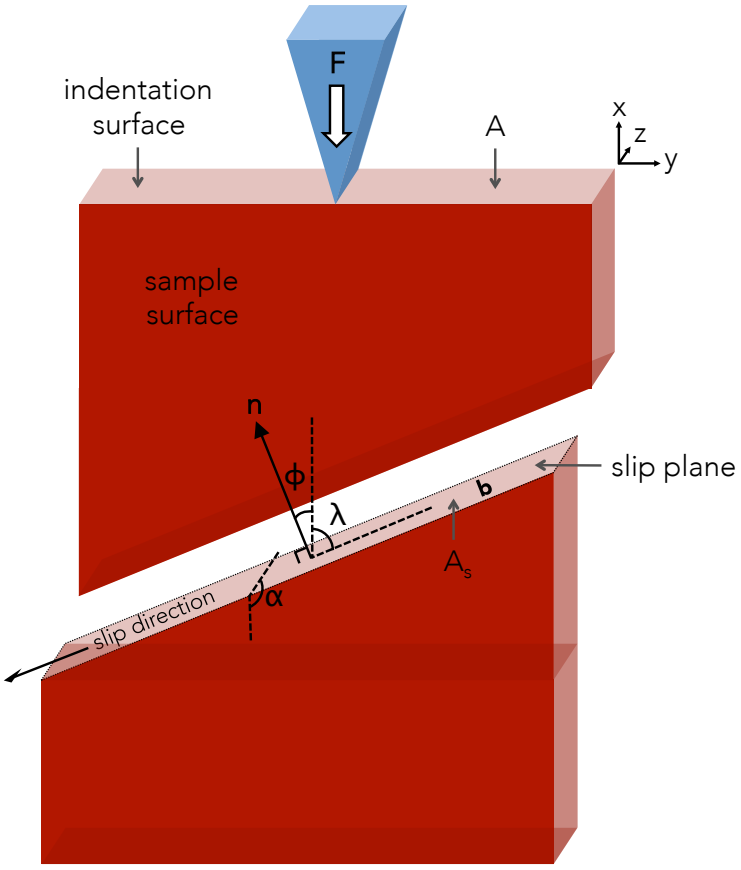

FIGURE 5.2 – *Model showing the effect on a crystal exhibiting slip when a force* **F** *is applied.* A_s *is the area of the slip plane and* A *is the area on which the force is applied on.* **n** *is the vector normal to the slip plane.*

plane. The Schmid factor $S = 0.5$, i.e., the slip system has the greatest chance to be activated.

Of course, this activation supposes that dislocations already exist with corresponding **b**. If the existing dislocation density is close to zero, the material needs to nucleate dislocations and this process is more dependent on stress concentration in the material (from cracks or impurities) than on the Schmid factor.

5.1.1.3 Derivation of the Nix model

The increase in length of the interfacial dislocation has an energy cost that must be overcome by the work of the applied stress responsible of the threading dislocation moving forward. In semiconductors, this process is supposed to occur during the deposition of epitaxial layers at high temperature. It has been

adapted to metals by Nix [Nix, 1989, Nix, 1998]. The energy of the trailed interfacial dislocation will be the classical function of μb^2 (μ being the shear modulus of the crystal it is in), plus a surface interaction term that will increase as it is closer to the surface (i.e. the film is thinner). Because it is in a thin film, this attraction to the surface is important. This attraction is usually calculated using image forces where a virtual dislocation of opposite sign is placed at an equal distance of the surface, in the vacuum. The resulting positive dipole interaction gives the stress felt by a dislocation near a surface [Hirth and Lothe, 1982]. In its more simplified form (substrate and film being the same material), the balance between the work of the threading dislocation under applied stress and the trailed interfacial dislocation energy is [Nix, 1989]:

$$\sigma_{\mathrm{Nix0}} = \frac{b\,\mu}{2\pi(1-\nu)h_{\mathrm{f}}} \ln\left(\frac{\beta_{\mathrm{s}} h_{\mathrm{f}}}{b}\right) \tag{5.3}$$

with b being the magnitude of the Burgers vector, μ the shear modulus, β_{s} a substrate constant and ν Poisson's ratio of the film. One can readily see that when h_{f} becomes small, σ_{Nix0} varies essentially like $1/h_{\mathrm{f}}$, with the $\ln$ term varying much slower.

The model can be refined by taking into account the various stiffness of the film and the substrate, i.e., adding image forces. This gives that μ is exchanged with the effective shear modulus μ_{eff}, which is described as

$$\mu_{\mathrm{eff}} = \frac{\mu_{\mathrm{f}}\mu_{\mathrm{s}}}{(\mu_{\mathrm{f}}+\mu_{\mathrm{s}})} \ln\left(\frac{\beta_{\mathrm{s}} h_{\mathrm{f}}}{b}\right) + \frac{\mu_{\mathrm{f}}\mu_{\mathrm{o}}}{(\mu_{\mathrm{f}}+\mu_{\mathrm{s}})} \ln\left(\frac{\beta_{\mathrm{o}} h_{\mathrm{o}}}{b}\right) \tag{5.4}$$

where the subscript f, s and o stands for film, substrate and oxide, and β_{s} and β_{o} are constants being 2.6 and 17.5, respectively [Nix, 1989].

By adding crystalline geometry of both the film and the substrate, i.e., adding the Schmid factor, eq. (5.3) can be expressed as

$$\sigma_{\mathrm{Nix}} = \frac{\sin\phi}{\cos\lambda\cos\phi} \frac{b\,\mu_{\mathrm{eff}}}{2\pi(1-\nu_{\mathrm{f}})h_{\mathrm{f}}} \tag{5.5}$$

Other models, that can be derived directly from eq. (5.5), are e.g. the source model, which predicts three times larger stresses [Von Blanckenhagen et al., 2001], or the Thompson model, which takes into account grain size strengthening [Thompson, 1990].

Despite its $1/h_{\mathrm{f}}$ dependency, and apparent simplicity, the adaptation of semiconductor model to metals failed to truly capture the mechanical properties of metals on substrates, except in the case of a crystalline/crystalline interface such as Al or Cu on Sapphire [Dehm et al., 2003, Heinz et al., 2010]. One reason could be the much easier generation and multiplication of dislocations

and defects in metals, but the character of the interface looks more critical.

In fact, according to the image force model developed above, sapphire substrate (being very stiff) should repeal dislocation further away and lead to a stronger size effect than in the case of a Si substrate.

TEM observations are thus essential to investigate dislocation/interfaces interactions. Interfacial dislocation have been linked to misfit strain between two semiconductor layers early on [Hull and Bean, 1989]. In metallic films on substrate, literature is more controversial. Propagation of threading dislocations is supposed to rule plastic deformation, but their observation in metals lead to different results [Korhonen et al., 1991]. In the case of oxidized substrates especially, where an amorphous layer separates the Si from the metal: In 1998, Müllner and Arzt [Müllner and Arzt, 1998] observed interface dislocations disappearing under prolonged exposure by the electron beam, which was the first evidence that interfacial dislocations might not be stable. They accounted this to be a result of irradiation-induced diffusion. The observation that dislocations were being absorbed by the interface was followed up by Legros et al. in 2002 [Legros et al., 2002] (also by Dehm et al. in 2000 [Dehm and Arzt, 2000]), where stress was induced through thermal cycling, stemming from the difference in thermal expansion coefficients (CTE). This experiment was not supposed to be an *in situ* one, but revealed the potential of the technique: *In situ* TEM presents the very unique capability to observe this interaction in a dynamic way.

To do so, the geometry of the specimen has to be adapted to keep the interface either in plane view or in cross-section [Legros et al., 2009]. Heating experiments on metal/Si substrates TEM specimen proved to be able to reproduce partly the stress levels experienced by metals in wafer curvature experiments [Keller et al., 2011, Keller et al., 1999] As predicted by continuum elasticity, it has been shown that threading dislocations are repulsed from a stiff crystalline interface (e.g. sapphire [Inkson et al., 2002]). Inversely, dislocations seem attracted by amorphous interfaces that act as a sink for small deformations in the metal [Legros et al., 2001]. This sink effect also prevent stress concentration and further dislocation multiplication, which may explain why metals on oxide systems appear stronger during thermal cycles [Dehm et al., 2003] [Heinz et al., 2010].

In fact, *in situ* TEM revealed an even more surprising behavior. Observing very thin polycrystalline Cu films strained in plane view using the difference of CTE between the metal and the Si substrate, Balk and co-workers observed the initiation of so-called "parallel dislocations" [Balk et al., 2003]. These dislocations are not activated by the applied stress (the Schmid factor for any dislocation gliding on the interface plane is nil), but seems to be the result of grain

boundary diffusion, as predicted by a recent model for polycrystalline thin film relaxations [Gao et al., 1999]. By just counting the dislocations emitted and absorbed (the process is almost perfectly reversible) at the grain boundary – interface junction, one can quantify this unusual relaxation mechanism. This pure *in situ* TEM discovery appears as the perfect complement of classical threading dislocation models for metals on oxidized substrates. In these cases, the dislocations where activated by thermal processes, e.g. grain boundary fast diffusion.

Here, we would like to see if these positive interaction between regular threading dislocations and metal/oxide interface persists at room temperature, using a different solicitation.

5.2 Mechanical straining holders — *In situ* TEM nanoindentation holders

After the first observation of moving dislocation in a TEM [Hirsch, 1986,Hirsch, 1999, Hirsch et al., 1956], many research laboratories designed and manufactured their own straining holders, often for high voltage microscopes essentially in Europe and Japan [Swann et al., 1974, Imura and Hashimoto, 1977, Messerschmidt et al., 1989, Louchet and Saka, 1993, Saka and Caillard, 2001]. Recent reviews of these early developments can be found in [Louchet and Saka, 2003] and [Mompiou et al., 2013]. These studies include low and high temperatures experiments made possible with such straining holders [Takeuchi et al., 1973, Takeuchi, 1973]. With the decline of high voltage microscopes and the extension of 200–300 kV side entry machines, standardized straining stages, became available commercially. Most of them are based on an electric motor pulling a movable arm on witch one hand of the electron transparent sample is attached while the other hand is maintained fixed. Straining speeds ranging from 10 nm/s to 10 μm/s, typically, are accessible although a given system rarely allows more than 2 decades in speed. These very versatile systems are used to stretch many types of samples, some being rather bulky with only an electron transparent zone in their middle, and do not contain force sensors, which implies that other ways to measure stress and strain have to be found [Couret et al., 1993].

Nanoindentation, or instrumented indentation is a technique that appeared in the early 1980's and consists in measuring the force and displacement of a hard tip (often diamond) forced into a bulk material, previously polished flat. This technique allows retrieving the hardness but also the elastic modulus of the tested material [Tsui et al., 2011]. The force and displacement are usually

measured through a change in capacitance between a reference and an movable electrostatic plate attached to the tip [Oliver and Pethica, 1989, Pethicai et al., 1983, Loubet et al., 1984]. Transferring this technique to *in situ* TEM represented a real challenge, technically (for miniaturizing sensors and actuators) and conceptually (because a thin sample has to replace a flat bulk sample). In the 1990's, various holders were developed taking advantage of the very accurate positioning capabilities of piezoelectric stacks and tubes to bend, pull or compress samples as small as carbon nanotubes [Ohnishi et al., 1998, Kizuka, 1998b, Kizuka et al., 1997, Poncharal, 1999, Wang et al., 2000, Wall and Dahmen, 1998]. Rapidly, nanoindentation tips were attached on top of these piezo-actuated holders to locally deform metals [Stach et al., 2001, Jin et al., 2004, Lockwood and Inkson, 2008]. The results obtained in term of plasticity mechanisms had a strong impact but were also criticized [Shan et al., 2004, Chen, 2005]. From 2003 to 2005, two companies further implemented these indenting holders by adjoining them a micro load cell. Hysitron, Inc.* constructed a TEM nanoindenter with a loading mode based on the capacitance variation inspired from the one found in large scale nanoindenters [Warren et al., 2007, Minor et al., 2006]. This piece of equipment was first available for JEOL microscopes before being adapted to other TEMs. Nanofactory Instruments AB chose to take advantage of the compactness of microelectromechanical systems (MEMS) [Svensson et al., 2003, Nafari et al., 2005] to propose nanomechanical testing units that could fit more TEMs and different force ranges. AFM holders were also proposed. In England, Inkson and coworkers also developed a custom piezo-actuated nanoindentation holder, but in that case, the load was not read electronically, and one had to measure the displacement of a calibrated spring platform [Bobji et al., 2006].

Beside their load sensors, Nanofactory and Hysitron holders differ in several ways: The Hysitron construction resembles a classical indenter set up where a hard tip is pressed against a sample that is fixed. Coarse positioning is insured by mechanical micrometers located on the back of the holder. Fine positioning is provided by a piezo tube in the three dimensions. In the Nanofactory holder† the tip is fixed on the top of the force sensor that is semi-mobile (Section 2.2.2.3). The coarse and fine motion of the sample towards the tip are both carried out by the nanomanipulator, as explained in Section 2.2.2.1. In this system, a single piezo tube is therefore able to do coarse and fine positioning, making it much more compact. Maximum loads accessible with such instruments are 5 mN, while the floor noise sets around 1 μN. Smaller load

*www.hysitron.com

†See *The Nanofactory User Group* at www.nanofactory-user-group.org.

cells were accessible at Nanofactory* before the company ceased activity and was bought by FEI Company† in the beginning of 2013.

In order to be indented, the TEM sample has to offer an area exposed to the diamond tip. At the same time, this location has to be transparent to electrons. The first sample investigated using this method was an Al layer deposited on a Si wedge [Minor et al., 2001], but more standard samples are nowadays shaped as wedges or H-bars (as seen in Fig. 5.3).

An early difficulty with nanoindentation holders was to set both the tip and the sample at the same height in the eucentric location of the TEM. The required precision, in the case of the pyramidal (or conical tip) is of the order of 10 nm. The introduction of wedge or punch shaped indenters with a length along z of about 1 to 3 μm, greatly facilitated the contact and prevents slipping while indentation is performed. The contact of the tip with the sample creates a very strong gradient of deformation, which also prevents maintaining good imaging conditions during the deformation. This can be partly overcome by capturing dynamic sequences in dark field [Kiener and Minor, 2011a], or by correcting the bending as the tests goes on (see Section 6.1.1.2).

The second intrinsic drawback of such mechanical test is that it is neither a compression test nor a real indentation test where known approximations can be applied [Oliver and Pharr, 1992] since both the tip and the sample geometries are complex and none of them is a flat surface. It is therefore almost necessary to perform finite element method (FEM) modeling to quantitatively determine the stress transmitted to the sample (Fig. 5.12). Flat punched tips can also serve to compress nanoparticles, but there too, modeling of the deformed sample is needed to really obtain quantitative data [Lahouij et al., 2011, Calvié et al., 2012, Deneen et al., 2006].

Working with samples that have a constant section allows to better take advantage of the load measurement capabilities of these nanoindentation holders. A main target of such holders seems to be the deformation of nanopillars [Kiener and Minor, 2011a,Shan et al., 2007] , which is an *in situ* TEM replication of micropillars compression testing that appeared in the classic experiment of 2004 by Uchic and co-workers [Uchic et al., 2004]. Because of the intriguing size effect observed on the strength, these pillar experiments opened an entire micromechanical testing domain [Greer and Nix, 2006, Volkert and Minor, 2007, Uchic et al., 2009a, Uchic et al., 2009b]. For these micro-compression tests, the diamond sharp indenter is replaced by a flat punch.

The FIB preparation also introduces many damages on the surfaces which is a constant concern when investigating very small objects (<50 nm). These

*Previously a partner of ESTEEM 2 (`www.esteem2.eu`).
†See `www.fei.com`.

implantation damages can strongly influence the mechanical response of the pillars [Bei et al., 2007], and other preparation routes are often preferred [Jennings et al., 2010, Mompiou et al., 2012, Phani et al., 2011].

The use of nanoindentation holders in tension was first proved possible by using negative-shaped grippers, directly carved in the diamond tip [Kiener and Minor, 2011b, Kiener et al., 2008]. This technique is however extremely time consuming and requires long milling times or specific lithography techniques [Jennings and Greer, 2011]. A more general way of transforming a compression force into tension is to use MEMS devices able to invert the direction of the load such as Θ (Theta) shaped MEMS [Lu et al., 2009, Lu et al., 2011] or "Push to Pull" devices.

5.3 Materials and methods

5.3.1 Cross-sectional sample configuration

The bulk sample was created by sputtering an Al thin film onto a (100) oxidized Si wafer. The 20 nm thick amorphous oxidation layer acted as a diffusion barrier, which is a common component for microelectronic applications to prevent the metal and semiconductor from reacting to one another [Ohring, 2002]. Following the 1.2 μm Al thin film, a $1\,\mu$m passivation layer of SiO_2 was deposited using low-pressure chemical vapor deposition at 300°C [Legros et al., 2002]. The passivation layer is the part that later will be in contact with the indenter diamond tip, thus having a cushioning effect on the applied force and therefore more evenly distributing the force in the Al layer. See Fig. 5.12 for a TEM micrograph showing the different layers and the diamond indenter tip. We chose this configuration because former compression or indentation experiments showed that imaging conditions are heavily distorted around the tip [Kiener and Minor, 2011a]. In particular, these distortions cause bend contours to appear and move around the indenter, which prevent continuous dislocation observations. See Fig. 5.6 for a micrograph showing the different layers and the diamond indenter tip.

5.3.2 H-bar sample preparation

If you push on a sheet of paper with your finger, it will most likely bend. This is what happens when you apply a force on a thin and large sample, i.e., a typically ideal TEM sample. Not only will this change the contrast (since bend contours will appear) and the focus (since the sample moves out of the plane), it will also result in the force-reading from the load cell on which the indenter

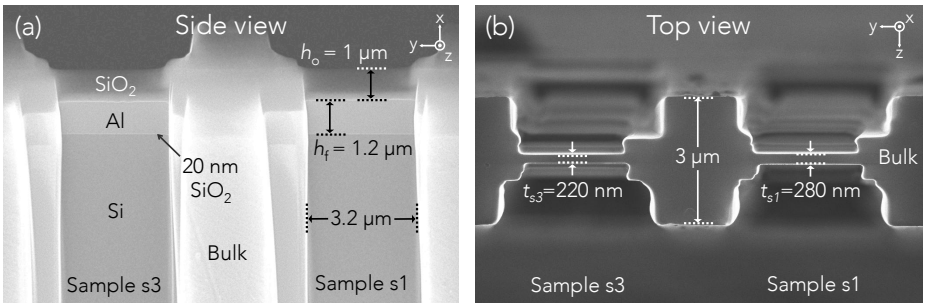

FIGURE 5.3 – *Samples* s3 *and* s1 *sculptured into an H-bar configuration using FIB-SEM, with (a) being side-view and (b) viewed from the direction of the applied force (with the H-shapes clearly visible).*

diamond tip sits on to be inaccurate (this is explained in Section A.1.1). Therefore, the sample should be made in a such a way so that bending is minimized when applying a force. In this chapter, we have used a combined focused ion beam scanning electron microscope (FIB-SEM) to cut out electron-transparent H-bar shaped windows of an originally 3 μm thick sample (See Fig. 5.3). The original sample was thinned down using tripod (as explained in Section 2.1.1). As can be seen, the windows are sided by thicker supports that prevent bending during indentation. The width of the windows were around 3 μm.

We started by milling the sample from 3 to 1 μm using an ion beam current of 700 pA and acceleration voltage of 30 kV. In order to minimize the damage to the sample and the implantation of Ga^+ ions, 70 pA was used for the final polishing.* Some of the removed material is redeposited. To compensate for this and to get as parallel surfaces as possible, the sample was tilted one degree from being parallel to the axis of the ion beam. Parallel surfaces are to prefer when comparing experimental data with a model.†

5.3.3 Finite element method; optimizing sample preparation and simulating stress fields for quantitative data

When making the H-bar windows, we had to find their optimum width. If they were too wide the sample would bend when a force was applied (as can be seen in Fig. A.2), and if they were too narrow, side effects from the bulk part of the sample would affect the results. To do this we used finite element method (FEM) modeling. By observing the created stress-field maps, we found for the force used, a width where only a negligible amount of stress reached the thicker structures. Further on, the stress-fields from the models were used

*Marks of the two differently intense beams can be seen in the step-like shapes in Fig. 5.3 (b).
†Parallel surfaces are also necessary for dark-field electron holography (see Section 6.1.1).

to quantitatively obtain values of the stress in the sample coming from the externally applied load. As before in this thesis, COMSOL Multiphysics 4.3 was used. The module handling stress and strain is the Structural Mechanics Module.

5.3.3.1 How the model was created

Having a two- or four-fold symmetric sample and applied force we could minimize the processor time by making a smaller model. The process time for a quarter of the sample was usually in the 10 minutes range, for a mesh count of around $100\,000$. The cases when we used a two-fold symmetry was when the force was not applied exactly in the middle. For example, in Fig. 5.5 we have used four-fold symmetry, which can be seen by the outlines of the different blocks to the right in (a) and (b). Then the result was mirrored along the x axis which created the images here. In other words, these images show half the sample, cut in half along the y axis (compare with Fig. 5.3).

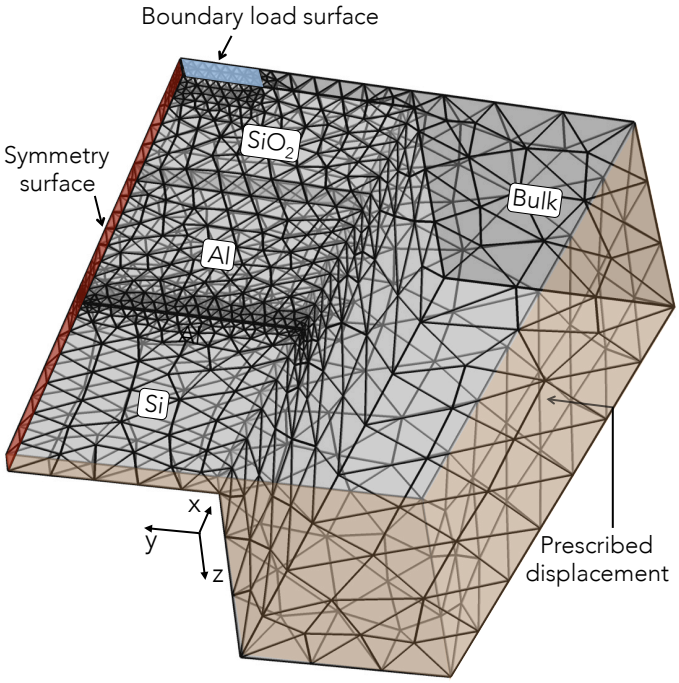

FIGURE 5.4 – *Mesh of a model of sample* s1*, with the various boundary conditions pointed out. The mesh has been de-densified to clearer show the different parts. The 3 nm AlO layer covering the Al film is not shown here.*

Single-crystal Si was used for the wafer material. Since it is anisotropic, a coordinate system for the $[110]$ direction was created and used together with

the default elasticity matrix. For Al, the default values below were used:

- Young's modulus $E_{\mathrm{f}} = 70$ GPa
- Poisson's ratio $\nu_{\mathrm{f}} = 0.33$
- Shear modulus $\mu_{\mathrm{f}} = 26$ GPa
- Lamé's first constant $\lambda_{\mathrm{L}} = 51$ GPa

For SiO_2, similarly the default values were utilized:

- Young's modulus $E_{\mathrm{o}} = 70$ GPa
- Poisson's ratio $\nu_{\mathrm{o}} = 0.17$

Isotropic `Linear Elastic Material Models` were chosen for the the Al and SiO_2 layers. Usually, Al deforms differentially for different directions, but as the SiO_2 passivation layer distributed the stress evenly on the Al thin film, the plastic deformation in the Al was negligible. This was also confirmed in Fig. 5.12, where only a small deformation can be observed in the Al layer. For Si, the anisotropic `Linear Elastic Material Model` was used.

Aluminum that has been exposed to air will be covered with an around 2 – 4 nm thick layer of Al_2O_3 [Wikipedia, 2013a]. Therefore a 3 nm thick Al_2O_3 layer was added on top of the Al film. The default values were:

- Young's modulus $E_{\mathrm{AlO}} = 400$ GPa
- Poisson's ratio $\nu_{\mathrm{AlO}} = 0.22$

Further on, to minimize processor time, only part of the bulk was modeled, as can be seen in Fig. 5.4. In order for this to not affect the results, the side of the bulk in the extreme $-y$ direction* a `Prescribed Displacement` for the boundary condition in y was used (orange surface). Similarly was done for the sides of the Si in the $-x$ direction. For the sample in Fig. 5.4, $1/4$ of the sample was modeled. The boundary condition `Symmetry` was used to sides where symmetry prevailed, illustrated by red (the entire side facing into the paper ($-z$ direction) had the symmetry boundary condition as well). For the applied load, $1/4$ of the force reading from the force sensor was incorporated as `Boundary Load`, illustrated as the blue surface. Apart from describing where the force was applied, it also shows the size of the contact area between the diamond tip and the sample. For all the remaining surfaces, which are the ones that were exposed to air, the boundary condition `Free` was selected.

*Remember that the sample later will be mirrored along the x axis.

5.3.3.2 *Which expression to use: von Mises or stress tensor in x?*

For the study of the optimum width we used the von Mises stress expression (in COMSOL called `smsld.mises`) since it shows the stress in all directions, albeit an average.* For comparing with our experimental data we used either the stress tensor in the direction of the applied force, being the x direction (`smsld.ex`), or the von Mises expression. If the dislocation was moving at an area centered more or less directly under the applied force, the stress tensor in the x direction was used. If it was threading closer to the bulk part of the sample, i.e., far from the center of the window, von Mises was used. See Fig. 5.5 for a comparison between the stress field from von Mises and the stress tensor in the x direction, where a force of $88\ \mu$N has been applied.

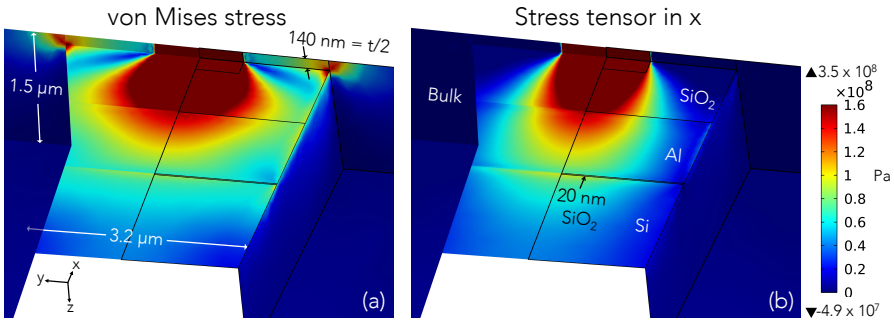

FIGURE 5.5 – *Simulation of sample* s1*, showing the difference in force distribution when using von Mises stress or stress tensor in the x direction. The color bar has been adjusted to show the stress inside the Al film. The simulation is without the 3 nm AlO layer.*

5.3.3.3 *Convergence simulations to verify model*

In Section 3.6, numerous convergence simulations were made in order to ensure that the miniaturization of the model would not affect the results. Here, this was less important since the real sample was largely smaller, comprising of the around 3 μm wide windows. A couple of uncertainties existed though, which we had a closer look at.

To begin with, apart from optimizing the width of the windows using FEM, we also included larger parts of the bulk and of the Si that is a part of the window, without seeing any difference on the results. Also, the true contact area is always uncertain in the TEM, having a projected image. But due to the SiO_2 layer, which distributed the force more evenly on the Al thin film, this

*Defined as: $\sigma_v^2 = \frac{1}{2}\left[(\sigma_{11}-\sigma_{22})^2+(\sigma_{22}-\sigma_{33})^2+(\sigma_{11}-\sigma_{33})^2+6(\sigma_{23}^2+\sigma_{31}^2+\sigma_{12}^2)\right]$ [Wikipedia, 2013b].

was less important. This was confirmed by simulations. For example, for the sample in Fig. 5.5 we found a difference in stress of 3.3% at a certain position when having a contact area of 0.5 and 1 μm.

5.3.3.4 The presence of an AlO layer and FIB-induced dislocations

The presence of the AlO layer clearly affects the stress at the surface, but in the center of the sample its presence played a minor role (a difference of 4 – 8% of the stress was found in the center of the sample when omitting the AlO layer in the model). This is also the area that we were interested in. From having used a FIB, a large amount of FIB-induced dislocation were created (see Kiener at al. where they discuss these effects [Kiener et al., 2007]) at the surfaces. By changing the focus in the TEM, these could easily be observed, aligned more or less in the same direction (see Grain 2 in Fig. 5.10). Therefore, we focused the TEM to not display these dislocations, but those more located in the center of the specimen.

5.4 Correlating experimental results with model (sample s1)

5.4.1 *In situ* TEM nanoindentation of sample s1

The first studied H-bar shaped sample (s1) had a thickness of 280 nm and a window width of 3.2 μm.* It is the sample displayed to the right of the SEM image in Fig. 5.3 and the one being simulated in Figs. 5.4 and 5.5. The sample, situated on the nanomanipulator, as shown in Fig. 2.2, was pushed into the diamond-tip equipped MEMS sensor. It was pressed further into the diamond tip, until the stress that reached the Al thin film was large enough to induce movement of the dislocations. The resolved shear stress τ on a dislocation was found using radius of curvature calculations. Correlation with the stress from the externally applied force using FEM verified the model.

Figure 5.6 shows a dark-field micrograph of the diamond tip and sample before the indentation. As seen, the diamond tip was quite large. Part of this was soft dirt. As mentioned in Section 5.3.3 the tip radius was less important since the stress was distributed evenly to the Al thin film by the SiO_2 layer. We estimated the diamond contact size to be around 500 nm in y and 280 nm in z (since the diamond tip is larger than the sample in z, the contact size in this direction is the thickness t_{s1} of the sample (see Fig. 5.3 (b))).

*This experiment was done in a JEOL2010 FEG at INSA Lyon operated at 200 kV, equipped with a Nanofactory TEM-NanoIndenter holder. An installed correlation option in the Nanofactory software enabled imprinting force and time stamps on each video frame. We are very grateful for their help.

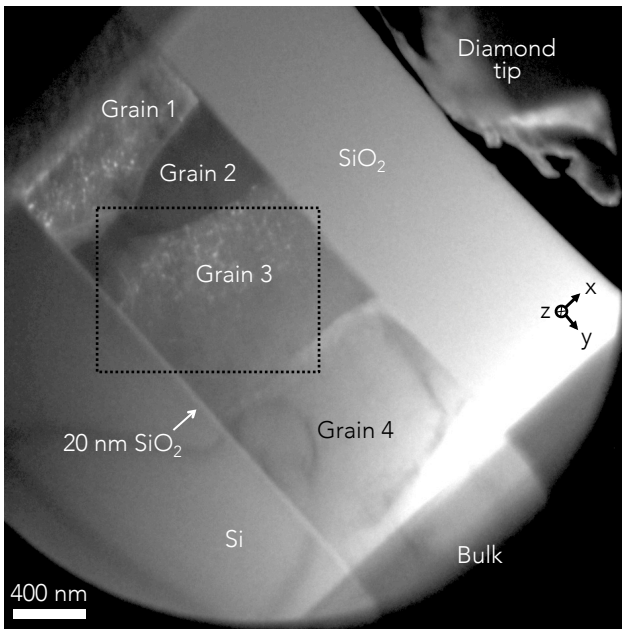

FIGURE 5.6 – *Dark-field micrograph of diamond tip and sample* s1 *before indentation. The area inside the black dotted box corresponds to the position of the sample in Fig. 5.7 (h).*

5.4.2 Stress from radius of curvature of sample s1

The resolved shear stress of a dislocation can be estimated using the following equation [Mompiou et al., 2012, Hirth and Lothe, 1982],

$$\tau = \frac{\mu_{\mathrm{f}} b}{r} \tag{5.6}$$

where $\mu_{\mathrm{f}} = 26$ GPa is the shear modulus of Al [Nix, 1989], b is the length of the Burgers vector and r is the radius of the dislocation before it starts to move. As mentioned before, the Burgers vector for Al is

$$\mathbf{b} = \frac{a}{2}\langle 110 \rangle \quad \Rightarrow b = 2.86\,\text{Å}, \tag{5.7}$$

where a is the unit cell length for Al.

To find the radius r in eq. (5.6) we started by looking at the projected radius of the dislocation. In the TEM micrograph in Fig. 5.7 (d) it was estimated to $r_{\mathrm{proj}} = 110 \pm 15$ nm. The dislocation is assumed to be pinned temporarily at the two surfaces of the sample, which should be plausible considering the thinness of the sample. By knowing the thickness $t_{\mathrm{s1}} = 280 \pm 10$ nm of the sample, we

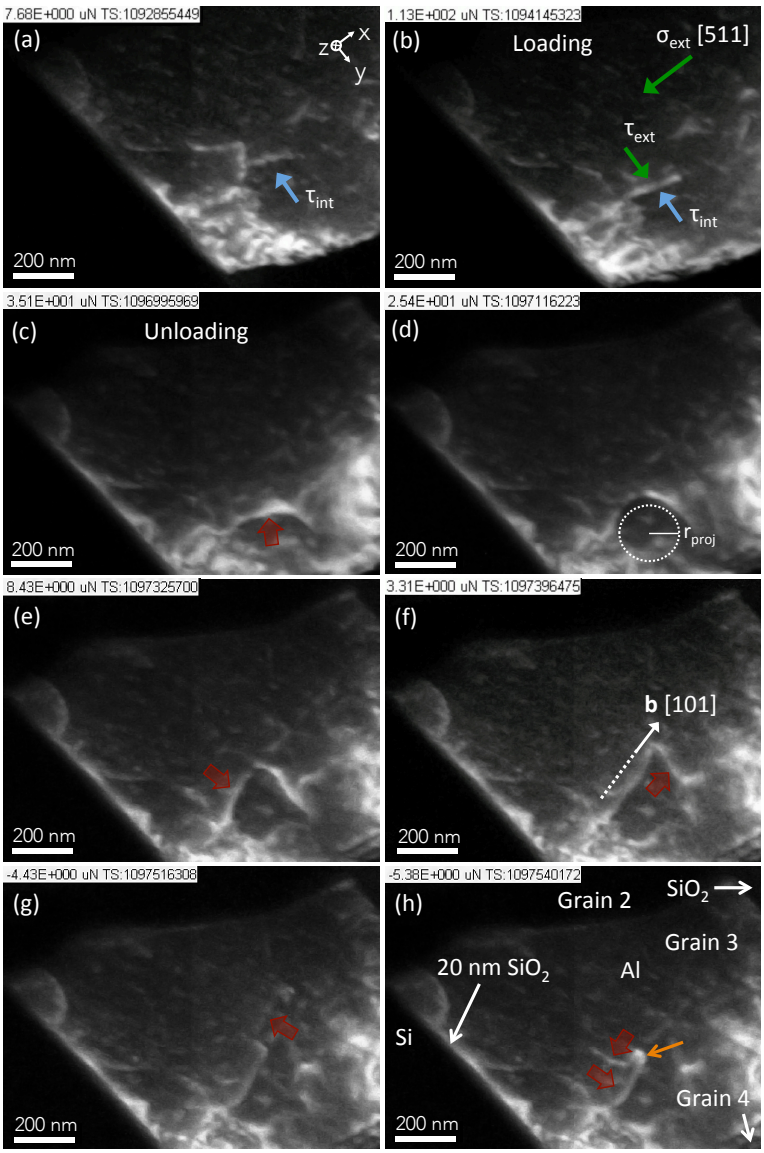

FIGURE 5.7 – *Snap-shots from movie obtained in dark-field mode during indentation of sample* s1 *(see dotted box in Fig. 5.6). The red arrows indicate which direction the dislocation is about to take, in (a) being the initial direction, (c) for the change in direction during the cross-slip event and (d) – (f) the circular motion about the pinning point that is indicated by an orange arrow in (f). Compare (f) and Fig. 5.6 for sample and grain orientation. The imprint of the force can be seen in the top left corner of each frame, together with a timestamp.*

can with simple geometry estimate the true radius r of the dislocation.

$$2r = \sqrt{t_{\mathrm{s1}}^2 + (2r_{\mathrm{proj}})^2} = 360 \pm 30 \text{ nm} \quad \Rightarrow r = 180 \pm 15 \text{ nm} \tag{5.8}$$

Combining equations 5.6, 5.7 and 5.8, and with the shear modulus for Al being $\mu_{\mathrm{f}} = 26$ GPa, the resolved shear stress on the dislocation is

$$\tau_{\mathrm{rad_{s1}}} = \frac{\mu_{\mathrm{f}} b}{r} = 41 \pm 4 \text{ MPa}. \tag{5.9}$$

In eq. (5.2) we defined the compressive strain as

$$\sigma = \frac{\tau}{S} \tag{5.10}$$

and from eq. (5.2) we have that $S = \cos\lambda \cos\phi$. In other words, to obtain the compressive strain in the area around the dislocation the angles λ and ϕ should be found. To begin with, a stereographic projection map was used. Such a map is used to e.g. measure angles between different directions. The intersection between the sphere and the vectors are illustrated as points in the projection map (see Fig. 5.8). The distance between each white line in Fig. 5.8 corresponds to 10°. The map was obtained using a commercially available software (`Wulfnet`) from DIGISTAR. Data was collected on a Philips CM20 FEG TEM. The DIGISTAR TEM add-on uses micro-diffraction to obtain diffraction patterns and by comparing these with predefined patterns, the true orientation can be found. The grain that we studied (Grain 3 in Fig. 5.6) had an orientation of $[\bar{1}\,\bar{5}\,10]$. Apart from this, also the two possible Burgers vectors and their corresponding slip planes could be obtained.

Then, as seen in Fig. 5.2, to find λ and ϕ also the direction of the applied force, the exact Burgers vector and the glide plane must be determined. Figure 5.7 shows snap-shots from a movie that was recorded during an *in situ* nanoindentation. The experiment comprised of a loading and an unloading part. The movie was correlated with the applied force, which can be seen in the upper left corner of each frame. During the unloading the dislocation starts to move in one direction, but between (e) and (f) it changes orientation. A dislocation that alters its direction usually experiences a cross-slip event (each Burgers vector in a fcc crystal is associated with three slip planes, in which the dislocation can move). When a dislocation slips over to a different glide plane, it is in a state of screw. At this instant, the Burgers vector is parallel to the line of the dislocation. Comparing the TEM micrograph in Fig. 5.7 (f) with different stereographic projection maps, the correct one could be found. Figure 5.8 illustrates the thus obtained Burgers vector $\mathbf{b} = [101]$, the initial glide plane $(\bar{1}\bar{1}1)$ and the cross-slip plane $(\bar{1}11)$. That is, the initial slip system was $(\bar{1}\bar{1}1)[101]$ and after the cross-slip event it was $(\bar{1}11)[101]$.* The other possible slip planes for this Burgers vector were (111) and $(1\bar{1}1)$.

*The dot product between them are zero, as they should, since the normal to the plane is perpendicular to the Burgers vector.

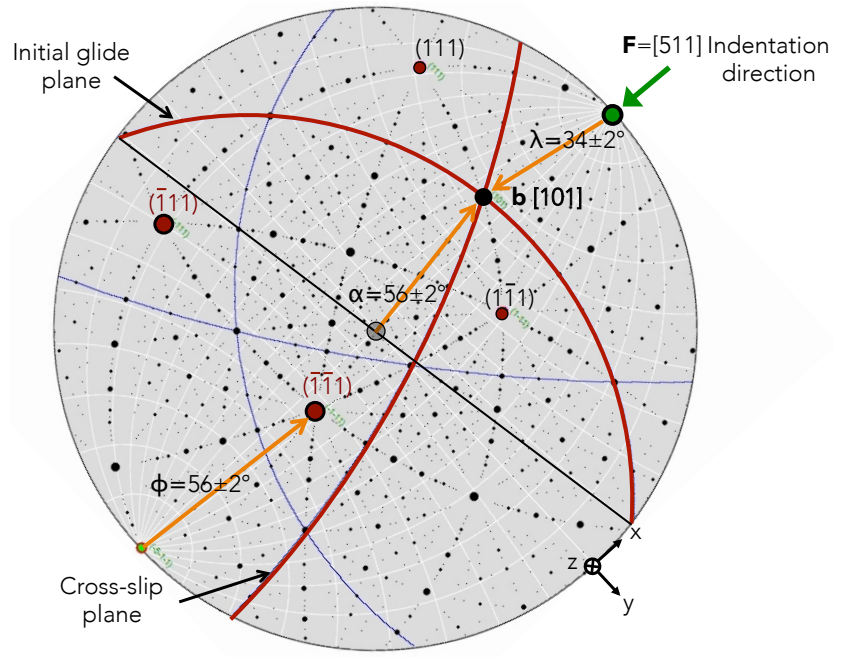

FIGURE 5.8 – *Stereographic projection map of sample* s1. *Crystal orientation of the sample, being the center, is* $[\bar{1}\,\bar{5}\,10]$.

Now, from Fig. 5.8 we found the angle between the applied force $\mathbf{F} = [511]$ and the Burgers vector $\mathbf{b} = [101]$ to be

$$\lambda = 34 \pm 2°. \tag{5.11}$$

Similarly the angle between $\mathbf{F}$ and the slip plane $(\bar{1}\bar{1}1)$ was

$$\phi = 56 \pm 2°. \tag{5.12}$$

And, as defined in Section 5.1.1.2, $\phi + \lambda \triangleq 90°$. The errors are estimated from the reading of the angles in Fig. 5.8. This gives a Schmid factor of:

$$S = \cos\lambda \cos\phi = 0.46 \pm 0.04 \tag{5.13}$$

which means that it is a highly activated slip system. Finally, using eqs. (5.9) and (5.13), the compressive stress on the dislocation was

$$\sigma_{\mathrm{rad_{s1}}} = \frac{\tau}{S} = 89 + 15\ \mathrm{MPa}. \tag{5.14}$$

The angle $\alpha = 56 \pm 2°$in Fig. 5.8 is the angle between the sample surface

$[\bar{1}\,\bar{5}\,10]$ and **b**. The angle can be verified using simple geometry, according to

$$\alpha = \arctan\frac{t}{2r_{\mathrm{proj}}} = 52 \pm 3^{\circ}. \tag{5.15}$$

That is, the different methods in measuring α seem to provide similar results.

5.4.3 Testing the model — Comparing with the stress from radius of curvature calculations

In order to test the model by comparing the stress from FEM with the stress obtained in eq. (5.14) above, first the external force that was applied in Fig. 5.7 (d) needs to be acquired. As mentioned above, the force is imprinted on each frame in the indentation movie. For (d), the force was around $\mathbf{F} = 25\,\mu$N. After this frame, when $\mathbf{F} \approx 0$, the dislocation surprisingly continues to move. An explanation could be that an internal stress σ_{int} is acting on the dislocation. In (a), the dislocation is curved in the $-y$ direction before any significant external force has been applied. When the force is increased, the dislocation starts to move in the y direction. In (b), when the external force $\mathbf{F} = 113\,\mu$N, an equilibrium seems to be reached and the dislocation is straightened out. At this moment we estimate that $\tau_{\mathrm{ext}} \approx \tau_{\mathrm{int}}$. Later on, in (d), just before the dislocation continued to move, $\mathbf{F} = 25\,\mu$N. If we assume that the internal stress is constant and not dependent on the externally applied force, the net force creating the stress on the dislocation is

$$\mathbf{F}_{\mathrm{net_{s1}}} = 113 - 25 = 88\,\mu\mathrm{N}. \tag{5.16}$$

This is the input force that we used in our model in the next section. The compressive stress-field map generated by FEM will be compared with the result from eq. (5.14).

The same reasoning should be valid also for the dislocation at its position in Fig. 5.7 (c). Here, the externally applied force $\mathbf{F}_2 = 35\,\mu$N, thus

$$\mathbf{F}_{\mathrm{net2_{s1}}} = 113 - 35 = 78\,\mu\mathrm{N}. \tag{5.17}$$

With the radius being larger, the stress to move the dislocation should be smaller. With a projected radius $r_{\mathrm{proj2}} = 155 \pm 15$ nm from Fig. 5.7 (c) and using the same calculations as in eqs. (5.8), (5.9) and (5.14), the compressive stress was

$$\sigma_{\mathrm{rad2_{s1}}} = 78 \pm 13\ \mathrm{MPa}. \tag{5.18}$$

This result will further down be compared with the stress-field map from a

model where the force in eq. (5.17) was used as input value.

5.4.4 FEM of sample s1

How the model was created is explained in Section 5.3.3. Figure 5.9 shows a superposition of the simulated stress-field map and Figs. 5.6 and 5.7 (d). The force used in the model was 88 μN (eq. (5.16)).

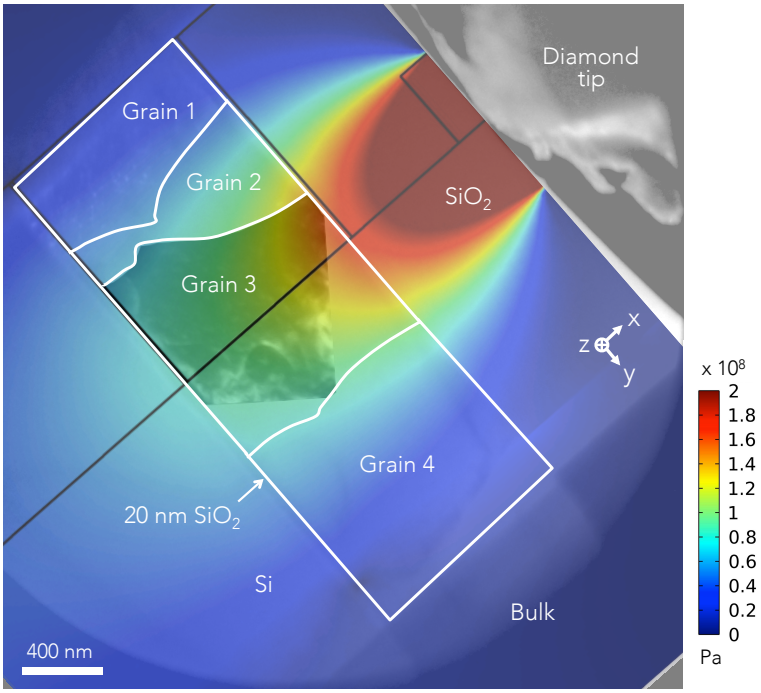

FIGURE 5.9 – *Sample* s1. *Simulated stress for an applied force of 88 μN superimposed with two dark-field TEM micrographs. The stress on the dislocation, which can be seen in the middle, was* $\sigma_{\mathrm{FEM_{s1}}} = 95 \pm 5$ *MPA. The Grain 3 micrograph is from Fig. 5.7 (d).*

In the darker inset of Grain 3 in Fig. 5.9, the curvature of the dislocation can be seen. At this position, the simulation show that the dislocation was under a stress of

$$\sigma_{\mathrm{FEM_{s1}}} = 87 \pm 5 \text{ MPa}. \tag{5.19}$$

The error is the maximum and minimum stress in the area of the dislocation. The stress from the radius of curvature in eq. (5.14) was $\sigma_{\mathrm{rad_{s1}}} = 89 \pm 15$ MPa. That is, a comparable result was obtained.

Similarly, for the position of the dislocation in Fig. 5.7 (c) the compressive stress from radius of curvature calculations was $\sigma_{\mathrm{rad2_{s1}}} = 78 \pm 13$ MPa (eq. (5.18)) and with the force from eq. (5.17) as input in the model, the stress-

field map showed that the simulated stress was $\sigma_{\mathrm{FEM2_{s1}}} = 77 \pm 4$ MPa.

To summarize, the FEM model seems to describe the true stress-field in the sample.

5.4.5 Stress from the Nix model for sample s1

As mentioned in Section 5.1.1.3, the Nix model states that the stress needed to move a dislocation is inversely proportional to the thin film's thickness h_f. In eq. (5.5) the s in the parameters μ_s and β_s stands for substrate, which together with the oxide passivation layer encapsulates the thin film. For our sample configuration, where the Al film is situated between two (SiO_2) oxide layers, one being the $1\,\mu$m passivation layer and the other being a 20 nm diffusion barrier, we changed the model so that $\mu_\mathrm{s} = \mu_\mathrm{o}$ and $\beta_\mathrm{s} = \beta_\mathrm{o}$, as seen below.

$$\sigma_{\mathrm{Nix}} = \frac{\sin\phi}{\cos\lambda\cos\phi}\frac{b}{2\pi(1-\nu_\mathrm{f})h_\mathrm{f}}\left[\frac{\mu_\mathrm{f}\mu_\mathrm{o}}{(\mu_\mathrm{f}+\mu_\mathrm{o})}\ln\left(\frac{\beta_\mathrm{o}h_\mathrm{f}}{b}\right) + \frac{\mu_\mathrm{f}\mu_\mathrm{o}}{(\mu_\mathrm{f}+\mu_\mathrm{o})}\ln\left(\frac{\beta_\mathrm{o}h_\mathrm{o}}{b}\right)\right] \tag{5.20}$$

From Fig. 5.8 we have $\lambda = 34 \pm 2^\circ$ and $\phi = 56 \pm 2^\circ$, from eq. (5.7) that $b = 2.86$ Å and in Fig. 5.3 (a) that $h_\mathrm{f} = 1.2$ μm and $h_\mathrm{o} = 1$ μm. The values used in the model in Section 5.3.3 for Young's modulus E, elastic shear modulus μ and Poisson's ratio ν, being $E_\mathrm{f} = 70$ GPa, $\nu_\mathrm{f} = 0.33$, $\mu_\mathrm{f} = 26$ GPa, $E_\mathrm{o} = 70$ GPa and $\nu_\mathrm{o} = 0.17$. Additionally for SiO_2, a shear modulus $\mu_\mathrm{o} = 31$ GPa was used. As stated in Section 5.1.1.3, $\beta_0 = 17.5$. These values gave a compressive stress of

$$\sigma_{\mathrm{Nix_{s1}}} = 22 \pm 3 \text{ MPa} \tag{5.21}$$

which is around four times smaller than the value obtained from the radius of curvature calculations and FEM. The Nix model describes a minimum stress that is needed to move a dislocation. But in reality, obstacles, e.g. point defects or other dislocations, hinder the motion of dislocations. Neither this nor the friction force (although negligible for an fcc crystal) of the dislocation movement has been taken into account in the equation, which should result in a higher stress in the material at the time of dislocation movement. The model was modified by Freund [Freund, 1994] and Nix [Nix, 1998] to take into account also the effect of obstacles hindering the movement of the dislocation that in reality diminishes the effective thickness of the thin film, which thus increases the strength of the film. These arguments could potentially partly explain the discrepancy.

A closer analysis shows that the biggest constraints on the dislocation should come not from the Al/SiO_2 interfaces, but from the Al/Al_2O_3 interfaces. That is, the dislocation moves in the confinement of a TEM lamella, which is a slip plane truncated by the FIB cut, and not in the entire thickness of the Al film. Since the lamella is 4 – 5 times thinner than the film, the strength of the film should be higher than the value acquired in eq. (5.21). Perchance the Nix-model could be used still, but in a slightly different way. If we see the TEM lamella as the film, the encapsulating materials will be the Al_2O_3 layers instead of the SiO_2 layers. This gives the following substitutions in eq. (5.20):

- Al film thickness h_f to the TEM lamella thickness $t_\mathrm{s1} = 280 \pm 10$ nm (see to the right in Fig. 5.3 (b))
- Shear modulus μ_o of SiO_2 to $\mu_\mathrm{AlO} = 124$ GPa of Al_2O_3
- Thickness h_o of the SiO_2 to $h_\mathrm{AlO} = 3 \pm 1$ nm for the Al_2O_3 layer

With these changes, we arrive at

$$\sigma_{\mathrm{Nix}'_{\mathrm{s1}}} = \frac{\sin\phi}{\cos\lambda\cos\phi}\frac{b}{2\pi(1-\nu_\mathrm{f})t_\mathrm{s1}}\left[\frac{\mu_\mathrm{f}\mu_\mathrm{AlO}}{(\mu_\mathrm{f}+\mu_\mathrm{AlO})}\ln\left(\frac{\beta_\mathrm{o}t_\mathrm{s1}}{b}\right) + \frac{\mu_\mathrm{f}\mu_\mathrm{AlO}}{(\mu_\mathrm{f}+\mu_\mathrm{AlO})}\ln\left(\frac{\beta_\mathrm{o}h_\mathrm{AlO}}{b}\right)\right] = 97 \pm 9 \text{ MPa} \tag{5.22}$$

These result is more in accordance with the results from the radius of curvature calculations and the FEM analysis. A note of caution should be made. In the work by Nix [Nix, 1989], it is not clear how the numerical constant $\beta_0 = 17.5$ was deduced. If this value would change from exchanging a common oxide like SiO_2 to the sturdier Al_2O_3, we do not know. Also, the model was made for a thin film which is encompassed by interfaces on two sides and not on four sides, like in our case. To summarize,

- $\sigma_{\mathrm{rad}_{\mathrm{s1}}} = 89 \pm 15$ MPa (eq. (5.14))
- $\sigma_{\mathrm{FEM}_{\mathrm{s1}}} = 87 \pm 5$ MPa (eq. (5.19))
- $\sigma_{\mathrm{Nix}'_{\mathrm{s1}}} = 97 \pm 9$ MPa (eq. (5.22)).

Considering the thinness of the sample, at the time of the dislocation moving, few obstacles should be hindering it.

5.5 Absorption of interfacial dislocations (samples s2 and s3)

For the samples in this section, the constraint was increased in steps. The force was raised until the first dislocation started to move, kept constant until it stopped, then increased again to the next dislocation motion and so on. The goal was to force a dislocation into the Al/SiO_2 interface and to measure the stress when this occurred.

Stress from the image dislocation was calculated in order to estimate at which distance from the interface that the dislocation should stop.

5.5.1 *In situ* TEM nanoindentation of samples s2 and s3

For these indentations we used a knife-shaped diamond tip. This ensures a firm contact that prevents slipping. Since the tip is around 1 μm in the z direction, and since it will never be neither perfectly aligned nor perfectly smooth, the tip radius that is in contact with the sample will be shadowed. But, as can be seen in Fig. 5.10, a negative of the tip can be seen in the indention mark, after an indention of around 10 μN was made.

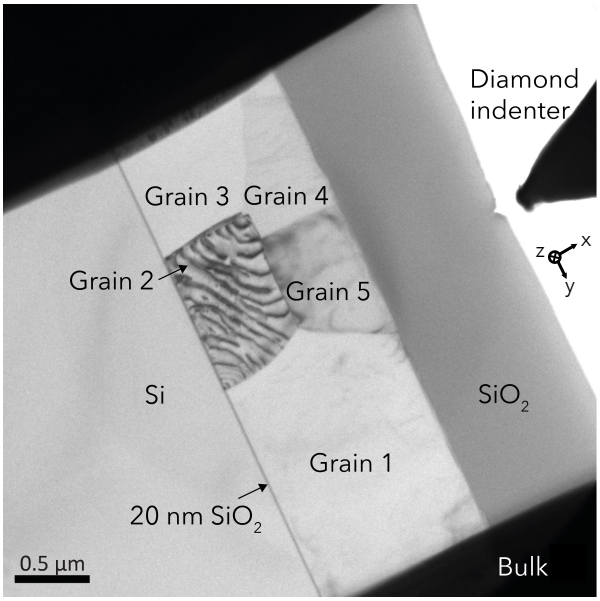

FIGURE 5.10 – *Sample* s2. *The indentation mark showing the tip radius after an indentation of around 10 μN. In Grain 2, FIB-induced dislocations can be seen.*

For sample s1 we observed a behavior that indicated the presence of an internal stress that was acting on it (see discussion in Section 5.4.3). This was not detected for the dislocations in samples s2 and s3.

5.5.2 Results from sample s2

The second h-bar sample s2 had a thickness $t_{s2} = 220$ nm and a width of $3\,\mu$m (see Fig. 5.3 (b)).

5.5.2.1 Stress from radius of curvature of sample s2

Figure 5.11 displays snapshots from a movie recorded during an *in situ* TEM indentation of sample s2. The sequence (a) – (c) shows how a threading dislocation moves towards the Al/SiO_2 interface upon an increase in applied force. In (e) the simultaneously recorded force plot can be seen. The arrow in (a) indicates how the dislocation momentarily is hindered by an obstacle before being released.

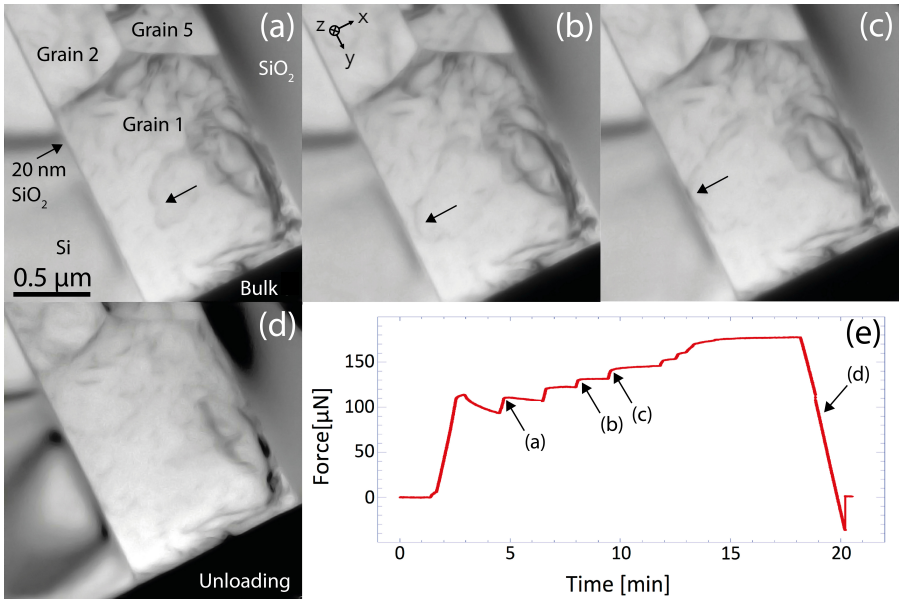

FIGURE 5.11 – *Sample* s2. *In situ TEM indentation sequence showing the movement of a threading dislocation towards the Al/SiO₂ interface. (a) – (c) Dislocation moving towards the interface upon an increase in stress. (d) After interaction with the amorphous interface and stress release, the dislocation does not go back. (e) Force plot recorded during the indentation sequence.*

From Fig. 5.11 (b) the radius of the dislocation was estimated to be $r_{\mathrm{proj}_{s2}} = 150 \pm 20$ nm. Here, we did not see that the dislocation was interacting with the Al/AlO interfaces (the two surfaces of the sample), therefore we could not find the true radius of the dislocation in the same way as was used with eq. (5.8). That is, the real radius could be larger and thus the value obtained was the maximum shear stress. Using eq. (5.6) we obtained a shear stress $\tau_{\mathrm{max}_{s2}} = 51 \pm 7$

MPa.

For this experiment we did not observe any cross-slip event. Therefore we could not unambiguously determine the Burgers vector (as explained in Section 5.4.2). But we assumed that, as in previous experiments, the slip system with the highest Schmid factor was activated, that is, $S \lesssim 0.5$ and from $\sigma = \tau/S$ (eq. (5.10)), we get that

$$\sigma_{\mathrm{rad_{s2}}} \approx 100 \pm 15 \text{ MPa}. \tag{5.23}$$

5.5.2.2 FEM of sample s2

A similar model as that used for sample s1 in Section 5.4.4 was made. The indentation did not occur exactly in the middle. Therefore half and not a quarter of the sample was modeled. The dislocation movement occurred not in the center, but closer to the bulk part. Therefore, the von Mises stress expression was used (see reasoning for which stress expression to use in Section 5.3.3).

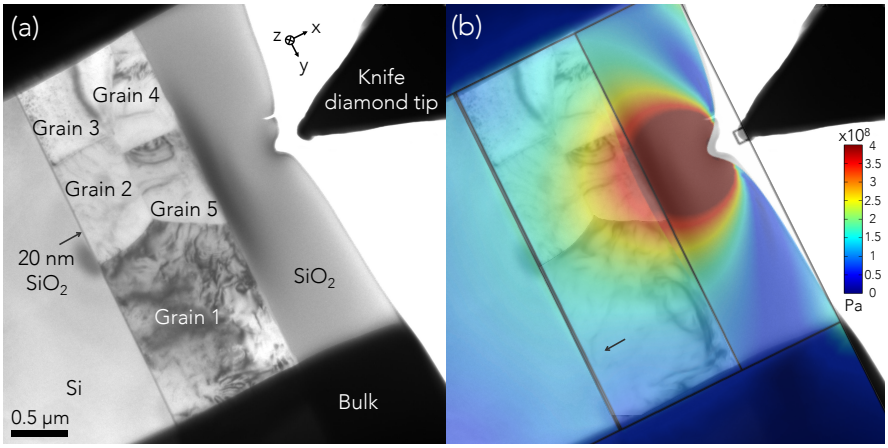

FIGURE 5.12 – *Sample* s2. *An indentation experiment where a force of 131 μN has been applied, with (a) showing the TEM micrograph after the experiment. (b) shows the simulation superimposed with a TEM micrograph (also, Grain 1 from Fig. 5.11 (b) has been added here). Note that the simulation shows the response at a time when the force was applied and not after, like in (a). That is, elastic relaxation occurring in (a) during the unloading is not shown in (b).*

By correlating the recorded movie with the force plot in Fig. 5.11 (e), the applied force at the time of the dislocation in Fig. 5.11 (b) was 131 μN. Using the force as input value for the FEM, a stress-field map was created. In Fig. 5.12 (a) a TEM micrograph can be seen after the indention cycle. In (b), the FEM stress-field map has been superimposed with the image in (a). Also in (b) shows a superimposition of Grain 1 from Fig. 5.11 (b), with the threading dislocation

being pointed out by the arrow. The compressive stress from the model in the area of dislocation movement was

$$\sigma_{\mathrm{FEM_{s2}}} = 118 \pm 10 \text{ MPa}. \tag{5.24}$$

Namely, $\sigma_{\mathrm{FEM_{s2}}} \approx \sigma_{\mathrm{rad_{s2}}}$.

5.5.2.3 *Image force in sample* s2

As can be seen in Fig. 5.11 (e) the load increases in (b) – (c). In (c), part of the dislocation get hindered before the Al/SiO_2 interface, while the other part continues into the interface. As discussed in Section 5.1.1.1 this should not happen since a dislocation that approaches an interface to a stiffer material experiences a repulsive force from image forces.

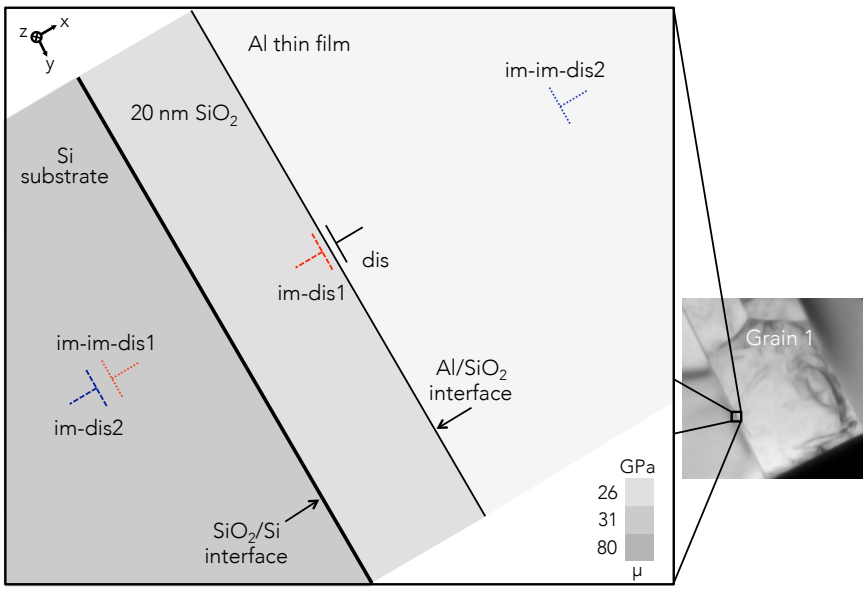

FIGURE 5.13 – *Sketch showing the notion of image dislocations.* dis *stands for dislocation and* im *for image. It is based on the samples used in this chapter.*

Equation (5.1) describes the image force F_{b} per unit length that an image dislocation is exerting on a screw dislocation situated opposite the image dislocation. The image dislocation is located the same distance from the Al/SiO_2 interface as the real dislocation. For convenience, the equation is repeated below.

$$F_{\mathrm{b}} = -\frac{\mu_{\mathrm{f}} b^2 k_\mu}{4\pi d}, \qquad k_\mu = \frac{\mu_{\mathrm{f}} - \mu_{\mathrm{s}}}{\mu_{\mathrm{f}} + \mu_{\mathrm{s}}} \tag{5.25}$$

It is normally straightforward to estimate the image force, but it becomes problematic in the four interface case. Figure 5.13 is a sketch of a zoom-in of the two interfaces surrounding the 20 nm SiO_2 diffusion barrier layer.* The third interface is between the Al thin film and the 1 μm SiO_2 passivation layer and the forth is the interface between the passivation layer and the vacuum. Here, we are only focusing on the first two interfaces, depicted in Fig. 5.13. With two interfaces, not only is a second image dislocation created, mirrored in the second interface. It also creates mirrored image dislocations of the the image dislocations, which in turn are mirrored yet again, and so on. It is somewhat similar to having an object reflected in two semi-transparent mirrors.

The reason for studying the image forces was to find an approximate distance from the interface that the dislocation *should* become stationary according to dislocation theory. Due to this and to the complexity of the solution when having multiple interfaces [Öveçoğlu et al., 1987, Chou, 1966], we only considered the two image dislocation `im-dis1` and `im-dis2`. Öveçoğlu et al. calculated the image force in multiple interface configurations. A graph from the paper from 1987 [Öveçoğlu et al., 1987] can be seen in Fig. 5.14. It shows how a dislocation within the thin film is repelled both by the Al/SiO_2 interface on one side and the native Al_2O_3 interface on the other. Since the Al_2O_3 interface is thin, the attractive force from the vacuum is opposing the repelling force from the Al_2O_3 interface. The sample we have is different because it has a 1 μm SiO_2 layer instead of the Al_2O_3, which means that the negative and attractive force from the vacuum is exchanged with a positive and repelling force. To the left in the graph, the sharp increase when the dislocation approaches the Al/SiO_2 interface can be seen as well.

For the first image dislocation `im-dis1`, the shear modulus of the substrate μ_s should be exchanged with the shear modulus μ_o of SiO_2. Using $\mu_\mathrm{f} = 26$ GPa, $\mu_\mathrm{o} = 31$ GPa, $b = 2.86$ Å and if we study a position for the dislocation of $d = 1$ nm from the Al/SiO_2 interface, eq. (5.25) will result in

$$\begin{aligned} k_{\mu_{\mathrm{im}\perp 1}} &= \frac{\mu_\mathrm{f} - \mu_\mathrm{o}}{\mu_\mathrm{f} + \mu_\mathrm{o}} = -0.088 \text{ and} \\ F_{\mathrm{b}_{\mathrm{im}\perp 1}} &= -\frac{\mu_\mathrm{f} b^2 k_\mu}{4\pi d} = 1.49 \times 10^{-2} \text{ Nm}^{-1}. \end{aligned} \tag{5.26}$$

With F_b being the force per unit length, the shear stress is obtained by

$$\tau_{\mathrm{im}\perp 1} = \frac{F_{\mathrm{b}_{\mathrm{im}\perp 1}}}{b} = 52 \text{ MPa}. \tag{5.27}$$

For the second image dislocation, since `im-dis2` in Fig. 5.13 is in the Si

*The TEM micrograph is Fig. 5.11 (c).

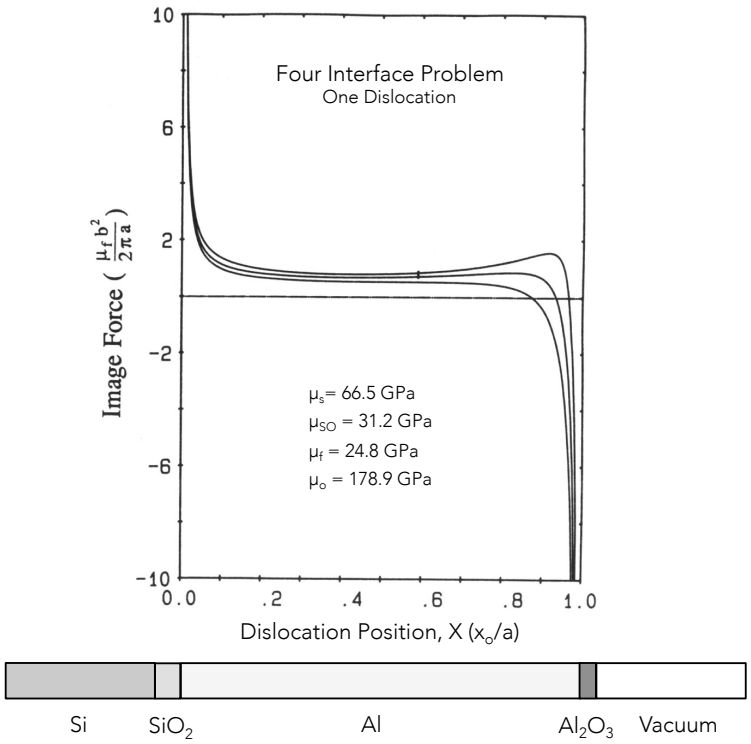

FIGURE 5.14 – *Variation of the image force with dislocation position for a screw dislocation in the $Si/SiO_2/Al/Al_2O_3$ four interface case (Figure and figure caption from Öveçoğlu et al. [Öveçoğlu et al., 1987]).*

substrate, eq. (5.25) should be used in its original form. The dislocation (`dis`) is 21 nm from the SiO_2/Si interface. This gives:

$$\begin{aligned} k_{\mu_{\mathrm{im}\perp 2}} &= \frac{\mu_\mathrm{f} - \mu_\mathrm{s}}{\mu_\mathrm{f} + \mu_\mathrm{s}} = -0.51 \text{ and} \\ F_{\mathrm{b}_{\mathrm{im}\perp 2}} &= -\frac{\mu_\mathrm{f} b^2 k_\mu}{4\pi d} = 7.86 \times 10^{-3}\ \mathrm{Nm}^{-1} \\ \tau_{\mathrm{im}\perp 2} &= \frac{F_{\mathrm{b}_{\mathrm{im}\perp 12}}}{b} = 28\ \mathrm{MPa} \end{aligned} \tag{5.28}$$

Adding the shear stress of the two image dislocations, a total shear stress of

$$\tau_{\mathrm{im}_{\mathrm{s}2}} \approx 80\ \mathrm{MPa} \tag{5.29}$$

is acting on the the real dislocation at the instant when it is 1 nm from the Al/SiO_2 interface. From the force plot in Fig. 5.11 (e) a force of 136 μN was applied by the load cell when the dislocation reached the interface. A FEM

model showed that this corresponded to a compressive stress of

$$\sigma_{\mathrm{ext_{s2}}} = 120 \pm 10 \text{ MPa} \tag{5.30}$$

Assuming that the slip plane is activated with the Schmid factor $S \lesssim 0.5$, the external shear stress is

$$\tau_{\mathrm{ext_{s2}}} \approx S\sigma_{\mathrm{ext_{s2}}} \approx 60 \text{ MPa} \tag{5.31}$$

In other words, at this position $\tau_{\mathrm{im_{s2}}} > \tau_{\mathrm{ext_{s2}}}$ and the image force should have rendered the dislocation stationary. Obviously it is not possible to distinguish a distance of 1 nm from the TEM micrographs in Fig. 5.11 (a) – (d). But, if the dislocation had been pinned against the Al/SiO_2 interface during loading in Fig. 5.11 (a) – (c), it should during the unloading in (d) move back into the thin film. This was not observed, which we interpret as that the dislocation was absorbed by the interface.

5.5.3 Results from sample s3

The third h-bar sample s3 had a thickness $t_{\mathrm{s3}} = 220$ nm and a width of $3.2\,\mu$m (the sample to the left in Fig. 5.3 (a) and (b)).

Figure 5.15 shows frames from the *in situ* movie that was obtained when a force was applied with the load cell. The movie was recorded with 10 frames per second. In (a), an overview image can be seen. The diamond tip is out of the field of view to the right of the SiO_2 layer. The thick red arrow shows the dislocation that is about to move. (b) is a magnification of the area indicated by the black square in (a). (c) – (d) shows the movement of the dislocation in the same magnified area. The movement of the dislocation from (b) to (c) takes place during a time frame that is less than the 0.1 second available time resolution. Part of the dislocation (blue arrow) seemingly undergoes a double cross slip, before threading onwards in its original slip plane. In (c), the two parts of the dislocation gets hindered, before moving into the interface in (d).

The large and thick black lines are fringes that can be seen in all frames are coming from the sample being bended, i.e., they are bend contours.

5.5.3.1 Stress from radius of curvature of sample s3

In Fig. 5.15 (b) the slip traces have been marked out. The slip traces are dislocations left behind at the interface between the Al and the Al_2O_3 at the two surfaces of the sample. That is, they provide the projected width of the slip plane. This information together with the thickness $t_{\mathrm{s3}} = 220$ nm of the TEM foil, the real radius of the dislocation in (b) was estimated to be around 120

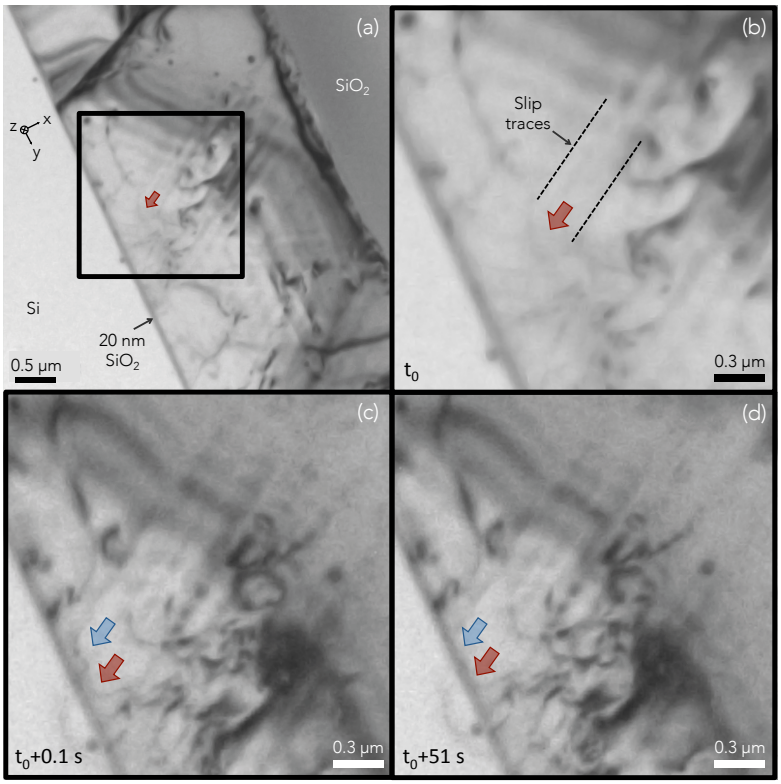

FIGURE 5.15 – *Sequence from an in situ TEM indentation movie of sample* s3*. The black square in (a) is the area showing in (b) – (d). (b) Slip traces and direction (thick read arrow) of the threading dislocation can be seen. In (c), part of the dislocation seems to have made a double cross-slip (indicated by the thick blue arrow). Both parts of the dislocation stop before the Al/SiO_2 interface, before being absorbed in (d).*

nm.* Similarly as in Section 5.4.2, eq. (5.6) was used to obtain the shear stress acting on the dislocation using radius of curvature calculations. It was found to be $\tau_{\mathrm{rad_{s3}}} \approx 60$ MPa. Assuming that the slip plane is activated and thus that the Schmid factor $S \lesssim 0.5$, the compressive stress $\sigma_{\mathrm{rad_{s3}}} \gtrsim 120$ MPa.

5.5.3.2 *FEM of sample* s3

As for the previously reported samples, a model using FEM was made. Correlating the *in situ* movie with the force recording, the load as a function of time could be obtained. In Fig. 5.15 (b), when the radius of curvature measurement was made, an external load of 125 μN was applied. The stress on the dislocation at this time was $\sigma_{\mathrm{FEM_{s3}}} \approx 150$ MPa. In other words, $\sigma_{\mathrm{FEM_{s3}}} \approx \sigma_{\mathrm{rad_{s3}}}$.

*The same way as the real radius of sample s1 using eq. (5.8) was obtained.

5.5.3.3 Image force in sample s3

Just as in Section 5.1.1.1, the shear stress from the image force that was acting on the dislocation 1 nm from Al/SiO_2 interface was $\tau_{\mathrm{im_{s3}}} \approx 80$ MPa. At the time when the dislocation moved into the interface in Fig. 5.15 (d), an external load of 141 μN was applied. The FEM model showed that the shear stress transported to the Al/SiO_2 interface was $\tau_{\mathrm{ext_{s3}}} \approx 80$ MPa. That is, here, the dislocation should be stationary. As in previous experiments, 1 nm is not possible to distinguish in the TEM micrographs in Fig. 5.15. But, during unloading, the dislocation did not move back into the Al thin film, which is deciphered as it was consumed by the interface.

5.6 Discussion

5.6.1 Dislocation/interface interaction

The main goal of the indentation experiments performed on several cross-sectional windows milled in a passivated Al film was to investigate the interaction of the incoming dislocations with the silicon oxide sandwiching the metal. As we saw in the introduction of this chapter, the inverse thickness dependence of film strength is explained by these interfacial dislocations whose energy depends essentially on image forces [Öveçoğlu et al., 1987]. The most common way of stretching a thin film on a substrate being to impose thermal cycles (and thus input some stress coming from the difference in CTE), the disappearance of interfacial dislocations [Müllner and Arzt, 1998, Legros et al., 2002] could be attributed to enhanced diffusion, favoring the dislocation decomposition inside the oxide layer. Here, the Al film was strained *in situ* at room temperature using a special TEM holder where a diamond wedge is attached to a MEMS sensor able to record the applied force that is applied by a piezo [de Knoop and Legros, 2014]. Again, threading dislocations reaching the Al/SiO_2 interface were seen to be absorbed by this interface instead of laying an interfacial segment there. At variance from thermal straining experiments, dislocations were not accelerating towards this interface all the way. The difference between the behavior observed in the literature and the current experiments could be attributed to local obstacles on which dislocations seem to anchor prior to reach the interface. These obstacles could be Ga^+-implanted defects or radiation loops, or initial dislocations present in the film. When a dislocation reached the Al/SiO_2 interface, an inversion of the applied stress was never sufficient to withdraw this dislocation from the interface. There is clearly absorption, at room temperature.

To further evaluate the stress needed for a dislocation to disappear at the crystal/amorphous interface, two ways of calculating the stress were made; using the radius of curvature of dislocations and evaluate the stress field in the various layers of the sample using FEM. Both methods were proven to be convergent when tested on a free dislocation loop. This further on allowed an estimation of the stress at the interface. This shear stress was in the order of 100 MPa, which is smaller than the film strength determined by thermal cycling (around 300 MPa [Flinn et al., 1987]).

The direct consequence of this observations and measurement is that the most cited model for the strength of thin films [Nix, 1989], relies on an assumption that is physically not correct, at least in the (very common) case of an Al film deposited on oxide. It is therefore not surprising that when an Al film is deposited on an oxidized Si substrate, its strength (for a given thickness) is larger than for the equivalent film deposited on sapphire [Dehm et al., 2003]. According to the interfacial dislocation model, the sapphire substrate should provide a much larger repulsive stress to interfacial dislocations, and therefore should lead to a larger film strength. The contrary is observed [Heinz et al., 2010]. What has been proposed is that the strength of Al films stem from a lack of dislocations [Legros et al., 2005]: The first ones are absorbed by the metal/oxide interfaces, and the nucleation/multiplication of fresh dislocations is prevented by impeding potential sources at these interfaces. In fact, the absorption of one or several dislocations (one Burgers vector each) does not add much more disorder to the large disorder already present at the amorphous Al/SiO_2 interface. A diffusive reconstruction has also been observed by Ju Li and co-workers in the case of Cu/Cu-Zr (Cu-Zr is amorphous) nanolaminates using molecular dynamics (MD) [Wang et al., 2007], and at grain boundaries (time dependent spreading of the dislocation core) during *in situ* TEM experiments [Mompiou et al., 2012]. It is therefore very difficult to have the necessary stress concentration at this interface to promote dislocation nucleation or multiplication.

5.6.2 *In situ* TEM nanoindentation

Performing a clean indentation test on a thin TEM lamella can prove to be difficult. First the sample and tip must be aligned to the same height. Using a combination of stage tilt and focus, facilitates this step. Once in contact, the usual tools that are available in a "regular" *in situ* TEM tests are here somewhat restricted; moving the stage can cause vibrations which creates incorrect force readings on the load cell.* If this sample is in contact with the diamond tip,

*This is largely dependent on microscope. For example, the latest JEOL and Hitachi microscopes have accurate and sometimes piezo-driven stages.

a large stage movement can also deform the sample. This implies that the viewing conditions have to be set once and for all, which is again challenging because those are heavily affected by the strong stress gradient created by the tip. Bend contours and drift away from Bragg's conditions are unavoidable. To minimize these difficulties, we have often worked in dark-field conditions, a method employed also by others [Kiener and Minor, 2011a, Kondo et al., 2012]. We found that z correction using piezo displacement was possible during the test without affecting the force measurement, which increased the chances of having good imaging conditions.

Finally, the choice of the sample geometry (H-bar windows) and configuration (passivated Al film) were also important: The H-bar provided a stiffer sample (and thus a slower invasion of bend contours during experiment), and the thick passivation layer (SiO_2) also served as a "cushion" that diffused the strong stress gradient at the tip, maintaining imaging conditions longer during indentation. A good alternative to avoid some of these drawbacks is to perform tensile test using the same type of holders, either directly [Kiener and Minor, 2011b] or MEMS push-to pull devices [Chisholm et al., 2012].

5.6.3 Quantitative stress measurements

Obtaining quantitative data from such experiments is also not straightforward, despite the load measurement capabilities and the dynamic images of the sample being deformed (that could serve to obtain the strain). Once the cross-section of the strained sample is not constant, transforming a load (read from the sensor) into a stress, which is the meaningful physical parameter, is almost impossible and simulations (FEM, MD, etc.) are needed. This combined approach has for example been carried out by in the case of nanospheres deformed in compression with a flat punch [Calvié et al., 2012, Deneen et al., 2006], or pillars that have a tapered tip [Lee et al., 2014].

Besides the significantly complicated analysis of *in situ* TEM indentation, simulations have to be taken with caution. Molecular dynamics simulations are known to depend on atomic potentials that do not capture all the parameters of a given material, and provide results obtained at a time scale that is orders of magnitude shorter than an actual experiment. FEM simulations, that we have used in this work, is supposed to be more realistic, especially in the elastic domain, but there too, some obvious discrepancies can cast a doubt on the data. To strengthen our findings, we cross-checked the local stress measured on curved moving dislocations, which gives a real and physically based value to stress fields calculated by FEM, derived from the force from the load cell in the holder. In this model however, the native 3 nm AlO layer, which

supposedly covers the Al surfaces after the FIB polishing (see Section 5.3.3.4), a stress of several hundreds of MPa is supposed to appear in this layer. This seems unlikely as such a stress should have prevented the dislocations from escaping the crystal, which they do: Slip traces vanish after a few seconds, proving that the native oxide layer is crossed (see e.g. Fig. 5.15). Disappearance of any TEM contrast at the surfaces is an indication that dislocations relaxed into the vacuum. Arguably, the AlO layer could therefore play a smaller role on the strength of the thin film. Also, Ga^+ implantation and the surface dislocations created by the FIB milling affects the layer and its hardness. In other words, the AlO Young's modulus value in the model might not be the accurate for the present layer. To our best knowledge, there is no easy way to model the possibility to cross the native oxide and to incorporate the change in moduli introduced by the FIB preparation. The model does not take into account plastic deformation. The SiO_2 layer in Fig. 5.12 is clearly deformed plastically, but the Al film seems to be only slightly deformed. In (b), a strain of around 8% in the SiO_2 layer was found.

A more straightforward way to compare FEM simulations to experiments would be to obtain a strain map of the Al layer. An approach that has been tried, but proven to be extremely difficult, is to combine *in situ* nanoindentation with dark-field electron holography. Some first results will be presented in Section 6.1.1.

More experiments are on their way using a new holder (Hysitron) and a new TEM, (I^2TEM from Hitachi), where the stability is better and where better resolved holograms can be captured thanks to the cold-FEG. Our findings that z displacements can be made during the indentation should also be tried in these new experiments to correct for the bending.

5.7 Summary and conclusions

In this chapter, we have studied plastic deformation of Al thin films. The specialized *in situ* TEM sample holder explained in Section 2.2.2 was used in its nanoindentation configuration to apply and measure a force.

H-bar shaped samples, sculpted with FIB, has been indented *in situ*. Such a structure allows an electron-transparent sample to be indented without bending too much when a force is applied. Finite element method (FEM) modeling was used to find the optimum width of the transparent window.

Stress measurements using radius of curvature calculations on bulging dislocations were compared with FEM, to in this way verify the FEM model.

Observed for the first time in room temperature, interfacial dislocations

have been absorbed by stiff interfaces, at odds with the prevailing model for strength in thin films. The model states that a thin film's strength is inversely proportional with its thickness. A dislocation in proximity of an interface to a stiffer material should be repelled by it. Using the concept of image forces, the stress has been calculated, being in the order of 100 MPa. With the force from the load cell and FEM, a stress in the area where the dislocation was absorbed by the interface was found, being inferior to the stress from the image forces. In spite of this, it was clearly observed how the dislocations were consumed by the interface, which confirms that metal/amorphous interfaces can act as dislocation sinks.

Part III

CONCLUSIONS AND OUTLOOK

Symbols and abbreviations in Chapter 6

CFE	Cold field emission
C-FEG	Cold-field emission gun
CCnT	Carbon cone nanotip
FIB-SEM	Focused ion beam-scanning electron microscope
F_{ext}	Externally applied force
FEM	Finite element method
r	Physical electron source tip radius
d	Tip-anode separation distance
V	Potential between anode and CCnT
E_{loc}	Local electric field around the apex of the tip
γ	Field enhancement factor
F-N	Fowler-Nordheim
ϕ	Work function [eV]

6 Conclusions and perspectives

IN this chapter we will speak about what experiments we plan for future experiments. After a short coverage of the continuation of the experiments of the previous chapters, a separate section will describe an experiment which we have worked with for some time, but which has proven difficult to realize.

In the end of the chapter, a summary and some conclusive remarks will be made.

6.1 Perspectives

For the cold-field emission (CFE) properties characterization of Chapter 3, we plan to use a dedicated *in situ* 300 kV TEM (the Hitachi I^{2}TEM). The CFE gun (C-FEG), multiple biprisms and better vacuum provides higher accuracy for the holography measurements. Apart from using carbon cone nanotips (CCnT), W tips will be tested in order to more easily compare the results with standard cold-field emitters.

To better understand the results from measuring charges on the cold-field emitting CCnT (Section 4.3), new experiments will be made. For these, the tip-anode separation distance will be diminished, in order to see if and how a smaller field emission current will alter the result. The same experiments will also be made on standard W tips.

In Chapter 5, interfacial dislocations were seemingly absorbed by interfaces to a stiffer material. Due to a repelling image force, this should not happen. The process would be interesting to observe at a higher magnification, in order

to resolve the distance where the dislocation should become stationary. But, this could prove to be difficult, since a too high beam intensity on a dislocation could cause it to be absorbed by the interface, as occurred in the work by Müllner and Arzt [Müllner and Arzt, 1998].

6.1.1 *In situ* dark-field electron holography

Here we present a step towards what we hope will be a way to directly measure the strain quantitatively using dark-field electron holography*, which is imposed *in situ* by an external load.

Work on this has been done before by Houdellier et al., which was presented at a conference in 2010.† In Fig. 6.1 (a), a TEM micrograph shows the diamond tip and a Si sample. In (b), a strain map that was obtained during loading can be seen. No force was recorded during this experiment.

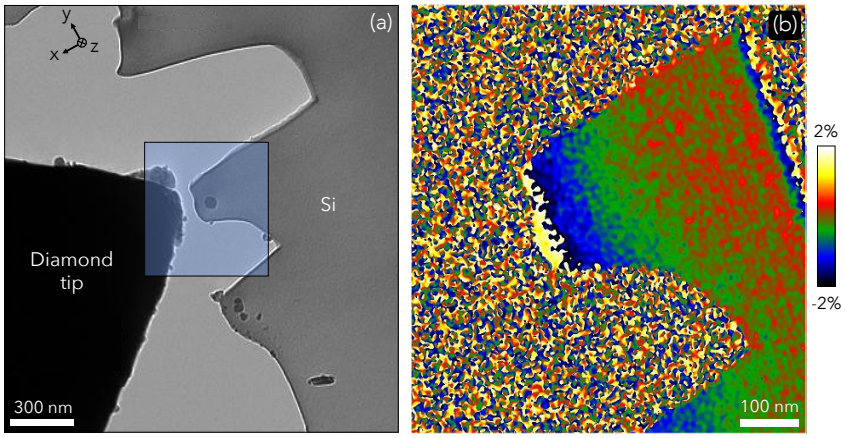

FIGURE 6.1 – *(a) TEM micrograph of a Si sample and the diamond indenter tip. (b) Strain map of the area zoomed in from (a). Images from Houdellier et al.*

6.1.1.1 Sample preparation

A number of different samples has been prepared. All the samples were made out of Si, with the first two from [001] grown wafers, and the last two from [110] grown wafers. The indentation direction was [220] for all samples.

For the first one, a Zeiss Gemini 1540X focused ion beam-scanning electron microscope (FIB-SEM) equipped with an Omniprobe was used to perform a lift-out.‡ When using a FIB, the outmost layer will be amorphous with Ga^+

*See Section 2.2.4 for the theory behind dark-field electron holography.
†The International Microscopy Conference (IMC 2010) in Rio de Janeiro, Brazil.
‡The lift-out was done by Robin Cours at CEMES-CNRS.

ions implanted. This can change the properties of the material [Kiener et al., 2007]. The common way to protect the material is to deposit Pt, first using the electron beam, followed by the ion beam. Even though this protects the sample, damage can still occur, either from the ion beam Pt deposition process or from thinning the sample. To avoid this, we tried using ink. After depositing 30 nm Pt with the electron beam, a pen was used to draw a protective layer of ink on the surface of the sample (Staedtler Lumocolor® permanent pen).

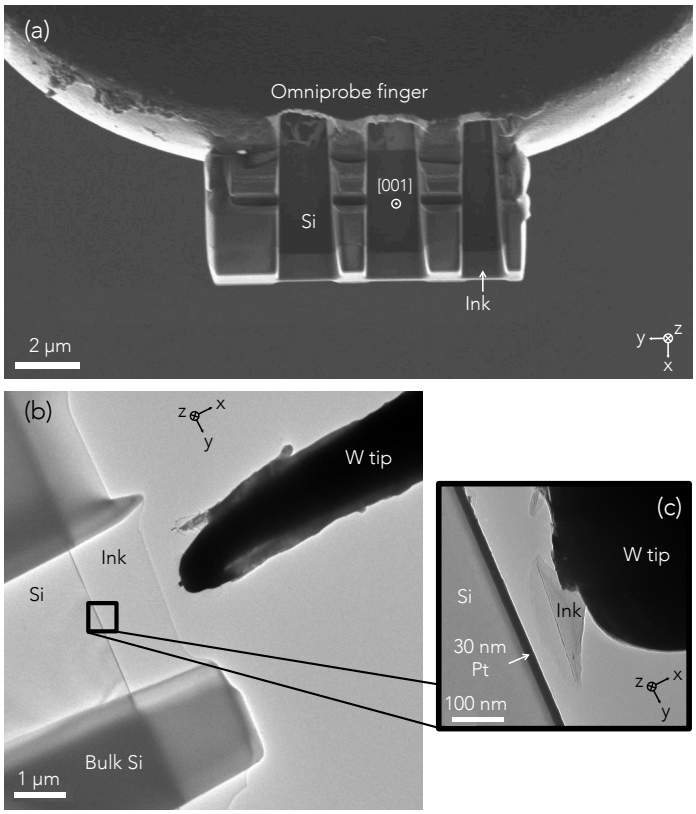

FIGURE 6.2 – *(a) SEM image of the lift-out sample being welded on top of a mounting finger. Three H-bar windows has been milled using the ion beam. (b) TEM micrograph showing the W tip used to apply a force. The ink layer has been mechanically removed using the W tip in (c).*

The lift-out was deposited using Pt deposition on the apex of a mounting finger on an Omniprobe Copper 5-Post Lift-Out Grid (see SEM image in Fig. 6.2 (a)). Like the sample in Fig. 5.3, H-bars were sculpted in order to stabilize the sample. After the H-bars were created, the sample was plasma cleaned (Fischione Model 1020) during 10 minutes in order to remove the ink.

The second sample was made as a wedge, using a tripod. With such a design, the thicker part of the wedge provides support for the electron trans-

parent part. In Fig. 6.3 (a), the thin edge can be seen colored red and yellow.* For Si, red corresponds to a thickness of less than 10 μm and yellow to less than 4 μm.

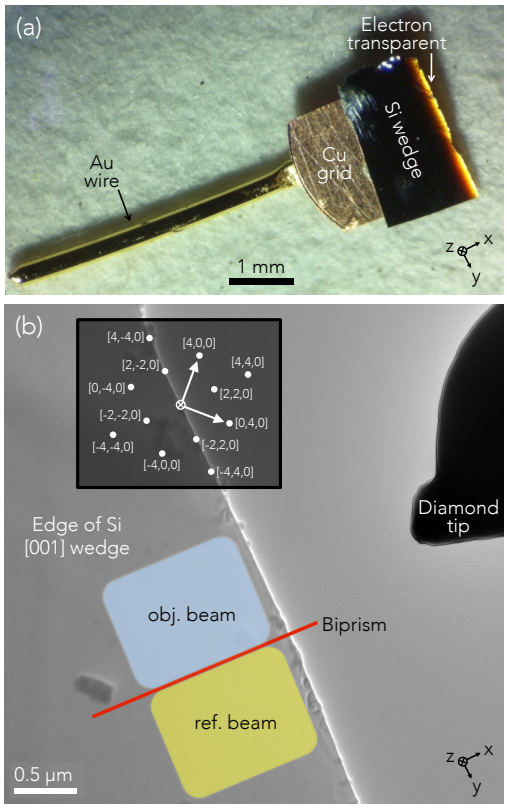

FIGURE 6.3 – *(a) Optical microscope image of the tripod Si wedge sample glued onto a cut Cu grid, which in turn is glued to a Au wire. In (b), a TEM micrograph shows the diamond tip and the Si wedge. The inset shows a simulated diffraction pattern for Si grown in the [001] direction, which shows the crystallographic alignment of the wedge. The sketch shows an approximate position of the biprism, the object beam and the reference beam.*

Figure 6.3 (a) displays the Si wedge glued onto a Cu half-grid with its sides cut off. A Au wire was glued onto the modified half-grid. The glue was a two-component conductive epoxy.† The Au wire was later inserted into the hat of the nanomanipulator, as can be seen in Fig. 2.2.

For the third and fourth sample, electron-beam lithography was utilized. For this method, a focused electron beam writes a line pattern in an electron sensitive resist. The resist had been spin coated on the wafer. Submerging

*The tripod step was done by Robin Cours at CEMES-CNRS.
†Circuit Works CW2400

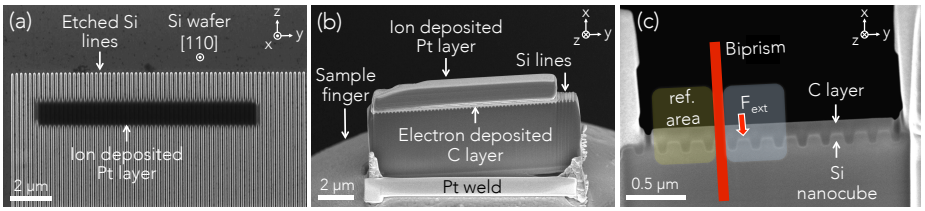

FIGURE 6.4 – *(a) FIB-SEM frontside lift-out of electron-beam lithography Si lines. (b) The lift-out after having been welded on a sample finger. (c) Electron transparent Si nanocubes after the final thinning with the FIB. The illustration shows where the biprism will be inside the TEM. F_{ext} symbols the externally applied force.*

the wafer in a solvent removed the resist that had not been exposed to the electron beam.* The resist that remained, protected the Si below it during the etching process. In the last step, all resist was removed, leaving Si lines on a Si substrate (see Fig. 6.4 (a)). To remove any remnant oxide layer, a bath of 5% HF followed by a bath of H_2O_2:H_2SO_4 1:1 was used.† The idea was to use a FIB-SEM to create clearly defined and aligned nanocubes from the Si lines. With sides and spacing of 100 nm, a force can be applied to one of the cubes and the neighboring one can be used as a reference area (see illustration in the SEM micrograph in Fig. 6.4 (c) where F_{ext} indicate the applied force). This would ensure having a un-strained reference area.

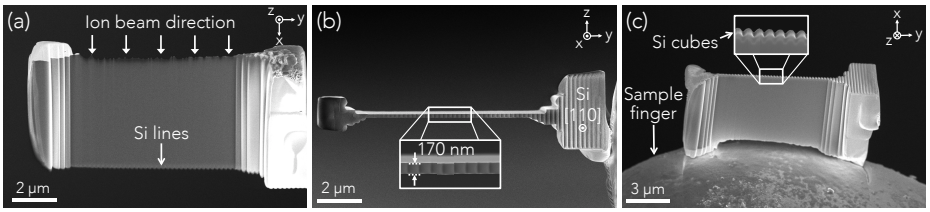

FIGURE 6.5 – *(a) – (b) FIB-SEM backside lift-out of electron-beam lithography Si lines. (c) The lift-out after having been welded on a sample finger.*

For the third sample, a lift-out was made using conventional front-side approach. That is, the ion beam is attacking the material from the top (in the $-x$ direction in Fig. 6.4 (b)). The lift-out was secured to an Omniprobe sample finger with a Pt weld (see Fig. 6.4 (b)). To protect the sample from the ion beam milling, 20 nm C was deposited using the electron beam. To shield the sample additionally, 2 μm Pt was deposited with the ion beam. Then, windows were milled out from the lift-out sample, and the Pt layer was removed using the

*This is solvent-dependent. The exposed parts can also be removed by the solvent.
†Electron beam lithography performed by Franck Carcenac at CNRS-LAAS.

ion beam. Now, Si nanocubes covered in a C layer remained, as can be seen in Fig. 6.4 (c).

The fourth sample was created where the ions attacked from the backside (see Fig. 6.5). With this technique the sample is thinned down while keeping the exposure to the ion beam to a minimum. Therefore a protective layer on the Si lines is not necessary. The Ga^+ implantation should be reduced as well.*

6.1.1.2 Results and discussion

Different problems were encountered. For the first sample (Fig. 6.2), the protective layer of ink was not successfully removed using the plasma cleaner. Instead, it was mechanically broken off in parts with the W tip (Fig. 6.2 (b) and (c) and Fig. A.2 (b)). During the dark-field electron holography measurements, bend contours prevented any phase to be observed. It is not know if this origins in the FIB milling or from the manipulation when removing the ink, but further experiments could be done where a different protective layer is used. For the second sample (Fig. 6.3), bend contours moved across the hologram when a force was applied, but some results could still be obtained.

Figure 6.6 shows five holograms and their corresponding phase maps†. In (a) and (b) no force was applied. In (c), the sample has advanced forward into the diamond tip with a force of 15 μN having been applied. The red arrow shows the direction of the force. In (e), bend contours starts to arrive. Artifacts from these can be seen in the phase map in (f). In order to prevent the bend contours from moving into the center of the hologram, the nanomanipulator was used to move the sample up and down (in z), which kept the bend contours stationed at more or less the same position. This should indicate that the sample was prevented from bending. The circled areas in the phase maps in the right hand column show a particle-created artifact that was used for orientation. The squares show the internal reference area. The camera artifacts have been removed by using the camera's Ronchigram.

There is no interpretation of the strain from the phase maps in Fig. 6.6 due to that we are unsure of the g-vector, which would thus first needed to be verified. Secondly, the reference area is not in a strain free region of the sample. Therefore, future work will be concentrated on samples like in Figs. 6.4 and 6.5, where an unstrained area would be easy to find. And further ahead, another patterned sample fabricated with electron beam lithography has been envisioned and started to be manufactured. For this, the use of FIB-SEM will be almost completely omitted.

*The FIB work above was made by Robin Cours at CEMES-CNRS.

†The FEI Tecnai F20 image-corrected 200 kV Schottky FEG TEM from Section 3.4.2 was used. A voltage of 120 V was applied to the biprism.

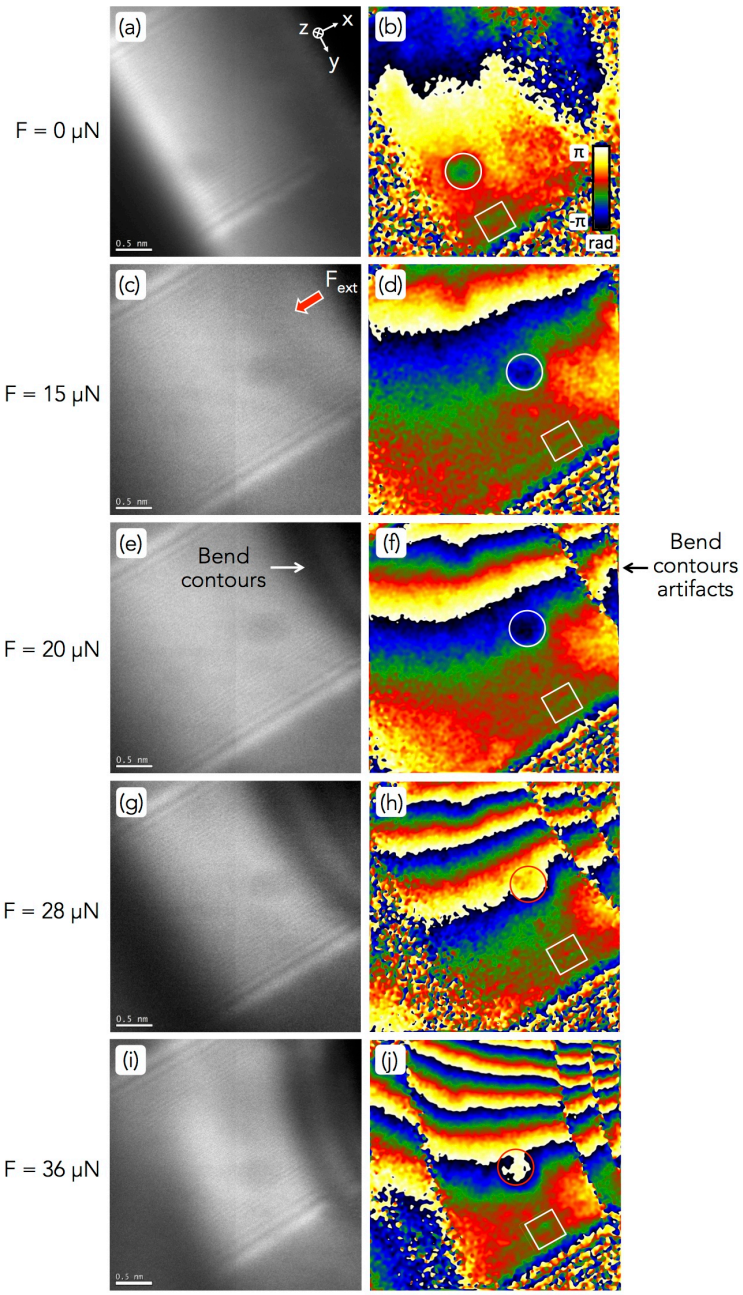

FIGURE 6.6 – *Dark-field electron holography holograms with corresponding geometric phase shift maps. The force has been increased from 0 to 36 μN, from top to bottom row.*

6.2 Summary and conclusions

In situ TEM has been used to study cold-field emission (CFE) from a carbon cone nanotip (CCnT) and plastic deformation of Al thin films. Quantita-

tive data was obtained combining the experiments with finite element method (FEM) modeling.

We introduced the subject matter in Chapter 1, and in Chapter 2 we described the experimental techniques. In particular we detailed a specialized TEM sample holder, which was used for *in situ* electrical probing and nanoindentation. The electron holography techniques were also explained in detail. The FEM was introduced in this chapter as well.

In Chapter 3, we studied CFE from a CCnT using a combination of electron holography and FEM. A focused ion beam (FIB) was used to extract the CCnT and to mount them on supports which were inserted into the specialized *in situ* TEM holder described in Section 2.2.2. Using the piezo-driven nanomanipulator, the CCnT was approached to a Au anode. A bias was increased between the anode and CCnT until the onset of field emission. For a tip radius of $r = 20$ nm and a tip-anode separation distance of $d = 680$ nm, the onset potential was $V = 80$ V.

The field emission current was recorded, and simultaneously, electron holography was used to measure the phase change of the electrons in the imaging beam. Coupling the phase shift from experiment with those from a FEM model, a quantitative value of the local electric field of $E_{\mathrm{loc}} = 2.55$ V/nm (for the above parameters) was found. Knowledge of the local electric field allowed the field enhancement factor γ to be determined. By combining experimentally determined values with the Fowler-Nordheim (F-N) equations, an exit work function of $\phi = 4.8 \pm 0.3$ eV of the CCnT could be obtained. This is a novel way in measuring the work function of a cold-field emitter.

Considering the superior field emission properties of a CCnT when compared with a carbon nanotube or W emitter, it has proven to be a possible candidate for the next generation of cold-FEGs.

In Chapter 4, a recently developed technique for counting elementary charge on nanoscopic samples was applied to the *in situ* field emission experiments. The evolution of charges was determined on a CCnT as the bias between the anode and the CCnT was increased. It was observed that after the onset of field emission, the number of charges saturated. Holographic measurements indicated that the electric field showed similar behavior. This is surprising, since at the same time the field emission current increased exponentially.

For Chapter 5, thin films were indented *in situ* using a specialized sample holder equipped with a piezo and a diamond tip mounted on a load cell. The sample comprised of Al thin films on oxidized Si wafers. A 1 μm passivation layer distributed an applied force onto the Al film, facilitating the observation. The sample was sculpted into an H-bar shape using a FIB. Such a structure allows the sample to be stable while at the same time having a large electron

transparent area.

With the load-cell equipped *in situ* holder, a force could be applied and measured. Radius of curvature calculations on the threading dislocations was utilized to estimate the local stress in the sample. With the force from the load-cell, a FEM model was created to compare the stress from the calculations, providing a good match.

Using the image force technique, it is possible to estimate the energy of dislocations close to an interface. Here, where the SiO_2 creates an interface with the Al film, interfacial dislocations should be repelled by the stiffer oxide, according to the inverse thickness dependence model of film strength. Contrary to this, interfacial dislocations were consumed by the interface. This had previously been observed during irradiation and heating experiments, but never at ambient temperature.

Interconnect durability is often linked to the failure of the interconnects. And the failure of interconnects is linked to the plasticity of the thin films. Therefore, it is of great importance to understand the plasticity of metallic thin films.

The power of *in situ* TEM allow us to better understand processes on the nano level. To be able to see changes in a sample while they happen, provides insight in how they function. But, results needs to be measurable. The combination of using a highly versatile *in situ* TEM holder, electron holography and finite element method modeling, observations could accurately be quantified.

A On mechanical and electrical probing

A.1 Comments on mechanical probing

In this section, a description of the nanoindenter microelectromechanical system (MEMS) force sensor and some comments on how to use it in an optimum way are covered.

A.1.1 Description of the force sensor

The MEMS sensor that was used for the force measurements, utilizes a capacitive force read-out. Figure A.1 (a) show a sketch of a nanoindenter MEMS sensor. The circle in the middle is the support for the diamond tip, which after the calibration process (see [Nafari et al., 2007]) is glued into place. The support structure and diamond tip hinges on eight Si springs. In (b), a cross-sectional view reveals the upper and lower capacitor plates (illustrated in red).

When a force is applied to the diamond tip, the distance between the plates will decrease, which changes the capacitance. After calibration, the change in capacitance can be translated into a force.

A detailed explanation of how the sensor was fabricated can be found in the PhD work of Alexandra Nafari [Nafari, 2010].

A.1.2 Recommendations when using the force sensor

A common problem when using a MEMS sensor with a capacitive force read-out is that the electrons from the beam can charge up the sensor, which thus is interpreted as an increase in force. Therefore the following points should be taken into account when using such a system:

1. Make sure to use a small electron dose while working in low magnification mode. Later, when the probe and sample are close to each other and

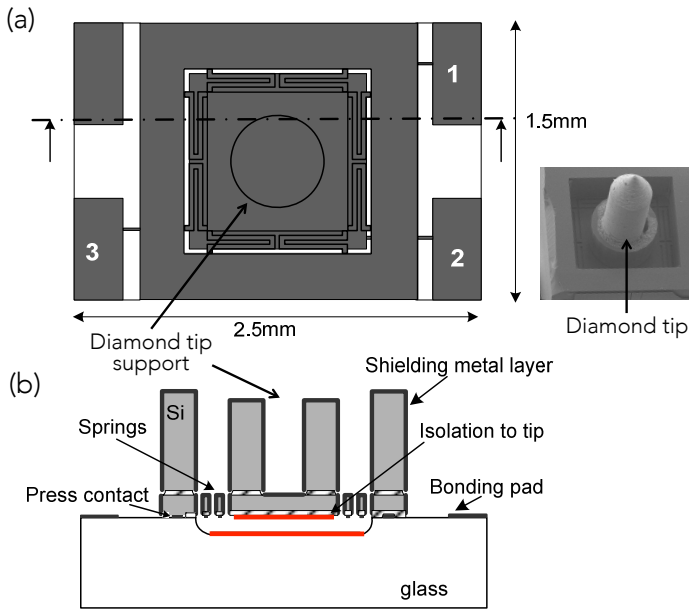

FIGURE A.1 – *Sketch of the MEMS sensor. (a) Top-view showing three contact pads and the eight Si springs that the diamond tip support and upper capacitive plate hinges on. The inset shows a SEM image of the diamond tip mounted in its support on the sensor. (b) Cross section view of (a). The two red lines illustrates the lower and upper capacitive plate. Image from PhD thesis of A. Nafari [Nafari, 2010].*

a higher magnification is used, the dose can be increased. For example, with the TEM used for these experiments, I started with spot size 8–9 and finished with spot size 1 at highest magnification (naturally the best condition has to be worked out for each TEM, since the electron dose largely depends also on the C2 aperture, extraction voltage, which type of gun, etcetera). The highest magnification used was around $\times 200\,000$.

2. In order to increase the diffraction contrast, the objective aperture can be inserted. The smaller the aperture the higher the contrast, with the trade–off being a decrease in resolution. The aperture plate, which consists of a plate with different sized holes (the apertures), is inserted just below the sample holder. If the plate is not well aligned, electrons hitting it will back-scatter onto the sensor, which accordingly will be charged. To align the plate, position it where the charging of the force-sensor is at a minimum. This should be done with the electron dose that is intended to be used.

A.1.3 Issues with sample bending

As mentioned in Chapter 5.3.2, when having a sample being too wide and/or thin, it will bend when a force is applied. Figure A.2 (a) is a post-indentation SEM top view micrograph, i.e., it shows a Si sample from the indentation direction. As is obvious, the sample is bent from the applied force due to a too wide and/or thin sample. The small crack in the middle shows the indentation mark from the wedge-shaped indentation tip. The width of the window is 10 μm and the force applied was in the tenth of μN range.

In Fig. A.2 (b), the effect of bending, much less than in (a), but still enough to make any observation possible, can be seen.

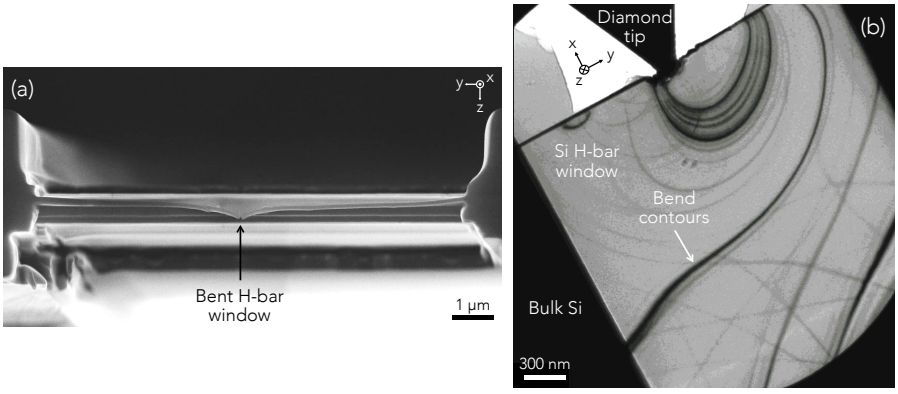

FIGURE A.2 – *(a) SEM micrograph of a 10 μm wide H-bar shaped sample, seen from the indentation direction. It being too wide, it bent even with a small applied force. (b) TEM micrograph of the H-bar shaped sample in Fig. 6.2. A force of around 20 μN was applied, resulting in a multitude of bend contours that obscured the observations.*

A.2 Comments on electrical probing

A.2.1 Cleaning the tip *in situ*

At times the thickness of the contamination and oxide layer requires the W tip to be heated to above its melting temperature* in order for the layer to be removed (see Fig. A.3). Here, the W tip was brought into contact to a Cu grid and the bias was increased until there was a break-through in the current (at around 15 V). This melted the W tip locally and consequently effectively removed the contamination layer.

*The melting temperature for bulk W is 3 422 °C.

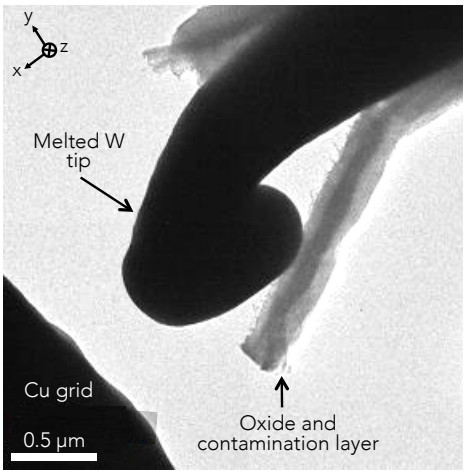

FIGURE A.3 – *A W tip that melted after a large current passed through it.*

The melted W tip in Fig. A.3 has a large tip radius, and might therefore not be functional for probing samples that are not easily accessible, e.g. multiple nanopillars separated by a short distance (see Fig. B.4 (c)). But for a free-standing sample it is usable, specially since all the contamination layer is guaranteed to have been removed on the entire surface of the end of the W probe.

A.2.2 Simulations of the field enhancement factor γ

As discussed in Section 3.8.3, the field enhancement factor is largely dependent on the tip-anode separation distance, which was shown in Fig. 3.22.

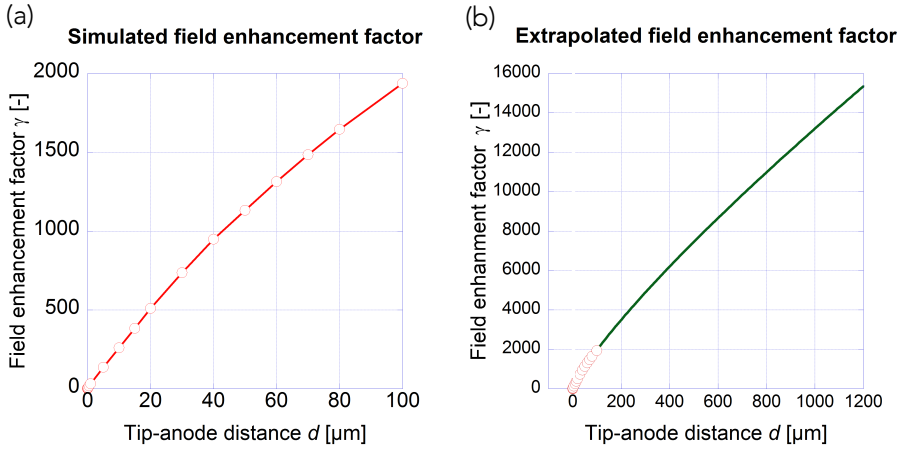

FIGURE A.4 – *The field enhancement factor γ as a function of the tip-anode separation distance d, for $r = 20$ nm and $V = 80$ V.*

The field enhancement factor γ in Fig. 3.22 was a magnified version of Fig. A.4 (a). In the latter, simulations for tip-anode separation distances of up to $d = 100\,\mu$m can be seen. In Fig. A.4 (b), an extrapolation of data in (a) show that for d equalling a couple of mm, a field enhancement factor $\gamma > 20\,000$ can easily be achieved. The simulations were made for a tip radius $r = 20$ nm and a potential on the anode of $V = 80$ V. Note that the extrapolation is only an indication, since the uncertainty of the values increases with d.

These plots show that it is necessary to specify the tip-anode separation distance (apart from the tip radius and applied voltage) when comparing different field-emission systems.

The plots could be useful to estimate the local electric field or field enhancement factor of similar systems.

B | Other experiments and sample preparation

The purpose of this section is to help other users of similar *in situ* TEM holders, by sharing some of the experiments and sample preparation that we have used.

B.1 Exploding tip during cold-field emission

In a cold-field emission gun, the distance between the emitting tip and anode is in the order of 10 mm. For the experiments performed here, the tip-anode separation distance was less than 1 μm.

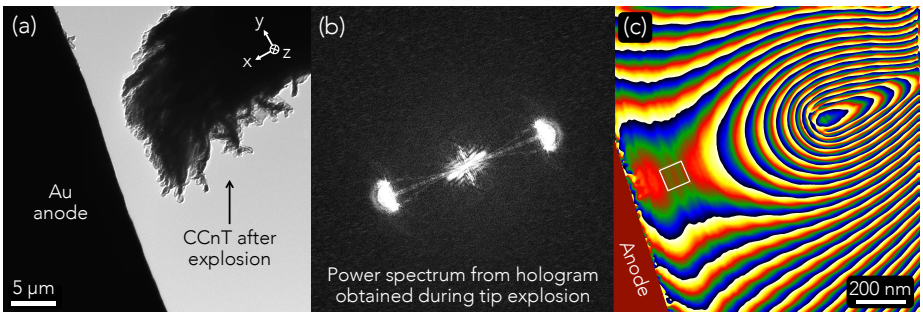

FIGURE B.1 – *(a) Remnants of the tip after explosion. (b) A 2x magnified power spectrum after Fourier transformation of a hologram that was recorded during the explosion. (c) The effect of the double-exposed hologram; one exposure with the biased tip in sight, and the other with the tip being out of sight, can be seen. The white box is the internal reference area.*

In one experiment, a tip-anode separation distance of only 320 nm was used. At the same time, the voltage on the anode was increased to 100 V until a field-emission current of 25 μA was reached. The results of that experiment can be seen in Fig. B.1 (a), which was that the tip exploded. A reason of this could

be a combination of a very strong local electric field and ion bombardment. With the extreme close proximity of the anode, anode degassing is important, thus creating a large number of ions bombarding the emitter.

The tip exploded about half-way in to the exposure of the hologram. Figure B.1 (b) show the Fourier transformation of the in-a-way doubly-exposed hologram. One exposure with the biased tip in sight, and the other after the explosion and the remnants of the tip was out of sight. In (c), the phase map created from (b) can be seen. Here, the effect of the double-exposure can clearly be seen from the undulating 2π phase jump lines. This accident has stimulated investigations into double-exposure holography (although in a more controlled way).

B.2 Charge measurements — Nanopillars for flash memory?

In Chapter 4 we showed how a newly developed technique was used to count elementary charges on a carbon cone nanotip (CCnT). Apart from a CCnT, we tried to use this technique also on other samples.

One idea was to use a W tip, mounted in the nanomanipulator in Fig. 2.1 totransfer charges to an Au island, which was isolated by a 5 nm SiO_2 layer. By using the technique described in Section 4.2 we should then be able to count the number of electrons that were transferred. If a sample on the nano-level could be charged and discharged this way, a possible future application could be for flash memory.

B.2.1 Sample preparation

The sample from where the nanopillars were created was made using chemical vapor deposition (CVD) techniques, comprising of a base of Si, followed by a 5 nm insulating SiO_2 layer and ending with a 75 nm layer of Au. The pillars were sculpted using a FIB-SEM.* See Fig. B.2, which also captions the FIB-implanted Ga-layer, which is a problem that will be discussed further down.

The W tip used for contacting the nanopillars was electro-mechanically etched using Kingswater, as explained in Section 3.3.3.

B.2.2 Preliminary results from nanopillars

Tungsten that has been exposed to air, is normally covered with a semiconducting layer of WO_3 [Xu et al., 1990].† To remove this, the experiment was

*The pillars were made by Rosa Córdoba at INA Zaragoza, Spain.

†Plus any contamination layer due to a prolonged exposure under the electron beam (as discussed in Section 3.3.1). See also Figs. A.3 and B.4 (b).

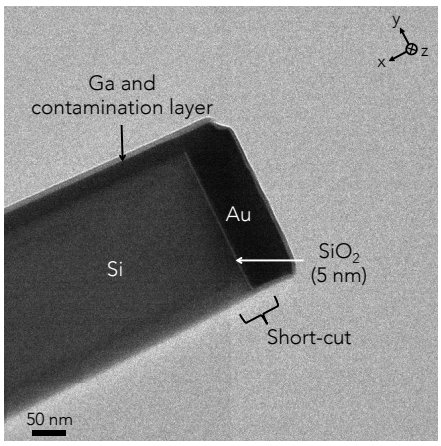

FIGURE B.2 – *TEM micrograph of the top section of the FIB-milled nanopillar.*

carried out by first contacting the Cu semi-grid that supported the nanopillars with the W tip and running a current through (see Section A.2.1).

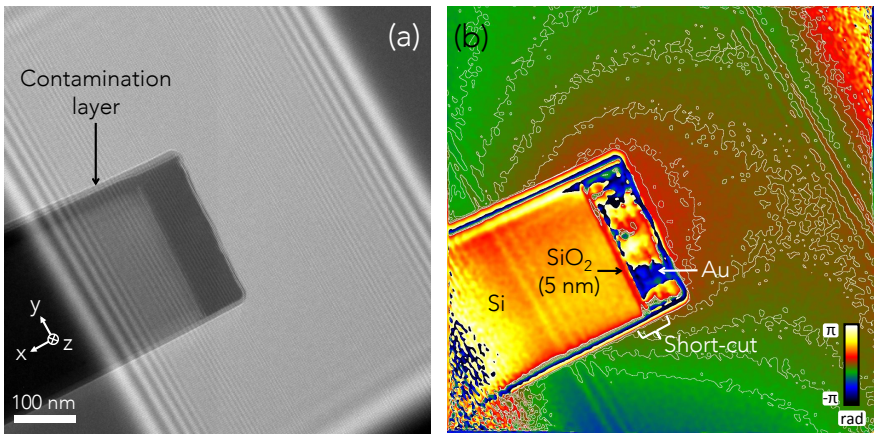

FIGURE B.3 – *(a) Hologram of the end of the nanopillar. (b) Phase shift image from the hologram in (a), after a potential of 10 V having been applied to the Au top.*

Secondly, the W probe was approached to the nanopillar, and lightly contacted to the Au top. Then, a bias of 5 V was applied followed by the tip being retracted and the recording of a hologram. Again, the tip was brought into contact, now with 10 V applied, retracted and a hologram recorded. This was repeated for a number of both positive and negative different potentials. As can be seen in Fig. B.3 (b), there is a phase shift from the electric field from the trapped charges, however, it is much smaller than expected. We believe the reason for this comes from a conductive layer covering the nanopillar, acting as

an escape path for the purposely trapped electrons. This most likely origins in a known problem of Ga implantation from the Ga^+ ion beam. Kiener et al. discuss this at length [Kiener et al., 2007], where they, using a TEM, discovered a 20% concentration of Ga several nm below the surface. Although the article focuses on the effects on the mechanical properties, others have found evidence of an conductive layer created by the FIB, as illustrated in Fig. B.2 [Cooper et al., 2006, Wolf et al., 2013, Cooper et al., 2009].

This work is in progress, but it looks promising. Further examples of samples that has been tried can be seen in Fig. B.4.

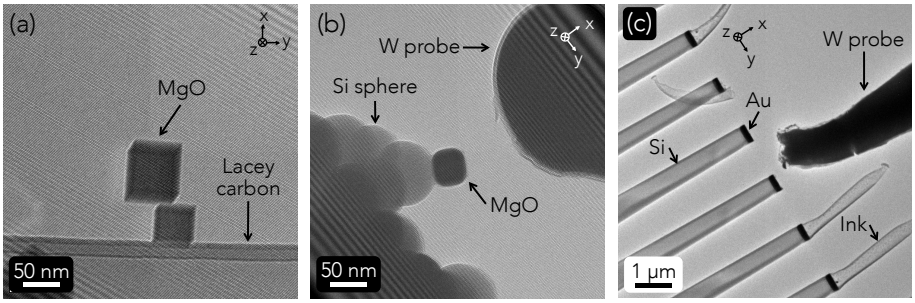

FIGURE B.4 – *(a) Hologram of MgO cubes on lacey carbon. (b) Hologram of MgO cubes on latex spheres. (c) TEM micrograph of Si pillars with Au deposited, with a protection layer of ink.*

In Fig. B.4 (a) MgO cubes were created and deposited on lacey carbon film by simply holding the carbon film over burning Mg. In (b), a MgO cube is sitting on top of Si spheres. A contamination and oxide layer on the W tip can be seen clearly as well. One problem with this setup was the deformation of the MgO cubes after a prolonged exposure under the electron beam. This can be seen in (b), where the corners of the MgO cube are rounded.

The sample in Fig. B.4 (c) was created by sputtering Au onto a Si substrate. Before a FIB was used to create pillar-shaped structures,* a protective layer of ink was used. As discussed in Section 6.1.1.2, removing the ink with a plasma cleaner did not work and therefore the probe was used to mechanically remove it. In (c), one can see how the ink has been completely removed on two and partially on one pillar. The problem with such a sample is similar to that of the nanopillars in Fig. B.2; a conductive layer probably created by the FIB, creates a short-circuit between the Au layer and the Si.

For future experiments, samples that are fabricated by electron beam lithography will be studied. This should circumvent the problem of a conductive layer providing an escape path for the charge.

*The pillars were made by Robin Cours at CEMES-CNRS.

C | Code and full list of abbreviations

C.1 The code for treating simulated phase maps

The instructions here describe how the simulated phase maps were treated using DigitalMicrograph (see Section 3.6.3.3).

1. In the exported COMSOL text-file, remove the header and the coordinates and replace all not-a-number entries with zeros, leaving only the phase shift data.
2. Import the data into DigitalMicrograph, using `Real 4 Byte` as `Data Type` and tick the options `Lines Are Rows` and `Get Size By Counting`.
3. Create a reference and a object half by dividing the phase map in two, with `Ctrl-C` and `Ctrl+Alt-V`.
4. Subtract the reference half from the object half, using the `Simple Math` functionality.
5. Use the script described below to remove the phase shift and phase gradient in the internal reference area.

```
// A script to treat COMSOL exports as holograms

number grad

// Gradient to remove internal reference area in simulated
phase map
grad = -0.075 // Iterate until the phase is zero in the
```

```
                    // internal reference area

// Removes the function of the reference area
// image phasemap = GetFrontImage()
phasemap = phasemap - grad*irow

// Normalize
phasemap = phasemap + 252.9 // The phase shift offset value

ShowImage(phasemap)
```

C.2 Complete list of symbols and abbreviations in Chapter 5

fcc	Face-centered cubic
CTE	Coefficient of thermal expansion
H_{f}	Film thickness
F_{b}	Force per unit length
μ_{f}	Shear modulus of film
μ_{s}	Shear modulus of substrate
$\mathbf{b}$	Burgers vector
b	Length of Burgers vector
d	Distance from dislocation to interface
$\mathbf{F}$	Externally applied force
A	Surface onto where $\mathbf{F}$ is applied; indentation surface
σ	Tensile or compressive stress
$\mathbf{n}$	Slip plane's normal
λ	Angle between $\mathbf{F}$ and $\mathbf{b}$
ϕ	Angle between $\mathbf{F}$ and $\mathbf{n}$
F_{s}	Shear force in the slip direction
A_{s}	Area of slip plane
τ	Resolved shear stress
S	Schmid factor
α	Angle between sample surface and the indentation surface A
β_{s}	Substrate constant in the Nix model
ν	Poisson's ration
σ_{Nix0}	Tensile stress in derivation of the Nix model
μ_{eff}	Effective shear modulus
μ_{o}	Shear modulus of oxide
β_{o}	Oxide constant in the Nix model
h_{o}	Thickness of oxide
σ_{Nix}	Tensile stress according to the Nix model
GB	Grain boundary
E_{f}	Young's modulus of film
ν_{f}	Poisson's ratio of film
λ_{L}	Lamé's first constant
E_{o}	Young's modulus of oxide
ν_{o}	Poisson's ratio of oxide
E_{AlO}	Young's modulus of Al_2O_3
ν_{AlO}	Poisson's ratio of Al_2O_3
σ_{v}	Von Mises stress

$s1$	Sample 1
t_{s1}	Thickness of sample 1
r	Radius of dislocation
a	Unit cell length for Al
r_{proj}	Projected radius of dislocation
$\tau_{\mathrm{rad}_{\mathrm{s1}}}$	Shear stress from radius of curvature calculations, sample s_1
$\sigma_{\mathrm{rad}_{\mathrm{s1}}}$	Compressive stress from radius of curvature calculations, sample s_1
τ_{int}	Shear stress from internal stress
τ_{ext}	Shear stress from externally applied force
$\mathbf{F}_{\mathrm{net}_{\mathrm{s1}}}$	Net force creating stress on dislocation, sample s_1
$\mathbf{F}_2$	Externally applied force on 2^{nd} position on dislocation, sample s_1
$\mathbf{F}_{\mathrm{net2}_{\mathrm{s1}}}$	Net force creating stress on dislocation, 2^{nd} position, sample s_1
$\sigma_{\mathrm{rad2}_{\mathrm{s1}}}$	Compressive stress, radius of curvature calculations, 2^{nd} position, sample s_1
$\sigma_{\mathrm{FEM}_{\mathrm{s1}}}$	Compressive stress from FEM, sample $s1$
$\sigma_{\mathrm{FEM2}_{\mathrm{s1}}}$	Compressive stress from FEM, 2^{nd} position, sample $s1$
$\sigma_{\mathrm{Nix}_{\mathrm{s1}}}$	Stress from the Nix model, sample $s1$
μ_{AlO}	Shear modulus of AlO
$\sigma_{\mathrm{Nix}'_{\mathrm{s1}}}$	Stress from modified Nix model, sample $s1$
$s2$	Sample 2
$s3$	Sample 3
t_{s2}	Thickness of sample 2
$r_{\mathrm{proj}_{\mathrm{s2}}}$	Projected radius of curvature, sample $s2$
$\tau_{\mathrm{max}_{\mathrm{s2}}}$	Maximum shear stress from radius of curvature calculation, sample $s2$
$\sigma_{\mathrm{rad}_{\mathrm{s2}}}$	Compressive stress from radius of curvature calculations, sample $s2$
$\sigma_{\mathrm{FEM}_{\mathrm{s2}}}$	Compressive stress from FEM, sample $s2$
$k_{\mu_{\mathrm{im}\perp 1}}$	Shear modulus term, image dislocation 1, sample $s2$
$F_{\mathrm{b}_{\mathrm{im}\perp 1}}$	Force per unit length, image dislocation 1, sample $s2$
$\tau_{\mathrm{im}\perp 1}$	Shear stress, image dislocation 1, sample $s2$
$k_{\mu_{\mathrm{im}\perp 2}}$	Shear modulus term, image dislocation 2, sample $s2$
$F_{\mathrm{b}_{\mathrm{im}\perp 2}}$	Force per unit length, image dislocation 2, sample $s2$
$\tau_{\mathrm{im}\perp 2}$	Shear stress, image dislocation 2, sample $s2$
$\tau_{\mathrm{im}_{\mathrm{s2}}}$	Shear stress from image force, sample $s2$
$\sigma_{\mathrm{ext}_{\mathrm{s2}}}$	Compressive stress at interface from FEM, sample $s2$
$\tau_{\mathrm{ext}_{\mathrm{s2}}}$	Shear stress from FEM, sample $s2$
t_{s3}	Thickness of sample 3
$\tau_{\mathrm{rad}_{\mathrm{s3}}}$	Shear stress from radius of curvature calculations, sample $s3$
$\sigma_{\mathrm{rad}_{\mathrm{s3}}}$	Compressive stress from radius of curvature calculations, sample $s3$
$\sigma_{\mathrm{FEM}_{\mathrm{s3}}}$	Compressive stress from FEM, sample $s3$

$\tau_{\mathrm{im_{s3}}}$	Shear stress from image force, sample $s3$
$\tau_{\mathrm{ext_{s3}}}$	Shear stress at interface from FEM, sample $s3$
MD	Molecular dynamics
$\tau_{\mathrm{rad_{si}}}$	Shear stress, radius of curvature calculations, sample si, i $= 1, 2, 3$
$\sigma_{\mathrm{rad_{si}}}$	Compressive stress, radius of curvature calculations, sample si, i $= 1, 2, 3$
$\tau_{\mathrm{int_{si}}}$	Shear stress from internal stress, sample si, i $= 1, 2, 3$
$\tau_{\mathrm{ext_{si}}}$	Shear stress from externally applied force, sample si, i $= 1, 2, 3$
$\mathbf{F}_{\mathrm{net_{s1}}}$	Net force creating stress on dislocation, sample s1
$\mathbf{F}_2$	Externally applied force on 2^{nd} position on dislocation, sample s1
$\mathbf{F}_{\mathrm{net2_{s1}}}$	Net force creating stress on dislocation, 2^{nd} position, sample s1
$\sigma_{\mathrm{FEM_{si}}}$	Compressive stress from FEM, sample si, i $= 1, 2, 3$
$\tau_{\mathrm{im_{s2,3}}}$	Shear stress from image force, sample s2, 3
$\sigma_{\mathrm{ext_{s2,3}}}$	Compressive stress at interface from FEM, sample s2, 3

D | Résumé en français

THIS chapter is a summary in French of this thesis. All images and text have been extracted from the chapters above.

D.1 Introduction

En Octobre 2005, j'ai participé à l'école européenne de microscopie électronique quantitative (QEM2009) sur la Côte d'Azur comme représentant des ventes pour l'entreprise Nanofactory Instruments (Suède) que j'avais rejointe seulement trois semaines plus tôt. Au cours de cette école, j'ai eu une discussion sur un projet de collaboration pour un nouveau type de porte-objet *in situ* avec Martin Hÿtch et Marc Legros du CEMES de Toulouse. En Janvier 2010, je suis venu au CEMES dans le cadre de l'achat de ce porte-objet pour la formation sur son utilisation. Huit mois plus tard, j'ai quitté mon poste pour commencer une thèse à Toulouse autour de ce porte-objet.

La microscopie électronique en transmission (MET) est un outil très performant pour étudier les matériaux à l'échelle nanométrique. Le plus souvent utilisée dans les expériences statiques, la MET permet également d'étudier directement la réponse d'un échantillon sous une sollicitation extérieure. Cette MET *in situ* permet une meilleure compréhension des propriétés de l'échantillon.

Les techniques *in situ* ont été développées dès le début de la MET. Dans un premier temps, le faisceau d'électrons a été utilisé pour des expériences d'irradiation ou de chauffage. D'importants progrès ont eu lieu dans le développement de porte-objets MET dédiés à des expériences *in situ*. Par exemple, il est possible de chauffer l'échantillon dans le microscope ou d'observer des phases liquides à l'aide de dispositifs adaptés. Les systèmes d'injections de gaz dans la colonne associés à un pompage différentiel permettent l'étude

de la croissance cristalline en phases vapeur et liquide ou bien les mécanismes d'oxydo-réduction; les systèmes micro-électromécaniques (MEMS) et dispositifs push-pull servent à appliquer et mesurer des forces mécaniques, ou bien une différence de potentiel pour mesurer la conductivité ou étudier l'électromigration. La présence de biprismes électrostatiques dans le microscope rend possible l'holographie électronique avec laquelle les champs magnétiques, électriques et de contrainte peuvent être observées. Le développement récent comprend des fibres optiques à l'intérieur des porte-objets ou directement dans la colonne permettent par exemple d'étudier la cathodoluminescence. En utilisant un laser pulsé à l'intérieur du canon électronique, il est possible d'obtenir des impulsions du faisceau d'électrons pour des mesures résolues en temps. Un bon et récent examen des différentes techniques est présenté dans le livre *In-situ Electron Microscopy*, édité par Dehm, Howe et Zweck [Dehm et al., 2012]. L'état de l'art est couvert en début de chaque section.

Dans cette thèse sur la microscopie électronique *in situ*, nous allons nous concentrer sur la nanoindentation et les mesures locales de champ électrique. Nous tenterons d'aller au-delà de la principale limitation de la MET *in situ* en quantifiant nos résultats. Pour cela, nous avons utilisé un porte-objet possédant des éléments piezo-électriques MEMS, un capteur de charge pour appliquer et mesurer une force mécanique, et un système destiné à enregistrer les mesures. En utilisant l'holographie électronique et la modélisation avec ce porte-objet, les données obtenues seront entièrement quantifiées.

Ce résumé est divisé de la façon suivante. Après cette section introductive, la préparation des échantillons et les techniques expérimentales sont décrites dans la Section D.2. Nous détaillerons ici le principe du fonctionnement du porte-objet *in situ* que j'ai utilisé et les techniques d'holographie électronique.

Les deux sections suivantes présenteront les résultats de l'émission de champ d'électrons par nanopointe constituée de nanocônes de carbone (CCnT). Plus précisément, la Section D.3 concerne l'étude des paramètres importants de l'émission de champ, et la section Section D.4 donne les résultats du comptage des charges élémentaires avant et pendant le début de l'émission de champ, grâce à une technique développée récemment.

La Section D.5 présente la déformation plastique d'un film mince d'oxyde d'aluminium déposé sur un substrat de silicium. Dans ce système, les dislocations d'interface semblent être absorbées par des interfaces d'un matériau plus rigide. Différents calculs de rayons de courbure ont été effectués pour vérifier les modèles d'éléments finis utilisés afin d'obtenir une cartographie de la contrainte mécanique dans le film.

Dans ce travail de thèse où j'ai eu l'occasion de collaborer avec plusieurs

personnes du CEMES, j'étais responsable de la manipulation et du contrôle du porte-objet *in situ* pour les expériences en MET. Concernant la préparation des échantillons, j'ai extrait les pointes de CCnT et utilisé le FIB (Focused Ion Beam) pour fixer ces nanopointes sur une pointe de tungstène. J'ai réalisé toute la modélisation présentée dans cette thèse et extrait les phases des hologrammes exceptés dans certains cas où certains de mes collègues m'ont apporté leur aide (leurs contributions sont mentionnées dans les parties concernées).

D.2 Techniques expérimentales

Ici, est décrit le porte-objet original utilisé pour la MET *in situ*.*

D.2.1 Le porte-échantillon MET *in situ*

Le porte-objet MET *in situ* (voir Fig. D.1) utilisé pour cette thèse est un produit commercial développé dans le cadre d'un projet de collaboration entre le CEMES et Nanofactory Instruments. Il est possible de l'utiliser pour étudier les propriétés électriques ou pour la nanoindentation. On peut ainsi appliquer jusqu'à 140 V entre une sonde et l'échantillon, et mesurer la force mécanique créer par une pointe de diamant sur l'échantillon en utilisant des capteurs micro-électromécaniques (MEMS). Pluisieurs capteurs de différentes plages de force ont été utilisés, avec des constantes de ressort de capteurs variant entre 450 N/m et 5000 N/m (ce qui correspond également à peu près à la force maximale en μN). Le seuil de bruit dépend du capteur, mais varie généralement de 0,5 à 3 μN.

La possibilité de double inclinaison (double-tilt) associée aus mesures électriques et mécaniques rend ce porte-objet unique: l'échantillon peut être incliné de $\pm 4^\circ$ autour d'un deuxième axe (l'inclinaison autour de l'axe principal, parallèle à l'axe du porte-objet est obtenue par la platine goniométrique du MET). Cette deuxième rotation est réalisée par un moteur pas à pas piézoélectrique, fixé à l'arrière du porte-objet. Il contrôle une tige et une plaque qui transfère le mouvement vers l'avant. Dans la partie avant, un cadre interne qui contient la partie tubulaire piézo-électrique, l'échantillon et le capteur, est incliné dans son ensemble. Ce cadre interne peut être vu dans la partie inférieure de la Fig. D.1. La longue armature intérieure associée à l'espace très restreint entre les pièces polaires du MET, explique le nombre limité l'inclinaison.

Le porte-objet dispose d'un système à déplacement piézo-électrique avec lequel le mouvement grossier et fin est contrôlé, du millimètre au nanomètre.

*Pour plus d'informations en anglais sur le polissage mécanique, la préparation par faisceau d'ions focalisé et la MET, voir les Sections 2.1.1, 2.1.2 and 2.2.1.

Ceci sera expliqué en détail dans la section suivante.

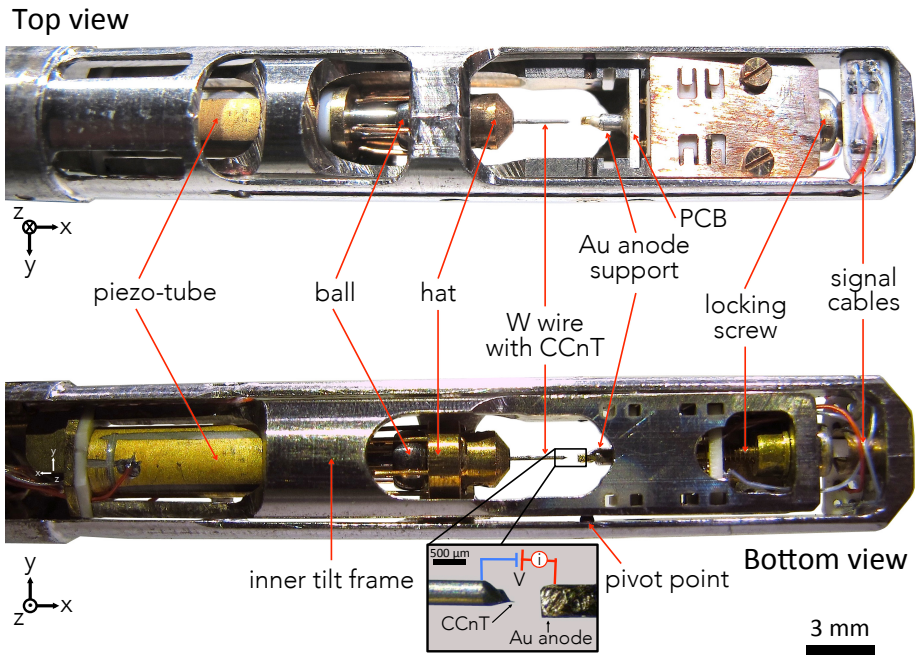

FIGURE D.1 – *La partie avant du support, ici configuré pour sonder les propriétés électriques. Le nanomanipulateur, qui comprend les tubes piezo-électriques, les billes et un chapeau supportant le fil de W, où une nanopointe à base de nanocônes de carbone (CCnT) est soudée dessus, est présenté dans les deux photographies ci-dessus. On place la nanopointe CCnT et l'anode de Au dans le tube fixé sur la carte de circuit imprimé (PCB). La vis de blocage fixe le PCB et s'assure que les contacts entre les câbles de signaux et le PCB sont bons. Sur la figure du bas, nous pouvons voir un des deux points pivot autour desquels tourne le bâti intérieur, permettant ainsi une inclinaison de $\pm 4°$. Dans la vue du dessous un schéma du circuit électrique est illustrée entre la CCnT et l'anode. La définition des directions x, y, z avec le faisceau électronique (parallèle à la direction z) utilisé pour l'imagerie, sera la même tout au long de cette thèse.*

D.3 Émission de champ froid d'une nanopointe constituée de nanocônes de carbone

L'émission de champ d'électrons a d'abord été observée par Wood en 1897 [Wood, 1897]. Lorsqu'un champ électrique suffisamment fort est présent autour d'une cathode, les électrons sont extraits par effet tunnel à travers la barrière de potentiel métal/vide. Lorsque ce phénomène apparait sur une cath-

ode à température ambiante, l'émission électronique de champ est dite froide (CFE). La barrière de potentiel joue un rôle significatif dans le processus et une partie de celui-ci constitue la fonction de travail de sortie ϕ. Un autre paramètre important pour une cathode en forme de pointe est la propreté et la planéité de sa surface. Etant donné que ces paramètres sont critiques pour l'apparition de l'émission de champ, ce travail s'est focalisé sur eux.*

En 1923, Schottky a observé la diminution de la barrière tunnel dans un fort champ électrique (effet Schottky) [Schottky, 1914]. Millikan et Lauritsen découvrent en 1929 que le logarithme du courant électronique d'émission de champ froid présente un comportement linéaire en fonction du champ électrique appliqué [Millikan and Lauritsen, 1928].

Toujours en 1929, Fowler et Nordheim ont décrit les phénomènes théoriquement et obtenu l'équation dite de Fowler-Nordheim (FN) [Fowler and Nordheim, 1928]. Müller créé un projecteur à émission de champ en 1936 [Müller, 1936], alors que Crewe et al. sont été les premiers à réaliser la CFE à des tensions élevées en 1968 [Crewe et al., 1968].

L'émission de champ concerne une large gamme d'applications, allant du dispositif qui permet d'assurer la neutralité électrique du fuselage des fusées ou des avions à des systèmes microélectroniques pour l'émission de courant sur de larges zones ou à l'intérieur des canons d'émission de champ froid afin d'obtenir un faisceau d'électrons présentant une forte cohérence pour l'interférométrie. L'étude présentée dans cette thèse a concerné l'utilisation d'un nouveau type de matériau carboné comme émetteur. L'objectif est d'améliorer considérablement les propriétés de la pointe du C-FEG. Nous avons donc utilisé le porte-échantillon dédié à la MET *in situ* afin d'appliquer une différence de potentiel suffisante entre l'anode et la pointe qui constitue la cathode pour étudier *in situ* par holographie électronique l'émission de champ froide des nanocônes de carbone. Grâce à l'holographie électronique combinée à la modélisation par éléments finis (FEM), nous avons établi des cartographies quantitatives du champ électrique local E_{loc} autour de la pointe d'émission. La corrélation de ces résultats avec les mesures de courants d'émission et l'équation FN a permis de mesurer la fonction de travail de sortie ϕ du CCnT. Ce travail présente une nouvelle façon à d'obtenir une émission de champ froide et d'en déterminer les paramètres importants.

D.3.1 Des matériaux carbonés pour l'émission de champ froide

À la suite de sa découverte par Iijima en 1991 [Iijima, 1991], les nanotubes de carbone (CNTs), et des structures de carbone similaires ont fait l'objet de nom-

*Une explication complète en anglais sur l'émission d'électrons peut être trouvé dans la Section 3.2.

breuses études en raison des applications possibles. L'une d'entre elles concerne l'émission de champ froide. En 1998 [Wang et al., 1998] et 2000 [Saito and Uemura, 2000], des écrans à émission de champ ont été développés en utilisant les CNTs en tant que sources d'émission d'électrons. D'autres travaux ont utilisé des matrices [Collins and Zettl, 1997], des fils à parois multiples [Chen et al., 2009] ou de films minces [Obraztsov et al., 2000, Sinitsyn et al., 1997, Nilsson et al., 2001a, Nilsson et al., 2001b] constitués de nanotubes de carbone pour étudier émission de champ* Pour une présentation de l'émission de champ froide à partir de nanotubes de carbone, se reporter de Jonge et Bonard [de Jonge and Bonard, 2004].

Nous allons nous concentrer uniquement sur l'utilisation de matériaux à base de carbone pur l'émission de champ à l'intérieur d'un C-FEG. La première réalisation d'un tel canon a été faite en 1995 par de Heer et al. avec un FEG à haute intensité d'un film de nanotubes de carbone alignés [de Heer et al., 1995].

Le CNT a des propriétés remarquables qui en font un choix excellent pur l'émission de champ froide. Tout d'abord leur rapport d'aspect (ratio longueur /largeur) élevé et le petit rayon (apex) augmente considérablement le champ électrique local assurant ainsi une tension d'extraction faible pour démarrer le processus d'émission. Ils sont chimiquement moins réactifs que le tungstène utilisé habituellement dans les pointes standards, évitant de cette façon que les adsorbants se fixent sur la pointe et perturbent. le processus d'émission. Ils possèdent également une résistance mécanique élevée et sont capables d'émettre une grande quantité d'électrons avec des propriétés uniformes. En 2002, de Jonge et al. ont présenté la CFE à partir d'un seul CNT [de Jonge et al., 2002], suivie de nombreuses autres études [Bonard et al., 2001, Collins and Zettl, 1996, de Heer et al., 1995, de Jonge, 2009, de Jonge and Bonard, 2004, de Jonge et al., 2005, Zhou et al., 2001].

Néanmoins, les CNTs souffrent de quelques problèmes importants. Premièrement, leur énorme rapport d'aspect les rend vulnérables aux vibrations, effet à éviter absolument dans un C-FEG [Gao et al., 2001]. En second lieu, ils sont petits et difficiles à manipuler, inconvénients dans le cas d'une future commercialisation.

Le type de structure de carbone avec laquelle nous avons travaillé dans cette thèse est une pointe à base de nanocônes de carbone (CCnTs) développés par Jacobsen et Monthioux en 1997 [Jacobsen and Monthioux, 1997]. Ils

*Beaucoup plus d'articles existent sur le sujet, par exemple [Bonard et al., 2002b, Dean and Chalamala, 2000, Dean and Chalamala, 1999b, Dean and Chalamala, 1999a, Dean et al., 1999, Fransen et al., 1999b, Gröning et al., 2000, Hazra et al., 2011, Jin et al., 2005, de Jonge and van Druten, 2003, de Jonge et al., 2004, Kim et al., 2011, Kokkorakis et al., 2002, Luo et al., 2002, Ribaya et al., 2008, Rinzler, 1995, Saito et al., 2005, Sanchez et al., 2007, Solá et al., 2009, Sveningsson et al., 2005, Yuge et al., 2012].

présentent une grande base de forme conique qui se termine avec une pointe de taille nanométrique. La forme conique évite les vibrations et la base permet une manipulation aisée. En d'autres termes, les CCnTs résout les problèmes posés par les CNTs pour l'émission de champ froide tout en conservant leurs propriétés favorables.

Les CCnTs ont été employés pour fonctionner dans un microscope électronique Hitachi HF2000 modifié [Houdellier et al., 2012]. Après avoir été montés sur un support classique de tungstène dans un C-FEG, nous avons obtenu un courant d'émission froide des CCnTs. Ce nouveau type de canon a présenté des performances remarquables une très grande monochromaticité (écart de faible énergie), une luminosité et une stabilité élevées ainsi qu'une durée d'émission accrue.

Dans un récent article, l'holographie électronique a été utilisé pour étudier *in situ* le changement de potentiel sur une jonction pn dans des nanofils de silicium biaisés en utilisant un porte-échantillon similaire à celui de cette thèse [He et al., 2013].

Enfin Cumings et al. ont publié un article y pionnier précédant le travail effectué dans cette thèse [Cumings et al., 2002]. Ils ont combiné l'holographie électronique *in situ* avec de la modélisation afin de déterminer quantitativement le champ électrique. Ils ont déterminé et discuté les fluctuations du courant d'émission de champ de nanotubes de carbone.

D.3.2 Matériels et méthodes

D.3.2.1 Production de la nanopointe de nanocônes de carbone (CCnT)

Les CCnT ont été présentés par de Jacobsen et Monthioux [Jacobsen and Monthioux, 1997] en 1997. Leur forme est singulière, avec une grande base dans la gamme du micromètre constitué d'un empilements de feuilles de graphène, suivis par deux cônes lisses de carbone sur les côtés, terminés par une extrémité très effilée dans la gamme du nanomètre, voire par un CNT.

Les CCnTs sont produits par un procédé catalytique afin de créer des nanofilaments de carbone d'un diamètre d'environ 5 nm. Ce procédé est suivi d'un second dépôt de carbone sur les filaments en utilisant un dépôt chimique en phase vapeur à une température de 1 300 °C [Jacobsen and Monthioux, 1997, Allouche et al., 2003].

D.3.3 Holographie électronique *in situ*

D.3.3.1 Traitement des hologrammes

J'ai utilisé une méthode développée au CEMES pour éliminer les déphasages indésirables provenant principalement des distorsions du système d'acquisition (caméra CCD) et des lentilles projecteurs. De plus j'ai supprimé numériquement les franges de Fresnel (F_f) dues à la diffraction de l'onde électronique sur les bords du biprisme électrostatique et isolé la contribution du potentiel interne du CCnT (V_{MIP}) au déphasage. Ainsi seul reste la contribution électrostatique provenant de la différence de potentiel appliquée entre le CCnT et l'anode de Au.

D.3.3.2 Déphasage de l'holographie électronique

Le début de l'émission de champ commence pour une tension appliquée de 80 V, ce qui correspond à la valeur seuil mesurée dans la courbe $i_e(V)$. J'ai donc choisi cette valeur de potentiel pour comparer l'image de phase expérimentale et celle simulée par éléments finis.

Ce choix a été fait pour la raison suivante: après l'apparition de l'émission de champ, les électrons émis vont diminuer le champ électrique local, ce qui ne peut être pris en compte dans notre modèle simulé. L'impact sur le déphasage et le champ électrique *après* le début de l'émission de champ sera détaillé sur la Section D.4.1.1.

Pour calculer le déphasage total du faisceau électronique, les sauts de phase 2π sur l'image de la Fig. D.2 (c) ont été supprimés: nous obtenons ainsi un déphasage comme présenté par la Fig. D.3 (a). Un profil du déphasage représenté par la flèche blanche est donné à la Fig. D.3 (a). La zone entourée par les pointillés à droite de la figure Fig. D.3 (a) schématise la position de la pointe constituée de CCnT alors que le carré blanc à gauche l'indique la zone de référence choisie pour l'origine du déphasage. La Fig. D.3 (b) correspond au gradient de la figure Fig. D.2 (c) et fournit des informations qualitatives du champ électrique autour de la pointe. La légende a été ajoutée seulement à titre indicatif.

D.3.4 Émission de champ *in situ* et l'équation de Fowler-Nordheim

Le Figure D.4 montre la courbe d'émission de champ $i_e(V)$ registrée au même momentque les hologrammes. Plus précisément, nous avons augmenté la tension V sur l'anode par pas de 1 V seconde et seules les mesures faites au cours de la première seconde après l'augmentation de la tension ont été conservées. Les hologrammes ont également été enregistrés juste après le pas tension. Le

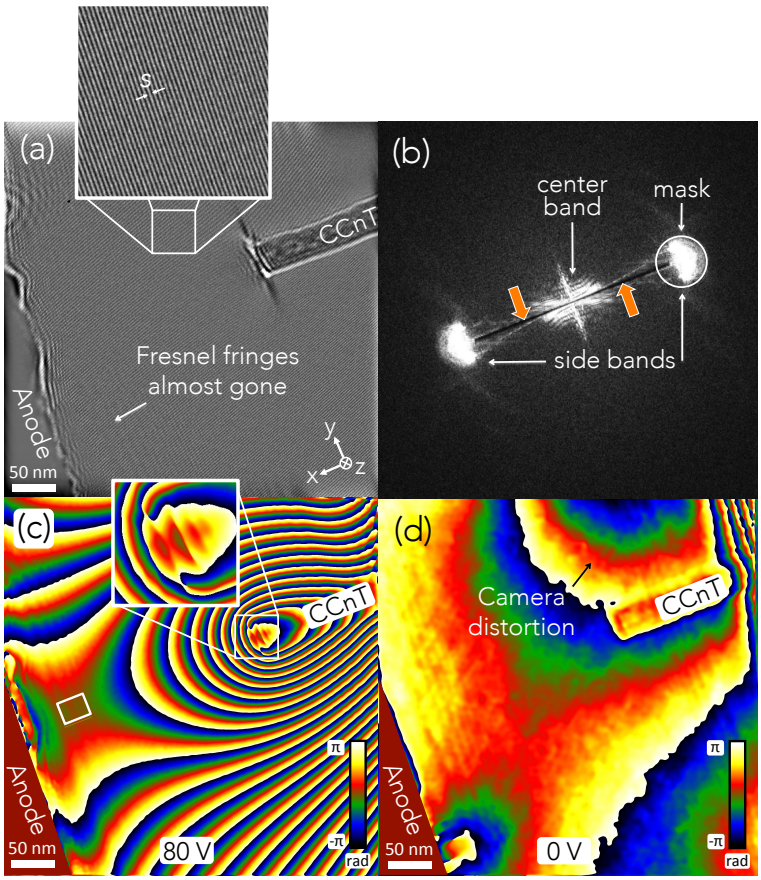

FIGURE D.2 – *(a) Hologramme donts les franges de Fresnel ont été supprimées numériquement. En (b), transformée de Fourier de l'hologramme où les flèches oranges indiquent les zones qui contenaient avant les franges de Fresnel. (c) Image de phase à 80 V: les principales distorsions ainsi que la contribution du MIP au déphasage ont été supprimées. Le zoom sur l'extrémité de la pointe sera discutée plus tard. (d) Image de phase à 0 V contenant les principales distorsions et la contribution du MIP. En résumé, l'image de phase en (c) contient seulement la contribution électrostatique qui nous intéresse, alors que l'image de phase en (d) contient toutes les contributions au déphasage devant être retirées.*

courant d'émission de champ apparait seulement à partir de 80 V, raison pour laquelle l'axe des abscisses de la figure E.4 débute à cette valeur. L'encart présente une courbe de Fowler-Nordheim réalisée en traçant $\ln(i_e/V^2)$ en fonction de $1/V$ (V variant de 80 V à 96 V).

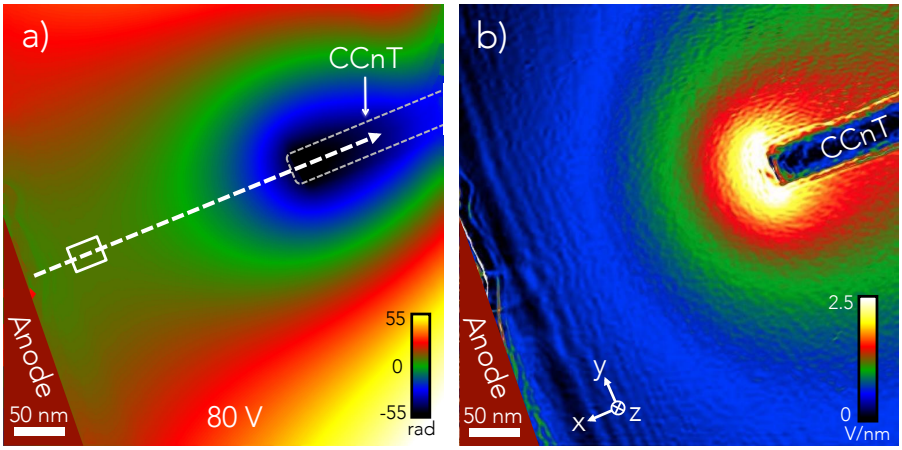

FIGURE D.3 – *(a) La carte de phase déroulée de la Fig. D.2 (c) avec la flèche en pointillés représentant la position et la direction de l'endroit où le profil de décalage de phase est obtenu (voir Fig. D.5). En (b), le gradient de la même, ce qui représente qualitativement le champ électrique.*

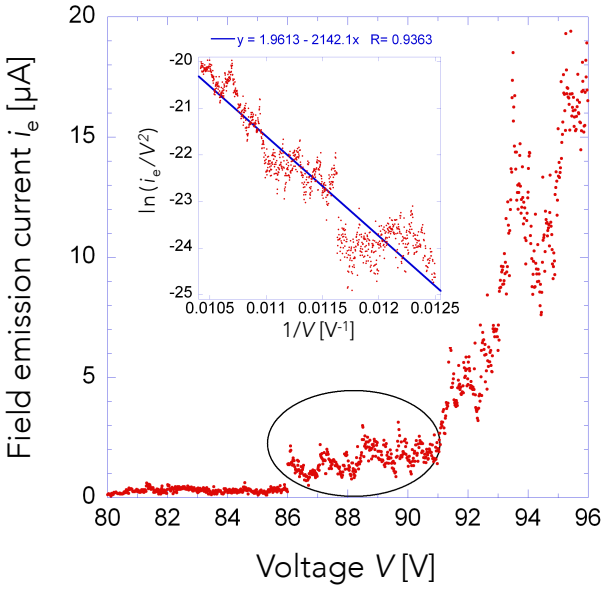

FIGURE D.4 – *Courbe $i_e(V)$ mesurée à partir du début de l'émission de champ à 80 V. L'encart correspond au tracé de Fowler-Nordheim: la ligne bleue montre le comportement linéaire de l'équation de Fowler-Nordheim.*

D.3.4.1 Facteur d'amplification du champ γ

Un des avantages de l'équation (D.1) de Fowler-Nordheim est d'obtenir le champ local E_{loc} autour de la pointe d'émission [Bonard et al., 2002b]. Le

courant d'émission de champ est décrit par:

$$i_{\mathrm{e}} = A\frac{1.54\times10^{-6}}{\phi}\left(\frac{V}{d}\right)^{2}\gamma^{2}\exp\left(\frac{10.4}{\sqrt{\phi}}\right)\exp\left(-\frac{6.44\times10^{9}\phi^{3/2}d}{V\gamma}\right) \quad \text{(D.1)}$$

Le champ local est amplifié autour de la pointe par rapport à une situation avec des plaques conductrices parallèles. Si l'on compare ce champ local avec le champ électrique de référence à partir de deux plaques parallèles, $E_{||} = V/d$, V étant la tension appliquée et d la distance de séparation, le champ est augmenté par un facteur γ exprimé par:

$$E_{\mathrm{loc}} = \gamma E_{||} = \gamma\frac{V}{d}. \quad \text{(D.2)}$$

Nous allons utiliser ces équations pour trouver la fonction de travail ϕ de la pointe CCnT. Ceci est possible car $-\frac{6.44\times10^{9}\phi^{3/2}d}{\gamma}$ correspond à la pente de la partie logarithmique de l'équation de FN dans la Fig. D.4 [Bonard et al., 2002b]. Et, connaissant V et d (facilement mesurable dans le MET), seul γ doit être trouvé pour obtenir le déphasage ϕ. De équation D.2, nous voyons que si nous déterminons le électrique local E_{loc}, nous aurons γ. Et pour obtenir ce champ électrique local, nous utiliserons les simulations par FEM et l'holographie électronique (EH), comme détaillé dans la section suivante. En d'autres termes,

$$\mathrm{FEM} + \mathrm{EH} \Longrightarrow E_{\mathrm{loc}} \overset{\text{Eq. D.2}}{\Longrightarrow} \gamma \overset{\text{Eq. D.1}}{\Longrightarrow} \phi. \quad \text{(D.3)}$$

D.3.5 Modélisation par éléments finis

La modélisation par éléments finis a été utilisé pour créer un modèle du système étudié. J'ai utilisé pour cela le logiciel COMSOL Multiphysics de COMSOL AB. Diverses simulations de convergence ont été faites afin de s'assurer la validité du modèle.*

D.3.6 Résultats

Dans cette section, nous allons comparer le déphasage des hologrammes et à celui des simulations. Puis nous corrélerons ces résultats avec l'équation de FN afin d'obtenir la fonction de travail ϕ de la CCnT.

D.3.6.1 Comparaison du déphasage entre les résultats expérimentaux de l'holographie électronique et les simulations par FEM

En comparant le déphasage de l'holographie électronique à celui des simulations par FEM (Fig. D.5), nous obtenons un excellent accord entre les données

*Explication détaillée en anglais sur ce qui peut être trouvé dans la Section D.3.5.

expérimentales et simulées. Non seulement les valeurs mais aussi les formes des courbes correspondent parfaitement (voir la Section D.3.6.3 pour l'analyse des erreurs possibles). L'ajustement est d'autant plus remarquable la coupe n'a pas été ajustée. C'est-à-dire que les paramètres comme le rayon de la pointe ou la valeur de la tension n'ont pas été modifiés pour obtenir le meilleur ajustement. Avoir cet accord, nous nous assurons de la validité du modèle et que le champ électrique modélisé correspond au champ électrique expérimental, avec $E_{\text{loc}} = 2.55$ V/nm.

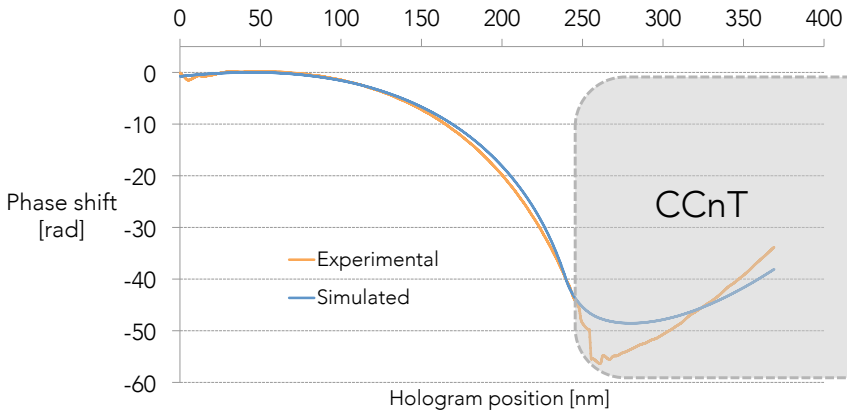

FIGURE D.5 – *Profils du déphasage expérimental (orange) et du déphasage simulé (bleu). La zone grisée indique la position de la pointe CCnT.*

Ayant maintenant une valeur quantitative du champ électrique local, nous pouvons obtenir la fonction de travail, de la manière suivante.

D.3.6.2 Travail de sortie ϕ

De équation D.2 nous obtenons le facteur d'amplification de champ

$$\gamma = \frac{d}{V} E_{\text{loc}} \tag{D.4}$$

et avec $E_{\text{loc}} = 2.55$ V/nm, $V = 80$ V et $d = 680$ nm nous constatons que $\gamma = 21.7$*. La théorie de F-N donne que:

$$-\frac{6.44 \times 10^9 \phi^{3/2} d}{\gamma} = \text{Pente sur l'équation de F-N.} \tag{D.5}$$

*D'autres travaux où le facteur d'amplification du champ de petits émetteurs a été discuté peuvent être trouvés dans les articles suivants [Pogorelov et al., 2009, Huang et al., 2005, Smith and Silva, 2009, Smith et al., 2005, Wang et al., 2004, Zeng et al., 2009].

Les données présentées dans l'encart de la Fig. D.4 peuvent être liées par une fonction linéaire dont les paramètres sont

$$y = 1.96 - 2142x,\ R = 0.9363 \tag{D.6}$$

où $y = \ln(i_e/V^2)$, $x = 1/V$ and R représente l'erreur dans l'approximation linéaire. En combiant les équations D.5 et D.6, nous obtenons

$$\phi = \left(\frac{2\,142\,\gamma}{6.44 \times 10^9\, d}\right)^{2/3} = \left(\frac{2\,142 \cdot 21.7}{6.44 \times 10^9 \cdot 680 \times 10^{-9}}\right)^{2/3} = 4.83\,\text{eV}. \tag{D.7}$$

D.3.6.3 Discussion — Analyse d'erreur de ϕ

Pour analyser l'erreur relative sur la mesure de la fonction de travail, il faut connaître l'incertitude de certains paramètres utilisés dans le modèle. Tout d'abord la précision de mesure du rayon de la pointe est connue au nanomètre près: $r = 20 \pm 11$ nm. Ensuite, à cause de l' irrégularité de la surface de l'anode, et de l'effet de l'alose-effet aussi lié à l'erreur typique d'agrandissement du TEM de 2 %, nous estimons la distance de séparation pointe – anode à $d = 680 \pm 10$ nm. Pour diminuer l'incertitude provenant de l'occultation de l'anode, la pointe CCnT a été légèrement mise en contact de l'anode avant d'être rétractée à la distance de séparation souhaitée.* A partir des résultats des simulations de convergence, l'erreur à partir de la diminution de la taille de l'anode modèle est d'environ 2 %. Toutes ces erreurs créent une imprécision de 4 % du champ électrique local simulé, c'est-à-dire $E_{\text{loc}} = 2.55 \pm 0.1$. Avec la prise en compte de ces erreurs dans l'équation D.4, nous arrivons à un facteur d'amplification du champ électrique de $\gamma = 21.7 \pm 0.8$.

Une contribution possible à l'erreur de l'équation de FN est de savoir si ou non tous les électrons émis sont collectés par la petite anode, et donc si le courant mesuré est réellement le courant émis par la pointe. Cependant compte tenu de la proximité de la pointe CCnT à l'anode, séparés seulement par 680 nm, nous supposons l'effet négligeable. L'erreur sur la forme de la courbe de F-N a été estimée à environ 7%. Ainsi, en combinant $\gamma = 21.7 \pm 0.8$ avec la pente de la courbe de FN $= 2\,142 \pm 138$ et en utilisant les extrémités des deux dans l'équation D.7, on obtient que $\phi = 4.8 \pm 0.3$ eV.

Enfin, une discussion sur l'effet que la charge d'espace peut avoir sur le courant d'émission de champ i_e et le champ électrique local E_{loc} est donnée dans la Section D.4.1.1.

*Dans le même temps nous nous nous sommes assurés que la pointe CCnT a été placée à peu près au milieu en face de l'anode.

D.3.7 Résumé et conclusion

Nous avons combiné différentes techniques d'une manière nouvelle afin d'extraire les paramètres importants d'un nouveau type de pointe en carbone pour l'émission de champ. Habituellement, lorsque l'équation de FN est utilisée pour extraire le champ électrique local E_{loc}, il est nécessaire de connaître soit le facteur d'augmentation du champ γ, soit le travail de sorti ϕ [Nilsson et al., 2001a, Bonard et al., 2002b, de Jonge and Bonard, 2004, Bonard et al., 2002a]. Dans notre cas, à partir de la même expérience, nous avons accédé à E_{loc}, γ, la distance d pointe - anode, le courant d'émission de champ i_{e} et, le résultat le plus important, au travail de sortie $\phi = 4.8 \pm 0.3$ eV, sans faire d'hypothèses sur aucun des paramètres. La valeur quantitative du champ électrique local a été obtenue en comparant le déphasage expérimental à celui issu d'une modélisation. Dans cette expérience, une valeur de début pour l'émission de champ d'$E_{\mathrm{loc}} = 2.55$ V/nm a été déterminée.

Pour les expériences à venir, nous allons travailler avec le nouveau microscope I^{2}TEM, dédié aux études d'interférométrie électronique et de MET *in situ*. Ce microscope développé par Hitachi présente plusieurs particularités qui en font une machine unique ouvrant de nouvelles perspectives avec, par example; le canon FEG froid permet de créer des faisceaux de très fortes cohérences spatiale et temporelle; quatre biprismes permettent de s'affranchir des franges de Fresnel et ouvrent la possibilité de créer différentes configurations d'interférométrie, et deux goniomètres pour placer l'échantillon à deux endroits différents de la colonne.

Nous souhaitons mesurer le courant d'émission $i_{\mathrm{e}}(V)$ en acquérant simultanément les hologrammes. Cela permettra de déterminer la fonction de travail avec une moindre erreur. Par exemple, en supprimant l'erreur sur la pente de la courbe de FN (voir Fig. D.4 et équation D.6) nous pourrions réduire l'erreur de 0.3 à 0.1 eV.

Il serait également intéressant de réaliser le même travail (expérience et simulations) pour une pointe constituée W utilisée dans les C-FEG standards. Les résultats obtenus pourraient être comparés directement à ceux obtenus par d'autres techniques.

D.3.7.1 Utilisation d'une pointe de nanocônes de carbone dans un C-FEG?

Un canon C-FEG équipé d'une pointe CCnT avec une très forte brillance serait d'une très grande utilité pour l'holographie électronique par exemple, car le contraste des franges holographiques dépendent fortement de la cohérence spatiale des électrons. Cela est particulièrement intéressant pour l'holographie en champ sombre en raison des faibles intensités des faisceaux diffractés.

Un brevet sur un tel C-FEG a déjà été déposé par Houdellier et al. qui ont obtenus des résultats très probants [Houdellier et al., 2012]. Pour cela ils ont modifié un microscope Hitachi HF2000 C-FEG afin d'intégrer un CCnT en tant que pointe émettrice. Parmis leurs résultats remarquables, ils ont montré que ce type de canon présente une brillance six fois plus élevée (1.6×10^9 A m^{-2} sr^{-1} V^{-1}), une dispersion en énergie bien plus faible (0.32 eV) et une meilleure stabilité à long terme (la pente d'amortissement est inférieure à 16 % par heure), par rapport au même microscope HF2000 équipé d'un C-FEG classique (W).

D.4 Mesures de charges

L'holographie électronique peut être utilisée non seulement pour mesurer le champ électrique, mais aussi comptabiliser les charges élémentaires. En utilisant une méthode développée récemment [Gatel et al., 2013] avec laquelle une précision d'une unité élémentaire de charge (1.6×10^{-19}) a été atteinte, nous allons dans cette section mesurer le nombre de charges élémentaires sur une nanopointe de nanocônes de carbone (CCnT).

Pour cela, nous avons utilisé les hologrammes de la pointe CCnT obtenus lors des mesures *in situ* présentées à la Section D.3 afin de calculer la répartition et le nombre de charges au sommet de la pointe CCnT avant et après le début de l'émission de champ.

D.4.1 Introduction

L'holographie électronique est utilisée depuis un certain temps pour mesurer les charges sur des nano-objets [Chen et al., 1989, Cherns and Jiao, 2001, Chung et al., 2011]. Ces mesures sont indirectes, c'est-à-dire qu'elles s'appuient sur la modélisation du potentiel électrostatique. Beleggia et al. ont proposé une méthode pour mesurer directement les charges à l'échelle nanométrique en utilisant la loi de Gauss [Beleggia et al., 2011], travail poursuivi et complété par Gatel et al. [Gatel et al., 2013].

D.4.1.1 Résultats de la CCnT

Le nombre d'électrons augmente avec la tension appliquée. Mais, lorsque l'émission de champ commencé à 80 V, ce nombre d'électrons commence à saturer. à 80 et 95 V, on obtient respectivement les valeurs de 1193 ± 5 e$^-$ et 1233 ± 5 e$^-$.

Le Figure D.6 représente le nombre d'électrons dans la partie avant de la pointe CCnT en fonction de la tension. On peut ici voir clairement que, au le

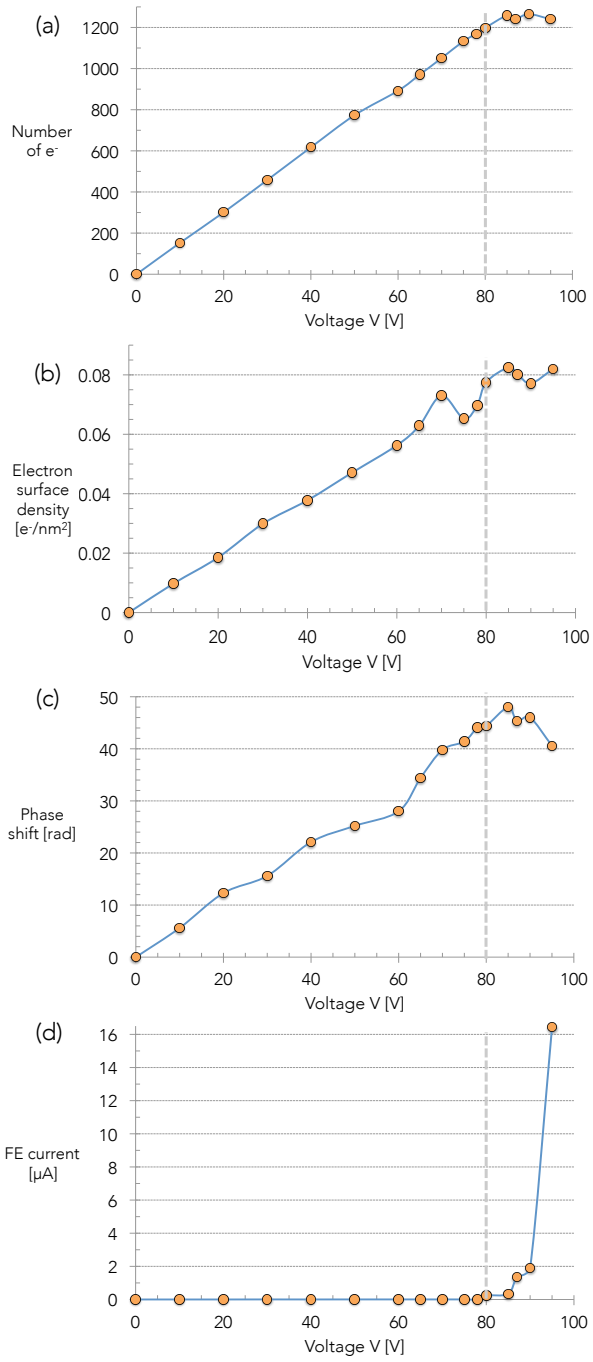

FIGURE D.6 – *(a) Nombre total d'électrons, (b) densité surfacique d'électrons dans la partie avant de la pointe CCnT, (c) le déphasage et (d) le courant de lémission de champ en fonction de la tension appliquée. La ligne en pointillés gris marque le début de de lémission de champ.*

début de l'émission de champ, ou juste après, un plateau est atteint. La Figure D.6 montre que la valeur moyenne de la densité surfacique de charge dans les 5 derniers nm de la CCnT est constante comme bien. Non seulement le nombre de charges, mais aussi le déphasage semble resté constant après le début de l'émission de champ, comme on peut le voir sur la Fig. D.6 (c).

D'après la Fig. D.6, le courant d'émission de champ augmente même après le début de l'émission de champ, en raison de l'augmentation de la tension appliquée. C'est-à-dire que la densité de charge est constante, tandis que simultanément la densité de courant croît de façon exponentielle.

D.4.2 Discussion

Comme on l'a vu dans la Fig. D.6, le nombre de charges dans la pointe CCnT tend vers une valeur de saturation lorsque l'émission de champ commence. Il est possible que tout excès de charge soit immédiatement émis une fois le processus d'émission de champ enclenché. Il ne serait plus alors possible d'accumuler des charges supplémentaires sur la pointe. Comme les nanotubes de carbone et les CCnTs sont des conducteur [de Knoop et al., 2005], les électrons se répartissent sur la surface.

La tension appliquée entre l'anode et la pointe (cathode), liée au champ électrique total E_0, continue à être augmentée après le début de l'émission de champ. Comme des électrons sont émis localement, le champ électrique doit être affecté. Etant donné que le nombre d'électrons dans la pointe CCnT reste constant d'après le début de l'émission de champ (Fig. D.6), le champ électrique autour de la pointe E_{loc} devrait également rester constant. Celui-ci à son tour affecte le déphasage mesuré à partir des images de phase. Nos résultats montrent que cela semble être le cas, avec un déphasage qui présente un plateau comme le montre la Fig. D.6 (c).

D'après la Fig. D.6 (d), nous observons une augmentation exponentielle du courant d'émission tandis que la densité de charge sur la pointe CCnT reste constante. La seule explication que nous pouvons avancer est que la pointe CCnT se charge et se décharge à un fréquence plus élevée, c'est à dire, la vitesse de dérive des électrons augmente de façon exponentielle.*

Il est curieux que le champ électrique local E_{loc} reste constant (Fig. D.6), alors que le courant d'émission augmente (d). Avec une valeur de E_{loc} convergente, la largeur et la hauteur de la barrière tunnel devraient aussi converger vers une valeur constante. Là encore, une augmentation de la vitesse de dérive des électrons peut expliquer l'augmentation actuelle de l'émission. Il convient de préciser que Hazra et al. ont trouvé que, pour des champs électriques élevés,

*A titre de référence, la vitesse de dérive, c'est-à la vitesse à laquelle se déplacent les électrons, dans un fil de Cu, est de l'ordre 300 μm/s.

la largeur de la barrière tunnel atteint une valeur à peu près constante [Hazra et al., 2011]. Mais ils conclu que l'effet serait de le courant d'émission, ce qui n'est pas un phénomène que nous avons vu.

Il existe un autre effet qui limite à la fois le courant d'émission et le champ électrique local dans l'émission de champ pour des valeurs élevées du champ électrique. Cet effet appelé la charge d'espace. Comme le courant d'émission augmente, le champ électrique dû à la charge d'espace écrante en partie la cathode et donc l'accélération globale des électrons créé par le champ électrique E_0 [Schamber, 1999]. La cathode sera écrantée à un niveau tel que le courant et donc le champ électrique local E_{loc} présentera une saturation. Il devient donc nécessaire d'augmenter la tension appliquée afin de conserver le même champ électrique [Anderson, 1993]. D'autres travaux expérimentaux ont constaté que la charge d'espace apparaît pour des densités de courant supérieures à 6×10^6 A/cm^2 [Dyke and Trolan, 1953,Barbour et al., 1953,Batrakov et al., 1999]. Nous ne connaissons pas la taille de la source virtuelle de la CCnT, et nous ne pouvons pas alors calculer cette densité de courant. D'ailleurs, nous n'avons pas observé cet effet.

D.4.3 Conclusion

Nous avons appliqué une méthode récemment développée pour comptabiliser le nombre de charges élémentaires directement sur une pointe CCnT. Nous avons constaté que, après une augmentation linéaire de la densité de charge avec la tension appliquée entre l'anode et la cathode, un plateau est atteint au début de l'émission de champ. Le déphasage mesuré présente un comportement similaire, indiquant que le champ électrique local est aussi saturé. Ce phénomène n'est pas encore bien compris et d'autres études sont prévues afin de pouvoir interpréter complètement les résultats.

D.5 Déformation plastique en MET *in situ* d'un film mince d'Aluminium

Les matériaux sous forme de films minces ont envahi la vie de notre quotidien sous la forme de revêtements durs (outils, produits céramiques), de filtres optiques (lunettes, pare-brise) ou des couches de protection (zinc ou aciers recouverts). Ce sont souvent des structures techniquement avancées, qui, une fois empilées, peuvent fournir les propriétés souhaitées pour une application donnée [Freund and Suresh, 2003].

En microélectronique, les films minces métallique, oxyde ou semi-conducteurs sont souvent lithographiés après leur dépôt pour obtenir des disposi-

tifs complexes avec des fonctions spécifiques. Lors de la fabrication, qui implique différents procédés de dépôt (physico-chimiques, température, pression), déformation et contrainte internes se développent dans la structure artificielle [Josell et al., 2002]. Leur impact en microélectronique peut être négatif (délamination, défaillances [Ciappa, 2002]) ou positifs (porteurs plus rapides dans le Si contraint [Welser et al., 1994]).

D.5.1 Introduction — Résistance mécanique des films minces métalliques

Ici, nous allons nous concentrer sur les films minces métalliques. Notamment ceux dont la structure est cubique à face centrée (fcc) tels que Cu, Al ou Au et qui sont souvent utilisés sous la forme d'interconnexions dans les dispositifs microélectroniques. Dans la plupart de ces dispositifs, la puissance électrique provoque un réchauffement de l'ensemble du composant par effet Joule. Avec l'intégration accrue et les réductions d'échelle, les concentrations de puissance et l'évacuation de la chaleur deviennent un problème. Mécaniquement, les cycles thermiques provoquent des contraintes qui proviennent de la différence de coefficient de dilatation thermique (CTE) entre les métaux, les oxydes et les pièces semi-conductrices. Le métal est la partie la plus déformable, avec le plus grand CTE, et a donc tendance à se déformer plastiquement en premier. Les essais thermo-mécaniques macroscopiques habituels sont effectués en utilisant une expérience dite de la courbure; la contrainte induite dans le film métallique dilaté lors des cycles thermiques impose un rayon de courbure au substrat. La relation entre ce rayon et la contrainte biaxiale dans le film est donnée par la formule Stoney [Flinn et al., 1987, Flinn, 1991, Stoney, 1909, Janssen et al., 2009]. Pour la plupart des films métalliques étudiés par cette méthode, un fort effet de taille a été trouvé; plus mince est le film, plus la contrainte nécessaire pour le déformer plastiquement est élevée. Pour mesurer cette limite d'élasticité (la "résistance" du film), on peut se référer à l'écart au comportement élastique dans les courbes contrainte – température, mais cela renvoie deux valeurs, l'une pour la partie chauffage et une deuxième pour le refroidissement. La plupart des auteurs ont donc considéré la contrainte à température ambiante comme la "résistance mécanique" du film, même si cette valeur n'est pas normalisée. Cela n'a à priori rien à voir avec une limite d'élasticité [Saada et al., 2007], cependant, une diminution progressive de l'amplitude des cycles thermiques (d'un maximum de 500°C généralement jusqu'à 200°C) montre que cette contrainte est maintenue même si la déformation plastique vu par le film est réduite à zéro (Legros in [Ponchet et al., 2011]). Une étude récente sur la résistance mécanique de plusieurs films sur des substrats peut être trouvée dans [Wiederhirn, 2007], où la contrainte à température ambiante après un cy-

cle thermique est normalisée par le module de cisaillement de chaque métal. Cela montre une claire augmentation de cette contrainte en $1/h_{\mathrm{f}}$, increase, h_{f} étant l'épaisseur du film (voir Fig. D.7) Les films libres, testés en traction ou en utilisant des tests de gonflement [Kalkman et al., 2001, Vlassak and Nix, 1992] montrent également une augmentation de la contrainte, mais pas autant que les films sur substrat. Cette augmentation est souvent liée à la taille du grain qui suis généralement l'épaisseur du film. Récemment, il a été constaté que les films Mg autoportants ne montrent pas d'augmentation du leur résistance mécanique [Sharon et al., 2014].

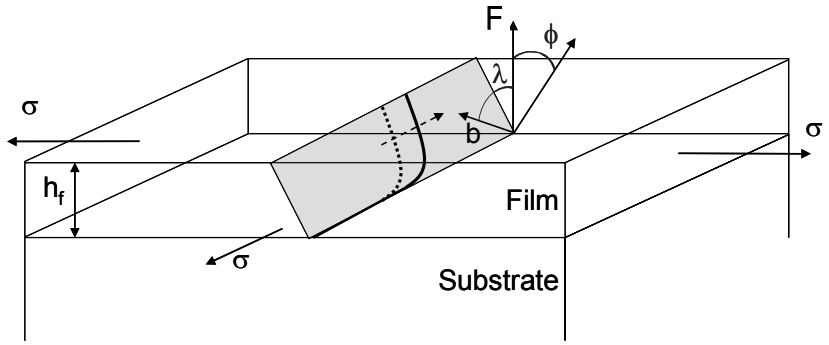

FIGURE D.7 – *Croquis montrant le modèle de Nix. La dislocation traversante dépose une dislocation interfaciale à l'interface couche/substrat [Nix, 1989].*

Le rôle du substrat dans la résistance mécanique du film est donc d'une importance primordiale, et, suite à l'analyse de Matthews et Blakeslee [Matthews and Blakeslee, 1974, Matthews and Blakeslee, 1975] pour les semiconducteurs épitaxiés, un calcul basé sur les dislocations traversantes, interfaciales et les forces image a été fait en supposant que la déformation plastique du film mince se fait par propagation de dislocations dans les plans (111). Chacune d'entre elles dépose une dislocation d'interface à l'intersection du plan de glissement et de l'interface. C'est l'énergie de cette dislocation d'interface, qui dépend essentiellement de sa distance à la surface, qui donne une dépendance en $1/h_{\mathrm{f}}$ de la contrainte critique.

D.5.2 Résultats de l'échantillon $\mathrm{s2}$

La deuxième échantillon "en H" $\mathrm{s2}$ avait une épaisseur $t_{\mathrm{s2}} = 220$ nm et une largeur de $3\,\mu$m.

D.5.2.1 Contrainte mesurée à partir du rayon de courbure dans l'échantillon s2

La figure D.8 affiche des instantanés extraits d'un film enregistré lors de l'indentation en MET *in situ* de l'échantillon s2. La séquence (a) – (c) montre comment un dislocation traversante se déplace vers l'interface Al/SiO_2 sous l'effet de l'augmentation de la force appliquée. On peut voir l'évolution correspondante de la force mesurée par la cellule de force du porte-objet en (e). La flèche en (a) indique comment la dislocation est momentanément entravée par un obstacle avant d'être libérée.

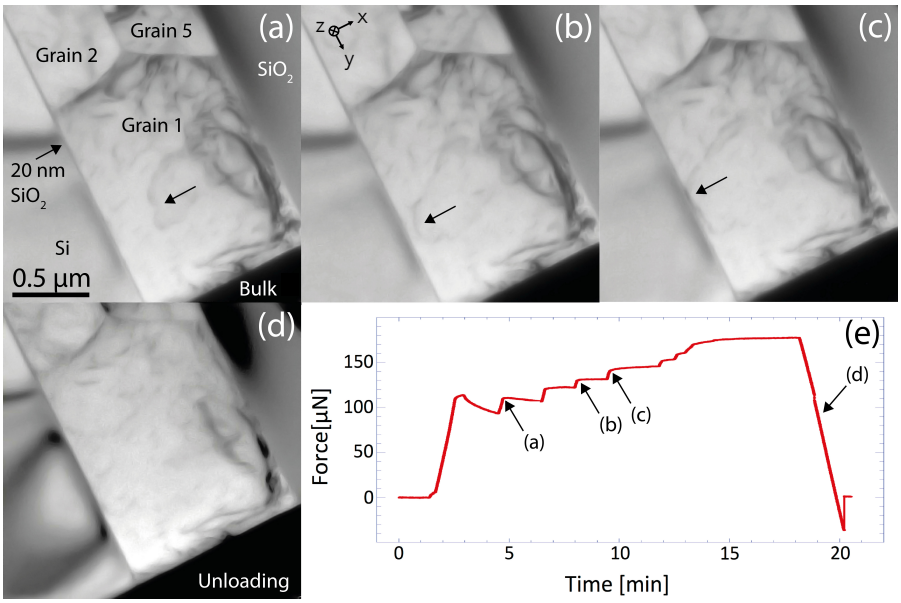

FIGURE D.8 – *Echantillon* s2. *Séquence d'indentation en MET in situ indiquant le mouvement d'une dislocation traversante vers l'interface* Al/SiO_2 *(a) – (c) Dislocation se déplaçant vers l'interface sous l'augmentation de la contrainte. (d) Après interaction avec l'interface cristal/amorphe et la suppression de la contrainte, la dislocation ne revient pas en arrière. (e) Enregistrement de la force au cours de la séquence d'indentation.*

A partir de la Fig. D.8, le rayon de la dislocation a été estimé à $r_{\mathrm{proj}_{\mathrm{s2}}} = 150 \pm 20$ nm. Ici, la dislocation n'interagit pas avec les interfaces Al/AlO (les deux surfaces de l'échantillon), donc nous n'avons pas pu mesurer un rayon de dislocation équivalent à celui obtenu précédemment. Autrement dit, le rayon réel pourrait être plus grand et donc la valeur obtenue plus faible. En utilisant cette $\tau = \frac{\mu_{\mathrm{f}} b}{r}$ nous avons donc obtenu une limite supérieure de la contrainte de cisaillement $\tau_{\mathrm{max}_{\mathrm{s2}}} = 51 \pm 7$ MPa.

Pour cette expérience, nous n'avons pas observé de glissement dévié. Par

conséquent, nous n'avons pas pu déterminer sans ambiguïté le vecteur de Burgers. Mais nous avons supposé que, comme dans les expériences précédentes, le système de glissement avec le plus grand facteur Schmid a été activé, c'est-à-dire, $S \lesssim 0.5$ et de $\sigma = \tau/S$, on obtient que

$$\sigma_{\mathrm{rad_{s2}}} \approx 100 \pm 15 \text{ MPa}. \tag{D.8}$$

D.5.2.2 FEM de l'échantillon s2

Un modèle aux éléments finis (FEM) de l'échantillon a été construit. L'indentation ne se produisant pas exactement au milieu, une moitié et non pas un quart de l'échantillon a été modélisée. Le mouvement de dislocation ayant eu lieu à côté de la partie épaisse du silicium, nous avons utilisé la contrainte de von Mises.

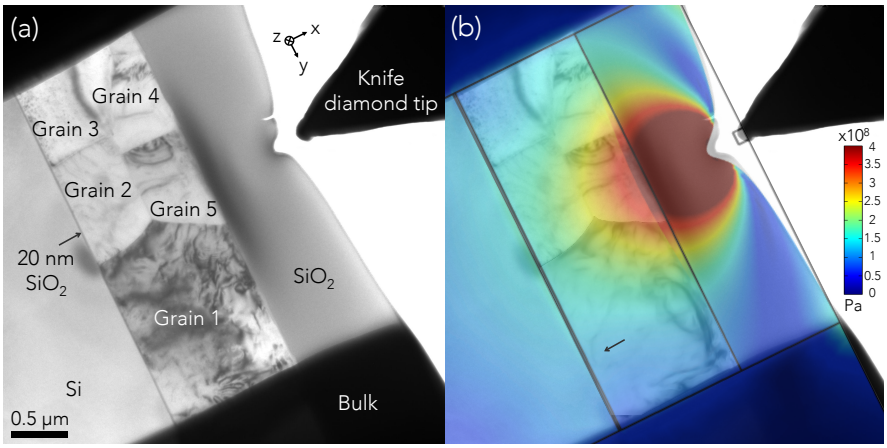

FIGURE D.9 – *Une expérience d'indentation où une force de 131 μN a été appliquée, où (a) montre la micrographie MET après l'expérience et (b) la simulation. A noter que la simulation montre la réponse à un moment où la force a été appliquée et non pas après, comme en (a). Autrement dit, la relaxation élastique se produisant en (a) pendant le déchargement n'a pas été représentée sur (b).*

En corrélant le film enregistré avec l'évolution de la force de la Fig. D.8 (e), on peut remonter à la force appliquée au moment où la dislocation est courbée dans la Fig. D.8 (b) soit 131 μN. En utilisant la force comme valeur d'entrée pour le modèle FEM, une carte du champ de contrainte a été créée. Dans la Fig. D.9 (a) une micrographie MET peut être vue après un cycle d'indentation. En (b), la carte FEM de la contrainte a été superposée à l'image (a). La figure (b) montre également la superposition des grains 1 de la Fig. D.8 (b), avec la dislocation traversante indiquée par la flèche. La contrainte de compression

dans la zone de mouvement de dislocation déduite du modèle est:

$$\sigma_{\mathrm{FEM_{s2}}} = 118 \pm 10 \text{ MPa}. \tag{D.9}$$

C'est-à-dire, $\sigma_{\mathrm{FEM_{s2}}} \approx \sigma_{\mathrm{rad_{s2}}}$.

D.5.2.3 Force image dans l'échantillon s2

Comme on peut le voir sur la Fig. D.8 (e) la charge augmente dans (b) – (c). En (c), une partie de la dislocation est bloquée avant l'interface Al/SiO_2, tandis que l'autre partie continue dans l'interface. Cela ne devrait pas se produire puisque une dislocation qui se rapproche d'une interface avec un matériau plus rigide subit une force répulsive que l'on peut estimer à l'aide des forces image.

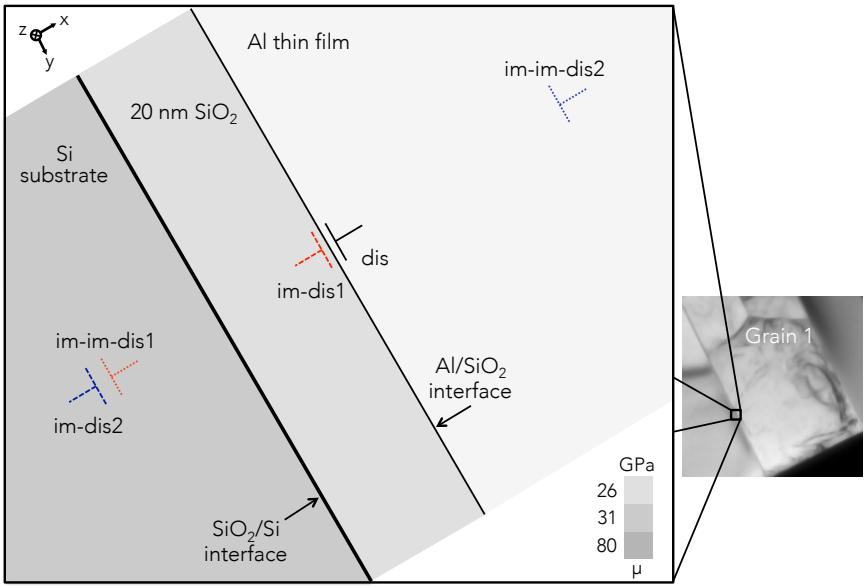

FIGURE D.10 – *Croquis montrant la notion de dislocations d'image.* dis *signifie dislocation et* im *pour image. La configuration est celle sur les échantillons utilisés dans cette section.*

L'équation D.10 décrit la force de l'image F_{b} par unité de longueur qu'une dislocation image exerce sur une dislocation vis située en face de son image. La dislocation image est située à la même distance de l'interface Al/SiO_2 que la véritable dislocation.

$$F_{\mathrm{b}} = -\frac{\mu_{\mathrm{f}} b^2 k_\mu}{4\pi d}, \qquad k_\mu = \frac{\mu_{\mathrm{f}} - \mu_{\mathrm{s}}}{\mu_{\mathrm{f}} + \mu_{\mathrm{s}}} \tag{D.10}$$

Il est normalement facile d'estimer la force image d'une dislocation linéaire

parallèle à une interface donnée, mais cela devient problématique dans le cas de quatre interfaces. La Figure D.10 est un croquis des deux interfaces entourant la barrière de diffusion de 20 nm de SiO_2.* La troisième interface entre le film mince et le Al est une couche de 1 μm de passivation de SiO_2 et la quatrième est l'interface entre la couche de passivation et le vide. Ici, nous nous concentrons sur les deux premières interfaces, représentées sur la Fig. D.10. Avec deux interfaces, une seconde dislocation image est créée, en miroir dans la deuxième interface. Il se crée également des dislocations image en miroir des dislocations image, qui à son tour se reflètent encore une fois, et ainsi de suite. Une situation semblable à un objet réfléchi dans deux miroirs semi-transparents.

Etudier les forces image devait permettre de trouver une distance approximative de l'interface à laquelle la dislocation *devrait* devenir fixe selon la théorie de l'élasticité. Grâce à cela et à la complexité de la solution en ayant plusieurs interfaces [Öveçoğlu et al., 1987,Chou, 1966], nous ne considérons que les deux dislocations image `im-dis1` et `im-dis2`. Öveçoğlu et al. ont calculé la force de l'image dans des configurations d'interfaces multiples.

Pour la première dislocation image `im-dis1`, le module de cisaillement du substrat us doit être échangé avec le module de cisaillement μ_s de SiO_2. Utilisation $\mu_\mathrm{f} = 26$ GPa, $\mu_\mathrm{o} = 31$ GPa, $b = 2.86$ Å et si nous étudions une dislocation située à $d = 1$ nm de l'interface Al/SiO_2, on obtient que:

$$\begin{aligned} k_{\mu_{\mathrm{im}\perp 1}} &= \frac{\mu_\mathrm{f} - \mu_\mathrm{o}}{\mu_\mathrm{f} + \mu_\mathrm{o}} = -0.088 \text{ and} \\ F_{\mathrm{b}_{\mathrm{im}\perp 1}} &= -\frac{\mu_\mathrm{f} b^2 k_\mu}{4\pi d} = 1.49 \times 10^{-2}\ \mathrm{Nm}^{-1}. \end{aligned} \tag{D.11}$$

Avec F_b étant la force par unité de longueur, la contrainte de cisaillement est obtenue par

$$\tau_{\mathrm{im}\perp 1} = \frac{F_{\mathrm{b}_{\mathrm{im}\perp 1}}}{b} = 52 \text{ MPa}. \tag{D.12}$$

Pour la deuxième dislocation image, `im-dis2` (Fig. D.10) est dans le substrat de Si, l'équation doit être utilisée sous sa forme originale. La dislocation (`dis`) est à 22 nm de l'interface SiO_2/Si. Cela donne:

$$\begin{aligned} k_{\mu_{\mathrm{im}\perp 2}} &= \frac{\mu_\mathrm{f} - \mu_\mathrm{s}}{\mu_\mathrm{f} + \mu_\mathrm{s}} = -0.51 \text{ and} \\ F_{\mathrm{b}_{\mathrm{im}\perp 2}} &= -\frac{\mu_\mathrm{f} b^2 k_\mu}{4\pi d} = 7.86 \times 10^{-3}\ \mathrm{Nm}^{-1} \\ \tau_{\mathrm{im}\perp 2} &= \frac{F_{\mathrm{b}_{\mathrm{im}\perp 12}}}{b} = 28 \text{ MPa} \end{aligned} \tag{D.13}$$

*Le cliché de MET est la Fig. D.8 (c).

L'ajout de la contrainte de cisaillement des deux dislocations image résulte en une contrainte de cisaillement totale de

$$\tau_{\mathrm{im_{s2}}} \approx 80 \text{ MPa} \tag{D.14}$$

qui agit sur la dislocation réelle à l'instant où elle est à 1 nm de l'interface Al/SiO_2. A partir du tracé de la force dans la Fig. D.8 (e) on peut voir qu'une force de 136 μN a été mesurée par la cellule de charge lorsque la dislocation atteint l'interface. Le modèle FEM a montré que ceci correspond à une contrainte de compression de

$$\sigma_{\mathrm{ext_{s2}}} = 120 \pm 10 \text{ MPa} \tag{D.15}$$

En supposant que le plan de glissement est activé par un facteur de Schmid $S \lesssim 0.5$, ceci correspond à une contrainte de cisaillement externe de

$$\tau_{\mathrm{ext_{s2}}} \approx S\sigma_{\mathrm{ext_{s2}}} \approx 60 \text{ MPa} \tag{D.16}$$

En d'autres termes, à cet endroit de l'échantillon $\tau_{\mathrm{im_{s2}}} > \tau_{\mathrm{ext_{s2}}}$ et la force image devrait avoir arrêté la dislocation. Il n'est évidemment pas possible de mesurer une distance de 1 nm à partir des micrographies MET en champ clair de la Fig. D.8 (a) – (d). Mais, si la dislocation avait été poussée contre l'interface Al/SiO_2 pendant le chargement de la Fig. D.8 (a) – (c), elle aurait du revenir dans le film mince lors du déchargement dans (d). Cela n'a pas été observé, ce que nous interprétons comme le fait que la dislocation a été absorbée par l'interface.

D.5.3 Discussion

D.5.3.1 Interaction dislocation/interface

L'objectif principal des expériences d'indentation effectuées sur plusieurs fenêtres en coupe transverse taillées dans un film d'Al passivé était d'étudier l'interaction des dislocations traversantes avec l'oxyde de silicium entourant le métal. Comme nous l'avons vu dans l'introduction de cette section, la dépendance de la force du film comme l'inverse de son épaisseur est expliquée par ces dislocations interfaciales dont l'énergie dépend essentiellement des forces image [Öveçoğlu et al., 1987]. La façon la plus courante de déformer un film mince sur un substrat étant d'impo-ser des cycles thermiques (la contrainte provenant de la différence de CTE), la disparition des dislocations interfaciales [Müllner and Arzt, 1998, Legros et al., 2002] pourrait être attribué à la diffusion accrue, qui favoriserait la décomposition des dislocations dans la couche d'oxyde. Ici, le film d'aluminium a été déformé *in situ* à température

ambiante en utilisant un porte objet de MET spécial où un coin de diamant est fixé à un capteur MEMS capable d'enregistrer la force appliquée à l'aide d'une céramique piézo-électrique. Comme dans les expériences en température, nous avons observé que les "dislocations traversantes" atteignent l'interface Al/SiO_2 et sont absorbées par cette interface au lieu d'y déposer un segment (dislocation interfaciale). Contrairement aux expériences en contrainte thermique, les dislocations n'accélèrent pas vers cette interface. La différence entre le comportement observé dans la littérature et les expériences décrites ici pourrait être attribuée à des obstacles locaux sur lesquels les dislocations semblent s'ancrer avant d'atteindre l'interface. Ces obstacles peuvent être des défauts de type Gallium implanté ou boucles d'irradiation, ou des dislocations présentes dans le film. Quand une dislocation atteint l'interface Al/SiO_2, une inversion de la contrainte appliquée n'a jamais été suffisante pour retirer cette dislocation de l'interface. Il y a donc clairement absorption de dislocation à température ambiante.

Pour évaluer quantitativement la contrainte nécessaire pour forcer une dislocation dans l'interface cristal/amorphe, nous avons utilisé deux méthodes; utiliser le rayon de courbure des dislocations et évaluer le champ de contraintes dans les différentes couches de l'échantillon modélisé par FEM. Les deux méthodes convergent lorsqu'elles sont testées sur une boucle de dislocation libre. Cette base a servi à estimer la contrainte de cisaillement à l'interface, de l'ordre de 100 MPa, ce qui est plus petit que la résistance mécanique du film déterminée par les expériences en cycles thermiques (de l'ordre de 300 MPa [Flinn et al., 1987]).

La conséquence directe de cette mesure et des observations est que le modèle le plus cité pour la force de couches minces [Nix, 1989], repose sur une hypothèse qui n'est physiquement pas correcte, au moins dans le cas (très fréquent) d'un film d'aluminium déposé sur oxyde. Il n'est donc pas surprenant que, quand un film d'Al déposé sur un substrat en Si oxydé, sa résistance (pour une épaisseur donnée) est plus grande que pour le film équivalent déposé sur saphir [Dehm et al., 2003]. Selon le modèle de dislocation interfaciale, le substrat de saphir doit fournir une contrainte de répulsion des dislocations interfaciales beaucup plus grand, et devrait donc conduire à une plus grande résistance mécanique du film. Le contraire est observé [Heinz et al., 2010]. Ce qui a été proposé est que la résistance des films d'Al découle d'un manque de dislocations [Legros et al., 2005]: Les dislocations initiales sont absorbées par les interfaces métal/oxyde, et la nucléation/multiplication de nouvelles dislocations est bloquée par absence de concentration de contrainte à ces interfaces. En fait, l'absorption d'un ou de plusieurs dislocations (un vecteur de Burgers chaque) n'ajoute pas beaucoup plus de désordre à celui

déjà présent à l'interface de Al/SiO_2 amorphe. Une reconstruction par diffusion a également été observée en dynamique moléculaire (MD) par Ju Li et ses collègues dans le cas de multicouches nanométriques Cu/Cu-Zr (Cu-Zr est amorphe) [Wang et al., 2007], et aux joints de grains (étalement progressif du cœur des dislocation) au cours d'expériences de TEM *in situ* [Mompiou et al., 2012]. Il est donc très difficile d'avoir à ces interfaces la concentration de contrainte nécessaire pour promouvoir la nucléation ou la multiplication de dislocations.

D.5.3.2 Nanoindentation in situ dans un MET

La réalisation d'un test de nanoindentation propre sur une lame mince de MET peut s'avérer difficile. L'échantillon et la pointe doivent d'abord être alignés à la même hauteur. Cela se fait en utilisant une combinaison de la rotation du porte-objet et de la mise au point du MET. Une fois en contact, les outils habituellement disponibles dans un test de MET *in situ* sont ici limités; déplacer le porte-objet peut provoquer des vibrations qui créent des pics artificiels sur la cellule de force. Si l'échantillon est en contact avec la pointe de diamant, un trop grand mouvement du porte-objet peut également déformer ou détruire l'échantillon. Cela implique que les conditions d'observation doivent être réglées une fois pour toutes, ce qui est difficile, car celles-ci sont vite affectées par le fort gradient de contrainte créé par la pointe. L'apparition de franges d'égale courbure et un écart rapide des conditions de Bragg sont inévitables. Afin de minimiser ces difficultés, nous avons souvent travaillé dans des conditions de champ sombre, une méthode également utilisée par d'autres [Kiener and Minor, 2011a, Kondo et al., 2012]. Nous avons constaté qu'une correction du déplacement en z (le long du trajet optique des électrons) à l'aide des piézo était possible pendant le test sans affecter la mesure de la force, ce qui augmente les chances d'avoir de bonnes conditions d'imagerie.

Enfin, le choix de la géométrie de l'échantillon (fenêtre en H) et la configuration (film Al passivé) sont également importantes: la fenêtre en H fournit un échantillon plus rigide (et donc une invasion lente des contours de courbure pendant l'expérience), et la couche de passivation épaisse (SiO_2) a aussi été un "coussin" qui amortit le fort gradient de contrainte dû à la pointe, et maintien des conditions d'imagerie durant le retrait. Une bonne alternative pour éviter certains de ces inconvénients est l'essai de traction en utilisant le même type de porte-objet à pointe, soit directement [Kiener and Minor, 2011b] soit en utilisant des dispositifs MEMS à inversion de contrainte ("Push to Pull") [Chisholm et al., 2012].

D.5.3.3 Mesures de contraintes quantitatives

Malgré les capacités de mesure de force et la capture d'images dynamiques de l'échantillon en cours de déformation (qui pourraient servir pour obtenir la déformation vraie), extraire des données quantitatives de ces expériences n'est pas simple. Comme la section transversale de l'échantillon contraint n'est pas constante, la transformation d'une force (lue par le capteur) en une contrainte, qui est le paramètre physique significatif, est pratiquement impossible et des simulations (FEM, MD, etcetera) sont nécessaires. Cette approche combinée a par exemple été réalisée dans le cas de nanosphères déformées en compression avec un poinçon plat [Calvié et al., 2012, Deneen et al., 2006], ou des piliers à section conique [Lee et al., 2014].

Outre qu'elles complexifient considérablement l'analyse des expériences de MET *in situ*, les simulations doivent être appréhendées avec prudence. Les simulations de dynamique moléculaire sont connues pour dépendre de potentiels atomiques qui ne capturent pas tous les paramètres d'un matériau donné, et pour travailler à des échelles de temps plusieurs ordres de grandeur supérieurs à une expérience réelle. Les simulations FEM, que nous avons utilisées dans ce travail, sont censées être plus réalistes, en particulier dans le domaine élastique, mais là aussi, certaines divergences évidentes peuvent jeter un doute sur les données renvoyées. Pour renforcer nos conclusions, nous avons croisé les résultat provenant de la contrainte locale mesurée sur les dislocations mobiles courbées, ce qui donne une valeur réelle et physique aux champs de contrainte calculés par FEM, eux-mêmes issus de la mesure de force de la cellule MEMS. Dans ce modèle, les 3 nm de couche d'oxyde d'aluminium natif, qui recouvrent les surfaces d'Al surfaces après polissage et FIB, sont censés générer une contrainte de plusieurs centaines de MPa dans cette couche. Cela semble peu probable car cette contrainte aurait dû empêcher les dislocations de s'échapper du cristal, ce qu'elles font: des traces de glissement disparaissent après quelques secondes, ce qui prouve que la couche d'oxyde natif est franchie. La disparition d'un contraste de TEM sur les surfaces est une indication que les dislocations sortent dans le vide. La couche d'AlO doit donc jouer un rôle peu important sur la résistance de la couche mince. L'implantation de Ga^+ et les dislocations de surface créées par l'usinage FIB doit aussi affecter la couche et sa dureté. En d'autres termes, le module d'Young de l'Al dans le modèle FEM peut ne pas être exact pour la couche réelle. à notre connaissance, il n'existe aucun moyen facile de modéliser la possibilité de traverser l'oxyde natif et le changement de module induit par la préparation FIB. Le modèle ne tient pas compte non plus de la déformation plastique. La couche de SiO_2 sur la Fig. D.9 est clairement déformée plastiquement, mais le film Al semble être

seulement légèrement déformé. En (b), nous avons trouvé une contrainte de l'ordre de 8% dans la couche de SiO_2.

Une façon plus simple de comparer les simulations FEM à des expériences serait d'obtenir une carte de déformation de la couche d'Al. Une approche tentée, mais qui s'est avérée extrêmement difficile, est de combiner nanoindentation *in situ* et holographie électronique en champ sombre.

D'autres expériences sont à venir à l'aide d'un nouveau porte-objet (Hysitron) et un nouveau MET, (I^2TEM–Hitachi), où la stabilité est meilleure, et la possibilité d'obtenir des hologrammes plus stables et plus grands est meilleure (cold-FEG). Nos résultats que les déplacements en z peuvent être corrigés en cours d'indentation doivent également être essayés dans ces nouvelles expériences pour corriger la courbure parasite induite.

D.5.4 Résumé et conclusions

Dans cette section, nous avons étudié la déformation plastique de couches minces d'Al. Le porte-échantillon de MET *in situ* détaillé dans la section D.2.1 a été utilisé dans sa configuration de nanoindentation afin d'appliquer et de mesurer une force.

Des échantillons en H, sculptés par FIB, ont été indenté *in situ*. Une telle structure permet à un échantillon transparent aux électrons d'être indenter sans trop plier quand une force est appliquée. Une modélisation par éléments finis (FEM) a été utilisée pour trouver la largeur optimale de la fenêtre transparente.

Des mesures de contraintes à partir du rayon de courbure des dislocations mobiles et courbées ont servie à valider le modèle FEM.

Pour la première fois à température ambiante, nous avons observé des dislocations interfaciales absorbées par des interfaces rigides, en contradiction avec les hypothèses physiques du principal modèle de déformation des films minces. Ce modèle indique que la résistance mécanique d'un film mince est inversement proportionnelle à son épaisseur. Ceci devrait être dû au fait qu'une dislocation à proximité d'une interface avec un matériau plus rigide est repoussée par celle-ci. En utilisant le concept des forces image, cette répulsion a été calculée aux alentours de 100 MPa. A partir des mesures de force données par la cellule de charge et les simulations FEM, une contrainte dans la zone où la dislocation a été absorbée par l'interface a été trouvée, inférieure à la contrainte des forces d'image. Pourtant, la dislocation a été absorbée par l'interface, qui agit donc comme un puits à dislocations.

Bibliography

[Allouche et al., 2003] Allouche, H., Monthioux, M., and Jacobsen, R. L. (2003). Chemical vapor deposition of pyrolytic carbon on carbon nanotubes. Part 1. Synthesis and morphology. *Carbon*, 41(15):2897–2912.

[Anderson, 1993] Anderson, W. A. (1993). Role of space charge in field emission cathodes. *Journal of Vacuum Science & Technology B: Microelectronics and Nanometer Structures*, 11(2):383–386.

[Balk et al., 2003] Balk, T. J., Dehm, G., and Arzt, E. (2003). Parallel glide: unexpected dislocation motion parallel to the substrate in ultrathin copper films. *Acta materialia*, 51(15):4471–4485.

[Banhart, 1999] Banhart, F. (1999). Irradiation effects in carbon nanostructures. *Reports on Progress in Physics*, 62(8):1181–1221.

[Barbour et al., 1953] Barbour, J. P., Dolan, W. W., Trolan, J. K., Martin, E. E., and Dyke, W. P. (1953). Space-charge effects in field emission. *Physical Review*, 92(1):45.

[Batrakov et al., 1999] Batrakov, A. V., Pegel, I. V., and I, P. D. (1999). Limitation of the field emission current density by the space charge of the emitted electrons. *Technical Physics Letters*, 25(6):454–455.

[Bei et al., 2007] Bei, H., Shim, S., Miller, M. K., Pharr, G. M., and George, E. P. (2007). Effects of focused ion beam milling on the nanomechanical behavior of a molybdenum-alloy single crystal. *Applied Physics Letters*, 91(11):111915.

[Beleggia et al., 2011] Beleggia, M., Kasama, T., Dunin-Borkowski, R. E., Hofmann, S., and Pozzi, G. (2011). Direct measurement of the charge distribution along a biased carbon nanotube bundle using electron holography. *Applied Physics Letters*, 98(24):243101.

[Bobji et al., 2006] Bobji, M. S., Ramanujan, C. S., Pethica, J. B., and Inkson, B. J. (2006). A miniaturized TEM nanoindenter for studying material deformation in situ. *Measurement Science and Technology*, 17(6):1324–1329.

[Bonard et al., 2002a] Bonard, J. M., Croci, M., Arfaoui, I., Noury, O., Sarangi, D., and Châtelain, A. (2002a). Can we reliably estimate the emission field and field enhancement factor of carbon nanotube film field emitters? *Diamond & Related Materials*, 11:763–768.

[Bonard et al., 2002b] Bonard, J. M., Dean, K., Coll, B., and Klinke, C. (2002b). Field Emission of Individual Carbon Nanotubes in the Scanning Electron Microscope. *Physical Review Letters*, 89(19):197602.

[Bonard et al., 2001] Bonard, J.-M., Kind, H., Stöckli, T., and Nilsson, L.-O. (2001). Field emission from carbon nanotubes: the first five years. *Solid-State Electronics*, 45(6):893–914.

[Boyes and Gai, 1997] Boyes, E. D. and Gai, P. L. (1997). Environmental high resolution electron microscopy and applications to chemical science. *Ultramicroscopy*, 67(1-4):219–232.

[Brodie and Spindt, 1992] Brodie, I. and Spindt, C. A. (1992). *Advances in Electronics and Electron Physics*, volume 83 of *Advances in Electronics and Electron Physics*. Academic Press Inc, San Diego.

[Bronsgeest et al., 2008] Bronsgeest, M. S., Barth, J. E., Swanson, L. W., and Kruit, P. (2008). Probe current, probe size, and the practical brightness for probe forming systems. *J. Vac. Sci. Technol. B*, 26(3):949.

[Calvié et al., 2012] Calvié, E., Joly-Pottuz, L., Esnouf, C., Clément, P., Garnier, V., and Chevalier, J. (2012). Real time TEM observation of alumina ceramic nano-particles during compression. *Journal of the European Ceramic Society*, 32:2067–2071.

[Chen et al., 2009] Chen, G., Shin, D. H., Roth, S., and Lee, C. J. (2009). Field emission characteristics of point emitters fabricated by a multiwalled carbon nanotube yarn. *Nanotechnology*, 20(31):315201.

[Chen et al., 1989] Chen, J. W., Matteucci, G., Migliori, A., Missiroli, G. F., Nichelatti, E., Pozzi, G., and Vanzi, M. (1989). Mapping of microelectrostatic fields by means of electron holography: Theoretical and experimental results. *Physical Review A*, 40(6):3136.

[Chen, 2005] Chen, M. (2005). Comment on "Grain Boundary-Mediated Plasticity in Nanocrystalline Nickel". *Science*, 308(5720):356c–356c.

[Cherns and Jiao, 2001] Cherns, D. and Jiao, C. G. (2001). Electron Holography Studies of the Charge on Dislocations in GaN. *Physical Review Letters*, 87(20):205504.

[Chisholm et al., 2012] Chisholm, C., Bei, H., Lowry, M. B., Oh, J., Syed Asif, S. A., Warren, O. L., Shan, Z. W., George, E. P., and Minor, A. M. (2012). Dislocation starvation and exhaustion hardening in Mo alloy nanofibers. *Acta materialia*, 60(5):2258–2264.

[Chou, 1966] Chou, Y. T. (1966). Screw dislocations in and near lamellar inclusions. *physica status solidi (b)*, 17(2):509–516.

[Chung et al., 2011] Chung, S., Berechman, R. A., McCartney, M. R., and Skowronski, M. (2011). Electronic structure analysis of threading screw dislocations in 4H–SiC using electron holography. *Journal of Applied Physics*, 109(3):034906.

[Ciappa, 2002] Ciappa, M. (2002). Selected failure mechanisms of modern power modules. *Microelectronics Reliability*, 42(4):653–667.

[Collins and Zettl, 1996] Collins, P. and Zettl, A. (1996). A simple and robust electron beam source from carbon nanotubes. *Applied Physics Letters*, 69(13):1969–1971.

[Collins and Zettl, 1997] Collins, P. and Zettl, A. (1997). Unique characteristics of cold cathode carbon-nanotube-matrix field emitters, PhysRevB, 1997. *Physical Review B*, 55(15):9391–9399.

[Cooper et al., 2009] Cooper, D., Truche, R., Twitchett, A. C., Dunin-Borkowski, R. E., and Midgley, P. A. (2009). Quantitative off-axis electron holography of GaAs p-n junctions prepared by focused ion beam milling. *Journal of Microscopy*, 233(1):102–113.

[Cooper et al., 2006] Cooper, D., Twitchett, A. C., Somodi, P. K., Midgley, P. A., Dunin-Borkowski, R. E., Farrer, I., and Ritchie, D. A. (2006). Improvement in electron holographic phase images of focused-ion-beam-milled GaAs and Si p-n junctions by in situ annealing. *Applied Physics Letters*, 88(6):063510.

[Couret et al., 1993] Couret, A., Crestou, J., Farenc, S., Molenat, G., Clement, N., Coujou, A., and Caillard, D. (1993). In situ deformation in T.E.M.: recent developments. *Microscopy Microanalysis Microstructures*, 4(2-3):153–170.

[Crewe et al., 1968] Crewe, A. V., Wall, J., and Welter, L. M. (1968). A High-Resolution Scanning Transmission Electron Microscope. *Journal of Applied Physics*, 39(13):5861–5868.

[Cumings et al., 2002] Cumings, J., Zettl, A., McCartney, M., and Spence, J. (2002). Electron Holography of Field-Emitting Carbon Nanotubes. *Physical Review Letters*, 88(5):056804 1–4.

[De Graef, 2003] De Graef, M. (2003). *Introduction to Conventional Transmission Electron Microscopy*. Cambridge University Press.

[de Heer et al., 1995] de Heer, W. A., Châtelain, A., and Ugarte, D. (1995). A Carbon Nanotube Field-Emission Electron Source. *Science*, 270:1179–1180.

[de Jonge, 2009] de Jonge, N. (2009). Carbon Nanotube Electron Sources for Electron Microscopes. In Hawkes, P., editor, *Advances in Imaging and Electron Physics*, pages 203–233. Elsevier, Amsterdam.

[de Jonge et al., 2004] de Jonge, N., Allioux, M., Doytcheva, M., Kaiser, M., Teo, K. B. K., Lacerda, R. G., and Milne, W. I. (2004). Characterization of the field emission properties of individual thin carbon nanotubes. *Applied Physics Letters*, 85(9):1607–1609.

[de Jonge et al., 2005] de Jonge, N., Allioux, M., Oostveen, J., Teo, K., and Milne, W. (2005). Optical Performance of Carbon-Nanotube Electron Sources. *Physical Review Letters*, 94(18):186807.

[de Jonge and Bonard, 2004] de Jonge, N. and Bonard, J. M. (2004). Carbon nanotube electron sources and applications. *Philosophical Transactions of the Royal Society A: Mathematical, Physical and Engineering Sciences*, 362(1823):2239–2266.

[de Jonge et al., 2002] de Jonge, N., Lamy, Y., Schoots, K., and Oosterkamp, T. H. (2002). High brightness electron beam from a multi-walled carbon nanotube. *Nature*, 420:393–395.

[de Jonge and van Druten, 2003] de Jonge, N. and van Druten, N. J. (2003). Field emission from individual multiwalled carbon nanotubes prepared in an electron microscope. *Ultramicroscopy*, 95:85–91.

[de Knoop et al., 2014] de Knoop, L., Houdellier, F., Gatel, C., Masseboeuf, A., Monthioux, M., and Hytch, M. (2014). Determining the work function of a carbon-cone cold-field emitter by in situ electron holography. *Micron*, 63:2–8.

[de Knoop and Legros, 2014] de Knoop, L. and Legros, M. (2014). Absorption of crystal/amorphous interfacial dislocations during in situ TEM nanoindentation of an Al thin film on Si. *Scripta Materialia*, 74:44–47.

[de Knoop et al., 2005] de Knoop, L., Svensson, K., Pettersson, H., and Olsson, E. (2005). Extraction and local probing of individual carbon nanotubes. *Electronic Properties of Novel Nanostructures*, 786:118–123.

[Dean and Chalamala, 1999a] Dean, K. A. and Chalamala, B. R. (1999a). Field emission microscopy of carbon nanotube caps. *Journal of Applied Physics*, 85(7):3832–3836.

[Dean and Chalamala, 1999b] Dean, K. A. and Chalamala, B. R. (1999b). The environmental stability of field emission from single-walled carbon nanotubes. *Applied Physics Letters*, 75:3017.

[Dean and Chalamala, 2000] Dean, K. A. and Chalamala, B. R. (2000). Current saturation mechanisms in carbon nanotube field emitters. *Applied Physics Letters*, 76:375–377.

[Dean et al., 1999] Dean, K. A., von Allmen, P., and Chalamala, B. R. (1999). Three behavioral states observed in field emission from single-walled carbon nanotubes. *Journal of Vacuum Science & Technology B: Microelectronics and Nanometer Structures*, 17(5):1959–1969.

[Dehm and Arzt, 2000] Dehm, G. and Arzt, E. (2000). In situ transmission electron microscopy study of dislocations in a polycrystalline Cu thin film constrained by a substrate. *Applied Physics Letters*, 77(8):1126–1128.

[Dehm et al., 2003] Dehm, G., Balk, T. J., Edongue, H., and Arzt, E. (2003). Small-scale plasticity in thin Cu and Al films. *Microelectronic Engineering*, 70:412–424.

[Dehm et al., 2012] Dehm, G., Howe, J. M., and Zweck, J., editors (2012). *In-situ Electron Microscopy*. Wiley-VCH, Weinheim.

[Deneen et al., 2006] Deneen, J., Mook, W. M., Minor, A., Gerberich, W. W., and Barry Carter, C. (2006). In situ deformation of silicon nanospheres. *Journal of Materials Science*, 41(14):4477–4483.

[Dunin-Borkowski et al., 2003] Dunin-Borkowski, R. E., McCartney, M. R., and Smith, D. J. (2003). Electron holography of nanostructured materials. In Nalwa, H. S., editor, *Encyclopedia of Nanoscience and Nanotechnology*, pages 1–59. American Scientific Publishers.

[Dyke and Dolan, 1956] Dyke, W. P. and Dolan, W. W. (1956). Field emission. *Advances in electronics and electron physics*, 8:89–185.

[Dyke and Trolan, 1953] Dyke, W. P. and Trolan, J. K. (1953). Field Emission: Large Current Densitites, Space Charge, and the Vacuum Arc. *Physical Review*, 89:1–11.

[Erts et al., 2001] Erts, D., Lõhmus, A., Lõhmus, R., and Olin, H. (2001). Instrumentation of STM and AFM combined with transmission electron microscope. *Applied Physics A: Materials Science & Processing*, 72(S1):S71–S74.

[Espinosa et al., 2012] Espinosa, H. D., Bernal, R. A., and Filleter, T. (2012). In Situ TEM Electromechanical Testing of Nanowires and Nanotubes. *Small*, 8(21):3233–3252.

[Faress et al., 1994] Faress, A., Levade, C., and Vanderschaeve, G. (1994). TEM in situ investigation of dislocation mobility in II-VI semiconductor compound ZnS cathodoplastic effect and the Peierls mechanism. *Philosophical Magazine A*, 68(1):97–112.

[Flinn, 1991] Flinn, P. A. (1991). Measurement and interpretation of stress in copper films as a function of thermal history. *Journal of materials research*, 6(07):1498–1501.

[Flinn et al., 1987] Flinn, P. A., Gardner, D. S., and Nix, W. D. (1987). Measurement and Interpretation of stress in aluminum-based metallization as a function of thermal history. *IEEE Transactions on Electron Devices*, 34(3):689–699.

[Forbes, 2008] Forbes, R. G. (2008). Call for experimental test of a revised mathematical form for empirical field emission current-voltage characteristics. *Applied Physics Letters*, 92(19):193105.

[Forbes, 2012] Forbes, R. G. (2012). Extraction of emission parameters for large-area field emitters, using a technically complete Fowler–Nordheim-type equation. *Nanotechnology*, 23(9):095706.

[Forbes and Deane, 2007] Forbes, R. G. and Deane, J. H. B. (2007). Reformulation of the standard theory of Fowler–Nordheim tunnelling and cold field electron emission. *Proceedings of the Royal Society A: Mathematical, Physical and Engineering Sciences*, 463(2087):2907–2927.

[Forbes et al., 2003] Forbes, R. G., Edgcombe, C. J., and Valdre, U. (2003). Some comments on models for field enhancement. *Ultramicroscopy*, 95:57–65.

[Forbes and Wikipedia, 2011] Forbes, R. G. and Wikipedia (2011). Field electron emission.

[Fowler and Nordheim, 1928] Fowler, R. and Nordheim, L. (1928). Electron Emission in Intense Electric Fields. *Proceedings of the Royal Society of London. Series A, Containing Papers of a Mathematical and Physical Character*, 119(781):173–181.

[Fransen et al., 1998] Fransen, M. J., Faber, J. S., Van Rooy, T. L., Tiemeijer, P. C., and Kruit, P. (1998). Experimental evaluation of the extended Schottky model for ZrO/W electron emission. *Journal of Vacuum Science & Technology B: Microelectronics and Nanometer Structures*, 16(4):2063–2072.

[Fransen et al., 1999a] Fransen, M. J., Overwijk, M., and Kruit, P. (1999a). Brightness measurements of a ZrO/W Schottky electron emitter in a transmission electron microscope. *Applied Surface Science*, 146(1):357–362.

[Fransen et al., 1999b] Fransen, M. J., Van Rooy, T. L., and Kruit, P. (1999b). Field emission energy distributions from individual multiwalled carbon nanotubes. *Applied Surface Science*, 146(1):312–327.

[Freund, 1994] Freund, L. B. (1994). The mechanics of dislocations in strained-layer semiconductor materials. *Advances in Applied Mechanics*, 30:1–67.

[Freund and Suresh, 2003] Freund, L. B. and Suresh, S. (2003). *Thin Film Materials*. Stress, Defect Formation and Surface Evolution. Cambridge University Press.

[Gabor, 1948] Gabor, D. (1948). A New Microscopic Principle. *Nature*, 161(4098):777–778.

[Gadzuk and Plummer, 1973] Gadzuk, J. W. and Plummer, E. W. (1973). Field emission energy distribution (FEED). *Reviews of modern physics*, 45(3):487.

[Gai, 2002] Gai, P. L. (2002). Development of wet environmental TEM (Wet-ETEM) for in situ studies of liquid-catalyst reactions on the nanoscale. *Microscopy and Microanalysis*, 8(1):21–28.

[Gao et al., 1999] Gao, H., Zhang, L., Nix, W. D., Thompson, C. V., and Arzt, E. (1999). Crack-like grain-boundary diffusion wedges in thin metal films. *Acta materialia*, 47:2865–2878.

[Gao et al., 2001] Gao, R., Pan, Z., and Wang, Z. L. (2001). Work function at the tips of multiwalled carbon nanotubes. *Applied Physics Letters*, 78(12):1757–1759.

[Gatel et al., 2013] Gatel, C., Lubk, A., Pozzi, G., Snoeck, E., and Hÿtch, M. (2013). Counting Elementary Charges on Nanoparticles by Electron Holography. *Physical Review Letters*, 111(2):025501.

[Good and Mueller, 1956] Good, R. H. and Mueller, E. W. (1956). *Handbuch der Physik*. Field Emission. Springer Verlag, Berlin, s fluegge edition.

[Greer and Nix, 2006] Greer, J. and Nix, W. (2006). Nanoscale gold pillars strengthened through dislocation starvation. *Physical Review B*, 73(24):245410.

[Gröning et al., 2000] Gröning, O., Küttel, O. M., Emmenegger, C., Gröning, P., and Schlapbach, L. (2000). Field emission properties of carbon nanotubes. *J. Vac. Sci. Technol. B*, 18(2):665–678.

[Hawkes, 2011] Hawkes, P. W., editor (2011). *Advances in Imaging and Electron Physics*, volume 165 of *Optics of Charged Particle Analyzers*. Academic Press, Elsevier Inc., first edition.

[Hawkes and Spence, 2007] Hawkes, P. W. and Spence, J. C. H. (2007). *Science of Microscopy*. Springer, xviii edition.

[Hazra et al., 2011] Hazra, K. S., Jain, V., and Misra, D. S. (2011). The role of tunneling barrier modification for the saturation current of carbon nanotube field emission in strong electric field. *Chemical Physics Letters*, 502(4-6):194–197.

[He et al., 2013] He, K., Cho, J.-H., Jung, Y., Tom Picraux, S., and Cumings, J. (2013). Silicon nanowires: electron holography studies of doped p–n junctions and biased Schottky barriers. *Nanotechnology*, 24(11):115703.

[Heinz et al., 2010] Heinz, W., Pippan, R., and Dehm, G. (2010). Investigation of the fatigue behavior of Al thin films with different microstructure. *Materials Science and Engineering: A*, 527(29-30):7757–7763.

[Hirsch, 1986] Hirsch, P. B. (1986). Direct Observations of moving dislocations: Reflections on the thirtieth anniversary of the first recorded observations of moving dislocations by transmission electron microscopy. *Materials Science and Engineering*, 84:1–10.

[Hirsch, 1999] Hirsch, P. B. (1999). *Topics in Electron Diffraction and Micrscopy of Materials*. IOP Publishing Ltd, Bristol.

[Hirsch et al., 1956] Hirsch, P. B., Horne, R. W., and Whelan, M. J. (1956). Direct observations of the arrangement and motion of dislocations in aluminium. *Philosophical Magazine*, 1(7):677–684.

[Hirth and Lothe, 1982] Hirth, J. P. and Lothe, J. (1982). *Theory of dislocations*. John Wiley and Sons, New York, second edition.

[Houdellier et al., 2012] Houdellier, F., Masseboeuf, A., Monthioux, M., and Hÿtch, M. J. (2012). New carbon cone nanotip for use in a highly coherent cold field emission electron microscope. *Carbon*, 50(5):2037–2044.

[Huang et al., 2005] Huang, J. Y., Kempa, K., Jo, S. H., Chen, S., and Ren, Z. F. (2005). Giant field enhancement at carbon nanotube tips induced by multistage effect. *Applied Physics Letters*, 87(5):053110.

[Hüe et al., 2008] Hüe, F., Hytch, M., Bender, H., Houdellier, F., and Claverie, A. (2008). Direct Mapping of Strain in a Strained Silicon Transistor by High-Resolution Electron Microscopy. *Physical Review Letters*, 100(15).

[Hull and Bean, 1989] Hull, R. and Bean, J. C. (1989). Variation in misfit dislocation behavior as a function of strain in the GeSi/Si system. *Applied Physics Letters*, 54(10):925–927.

[Hÿtch et al., 2008] Hÿtch, M. J., Houdellier, F., Hüe, F., and Snoeck, E. (2008). Nanoscale holographic interferometry for strain measurements in electronic devices. *Nature*, 453(7198):1086–1089.

[Hÿtch et al., 2003] Hÿtch, M. J., Putaux, J.-L., and Pénisson, J.-M. (2003). Measurement of the displacement field of dislocations to 0.03 A by electron microscopy. *Nature*, 423(6937):270–273.

[Hÿtch et al., 1998] Hÿtch, M. J., Snoeck, E., and Kilaas, R. (1998). Quantitative measurement of displacement and strain fields from HREM micrographs. *Ultramicroscopy*, 74(3):131–146.

[Iijima, 1991] Iijima, S. (1991). Helical microtubules of graphitic carbon. *Nature*, 354:56–58.

[Imura and Hashimoto, 1977] Imura, T. and Hashimoto, H. (1977). High Voltage Electron Microscopy. In Imura, T. and Hashimoto, H., editors, *5th International Conference on High Voltage Electron Microscopy*. The Japanese Society for Electron Microscopy.

[Inkson et al., 2002] Inkson, B. J., Dehm, and Wagner, T. (2002). In situ TEM observation of dislocation motion in thermally strained Al nanowires. *Acta materialia*, 50(20):5033–5047.

[Jacobsen and Monthioux, 1997] Jacobsen, R. L. and Monthioux, M. (1997). Carbon beads with protruding cones. *Nature*, 385:211–212.

[Janssen et al., 2009] Janssen, G. C. A. M., Abdalla, M. M., van Keulen, F., Pujada, B. R., and van Venrooy, B. (2009). Celebrating the 100th anniversary of the Stoney equation for film stress: Developments from polycrystalline steel strips to single crystal silicon wafers. *Thin solid films*, 517(6):1858–1867.

[Jennings et al., 2010] Jennings, A. T., Burek, M. J., and Greer, J. R. (2010). Microstructure versus Size: Mechanical Properties of Electroplated Single Crystalline Cu Nanopillars. *Physical Review Letters*, 104(13):135503.

[Jennings and Greer, 2011] Jennings, A. T. and Greer, J. R. (2011). Tensile deformation of electroplated copper nanopillars. *Philosophical Magazine*, 91(7-9):1108–1120.

[Jin et al., 2005] Jin, C., Wang, J., Wang, M., Su, J., and Peng, L.-M. (2005). In-situ studies of electron field emission of single carbon nanotubes inside the TEM. *Carbon*, 43(5):1026–1031.

[Jin et al., 2004] Jin, M., Minor, A. M., Stach, E. A., and Morris, Jr., J. W. (2004). Direct observation of deformation-induced grain growth during the nanoindentation of ultrafine-grained Al at room temperature. *Acta materialia*, 52(18):5381–5387.

[Josell et al., 2002] Josell, D., Weihs, T. P., and Gao, H. (2002). Diffusional Creep: Stresses and Strain Rates in Thin Films and Multilayers. *MRS Bulletin*, 27(01):39–44.

[Kalkman et al., 2001] Kalkman, A. J., Verbruggen, A. H., and Janssen, G. C. A. M. (2001). Young's modulus measurements and grain boundary sliding in free-standing thin metal films. *Applied Physics Letters*, 78(18):2673.

[Kear, 1960] Kear, B. H. (1960). Apparatus for the Deformation of Foils at Elevated Temperatures in an Electron Microscope. *Review of Scientific Instruments*, 31(9):1007–1008.

[Keller et al., 1999] Keller, R.-M., Baker, S. P., and Arzt, E. (1999). Stress–temperature behavior of unpassivated thin copper films. *Acta materialia*, 47(2):415–426.

[Keller et al., 2011] Keller, R.-M., Sigle, W., Baker, S. P., Kraft, O., and Arzt, E. (2011). In-Situ Tem Investigation During Thermal Cycling of thin Copper Films. *MRS Proceedings*, 436:221.

[Kiener et al., 2008] Kiener, D., Grosinger, W., Dehm, G., and Pippan, R. (2008). A further step towards an understanding of size-dependent crystal plasticity: In situ tension experiments of miniaturized single-crystal copper samples. *Acta materialia*, 56(3):580–592.

[Kiener and Minor, 2011a] Kiener, D. and Minor, A. M. (2011a). Source-controlled yield and hardening of Cu(100) studied by in situ transmission electron microscopy. *Acta materialia*, 59(4):1328–1337.

[Kiener and Minor, 2011b] Kiener, D. and Minor, A. M. (2011b). Source Truncation and Exhaustion: Insights from Quantitative in situ TEM Tensile Testing. *Nano Letters*, 11(9):3816–3820.

[Kiener et al., 2007] Kiener, D., Motz, C., Rester, M., Jenko, M., and Dehm, G. (2007). FIB damage of Cu and possible consequences for miniaturized mechanical tests. *Materials Science and Engineering: A*, 459(1-2):262–272.

[Kim et al., 2011] Kim, H. J., Bae, M. J., Kim, Y. C., Cho, E. S., Sohn, Y. C., Kim, D. Y., Lee, S. E., Kang, H. S., Han, I. T., Kim, Y. H., Patole, S. P., and Yoo, J. B. (2011). Growth of carbon nanotube field emitters on single strand carbon fiber: a linear electron source. *Nanotechnology*, 22(9):095602.

[Kim et al., 1997] Kim, H. S., Yu, M. L., Thomson, M., Kratschmer, E., and Chang, T. (1997). Energy distributions of Zr/O/W Schottky electron emission. *Journal of Applied Physics*, 81(1):461–465.

[Kizuka, 1998a] Kizuka, T. (1998a). Atomic process of point contact in gold studied by time-resolved high-resolution transmission electron microscopy. *Physical Review Letters*, 81(20):4448.

[Kizuka, 1998b] Kizuka, T. (1998b). Atomistic visualization of deformation in gold. *Physical Review B*, 57(18):11158.

[Kizuka et al., 1997] Kizuka, T., Yamada, K., and Tanaka, N. (1997). Time-resolved high-resolution electron microscopy of solid state direct bonding of gold and zinc oxide nanocrystallites at ambient temperature. *Applied Physics Letters*, 70(8):964.

[Kohno et al., 2010] Kohno, Y., Okunishi, E., Tomita, T., Ishikawa, I., Kaneyama, T., Ohkura, Y., Kondo, Y., and Isabell, T. (2010). Development of a Cold Field-Emission Gun for a 200kV Atomic Resolution Electron Microscope. *Microscopy and analysis*, 24(7):S9.

[Kokkorakis et al., 2002] Kokkorakis, G. C., Modinos, A., and Xanthakis, J. P. (2002). Local electric field at the emitting surface of a carbon nanotube. *Journal of Applied Physics*, 91(7):4580.

[Kondo et al., 2012] Kondo, S., Shibata, N., Mitsuma, T., Tochigi, E., and Ikuhara, Y. (2012). Dynamic observations of dislocation behavior in SrTiO3 by in situ nanoindentation in a transmission electron microscope. *Applied Physics Letters*, 100(18):181906.

[Korhonen et al., 1991] Korhonen, M. A., Black, R. D., and Li, C. Y. (1991). Stress relaxation of passivated aluminum line metallizations on silicon substrates. *Journal of Applied Physics*, 69(3):1748–1755.

[Krivanek et al., 2013] Krivanek, O. L., Lovejoy, T. C., Dellby, N., and Carpenter, R. W. (2013). Monochromated STEM with a 30 meV-wide, atom-sized electron probe. *Microscopy*, 62(1):3–21.

[Lahouij et al., 2011] Lahouij, I., Dassenoy, F., de Knoop, L., Martin, J.-M., and Vacher, B. (2011). In Situ TEM Observation of the Behavior of an Individual Fullerene-Like MoS2 Nanoparticle in a Dynamic Contact. *Tribology Letters*, 42(2):133–140.

[Lee et al., 2014] Lee, S., Im, J., Yoo, Y., Bitzek, E., Kiener, D., Richter, G., Kim, B., and Oh, S. H. (2014). Reversible cyclic deformation mechanism of gold nanowires by twinning–detwinning transition evidenced from in situ TEM. *Nature Communications*, 5.

[Legros et al., 2009] Legros, M., Cabié, M., and Gianola, D. S. (2009). In situ deformation of thin films on substrates. *Microscopy Research and Technique*, 72(3):270–283.

[Legros et al., 2005] Legros, M., Dehm, G., and Balk, T. J. (2005). In-situ TEM study of plastic stress relaxation mechanisms and interface effects in metallic films. In *MATERIALS RESEARCH SOCIETY SYMPOSIUM PROCEEDINGS*. Cambridge Univ Press.

[Legros et al., 2001] Legros, M., Dehm, G., Keller-Flaig, R. M., Arzt, E., Hemker, K. J., and Suresh, S. (2001). Dynamic observation of Al thin films plastically strained in a TEM. *Materials Science and Engineering: A*, 309:463–467.

[Legros et al., 2010] Legros, M., Gianola, D. S., and Motz, C. (2010). Quantitative In Situ Mechanical Testing. *MRS Bulletin*, 35.

[Legros et al., 2002] Legros, M., Hemker, K. J., Gouldstone, A., Suresh, S., Keller-Flaig, R. M., and Arzt, E. (2002). Microstructural evolution in passivated Al films on Si substrates during thermal cycling. *Acta materialia*, 50(13):3435–3452.

[Lichte, 1986] Lichte, H. (1986). Electron holography approaching atomic resolution. *Ultramicroscopy*, 20(3):293–304.

[Liu et al., 2008] Liu, P., Sun, Q., Zhu, F., Liu, K., Jiang, K., Liu, L., Li, Q., and Fan, S. (2008). Measuring the Work Function of Carbon Nanotubes with Thermionic Method. *Nano Letters*, 8(2):647–651.

[Lockwood and Inkson, 2008] Lockwood, A. J. and Inkson, B. J. (2008). In situTEM nanoindentation and deformation of Si-nanoparticle clusters. *Journal of Physics D: Applied Physics*, 42(3):035410.

[Loubet et al., 1984] Loubet, J. L., Georges, J. M., Marchesini, O., and Meille, G. (1984). Vickers Indentation Curves of Magnesium Oxide (MgO). *Journal of Tribology*, 106(1):43.

[Louchet and Saka, 1993] Louchet, F. and Saka, H. (1993). French-Japanese Seminar on In Situ Electron Microscopy. *Microscopy Microanalysis Microstructures*, 4.

[Louchet and Saka, 2003] Louchet, F. and Saka, H. (2003). Comments on the paper: observation of dislocation dynamics in the electron microscope, by BW Lagow et al. *Materials Science and Engineering: A*, 352(1):71–75.

[Lu et al., 2009] Lu, Y., Ganesan, Y., and Lou, J. (2009). A Multi-step Method for In Situ Mechanical Characterization of 1-D Nanostructures Using a Novel Micromechanical Device. *Experimental Mechanics*, 50(1):47–54.

[Lu et al., 2011] Lu, Y., Peng, C., Ganesan, Y., Huang, J. Y., and Lou, J. (2011). Quantitative in situTEM tensile testing of an individual nickel nanowire. *Nanotechnology*, 22(35):355702.

[Luo et al., 2002] Luo, J., Peng, L. M., Xue, Z., and Wu, J. (2002). End potential barriers of single-walled carbon nanotubes and their role in field emission. *Physical Review B*, 66(15):155407.

[Lutwyche and Wada, 1995] Lutwyche, M. I. and Wada, Y. (1995). Observation of a vacuum tunnel gap in a transmission electron microscope using a micromechanical tunneling microscope. *Applied Physics Letters*, 66(21):2807–2809.

[Marton, 1935] Marton, L. (1935). La microscopie électronique des onjectes biologiques. *Bull. Acad. Belg. Cl. Sci.*, 20:439–466.

[Matthews and Blakeslee, 1974] Matthews, J. W. and Blakeslee, A. E. (1974). Defects in epitaxial multilayers: I. Misfit dislocations. *Journal of Crystal Growth*, 27:118–125.

[Matthews and Blakeslee, 1975] Matthews, J. W. and Blakeslee, A. E. (1975). Defects in epitaxial multilayers: II. Dislocation pile-ups, threading dislocations, slip lines and cracks. *Journal of Crystal Growth*, 29(3):273–280.

[McCartney and Smith, 2007] McCartney, M. R. and Smith, D. J. (2007). Electron Holography: Phase Imaging with Nanometer Resolution. *Annual Review of Materials Research*, 37(1):729–767.

[Messerschmidt et al., 1989] Messerschmidt, U., Appel, F., Heydenreich, J., and Schmidt, V. (1989). Electron Microscopy in Plasticity and Fracture Researchof Materials. *Proceedings of the International Symposium held at Holzhau near Dresden*, pages 1–5.

[Midgley, 2001] Midgley, P. A. (2001). An introduction to off-axis electron holography. *Micron*, 32(2):167–184.

[Millikan and Lauritsen, 1928] Millikan, R. A. and Lauritsen, C. C. (1928). Relations of field-currents to thermionic-currents. *Proceedings of the National Academy of Sciences of the United States of America*, 14(1):45.

[Minor et al., 2001] Minor, A. M., Morris, J. W., and Stach, E. A. (2001). Quantitative in situ nanoindentation in an electron microscope. *Applied Physics Letters*, 79(11):1625.

[Minor et al., 2006] Minor, A. M., Syed Asif, S. A., Shan, Z., Stach, E. A., Cyrankowski, E., Wyrobek, T. J., and Warren, O. L. (2006). A new view of the onset of plasticity during the nanoindentation of aluminium. *Nature Materials*, 5(9):697–702.

[Möllenstedt and Düker, 1955] Möllenstedt, G. and Düker, H. (1955). FRESNELscher Interferenzversuch mit einem Biprisma für Elektronenwellen. *Naturwissenschaften*, 42(2):41–41.

[Mompiou et al., 2013] Mompiou, F., Legros, M., Boé, A., Coulombier, M., Raskin, J. P., and Pardoen, T. (2013). Inter- and intragranular plasticity mechanisms in ultrafine-grained Al thin films: An in situ TEM study. *Acta materialia*, 61(1):205–216.

[Mompiou et al., 2012] Mompiou, F., Legros, M., Sedlmayr, A., Gianola, D. S., Caillard, D., and Kraft, O. (2012). Source-based strengthening of submicrometer Al fibers. *Acta materialia*, 60(3):977–983.

[Müller, 1936] Müller, E. W. (1936). Versuche zur Theorie der Elektronenemission unter der Einwirkung hoher Feldstärken. *Zeitschrift für Techniche Physik*, 17:412.

[Müllner and Arzt, 1998] Müllner, P. and Arzt, E. (1998). Observation of Dislocation Disappearance in Aluminum Thin Films and Consequences for Thin Film Properties. *MATERIALS RESEARCH SOCIETY SYMPOSIUM PROCEEDINGS*, 505:149–154.

[Murphy and Good, 1956] Murphy, E. L. and Good, R. H. (1956). Thermionic Emission, Field Emission, and the Transition Region. *Physical Review*, 102(6):1464–1473.

[Nafari, 2010] Nafari, A. (2010). *Microsensors for* in situ *electron microscopy applications*. PhD thesis, Chalmers University of Technology, Gothenburg.

[Nafari et al., 2005] Nafari, A., Danilov, A., Rödjegård, H., Enoksson, P., and Olin, H. (2005). A micromachined nanoindentation force sensor. *Sensors and Actuators A: Physical*, 123-124:44–49.

[Nafari et al., 2007] Nafari, A., Ghavanini, F. A., Bring, M., Svensson, K., and Enoksson, P. (2007). Calibration methods of force sensors in the micro-Newton range. *Journal of Micromechanics and Microengineering*, 17:2102–2107.

[Nafari et al., 2008] Nafari, A., Karlen, D., Rusu, C., Svensson, K., Olin, H., and Enoksson, P. (2008). MEMS Sensor for In Situ TEM Atomic Force Microscopy. *Journal of Microelectromechanical Systems*, 17(2):328–333.

[Nilsson et al., 2001a] Nilsson, L., Groening, O., Groening, P., Kuettel, O., and Schlapbach, L. (2001a). Characterization of thin film electron emitters by scanning anode field emission microscopy. *Journal of Applied Physics*, 90(2):768.

[Nilsson et al., 2001b] Nilsson, L., Gröning, O., Gröning, P., Küttel, O., and Schlapbach, L. (2001b). Carbon nano-/micro-structures in field emission: environmental stability and field enhancement distribution. *Thin solid films*, 383(1):78–80.

[Nix, 1989] Nix, W. D. (1989). Mechanical properties of thin films. *Metallurgical and Materials Transactions A*, 20(11):2217–2245.

[Nix, 1998] Nix, W. D. (1998). Yielding and strain hardening of thin metal films on substrates. *Scripta Materialia*, 39:545–554.

[Obraztsov et al., 2000] Obraztsov, A. N., Volkov, A. P., and Pavlovsky, I. (2000). Field emission from nanostructured carbon materials. *Diamond & Related Materials*, 9(3):1190–1195.

[Ohnishi et al., 1998] Ohnishi, H., Kondo, Y., and Takayanagi, K. (1998). Quantized conductance through individual rows of suspended gold atoms. *Nature*, 395(6704):780–783.

[Ohring, 2002] Ohring, M. (2002). *Materials Science of Thin Films*. Academic Press, San Diego, second edition.

[Oliver and Pethica, 1989] Oliver, W. C. and Pethica, J. B. (1989). Method for continuous determination of the elastic stiffness of contact between two bodies. *US Patent 4,848,141*.

[Oliver and Pharr, 1992] Oliver, W. C. and Pharr, G. M. (1992). Improved technique for determining hardness and elastic modulus using load and displacement sensing indentation experiments. *Journal of materials research*, 7(6):1564–1583.

[Öveçoğlu et al., 1987] Öveçoğlu, M. L., Doerner, M. F., and Nix, W. D. (1987). Elastic interactions of screw dislocations in thin films on substrates. *Acta Metallurgica*, 35(12):2947–2957.

[Pethicai et al., 1983] Pethicai, J. B., Hutchings, R., and Oliver, W. C. (1983). Hardness measurement at penetration depths as small as 20 nm. *Philosophical Magazine A*, 48(4):593–606.

[Petkov, 2013] Petkov, N. (2013). In Situ Real-Time TEM Reveals Growth, Transformation and Function in One-Dimensional Nanoscale Materials: From a Nanotechnology Perspective. *ISRN Nanotechnology*, 2013(11):1–21.

[Phani et al., 2011] Phani, P. S., Johanns, K. E., Duscher, G., Gali, A., George, E. P., and Pharr, G. M. (2011). Scanning transmission electron microscope observations of defects in as-grown and pre-strained Mo alloy fibers. *Acta materialia*, 59(5):2172–2179.

[Pogorelov et al., 2009] Pogorelov, E. G., Zhbanov, A. I., and Chang, Y.-C. (2009). Field enhancement factor and field emission from a hemi-ellipsoidal metallic needle. *Ultramicroscopy*, 109(4):373–378.

[Poncharal, 1999] Poncharal, P. (1999). Electrostatic Deflections and Electromechanical Resonances of Carbon Nanotubes. *Science*, 283(5407):1513–1516.

[Ponchet et al., 2011] Ponchet, A., Forest, S., and Thomas, O. (2011). *Mechanics of Nano-Objects*. Presses des MINES.

[Ribaya et al., 2008] Ribaya, B. P., Leung, J., Brown, P., Rahman, M., and Nguyen, C. V. (2008). A study on the mechanical and electrical reliability of individual carbon nanotube field emission cathodes. *Nanotechnology*, 19(18):185201.

[Richardson, 1901] Richardson, O. W. (1901). On the negative radiation from hot platinum. *Philosophical of the Cambridge Philosophical Society*, 11:286–295.

[Rinzler, 1995] Rinzler, A. (1995). Unraveling Nanotubes: Field Emission from an Atomic Wire. *Science*, 269:1–4.

[Saada et al., 2007] Saada, G., Verdier, M., and Dirras, G. F. (2007). Elastoplastic behaviour of thin metal films. *Philosophical Magazine*, 87(31):4875–4892.

[Saito et al., 2005] Saito, Y., Seko, K., and Kinoshita, J.-i. (2005). Dynamic behavior of carbon nanotube field emitters observed by in situ transmission electron microscopy. *Diamond & Related Materials*, 14(11-12):1843–1847.

[Saito and Uemura, 2000] Saito, Y. and Uemura, S. (2000). Field emission from carbon nanotubes and its application to electron sources. *Carbon*, 38(2):169–182.

[Saka and Caillard, 2001] Saka, H. and Caillard, D. (2001). French-Japanese workshop on In Situ Experiments. *Journal of Microscopy*, 203.

[Sanchez et al., 2007] Sanchez, J. A., Wong, B. T., Pinar Mengüç, M., and Albella, P. (2007). Field emission and electron deposition profiles as a function of carbon nanotube tip geometries. *Journal of Applied Physics*, 101(11):114313.

[Schamber, 1999] Schamber, F. (1999). Emission Myths. *Microscopy Today*, pages 1–10.

[Schottky, 1914] Schottky, W. (1914). . *Physikalische Zeitschrift*, 15:872.

[Sciammarella, 1982] Sciammarella, C. A. (1982). The moiré method—a review. *Experimental Mechanics*, 22(11):418–433.

[Shan and Cho, 2005] Shan, B. and Cho, K. (2005). First Principles Study of Work Functions of Single Wall Carbon Nanotubes. *Physical Review Letters*, 94(23):236602.

[Shan and Cho, 2006] Shan, B. and Cho, K. (2006). First-principles study of work functions of double-wall carbon nanotubes. *Physical Review B*, 73(8):081401.

[Shan et al., 2004] Shan, Z., Stach, E. A., Wiezorek, J., Knapp, J. A., Follstaedt, D. M., and Mao, S. X. (2004). Grain boundary-mediated plasticity in nanocrystalline nickel. *Science*, 305(5684):654–657.

[Shan et al., 2007] Shan, Z. W., Mishra, R. K., Asif, S. S., Warren, O. L., and Minor, A. M. (2007). Mechanical annealing and source-limited deformation in submicrometre-diameter Ni crystals. *Nature Materials*, 7(2):115–119.

[Sharon et al., 2014] Sharon, J. A., Zhang, Y., Mompiou, F., Legros, M., and Hemker, K. J. (2014). Discerning size effect strengthening in ultrafine-grained Mg thin films. *Scripta Materialia*, 75:10–13.

[Shiraishi and Ata, 2001] Shiraishi, M. and Ata, M. (2001). Work function of carbon nanotubes. *Carbon*, 39(12):1913–1917.

[Sinitsyn et al., 1997] Sinitsyn, N. I., Gulyaev, Y. V., Torgashov, G. V., Chernozatonskii, L. A., Kosakovskaya, Z. Y., Zakharchenko, Y. F., Kiselev, N. A., Musatov, A. L., Zhbanov, A. I., and Mevlyut, S. T. (1997). Thin films consisting of carbon nanotubes as a new material for emission electronics. *Applied Surface Science*, 111:145–150.

[Smith et al., 2005] Smith, R. C., Forrest, R. D., Carey, J. D., Hsu, W. K., and Silva, S. R. P. (2005). Interpretation of enhancement factor in nonplanar field emitters. *Applied Physics Letters*, 87(1):013111.

[Smith and Silva, 2009] Smith, R. C. and Silva, S. R. P. (2009). Interpretation of the field enhancement factor for electron emission from carbon nanotubes. *Journal of Applied Physics*, 106(1):014314.

[Solá et al., 2009] Solá, F., Biaggi-Labiosa, A., Fonseca, L. F., Resto, O., Lebrón-Colón, M., and Meador, M. A. (2009). Field Emission and Radial Distribution Function Studies of Fractal-like Amorphous Carbon Nanotips. *Nanoscale Research Letters*, 4(5):431–436.

[Spindt et al., 1976] Spindt, C. A., Brodie, I., Humphrey, L., and Westerberg, E. R. (1976). Physical properties of thin film field emission cathodes with molybdenum cones. *Journal of Applied Physics*, 47(12):5248–5263.

[Stach et al., 2001] Stach, E. A., Freeman, T., Minor, A. M., Owen, D. K., Cumings, J., Wall, M. A., Chraska, T., Hull, R., Morris, J. W., and Zettl, A. (2001). Development of a nanoindenter for in situ transmission electron microscopy. *Microscopy and Microanalysis*, 7(6):507–517.

[Stoney, 1909] Stoney, G. G. (1909). The tension of metallic films deposited by electrolysis. *Proceedings of the Royal Society of London. Series A, Containing Papers of a Mathematical and Physical Character*, 82(553):172–175.

[Suzuki et al., 2000] Suzuki, S., Bower, C., Watanabe, Y., and Zhou, O. (2000). Work functions and valence band states of pristine and Cs-intercalated single-walled carbon nanotube bundles. *Applied Physics Letters*, 76(26):4007–4009.

[Suzuki et al., 2004] Suzuki, S., Watanabe, Y., Homma, Y., Fukuba, S.-y., Heun, S., and Locatelli, A. (2004). Work functions of individual single-walled carbon nanotubes. *Applied Physics Letters*, 85(1):127–129.

[Sveningsson et al., 2005] Sveningsson, M., Hansen, K., Svensson, K., Olsson, E., and Campbell, E. (2005). Quantifying temperature-enhanced electron field emission from individual carbon nanotubes. *Physical Review B*, 72(8):085429.

[Svensson et al., 2003] Svensson, K., Jompol, Y., Olin, H., and Olsson, E. (2003). Compact design of a transmission electron microscope-scanning tunneling microscope holder with three-dimensional coarse motion. *Review of Scientific Instruments*, 74(11):4945.

[Swann et al., 1974] Swann, P. R., Humphreys, C. J., and Goringe, M. J. (1974). High voltage electron microscopy. In *Proceedings of the third international conference held at Oxford*, Oxford, England.

[Swanson and Schwind, 2009] Swanson, L. W. and Schwind, G. A. (2009). Review of ZrO/W Schottky Cathode. In Orloff, J., editor, *Handbook of Charged Particle Optics, Second Edition*. CRC Press, Boca Raton, FL.

[Takeuchi, 1973] Takeuchi, T. (1973). Load-Elongation Curves of Pure Body-Centred Cubic Metals at Low Temperatures. *Journal of the Physical Society of Japan*, 35(4):1149–1160.

[Takeuchi et al., 1973] Takeuchi, T., Ikeda, S., Ikeno, S., and Furubayashi, E.-i. (1973). A Specimen Stage for Low Temperature Tensile Deformation in an Electron Microscope. *Japanese Journal of Applied Physics*, 12(1).

[Thompson, 1990] Thompson, C. V. (1990). Grain Growth in Thin Films. *Annual Review of Materials Science*, 20(1):245–268.

[Todokoro et al., 1982] Todokoro, H., Saitou, N., and Yamamoto, S. (1982). Role of ion bombardment in field emission current instability. *Jap. J. Appl. Phys*, 21:1513–1516.

[Tonomura, 1987] Tonomura, A. (1987). Applications of electron holography. *Reviews of modern physics*, 59(3):639.

[Tsui et al., 2011] Tsui, T. Y., Oliver, W. C., and Pharr, G. M. (2011). Influences of stress on the measurement of mechanical properties using nanoindentation: Part I. Experimental studies in an aluminum alloy. *Journal of materials research*, 11(03):752–759.

[Uchic et al., 2004] Uchic, M. D., Dimiduk, D. M., Florando, J. N., and Nix, W. D. (2004). Sample dimensions influence strength and crystal plasticity. *Science*, 305(5686):986–989.

[Uchic et al., 2009a] Uchic, M. D., Shade, P. A., and Dimiduk, D. M. (2009a). Micro-compression testing of fcc metals: A selected overview of experiments and simulations. *JOM*, 61(3):36–41.

[Uchic et al., 2009b] Uchic, M. D., Shade, P. A., and Dimiduk, D. M. (2009b). Plasticity of Micrometer-Scale Single Crystals in Compression. *Annual Review of Materials Research*, 39(1):361–386.

[Vlassak and Nix, 1992] Vlassak, J. J. and Nix, W. D. (1992). A new bulge test technique for the determination of Young's modulus and Poisson's ratio of thin films. *Journal of materials research*, 7(12):3242–3249.

[Volkert and Minor, 2007] Volkert, C. A. and Minor, A. M. (2007). Focused Ion Beam Microscopy and Micromachining. *MRS Bulletin*, 32(05):389–399.

[Völkl et al., 1999] Völkl, E., Allard, L. F., and Joy, D. C. (1999). *Introduction to electron holography*. Plenum Publishing Corporation, New York.

[Von Blanckenhagen et al., 2001] Von Blanckenhagen, B., Gumbsch, P., and Arzt, E. (2001). Dislocation sources in discrete dislocation simulations of thin-film plasticity and the Hall-Petch relation. *Modelling and Simulation in Materials Science and Engineering*, 9(3):157.

[Vurpillot et al., 1999] Vurpillot, F., Bostel, A., and Blavette, D. (1999). The shape of field emitters and the ion trajectories in three-dimensional atom probes. *Journal of Microscopy*, 196:332–336.

[Wall and Dahmen, 1998] Wall, M. A. and Dahmen, U. (1998). An in situ nanoindentation specimen holder for a high voltage transmission electron microscope. *Microscopy Research and Technique*, 42(4):248–254.

[Wang et al., 1998] Wang, Q. H., Setlur, A. A., Lauerhaas, J. M., Dai, J. Y., Seelig, E. W., and Chang, R. (1998). A nanotube-based field-emission flat panel display. *Applied Physics Letters*, 72(22):2912–2913.

[Wang et al., 2004] Wang, X. Q., Wang, M., He, P. M., Xu, Y. B., and Li, Z. H. (2004). Model calculation for the field enhancement factor of carbon nanotube. *Journal of Applied Physics*, 96(11):6752.

[Wang et al., 2007] Wang, Y., Li, J., Hamza, A. V., and Barbee, T. W. (2007). Ductile crystalline–amorphous nanolaminates. *Proceedings of the National Academy of Sciences*, 104(27):11155–11160.

[Wang et al., 2000] Wang, Z. L., Poncharal, P., and De Heer, W. A. (2000). Measuring physical and mechanical properties of individual carbon nanotubes by in situ TEM. *Journal of Physics and Chemistry of Solids*, 61(7):1025–1030.

[Warren et al., 2007] Warren, O. L., Shan, Z., Syed Asif, S. A., Stach, E. A., Morris, J. W., and Minor, A. M. (2007). In situ nanoindentation in the TEM. *Materials Today*, 10:59–60.

[Welser et al., 1994] Welser, J., Hoyt, J. L., Takagi, S.-I., and Gibbons, J. F. (1994). Strain dependence of the performance enhancement in strained-Si n-MOSFETs. *Technical Digest., International*, pages 373–376.

[Wiederhirn, 2007] Wiederhirn, G. (2007). *The Strength Limits of Ultra-Thin Copper Films*. PhD thesis, University of Stuttgart, Max Planck Institute for Metals Research and Institute of Physical Metallurgy.

[Wikipedia, 2013a] Wikipedia (2013a). Aluminium oxide.

[Wikipedia, 2013b] Wikipedia (2013b). Von Mises yield criterion.

[Williams and Carter, 2009] Williams, D. B. and Carter, C. B. (2009). *Transmission Electron Microscopy*. A Textbook for Materials Science. Springer.

[Wilsdorf, 1958] Wilsdorf, H. (1958). Apparatus for the Deformation of Foils in an Electron Microscope. *Review of Scientific Instruments*, 29(4):323–324.

[Wolf et al., 2013] Wolf, D., Lubk, A., Lenk, A., Sturm, S., and Lichte, H. (2013). Tomographic investigation of fermi level pinning at focused ion beam milled semiconductor surfaces. *Applied Physics Letters*, 103(26):264104.

[Wood, 1897] Wood, R. W. (1897). A new form of cathode discharge and the production of X-rays, together with some notes on diffraction. Preliminary communication. *Physical Review (Series I)*, 5(1):1.

[Xu et al., 1990] Xu, Z., Vetelino, J. F., Lec, R., and Parker, D. C. (1990). Electrical Properties of Thin Tungsten Trioxide Films. *Journal of Vacuum Science & Technology A*, 8:3634–3638.

[Yuge et al., 2012] Yuge, R., Toyama, K., Ichihashi, T., Ohkawa, T., Aoki, Y., and Manako, T. (2012). Characterization and field emission properties of multi-walled carbon nanotubes with fine crystallinity prepared by CO2 laser ablation. *Applied Surface Science*, 258(18):6958–6962.

[Zeng et al., 2009] Zeng, W., Fang, G., Liu, N., Yuan, L., Yang, X., Guo, S., Wang, D., Liu, Z., and Zhao, X. (2009). Numerical calculations of field enhancement and field amplification factors for a vertical carbon nanotube in parallel-plate geometry. *Diamond & Related Materials*, 18(11):1381–1386.

[Zhang and Kamino, 2006] Zhang, X. F. and Kamino, T. (2006). Imaging gas-solid interactions in an atomic resolution environmental TEM. *Microscopy Today*, 14:16–18.

[Zhou et al., 2001] Zhou, G., Duan, W., and Gu, B. (2001). Electronic Structure and Field-Emission Characteristics of Open-Ended Single-Walled Carbon Nanotubes. *Physical Review Letters*, 87(9):095504.

Abstract

This thesis has focused on the development of quantitative *in situ* transmission electron microscopy (TEM) techniques. We have used a special nano-probe sample holder, which allows local electrical biasing and micro-mechanical testing. The finite element method (FEM) was used to compare models with the experimental results. In addition to conventional imaging techniques, electron holography has been used to measure electric fields and strains.

The first part addresses cold-field emission from a carbon cone nanotip (CCnT). This novel type of carbon structure may present an alternative to W-based cold-field emission sources, which are used in the most advanced electron guns today. When a sufficiently strong electric field is applied to the CCnT, electrons can tunnel through the energy barrier with the vacuum, which corresponds to the phenomenon of cold-field emission. Using electron holography and FEM, a quantified value of the local electric field at the onset of field emission was found (2.5 V/nm). Combining this with one of the Fowler-Nordheim equations, the exit work function of the CCnT was determined to be 4.8±0.3 eV. The number of charges on the CCnT before and after the onset of field emission was also measured.

The second part focuses on the plastic deformation of Al thin films to test dislocation-interface interactions. A dislocation close to an interface with a stiffer material should be repelled by it. Here, we find to the contrary that dislocations moving towards the oxidized interface are absorbed, even at room temperature. The stress was derived from a combination of load-cell measurements and FEM calculations. Finally, preliminary experiments to combine *in situ* indentation and dark-field electron holography are reported.

Keywords
In situ, transmission electron microscopy, cold-field emission, finite element method, electron holography, elementary charges, nanoindentation, stress, strain.

Résumé

Cette thèse porte sur le développement d'analyse quantitative d'expérience *in situ* de microscopie électronique en transmission (MET). Nous avons utilisé un porte objet spécial, qui combine les fonctions de polarisation électrique locale et tests de micro-mécanique. La méthode des éléments finis (MEF) a été mise en œuvre afin de comparer les résultats issus de la modélisation avec les résultats expérimentaux. En plus des techniques d'imagerie classique, l'holographie électronique a été employée pour mesurer des champs électriques et de déformation.

La première partie traite de l'émission de champ d'une nanopointe faite d'un cône de carbone (CCnT). Ce nouveau type de matériaux pourrait remplacer les pointes de tungstène qui sont utilisés dans les canons d'électrons les plus avancés. Quand un champ électrique suffisamment fort est appliqué au CCnT, les électrons peuvent passer à travers la barrière d'énergie avec le vide par effet tunnel, ce qui correspond au phénomène d'émission de champ. En combinant holographie électronique avec les simulations MEF, une valeur quantitative du champ électrique local a été obtenue pour l'émission (2,5 V/nm). En faisant appel aux équations de Fowler-Nordheim, une valeur de la fonction de travail de sortie du CCnT est déterminée (4,8±0,3 eV). Nous avons également mesuré les charges sur le CCnT, avant et après le début de l'émission de champ.

La deuxième partie porte sur la déformation plastique d'un film mince d'Al pour tester les interactions des dislocation – interface. Une dislocation à proximité d'une interface avec un matériau plus rigide doit être repoussée par celle-ci. Ici, nous constatons que les dislocations qui vont vers l'interface oxydée sont absorbées par cette interface rigide, même à température ambiante. La contrainte locale est déterminée par une combinaison de mesures de forces par le capteur et de calculs MEF. Enfin, des résultats préliminaires de combiner indentation *in situ* et holographie électronique en champ sombre sont présentés.

Mots-clés
In situ, microscopie électronique à transmission, émission de champ froid, méthode des éléments finis, holographie électronique, charges élémentaires, nanoindentation, contrainte, déformation.